# Creating Nano- and Microstructure Catalyst Coated Membrane Interfaces for Improving the Performance of Proton Exchange Membrane Fuel Cells

**by**

**Michael T.Y. Paul**

B.Sc., Simon Fraser University, 2010

Thesis Submitted in Partial Fulfillment of the
Requirements for the Degree of
Doctor of Philosophy

in the
Department of Chemistry
Faculty of Science



**SIMON FRASER UNIVERSITY**

**Summer 2018**

# Approval

**Name:** **Michael T.Y. Paul**

**Degree:** **Doctor of Philosophy (Chemistry)**

**Title:** ***Creating Nano- and Microstructure Catalyst Coated Membrane Interfaces for Improving the Performance of Proton Exchange Membrane Fuel Cells***

**Chair:** Charles J. Walsby
Associate Professor

**Examining Committee:**

**Byron D. Gates**
Senior Supervisor
Associate Professor

**Michael H. Eikerling**
Supervisor
Professor

**Daniel B. Leznoff**
Supervisor
Professor

**Jeffrey J. Warren**
Internal Examiner
Assistant Professor

**Dan Bizzotto**
External Examiner
Professor
Department of Chemistry
University of British Columbia

Date Defended/Approved: June 21, 2018

# Abstract

Proton exchange membrane fuel cells (PEMFCs) are an important low-emission energy generation system that can be utilized for automotive applications. These systems are, however, limited by the use of Pt as the cathode catalyst, where the relatively expensive cost of Pt limits the competition of PEFMCs against petroleum based systems. Due to the unique characteristics of these PEMFC systems, an optimal balance of hydration of the PEM and the catalyst layers must be maintained within the fuel cell. The current densities achievable with the system can be impacted by an inefficient mass transport of the reactants and products that result in over- or under-hydration of the system. Improvements for increasing effective utilization of Pt and optimizing transport characteristics of PEMFCs could further propel this technology into the mainstream. The work presented in this thesis demonstrates an array of approaches to control the interfaces at or within the cathode catalyst layer (CCL). Architectures at the micro- and nanoscale were sought for improving the performance of PEMFCs. These approaches included creating microscale (5 to 50 μm) patterns of the PEM to CCL interface by the direct printing of CCLs and the hot-embossing of the PEMs. Catalyst materials with tuned pore sizes (1 to 0.05 μm) were also prepared with a coating of catalytic nanoparticles (NPs) through the use of polymeric sacrificial templates. Finally, CCLs containing mesoporous (<10 nm) Pt catalysts were prepared by electrodeposition. These CCL architectures were extensively characterized by electron microscopy and electrochemical techniques. Electron microscopy and related spectroscopy techniques were utilized for determining the morphologies and elemental compositions of the structured materials. The performances of these materials were analyzed using *ex situ* solution-based, three-electrode electrochemical cells. Some of the prepared catalysts were further analyzed with laboratory scale [membrane electrode assemblies (MEAs) with a geometric surface area of 5 $cm^2$] and industrial relevant scale [MEAs with a geometric surface area of 40 $cm^2$] fuel cell test stations. The goal of this thesis is to demonstrate the preparation of these materials with commercially available materials and industrially compatible processes, which can be extended to further catalytic materials in the future for further enhancing the efficiencies of PEMFC systems.

*This thesis is dedicated to all of my family, especially my wife, Lena who looks after me tirelessly.*

# Acknowledgements

I would like to thank the following people who contributed to the studies that are presented in this thesis. The work presented in this thesis would not be possible without the input from these individuals.

## Chapter 4.

### Patterning Catalyst Layers with Microscale Features for Proton Exchange Membrane Fuel Cells

- Dongho Kim: Undergraduate student at SFU who optimized the spray coating procedures for preparing microstructured CCLs
- Dr. Madhu S. Saha: Senior scientist at the Automotive Fuel Cell Corporation (AFCC) who provided training and assistance for the Mayer bar coating processes
- Dorina Manolescu: Senior technician at AFCC who provided assistance in the repeated Mayer bar coating of membrane and reference samples.
- Mickey Tam: Senior testing engineering at AFCC who provided assistance in setting up the fuel cell test station analytical procedures used in this study.
- Dr. Juergen Stumper: Principle investigator at AFCC
- Dr. Byron D. Gates Principle investigator at SFU

## Chapter 5.

### Microstructured Membrane for Improving Transport Resistances in Proton Exchange Membrane Fuel Cells

- Dr. Madhu S. Saha: Senior scientist at the AFCC who provided training and assistance for the Mayer bar coating processes
- Dorina Manolescu: Senior technician at AFCC who provided assistance in the repeated Mayer bar coating of membrane and reference samples.
- Mickey Tam: Senior testing engineering at AFCC who provided assistance in setting up the fuel cell test station analytical procedures used in this study.

- Kai Zubrod: Co-op student at AFCC who provided assistance in preparing the membrane electrode assemblies (MEAs) and repeated measurements on the PEMFC test station.
- William Qi: Co-op student at AFCC who provided assistance in preparing the membrane electrode assemblies (MEAs) and repeated measurements on the PEMFC test station.
- Brianna Bailey: Co-op student at AFCC who provided assistance in preparing multiple MEA cross-sections and scanning electron microscopy (SEM) analyses for determining the membrane microstructures.
- Dr. Juergen Stumper: Principle investigator at AFCC
- Dr. Byron D. Gates Principle investigator at SFU

## Chapter 6.

## Template Assisted Preparation of High Surface Area Macroporous Supports with Uniform and Tunable Nanocrystal Loadings

- Brenden B. Yee: Undergraduate student at SFU who provided assistance in preparing multiple samples of nanoparticles (NPs) coated polymer template and optimizing the sol-gel processes used in this study.
- Dr. Xin Zhang: Staff scientist and Advanced Characterization Specialist for who provided training and assistance in performing the focused ion beam milling process and TEM for obtaining the nanoscale cross-sectional images.
- Eiji Alford: Undergraduate student at SFU who provided assistance in preparing multiple samples of NPs coated polymer template and optimizing the electrodeposition processes used in this study.
- D. Brandy K. Pilapil: Graduate student at SFU who provided assistance in the preparation of NPs coated polymer templates and the nanobowls used in this study.
- Dr. Woo Hyuk Lee: Graduate student at SFU who provided assistance in performing the physical vapor deposition process for creating the nanobowls in this study.
- Dr. John-Cristopher Boyer: Post-doctoral fellow at SFU who provided assistance for synthesising the photo up-converting nanoparticles used in this study.
- Dr. Byron D. Gates Principle investigator at SFU

## Chapter 7.

### Mesoporous Platinum Prepared by Electrodeposition for Ultralow Loading Proton Exchange Membrane Fuel Cells

- Dr. Mat Bilton: Post-doctoral fellow at SFU who provided training and assistance in obtaining the transmission electron microscopy (TEM) tilt series for the thee-dimensional reconstruction analyses
- Dr. Stefano Rubino: Post-doctoral fellow at SFU who provided training and assistance in obtaining the X-ray fluorescent (XRF) spectroscopy and inductive coupled plasma mass spectrometry data for the quantification of Pt nanoparticles within the CCLs
- Byron D. Gates Principle investigator at SFU

# Table of Contents

# List of Tables

# List of Figures

# List of Acronyms

| | |
|---|---|
| µCP | Microcontact Printing |
| µTM | Microtransfer Molding |
| 1-BuOH | 1-Butanol |
| 2D | Two Dimensional |
| 3D | Three Dimensional |
| A | Surface Area |
| a.u. | Arbitrary Units |
| ACL | Anode Catalyst Layer |
| $A_{ecsa}$ | Electrochemically active surface area |
| $C$ | Concentration |
| CA | Chornoamperometry |
| CCL | Cathodic Catalyst Layer |
| $C_{DL}$ | Double Large Charging |
| CE | Counter Electrode |
| cps | Counts Per Second |
| CV | Cyclic Voltammetry |
| DCM | Dichloromethane |
| DFT | Density Functional Theory |
| DMF | Dimethylformamide |
| ECSA | Electrochemical Surface Area |
| EDS | Energy Dispersive X-ray Spectroscopy |
| EG | Ethylene Glycol |
| EIS | Electrochemical Impedance Spectroscopy |
| EM | Electron Microscopy |
| $E_o$ | Thermodynamic Electrode Potential |
| EtOH | Ethanol |
| F | Faraday's Constant |
| FAAS | Flame Atomic Absorption Spectroscopy |
| FC | Fuel Cell |
| FEG | Field Emission Gun |

| | |
|---|---|
| FTIR | Fourier Transform Infrared |
| FWHM | Full Width at Half Maximum |
| $G_0$ | Free Energy |
| GDL | Gas Diffusion Layer |
| HAADF | High-Angle Annular Dark Field |
| HOR | Hydrogen Oxidation Reaction |
| HOT | hot fuel cell conditions with lower fuel cell temperatures (above 80 °C) than standard conditions |
| $H_{UPD}$ | Underpotential Desorption of Hydrogen |
| ICP-MS | Inductively Coupled Plasma Mass Spectrometry |
| IR | Infrared |
| $j$ | Current Density |
| $j_{H2}$ | Hydrogen Cross-over Current Density |
| $j_k$ | Kinetic Current Density |
| KL | Koutecký–Levich |
| LB | Langmuir Blodgett |
| LSV | Linear Sweep Voltammetry |
| MEA | Membrane Electrode Assembly |
| MeOH | Methanol |
| MPL | Microporous Layer |
| MPL | microporous layer |
| $N$ | Number |
| η | Overpotential |
| NP | Nanoparticle |
| ø | Diameter |
| ORR | Oxygen Reduction Reaction |
| PEM | Proton Exchange Membrane |
| PS | Polystyrene |
| PVP | Poly(vinylpyrrolidone) |
| q | Charge |
| RE | Reference Electrode |
| RF | Roughness Factor |
| RHE | Reversible Hydrogen Electrode |

| | |
|---|---|
| $R_{id}$ | Pressure Independent Oxygen Transport Resistance |
| $R_{id}$ | Pressure Independent Oxygen Transport Resistance |
| $R_{ion}$ | Proton Resistance |
| $R_{mt}$ | Oxygen Transport Resistance |
| $R_{ohm}$ | Membrane Resistance |
| $R_{pd}$ | Pressure Dependent Oxygen Transport Resistance |
| $R_{short}$ | Short-circuit Resistance |
| RT | Room Temperature |
| RT | Room Temperature |
| SEM | Scanning Electron Microscopy |
| SEM | Scanning Electron Microscopy |
| STEM | Scanning Transmission Electron Microscopy |
| TEM | Transmission Electron Microscopy |
| US DOE | United States Department of Energy |
| WE | Working Electrode |
| WUP | start-up or warm up fuel cell conditions with lower fuel cell temperatures (below 80 °C) than standard conditions |
| γ | surface energy (interfacial tension) |
| ω (in EIS measurements) | Angular Frequency ($s^{-1}$) |
| ω (in RDE experiments) | Rotational Speed of the Electrode in rad/s |

# Glossary

| | |
|---|---|
| Agglomerate | A reversible cluster of nanoparticles. |
| Aggregate | An irreversible cluster of nanoparticles. |
| Faradaic Process | The generation of current through interfacial charge-transfer resulting from an electrochemical reaction at an electrode surface. |
| Fuel Cell | A device which generates electricity from the controlled electrochemical reaction of gaseous fuel (e.g., $H_2$) with oxygen. |
| Nanoparticle | Particles with at least one dimension between 1 and 100 nm. |
| Non-Faradaic Process | The generation of current due to the movement of charged species (e.g., ions) at the electrode-electrolyte interface. |
| Overpotential | Difference between the measured potential onset and the thermodynamic electrode potential for a particular electrochemical reaction. |
| Oxidation | A process that describes the loss of electrons or an increase in oxidation state of a molecule, atom, or ion. |
| Electrochemically active surface area | The surface area of an electrode as measured by electrochemical methods. This value defines the area of the electrode that is accessible for performing electrochemical reactions. |
| Reduction | A process that describes the gain of electrons or a decrease in oxidation state of a molecule, atom, or ion. |
| Thermodynamic Electrode Potential | The thermodynamically determined redox potential for a half-reaction of interest. This value is determined experimentally under standard conditions. |
| Underpotential deposition | The electrodeposition of a species at a less negative potential than its equilibrium reduction potential. This process typically occurs between metal cations and solid metal surfaces. |
| Microstructure | The fine structure of a material that can only be revealed by microscopy. By definition the structures have critical features of less than 0.1 mm. |
| Photolithography | A process used in microfabrication using light to transfer patterns from a photomask to a light sensitive photoresist for creating patterns with thin film or bulk materials. |
| Soft lithography | A family of fabrication or replication techniques utilizing elastomeric, for example, stamps, molds, or conformable photomasks. |
| Macroporous | A material that has large number of pores with diameters in the range of 50 nm to 1 µm. |

| | |
|---|---|
| Mesoporous | A material that contain pores with diameters between 2 and 50 nm. |

## Executive Summary

Proton exchange membrane fuel cells (PEMFCs) are important alternative systems for energy conversion than can reduce our society's dependence on fossil fuels. Although there exist many important implementations necessary for the optimal function of a fuel cell, this thesis focuses on customizing micro- and nanostructured interfaces between the cathode catalyst and the proton exchange membrane (PEM) for improving the performance of PEMFCs. An array of materials with critical feature sizes from 50 μm to <10 nm were prepared and analyzed for their physical and electrochemical properties. The first chapter introduced the operation and prior art for tuning the cathode catalyst layer (CCL) to PEM interfaces. Chapter 2 reviewed the chemical processes that are required for the preparation of the samples, as well as the operation of the PEMFCs. Chapter 3 provided details on the principles of and interpretation of results from the characterization techniques used for analyzing the samples prepared in this thesis. These techniques include methods to study morphological features, elemental compositions, and *ex situ* and *in situ* electrochemical performance of the samples. Chapter 4 detailed the preparation of microstructured CCLs with regular, repeating patterns to improve Pt utilization and CCL water management. Chapter 5 detailed the preparation of microstructured PEMs for improving PEMFC performance under a range of different operating conditions. Chapter 6 demonstrated a range of methods for creating nanoparticle covered macroporous electrodes. These methods were demonstrated with control over both the pore size distributions and a range of elemental compositions. Finally, Chapter 7 provided details on the electrochemical preparation of mesoporous Pt catalysts for use in PEMFCs that exhibited a drastic improvement in Pt utilization over conventionally prepared Pt ink. The works demonstrated in this thesis could serve as a reference and an inspiration for future CCL designs to further improve PEMFC systems for the goal of achieving a sustainable energy future.

# Chapter 1. Introduction

## 1.1 Proton Exchange Membrane Fuel Cells (PEMFCs)

### 1.1.1 Overview of Fuel Cell Systems

To combat climate change and decrease our societies' dependence on fossil fuels, recent efforts have established many viable alternative energy sources, such as harnessing wind and solar energy. Due to the intermittent nature of these power sources, the excess energy generated from these systems must be effectively stored for later use. The methods for energy storage can include batteries (e.g., lead-acid and lithium ion), pumped hydro-power, compressed air storage, and gas generation (i.e., hydrogen and oxygen generation from the electrolysis of water).[1–3] Out of these options for energy storage, hydrogen has been identified as one of the candidates that can be generated from abundant water sources and be stored with at a relatively high energy density (1.5 kWh/kg per system, as of April 2018) compared to other energy storage systems such as lithium ion batteries (~0.25 kWh/kg[248]) and gasoline (12 kWh/kg) , and easily transported to distant locations for off-site usage.[1,2,4] The stored hydrogen gas can be converted back to electrical power with the use a hydrogen fuel cell for applications that include automotive transportation and stationary power generation. To demonstrate the feasibility of the hydrogen economy, fuel cell (FC) systems must be able to convert hydrogen into power both reliably and efficiently.

Some FC designs that can produce emissions-free energy from the reaction of $H_2$ and $O_2$ gases include: anion exchange membrane (AEM) FCs, solid oxide FCs, and proton exchange membrane (PEM) FCs. Solid oxide fuel cells operate at temperatures >500 °C, which limits their deployment to mostly grid-scale facilities. Both alkaline and PEM FCs commonly operate at milder temperatures (<100 °C) that are suitable for smaller scale applications, such as for facility power backup and automotive applications.[3] The development of AEMFCs is currently limited by a lack of anion exchange membranes that

are stable over long-term operation (> 5,000 h).[3,5] The work in this thesis focused on advancing the design of catalyst layers for improving the more well-developed PEMFC system to further improve their utility in automotive applications. The methods demonstrated herein seek to refine the interface between the catalyst and membrane from with microscale features (5 to 50 µm), macroporous catalyst supports (1 µm to 50 nm), and mesoporous catalysts (<10 nm) to improve catalyst utilization, as well as reactant and product mass transport. These structure-to-function demonstrations are not limited to PEMFC technology and could also be extended to other types of membrane-based systems in the future.

### 1.1.2 Overview of the Components of PEMFC

The PEMFC is comprised of several different components that serve a range of purposes for the operation of the FC (**Figure 1.1**). These components include the current collector/gas flow-field plates, gas diffusion layer (GDL), catalyst layers, and proton exchange (polymer electrolyte) membrane. The central part of the PEMFC consists of a PEM that is insulating to electrons, but is permeable to protons. The PEM separates the two half-cells. The PEM is flanked by the anode and cathode catalyst layers on either side, as well as the gas diffusion layers.

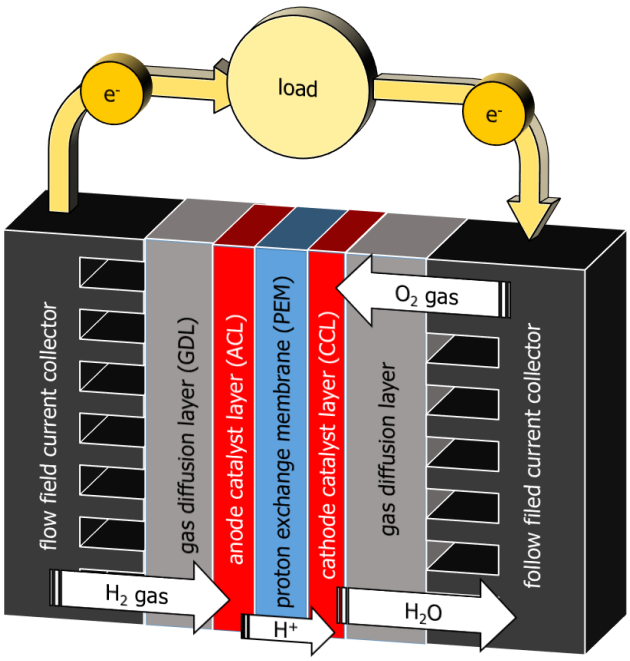


**Figure 1.1** **Schematic of a proton exchange membrane fuel cell (PEMFC) that consist of an electronically insulating PEM that separates the anode and cathode catalyst layers, gas diffusion layers, and current collectors (gas flow plates); the $H_2$ and $O_2$ gases are supplied to the anode and cathode, respectively; and the $H_2O$ generated at the cathode also leaves via the cathode current collector.**

The catalyst layers are used for the catalysis of their respective electrochemical reactions during the operation of PEMFCs. The GDLs are used for providing a conductive path to the catalyst layers, the delivery of reactant gases, and the removal of products. This construct of the catalyst coated membrane (CCM) and gas diffusion layers is often referred as the membrane electrode assembly (MEA). On either side of the MEA, a current collector is placed on top of the MEA for conducting the electrons generated by the catalysts to an external circuit to perform work (e.g., to operate an electric motor). The current collectors are also grooved for the inlet and outlet of reagent gasses and reaction products, respectively. The studies demonstrated in this thesis focus on the interface between the cathode catalyst layer (CCL) and the PEM. This interface is especially important because the rate limiting reaction of the PEMFC occurs at the CCL.[6–9] The details of the chemical reactions that occur during the operation of a PEMFC are described in the follow section (**Section 1.1.3).**

### 1.1.3 Overview of PEMFC Reactions

The operation of a PEMFC relies on the oxidation and reduction of hydrogen and oxygen gas at the anode and cathode, respectively. For a PEMFC, $H_2$ gas is supplied to the anode through the flow-field current collector, where it is oxidized at the anode catalyst layer (ACL) to produce protons ($H^+$) and electrons ($e^-$) (**Equation 1.1**). The protons pass from the anode to the cathode by crossing the PEM. Due to the electrically insulating properties of the PEM, the electrons travel through the external circuit to the cathode. The movement of electrons can be used to power a load that is connected to the external circuit. Oxygen gas (from air or pure oxygen) is supplied to the cathode through the cathode flow-field current collector and reacts the $H^+$ (that diffused across the PEM) and $e^-$ (that were conducted through the external circuit) to produce $H_2O$ (**Equation 1.2**). The overall reaction is the production of water from the oxidation of hydrogen and the reduction of oxygen (**Equation 1.3**).

$$H_2 \rightarrow 2H^+ + 2e^- \tag{1.1}$$

$$2H^+ + 2e^- + \frac{1}{2}O_2 \rightarrow H_2O \tag{1.2}$$

$$H_2 + \frac{1}{2}O_2 \rightarrow H_2O \tag{1.3}$$

The cathodic oxygen reduction reaction (ORR) is the kinetically limiting reaction for PEMFCs, relative to the anodic hydrogen oxidation reaction (HOR).[10] When compared to Pt catalyzed HOR, the Pt catalyzed ORR has slower reaction kinetics that requires in a larger overpotential. This overpotential ($\eta$) is the difference between the thermodynamically predicted reduction potential and the observed reduction potential for the ORR.[11] Electrocatalysts, such as Pt, are required to lower the overpotential of the ORR and the HOR and, thereby, increase the rate of these electrochemical reactions. The anodic HOR has much faster kinetics. The reaction kinetics for the HOR is approximately ~$10^6$ times faster than that for the ORR.[12–14] Currently, platinum is the most commonly used electrocatalyst for both the ORR and the HOR in PEMFCs.[15] Due to the differences in reaction kinetics between the cathodic and anodic reactions, a larger mass (at least 3 to 4 times higher) of electrocatalyst, namely Pt, is required at the cathode than at the

anode.[15–17] A great deal of research has focused on investigating alternative electrocatalysts for reducing the amount of Pt used in the CCL.[15,18,19] Platinum does, however, remain the most suitable cathode electrocatalyst after accounting for catalytic efficiencies and electrochemical stability. This high mass of Pt is one of the cost hurdles that PEMFCs must overcome for the commercialization and widespread adoption of PEMFC technologies.[15,18,19]

A balance of water within the fuel must be achieved to promote the proton conductivity of the PEM and the ionomer phase in the CCL, while not inhibiting the infiltration of the gaseous reactant to the catalytic sites (**Equation 1.1, 1.2, and 1.3**).[20–22] Underhydration and overhydration of the PEMFCs can lead to increased proton and oxygen transport resistances, respectively.[22–24] These inefficiencies can reduce the performance of PEMFCs and the utilization of the Pt catalytically active surface area. The research described in this thesis focuses on modifications to the CCL and PEM interface to seek improvements to the maximum current densities achievable for PEMFCs. Further knowledge of how to improve the CCL and PEM interface could lead to an improved performance of PEMFCs. The design sought in this thesis included modifications to the current design of Pt-based CCLs (a mixture of Pt NPs, C NPs, and ionomer), as well as the design of new CCLs with different catalyst compositions.

## 1.2 The Design of PEMFC Cathode Catalyst Layers (CCLs)

### 1.2.1 History and Evolution of the Designs of Pt-Based Cathode Catalyst Layers

The many components of a PEMFC (see **Section 1.1.1**) can each play a role on influences to its performance. Components, such as the flowfield/bipolar plates and the gas diffusion layer, are shown to greatly impact the performance of the fuel cell by influencing the mass transfer characteristics of the PEMFC.[25–28] Different polymer electrolyte membranes can influence the proton conductivity, long-term durability, and water management of the fuel cell.[5,20,29] The PEMFC characteristics that can be directly

influenced by the CL design include the mass transfer of reactants and products, proton conductivity, stability of the catalyst and its support material, and the utilization of catalyst (current per mass of Pt). These fuel cell characteristics can be tuned by varying the composition and relative amount of materials in the CLs (i.e., Pt NPs, catalyst support, and ionomer), and the processes used to construct the CL.[30–32] For example, the use of different amounts of ionomer or different types of carbon supports can significantly influence the proton conductivity and mass transport characteristics of the PEMFCs.[24,30] The efficiency of a PEMFC is largely influenced by the design of its CCLs due to the rate-limiting nature of the ORR reaction that occurs at the cathode.[30,32–34]

The goals of the recent investigations into the optimization of PEMFC CCLs have been aimed at controlling the mass transfer properties, proton conductivity, electrochemically active Pt surface area, and electrochemical stabilities of the catalyst and its support materials during FC operation.[30–38] Furthermore, in order for PEMFCs to be cost effective against other energy conversion systems, the Pt loading within the system must be kept to a minimum.[15,39,40] The first utilization of PEMFCs in the Gemini project (ca. 1965) used a relatively large mass of Pt (~4 mg $cm^{-2}$) compared to their modern counterparts.[41,42] The early CCLs consisted of mostly Pt black mixed with Teflon® that were hot-pressed onto the PEM.[43] These unsupported Pt particles are prone to agglomeration, leading to an overall decrease in Pt utilization. The lack of a support medium for the catalyst also resulted in an inefficient proton conductance and mass transfer properties. To increase the utilization of Pt, research in the 1990s developed CLs prepared from Pt nanoparticles deposited onto a non-catalytic, high surface area conductive carbon support. One of the pioneering studies by Wilson and Gottesfeld of the Los Alamos National Laboratory started with directly spray coating the PEMs with an ink that contained carbon NPs supporting Pt NPs (C NPs ~50-nm diameter; E-TEK 20 wt/wt % Pt/C) and a solubilized ionomer (Nafion®).[41] This approach greatly increased the Pt utilization by improving Pt mass to surface area ratio, reducing Pt NPs agglomeration, and creating a bicontinuous porous network within the CL for the efficient infiltration and removal of reactants and products to and from the catalytic Pt surfaces, respectively. A series of transmission microscopy images (TEM) of the Pt NPs, C particle, and ionomer binder are presented in **Figure 1.2**. The addition of ionomer within the CLs increased their proton conductivity.[44] Some recent studies have also started to utilize graphene and

carbon nanotubes as catalyst supports with an improved resistance to corrosion and further improvements to CL porosities for enhanced mass transport characteristics over a range of fuel cell operating conditions.[45,46]

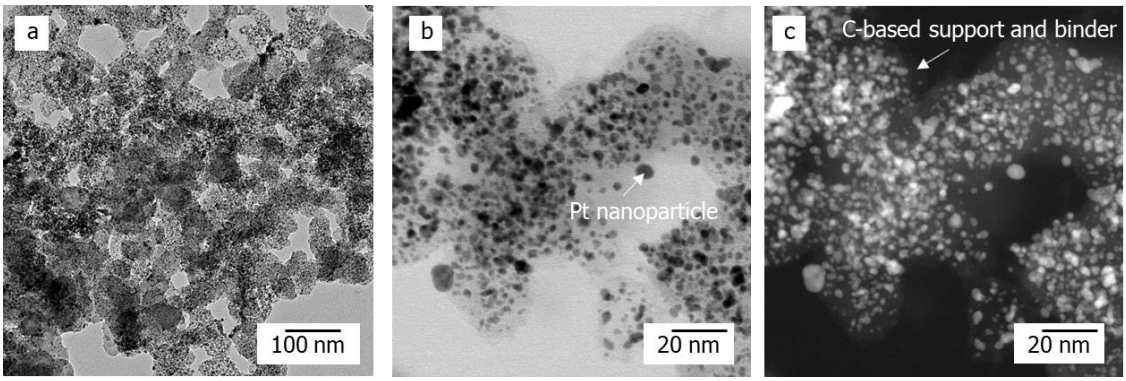


**Figure 1.2. Transmission electron microscopy (TEM) images of the conventional catalyst layers (CLs) that is composed of Pt NPs, C particles, and ionomer binder. (a) a lower magnification TEM image of the CL; (b) a higher magnification scanning transmission electron (STEM) images with an arrow indicating the location of a Pt NP; and (c) a STEM image collected by a high angle annular dark field detector (HAADF) with an arrow indicating the location of the lower density C-based materials.**

Currently, the carbon particle supported Pt NPs is still one of the best catalysts with the highest Pt mass specific surface area, and is currently the most commonly used commercial catalyst, designed for PEMFCs.[7] Some studies have aimed to create microstructured pores within this Pt ink composition for improved PEMFC performance. Soboleva *et al.* investigated microstructures of these conventional CLs and suggested that an increased volume fraction of pores with a diameter of >20 nm could lead to an improved removal of water within the CCLs.[30] Another study by Marquis *et al*. suggested that a void fraction of >1 µm pores created within the CCL can increase the percolation threshold (i.e., threshold where water is transported as accumulated liquid rather than water vapor) to prevent water accumulation within the CCLs.[47] These microstructured CCLs were reported to have a 30-fold higher Pt utilization over CCLs without the microscale pores. A study by Saha *et al.* also suggested that the creation of larger voids within the CL using a modified decal transfer technique to transfer a colloidal catalyst ink could improve the overall performance of PEMFCs by as much as 45% in comparison to reference samples.[48] The void spaces created in all of the aforementioned studies are, however, randomly distributed and have irregular shapes. A technique that involved the use of

sacrificial, monodispersed PS microparticles (500-nm ø) was used by Kinkead *et al.* for creating ordered porous Pt catalyst as a designer catalyst for use in PEMFCs.[49] This technique can was demonstrated to have fine control over the porosity of the resulting material. A study by Zlotorowicz *et al.* further demonstrated the use of this sacrificial template techniques to create regular spherical void spaces (diameters of 500 nm and 1 µm) within the CL that achieved a Pt utilization that was twice the value of the United States Department of Energy (US DOE) target for 2020.[35] In Chapter 4 of this thesis, we aimed to create microscale features organized into regular arrays within the CCL. These microstructured interfaces were demonstrated to improve Pt utilization and water management in a PEMFC when compared to a CCL prepared from continuous films.

For CCLs that are composed of conventional Pt and C nanoparticles, the porosities and the ionomer content of the CCL can be tuned to improve proton conductance of the CCL (see **Section 3.5.2** for clarifications on the different resistances that can impede the performance of PEMFCs).[21,22] Generally, an optimally balanced ionomer content within the CCL is required for improving PEMFC performance.[21,22] A study by Afsahi *et al.* indicated that the ionomer (Nafion®) content may need to be tuned between 25 and 35 wt/wt % to the total weight of the CCL for operating under conditions that require a relatively low or high overpotential, respectively.[21] A higher ionomer content within the CCLs (e.g., greater than 30 wt/wt%) can lead to an increase in oxygen mass transfer resistance, as well as overall system resistance by forming a gas impermeable and electrically resistive layer over the Pt catalysts.[22,50] A study performed by Karst *et al.* demonstrated that the introduction of 10 to 40-µm wide cracks in the PEM can improve water management under conditions leading to drying and flooding of fuel cells without changing the ionomer content of the CCLs.[8] The water formation was observed to be collecting near cracks of the CLs when compared to smooth CLs. In Chapter 5, regular 20-µm diameter microstructures at the PEM and CCL interface were created with the aim of improving water management in PEMFCs. These interfaces were created by hot-embossing PEMs with lithographically created masters and spray coating these microstructured PEMs with layers of CCL inks. This fabrication process enabled control over the aspect ratio of the features created at this interface by tuning the dimensions of the patterns in the masters, as well as by adjusting the embossing temperature and

pressure. It was demonstrated that these microstructured interfaces between the PEM and CCLs exhibited a significant improvement in FC operation over planar interfaces.

The most direct method for tuning the performance of PEMFCs is to change the compositional makeup of the CCL. It was demonstrated by Wilson and Gottesfeld that the use of high surface area carbon catalyst supports can improve the performance of PEMFCs.[51] The diameters of these support particles can also be tuned to improve the mass transfer characteristics of the CL. These carbon particles can, however, degrade through the long-term operation of the FC (>5,000 h) that can lead to agglomeration and loss of Pt catalysts.[52,53] Recent studies have started investigating different types of carbon materials, such as graphene and carbon nanotubes with a higher resistance to corrosion than graphitized carbon nanoparticles (i.e., Vulcan XC-72 and Ketjenblack). Studies have also demonstrated that the use of niobium and tantalum doped Pt supports can exhibit an improved corrosion resistance in comparison to pure carbon materials.[53–56] Chapter 6 of this thesis demonstrated a range of different methods for preparing catalyst nanoparticles that are supported on a range of ordered macroporous materials (with pore sizes of 300 to 50 nm in diameter). The outlined methods to prepare these porous support materials offered great control over the composition of both the catalysts and catalyst supports, as well as the pore sizes of the catalyst supports. The interaction between designed composition of NPs and the porous support can also further improved the efficiencies of the catalysts by forming strong metal-support interactions.[57,58] The catalyst supported materials prepared in the Chapter 6 included thin metal films prepared by physical vapor deposition, metal matrices prepared by electrodeposition, and metal oxides prepared by sol-gel processes. These arrays of supported catalysts are not only potential candidates for use as PEMFC catalysts, but various combinations of materials were also prepared as a demonstration of their extension to applications such as photovoltaics and direct alcohol fuel cells. A study by Kim *et al.* also demonstrated that CCLs consisted of ordered macropores films can enhance the Pt mass activity of the PEMFC when compared to conventional ink-based CCLs.[59] These catalyst support architectures and their processes for preparation were not demonstrated in prior literature and showed a great promise for use in preparing materials for various electrochemical systems.

Currently, most commercial CLs are prepared with similar ink formulations to those developed by Wilson and Gottesfeld, which consisted of randomly distributed Pt NPs, carbon NPs, ionomer, and pores spaces.[41] To further improve the mass activities of PEMFC catalysts, mesoporous Pt catalyst prepared by electrochemical deposition was demonstrated in Chapter 7 in comparison to conventionally prepared CLs. These catalysts were determined with pore sizes that are in the range between 10 to 3 nm in diameter. These mesoporous Pt also exhibited an increase in the surface area that resulted from a high degree of porosity (60 % pore spaces by volume) within the material formed during the electrodeposition process. In a study performed by Tajabadi *et al.,* they demonstrated that high surface area Pt nanoflowers can greatly enhance the performances of electrochemical systems.[60] This study presented in Chapter 7 is one of the two studies reported to date that have demonstrated that electrodeposition is a more suitable method for preparing electrocatalysts by selectively depositing catalysts at sites within the CCL that have sufficient ionic and electronic conductivities.[60,61] It is suggested that the improved performance of electrodeposited Pt arose from not only the selective deposition of Pt particles, but also the discrete segregation of the Pt catalyst from the mixture of C and ionomer.[62] The study demonstrated in Chapter 7 is also the first study—to the best of our knowledge—that has demonstrated the use of CCLs containing electrodeposited mesoporous Pt in PEMFCs.

The investigations of structure to function correlations in this thesis demonstrated methods for increasing the performance of PEMFC with interfacial features on different length scales. In summary, the interfacial features demonstrated herein included microscale CCL to PEM features (5 to 50 μm), macroporous CCL materials (1 μm to 50 nm), and mesoporous Pt containing CCLs (<10nm). These implementations sought to improve the performance of PEMFCs and to enable this technology to become a more cost effective energy conversion technology for the world-wide market.[63]

# Chapter 2.

# The Chemistry of Lithographic Preparations and the Oxygen Reduction Reaction

## 2.1 Overview

The most import chemistries of the polymers, surfaces, and catalytic processes involved in this thesis are described in detail in this Chapter. The aim of this thesis is to prepare nano- to micro-structured interfaces between the CCL and the PEM for improving the performance of PEMFCs. Photolithgraphically prepared masters for embossing and elastomeric stamps were used to create the desired interfaces in this thesis. The masters were used as molds for casting elastomeric stamps and for mechanically imprinting microscale interfacial patterns into the PEMs. The elastomeric stamps were used for printing CCLs with regular arrays of repeating microscale patterns. The chemical reactions involved in the preparation of these masters and the elastomeric stamps are described in **Section 2.2** and **2.3**. In this thesis, nanoparticles coated on macroporous support materials were prepared for use as electrochemical electrodes. This preparation method involved the use of sacrificial PS templates that were coated with catalytic nanoparticles. This coating process is facilitated by the self-assembly of nanoparticles onto the polymer templates. The surface chemistry of the self-assembly process is described in **Section 2.4**. All of the catalytic materials prepared in this thesis were aimed at improving the performance of PEMFCs. Therefore, the rate limiting chemical reaction that dictates the reaction of a PEMFC, namely the oxygen reduction reaction, is also described in detail in **Section 2.5**.

## 2.2 Photolithographic Preparation of Rigid Templates

In Chapters 4 and 5 of this thesis, microstructured PEM and CCL interfaces were demonstrated to reduce proton resistances of PEMFCs for both standard and under-hydrated operating conditions. These microscale patterns were imprinted into the PEM by photolithographically prepared SU-8 templates. The SU-8 photoresist is a commonly used

epoxy-containing negative photoresist with good mechanical and chemical stability.[64] The SU-8 consists of an organic solvent, such as toluene and gamma-butyrolactone, a triarylsulfonium salt based photoacid, and the SU-8 monomers.[64,65]

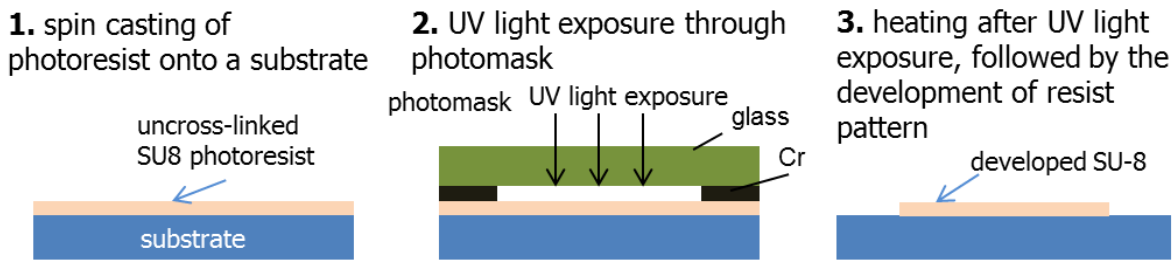


**Figure 2.1. Schematic diagram of the photolithographic process for the preparation of SU-8 patterns.**

The photolithographic processes to prepare masters for embossing consisted of using defined SU-8 microstructures on polished Si wafers as depicted in **Figure 2.1**. The SU-8 is a photoresist, where exposure of the uncross-linked polymer to UV-light will yield a rigid cross-linked polymer at the end of the lithographic process. The spin-cast photoresist is exposed by UV light through a photomask, which consists of Cr patterns on a borosilicate glass plate. The negative image of this Cr pattern is replicated into cross-linked regions of SU-8 at the end of the photolithographic procedure. This pattern reversal process is the reason why SU-8 is categorized as a "negative" photoresist. A depiction of the proposed reaction mechanism for this photo-catalyzed reaction is shown in **Figure 2.2**. After exposure to UV light, a photoacid is generated by the triarylsulfonium salt in the commercially purchased SU-8 prepolymer solution.[66] The irradiated triarylsulfonium salt is excited to a singlet state to yield a phenyl radical and a diphenylsulfonyl radical cation pair. The diphenylsulfinyl radical cation and the phenyl cation react further to produce protons, but the exact mechanism of acid generation is largely unknown.[66] An epoxide group of the SU-8 prepolymer is protonated by the acid, which leads to a nucleophilic attack by a second, non-protonated epoxide (on the same SU-8 monomer or on another monomer), and ring opening of the first epoxide. Further polymerization can be propagated at relatively low temperatures (~65 °C). Once the materials are cooled, the polymerization reaction can be terminated naturally by the depletion of the available nucleophiles, or by alcohol groups that are introduced via the SU-8 developer. The region of the spin cast SU-8 that was exposed to UV light is polymerized, leaving the unexposed region to be

dissolved in the developer. This development process reveals a pattern that replicates the pattern of UV light that was projected through the photomask. The thickness of the photoresist can be controlled by the viscosity of the pre-polymer, for example, by tuning the solvent content and/or by spin-casting these pre-polymers at different spin speeds. These solidified, micropatterned SU-8 templates can be directly used for imprinting PEMs. These SU-8 features can also be used as templates for casting poly(dimethylsiloxane) (or PDMS) elastomers used in printing of the CCLs.

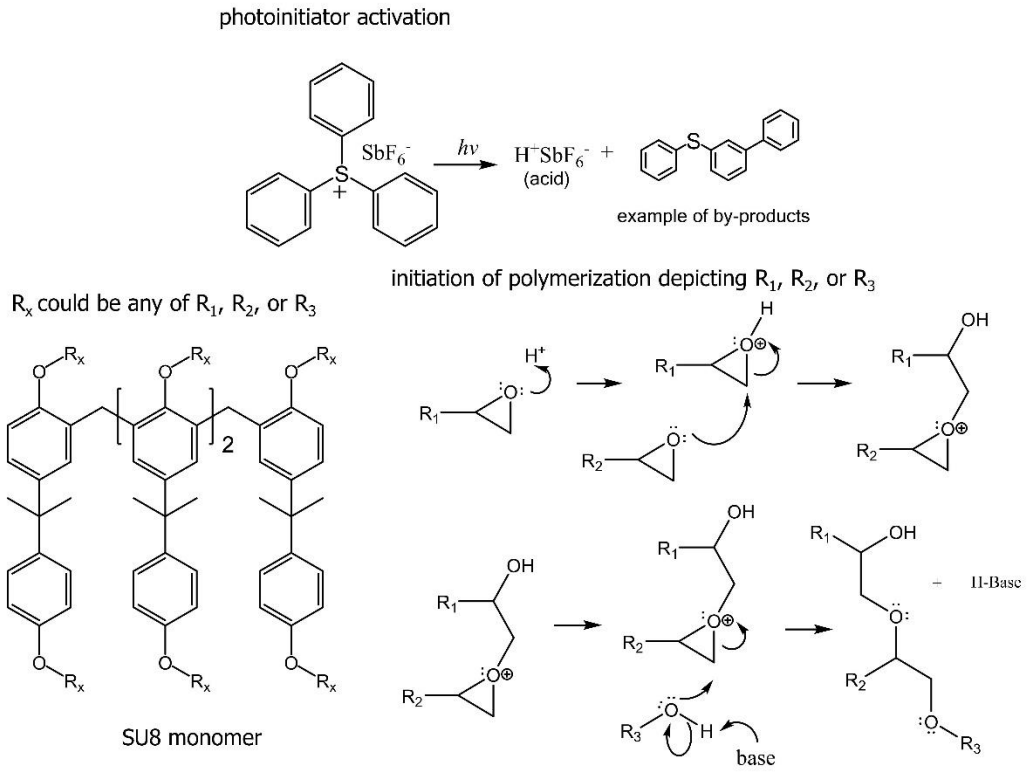


**Figure 2.2. A proposed reaction mechanism for photo-activation of triarylsulfonium acid and polymerization of SU-8.**

## 2.3 Preparation of Elastomeric Stamps for Soft Lithography

In Chapter 4 of this thesis, soft lithography techniques were used to print patterned CCLs onto PEMs. The patterned CCLs exhibited improved mass transfer characteristics than CCLs that consist of continuous films. These patterns were achieved using PDMS based elastomeric stamps. These stamps replicated the features of SU-8 templates with

good feature fidelity, such as for feature width to height ratios of ~10, and minimum feature sizes of ~1 μm.

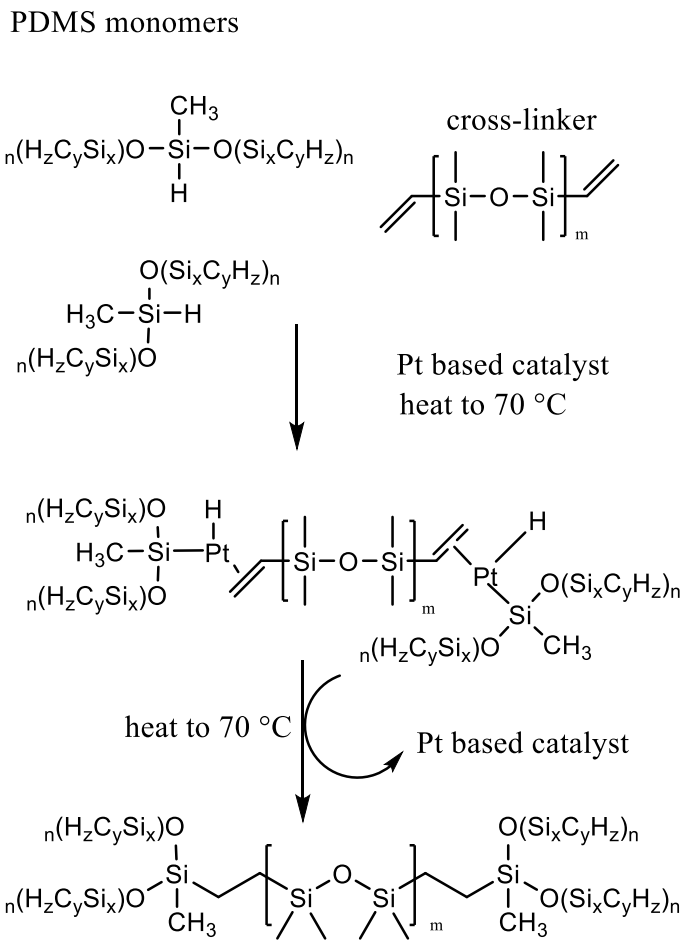


**Figure 2.3. The general mechanisms of polymerization for preparing crosslinked PDMS through the use of a cross-linker and a Pt-based catalyst.**

The commercial precursor to the PDMS elastomer is a two-part reagent. One part consists of an uncross-linked siloxane, and the other part a hardening agent containing a cross-linker and a Pt based catalyst (e.g., inorganic Pt, Karstedt's catalyst, alkane stabilized platinum, or $H_2PtCl_6$).[67–69] The cross-linking of PDMS occurs through a Pt catalyzed hydrosilation that links the hydrosilane groups on the cross-linker molecules to the alkenes of the uncross-linked siloxane through sigma-bond metathesis (**Figure 2.3**).[70,71] This reaction is propagated at 70 °C until there are insufficient alkene, hydrosilane, and catalyst within proximity of each other for further reaction. The advantages of PDMS included: (i) good elastomeric properties as a stamp because it is

sufficiently flexible for the ease of its release from other materials, such as carbon nanoparticle based ink coatings within the recesses of the stamp; (ii) it is stable up to 270 °C, which is important for the integrity of the microstructures within the stamps, as the bonding process of preparing the CCL as part of the MEA can require elevated temperatures (~150 °C); and (iii) the surface of PDMS can be modified with different reactive silanes to achieve an optimal surface energy (e.g., tuning the wetting properties) as needed for coating and printing of the CCL inks.[72,73]

Surfaces containing Si and C atoms, such as surfaces of the SU-8 polymer, PDMS and Si wafers, can be treated with oxygen plasma to form surface hydroxyl groups.[74,75] After this plasma treatment, chlorosilane molecules can be easily grafted onto the hydroxyl terminated surfaces through a condensation reaction (**Figure 2.4**).[76] This surface treatment was performed for the ease of releasing cured PDMS from the masters. It was determined from our studies that a PDMS stamp with a film of octadecyltrichlorosilane yielded an optimal surface chemistry for use in the coating and printing of CCL inks, and a perfluoro silane is suitable for use as a PDMS release layer.

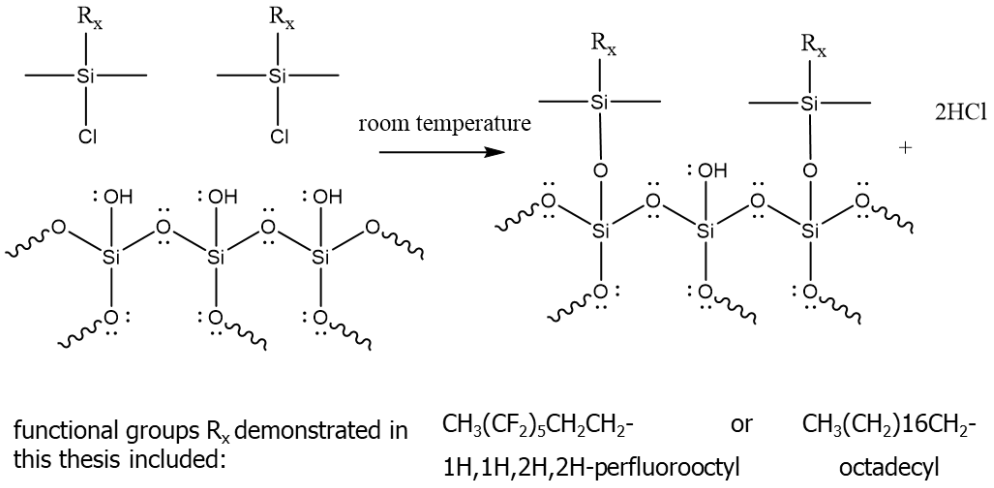


**Figure 2.4. The general mechanism for anhydrous grafting of cholorosilanes onto surfaces containing reactive silanol.**

## 2.4 Heterocoagulation of Nanoparticles on Sacrificial Polymeric Templates

In Chapter 6 of this thesis, ordered macroporous materials with NP coatings were prepared to improve catalyst utilization and sought to enhance the mass transfer of reagents and products involved in the catalytic reaction. The first step in preparing these NP coated macropores was a heterocoagulation of metal NPs (guest material) onto the surfaces of polystyrene (PS) microspheres (host material). An example of this heterocoagulation is presented in **Figure 2.5**.

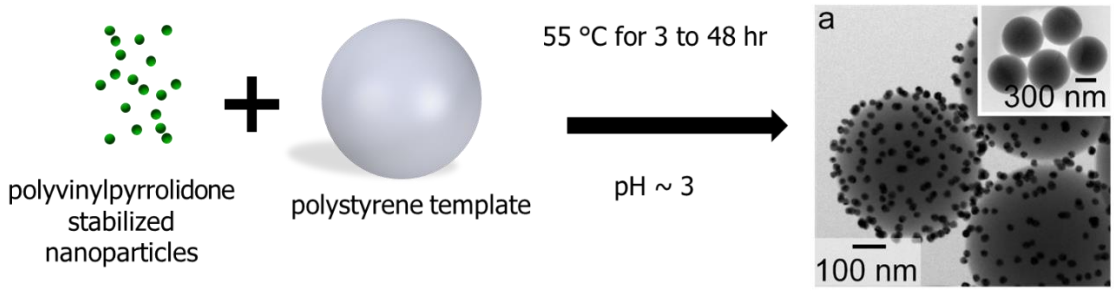


**Figure 2.5. Schematic diagram of the heterocoagulation process between metallic NPs and polymer templates. (a) A TEM image of Au NPs coated polystyrene templates; and inset is a TEM image of the bare polystyrene templates.**

This heterocoagulation process is driven by a reduction of interfacial tension (surface energy) between the PS particles and the solvent. The PVP-coated metal nanoparticles act as a steric stabilizer, coating the surfaces of both the NPs and the PS particles.[77,78] The total interfacial free energy, $G$, is described as the sum of the products of the respective interfacial areas (A) and surface energy ($\gamma$). Assuming a single host particle with a number of non-coagulated ($N$) guest particles, the total interfacial free energy, $G_0$, can be expressed as:

$$G_0 = \gamma_{hm}A_{hm} + N_t\gamma_{gm}A_{gm} \quad (2.1)$$

The subscripts h, g, m, and t denote the host, guest, medium, and target (final hetercoagulation assembly), respectively. Upon the heterocoagulation process, when the guest particles are readily immobilized onto the host particle (assuming a homogeneous

interaction between the guest and the host particles), the expression can be written follows:

$$G_t = (A_{hm} - N_t A_{gh})\gamma_{hm} + N_t(A_{gm} - A_{gh})\gamma_{gm} + N_t A_{gh}\gamma_{gh} \quad (2.2)$$

The total free energy change, $\Delta G$, can then be expressed as:

$$\Delta G = G_t - G_0 = -N_t A_{gh}(\gamma_{hm} + \gamma_{gm} - \gamma_{gh}) \quad (2.3)$$

The process is thermodynamically favorable if $\Delta G$ is negative. When preparing NP coated polymer templates in this thesis, this heterocoagulation process occurs almost instantaneously. The association between NPs and polymeric templates were observed to be physically stable over a period of up to months. These assemblies also exhibit no change in morphology upon purification and resuspension in various solvents including water, ethanol, and 1-butanol. These experimental observations suggest that the thermodynamic interaction between the NPs and polymer templates is favorable for by minimizing the interfacial tension.

## 2.5 The Chemistry of the Oxygen Reduction Reaction at the Cathode of a PEMFC

The cathodic ORR is the rate determining step for the PEMFC. The activation energy of the ORR is orders of magnitudes higher than the hydrogen oxidation reaction that occurs at the anode of a PEMFC.[79] There are two potential pathways for the ORR under acidic conditions. The first is a dissociative pathway that includes the transfer of 4 electrons and 4 protons in a process that reduces $O_2$ gas directly to $H_2O$.[80] The second pathway involves the formation of $H_2O_2$ intermediates through a 2 electron pathway. A simplified summary of the reaction mechanisms for both of these pathways are described below.

For the pathway that proceeds through a 4 electron process with $O_2$ dissociation, $O_2$ is adsorbed onto the surfaces of the Pt and the oxygen–oxygen bond breaks to form 2 adsorbed oxygen atoms on the Pt surfaces:

$$½\, O_2 + \ Pt \ \rightarrow \ O\text{—}Pt \tag{2.3}$$

These oxygen atoms are protonated by $H^+$ that have diffused through the PEM from the anode, and are reduced by electrons provided through the external circuit to produce surface bound hydroxide groups:[81]

$$O\text{—}Pt \ + \ H^+ + e^- \rightarrow \ OH\text{—}Pt \tag{2.4}$$

The surface bound OH is further reduced and protonated to produce water that is released from the Pt surfaces:

$$OH\text{—}Pt + H^+ + e^- \rightarrow H_2O + Pt \tag{2.5}$$

An alternative ORR pathway is through an associative mechanism where the $O_2$ bond does not break during the adsorption of oxygen onto the metal surfaces.[82]

$$\mathrm{O}_2 + Pt \rightarrow \ \mathrm{O}_2\text{—}Pt \tag{2.6}$$

$$O_2\text{—}Pt \ + \ \mathrm{H}^+ + e^- \rightarrow HO_2\text{—}Pt \tag{2.7}$$

Since the oxygen bonds are not broken in the associative pathway, the adsorbed $H_2O_2$ is formed upon further reduction:

$$HO_2\text{—}Pt + H^+ + e^- \rightarrow H_2O_2\text{—}Pt \tag{2.8}$$

The $H_2O_2$ may desorb from the Pt surfaces or react further to produce 2 water molecules:

$$H_2O_2\text{—}Pt \rightarrow H_2O_2 + Pt \tag{2.9}$$

$$H_2O_2\text{—}Pt \ + 4H^+ + e^- \rightarrow 2H_2O \tag{2.10}$$

The formation of $H_2O_2$ is undesirable because it could lead to the degradation of the carbon particles that supports the Pt catalyst, as well as degradation of the GDL. The $H_2O_2$ can also diffuse into the PEM and lead to radical degradation of the membrane.[83]

The nature of the reaction (e.g., whether a 2 or 4 electron process that occurs at the working electrode) can be probed using a rotating disk electrode setup. The details of this method for determining the ORR reaction pathways are described in detail in **Section 3.4.3**.

# Chapter 3.

# Characterization Methods

## 3.1 Overview

The preparation of micro- and nanostructured PEMFC cathode catalysts were investigated in this thesis. A range of characterization methods were used for analyzing the elemental composition, morphology, and electrochemical properties of these catalysts. Electron microscopy was used for visualizing the submicron morphologies of the materials, as well as to provide valuable elemental information regarding the analyzed samples. The X-ray fluorescence (XRF) technique was used for the detection and quantification of the precious metal contents of the CLs. *Ex situ* three-electrode, electrochemical experiments were performed to assess the ORR activities of the catalytic materials. *In situ* electrochemical and PEMFC experiments were performed for evaluating the prepared catalytic materials for their intended applications.

## 3.2 Electron Microscopy and Related Techniques

Electron microscopy (EM) is an indispensable technique for visualizing the nano- to microscale features that could not be observed in detail with optical microscopy techniques. The increased resolving capability of an electron microscope is due to the use of electrons with significantly reduced incident wavelengths when compared to the wavelengths of visible light commonly used in optical microscopy. This reduction in incident wavelength decreases its diffraction limit and improves the spatial resolution of the corresponding microscopy techniques. The small wavelength of the electron beam (~2.51 pm at 200 kV in the system used in this study; the wavelength is inversely proportional to the acceleration voltage of the electron beam) enabling the observation of nanostructures and nanostructured surfaces.[84] In addition, the interactions between the electron beam (an ionizing radiation source) and the sample can also produce a wide variety of secondary signals that can provide insight into the composition of the materials

within the sample.[84–86] Examples of different signals that can be produced when an incident electron beam interacts with a sample are shown in **Figure 3.1**.

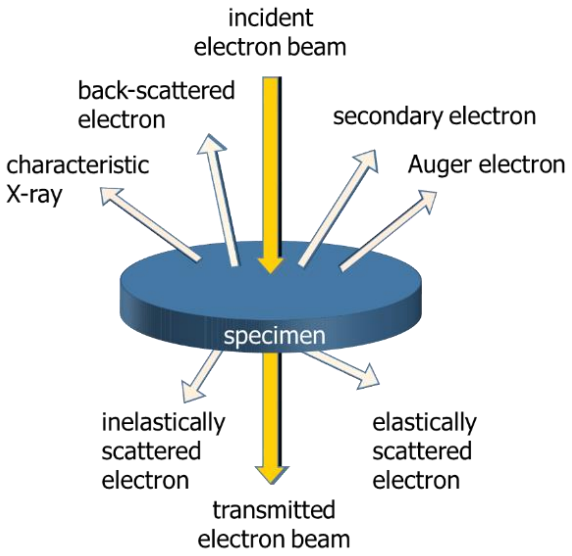


**Figure 3.1. A schematic depiction of the various signals generated from the interaction of a high energy electron beam with a thin sample.**

For TEM, electrons can be emitted from a field emission gun (FEG) and focused into a narrow beam that is projected onto a thin sample (<100 nm in thickness). The transmitted electrons are refocused to generate a projected image of the sample. The contrast in the bright-field TEM images arises from differences in electron density within and thickness of the sample. An increase in the sample thickness, and electron density of the elements therein, can limit the transmission of electrons through the sample. Regions with the greatest thickness or materials with the greatest Z number (electron density) are visualized as dark regions in the sample when compared than those with a lesser Z number or thickness. Scanning TEM (STEM) images are acquired by scanning a focused electron beam across the sample.[87] The projected e-beam resulting from the scanned beam is reconstructed into an image. A high-angle annular dark-field (HAADF) detector, at a position beyond the specimen with respect to the direction of the incident beam, can be used to collect the inelastically scattered electrons at high angles (typically 3.4 to 9.1° from the incident beam).[84,88] A dark-field image is created with brighter regions corresponding to positions of the sample indicating a higher electron scattering power (i.e., higher Z number of elements within the sample). This imaging mode can also be coupled with energy-dispersive X-ray spectroscopy (EDS) to collect valuable chemical information

across the sample for the spatial identification of its elemental composition (**Figure 3.2**).[84–86] The emitted X-rays are characteristic of the elements within the sample. Both STEM and TEM techniques are used extensively for the studies presented in Chapters 4 and 5 to provide spatial information on the atomic composition and for high-resolution visualization of the mesostructures (<10 nm features), respectively.

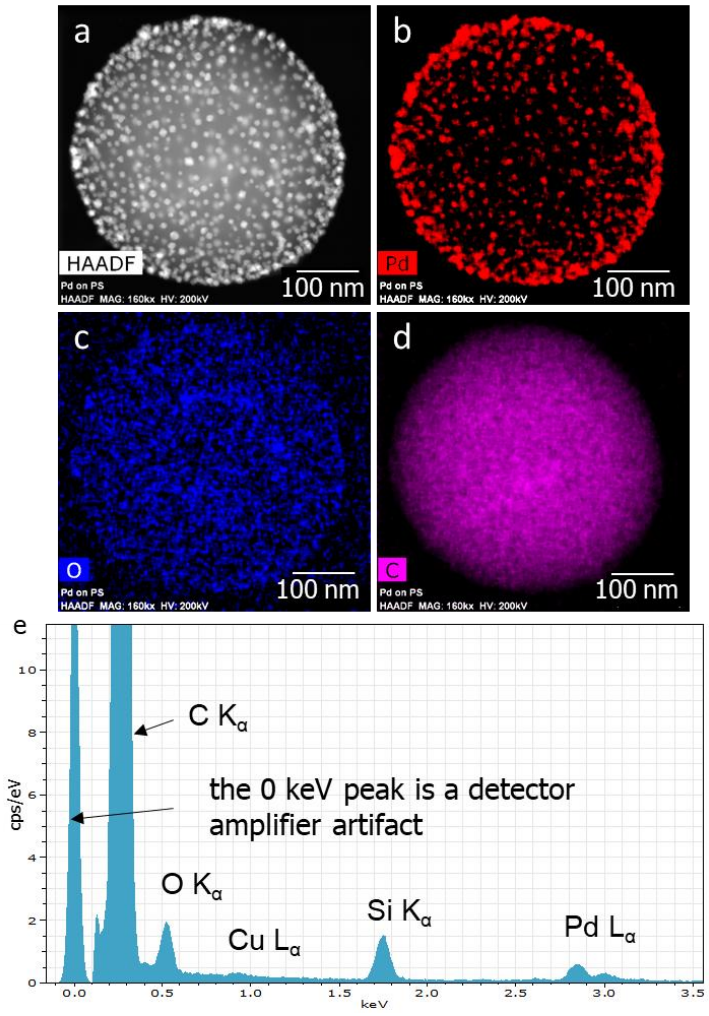


**Figure 3.2. The STEM image, EDS maps, and the corresponding overall EDS spectrum of Pd nanoparticles (~10-nm ø) coated onto a polystyrene sphere (500-nm ø): (a) A HAADF image; and EDS elemental maps of the (b) Pd, (c) O, (d) C signals; and a representative EDS spectrum.**

In scanning electron microscopy (SEM), a focused electron beam is scanned across the sample in a manner similar to STEM analyses. The images in SEM are, however, generated from the detection of secondary and/or backscattered electrons.[87]

The contrast in an SEM image can arise from variation in sample composition, as well as sample topography (e.g., edge effects).[87] The differences in elemental compositions can result in variations in the amount of backscattered and/or secondary electrons emitted from the surfaces of the samples. Generally, elements with higher Z number, or materials with a higher conductivity, are visualized as brighter regions in an SEM image. Because of their higher scattering power, more electrons are scattered and detected by the electron backscatter detector. Conductive materials are also viewed as brighter regions in the secondary electron image because they could interact with the incident electron more easily to produce secondary electron signals. The emission of secondary electrons is also sensitive to the location of the incident electron beam relative to the morphological features of the sample. The closer the incident beam is to an edge of a feature, the more secondary electrons can escape from the sample and, thus, generate apparent topographical contrast in the resulting SEM image.[84–86] This "edge effect" was depicted schematically in **Figure 3.3**. The interactions between the electron beam and the sample can also generate characteristic X-rays that are detected by an EDS detector for elemental identification (**Figure 3.4**). The incident electron interacts with the material and displaces an inner shell electron. A higher shell electron drops (relaxes) to fill the vacancy created by the displaced electron. The difference in energy of this electronic transition is released as an emitted X-ray. The kinetic energy of this emitted X-ray is characteristic of the Z number of the source element. When EDS is used in conjunction with rastering of the focused electron beam, a map of the detected X-ray emission lines can be produced to spatially resolve the locations of different elements within the sample. This series of SEM techniques were used extensively in this thesis for visualizing small features within the samples, which were incompatible with TEM analyses (e.g., too thick of a sample).

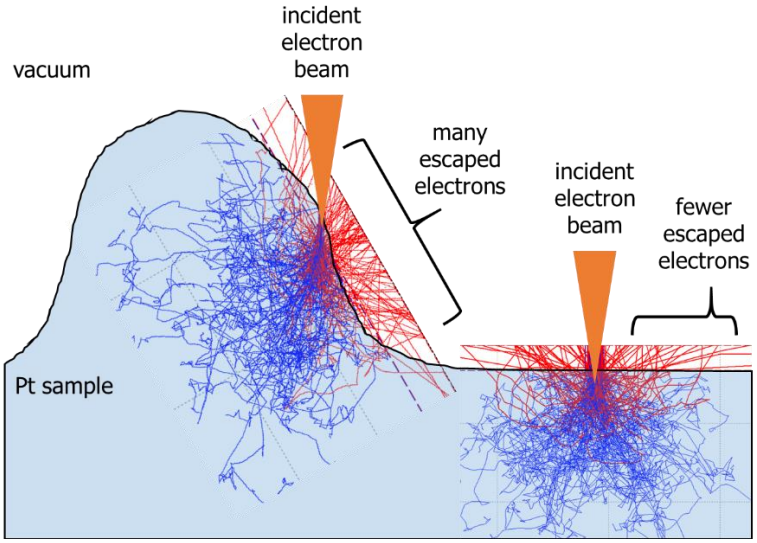


**Figure 3.3.** **Monte Carlo simulation (by CASINO; Université de Sherbrooke, Québec) of electron trajectories (e.g., with an incident acceleration potential of 15 kV) in a Pt sample. The diagram depicts an increase in the number of escaped electrons when the focused electron beam is near to an edge of the surfaces.**

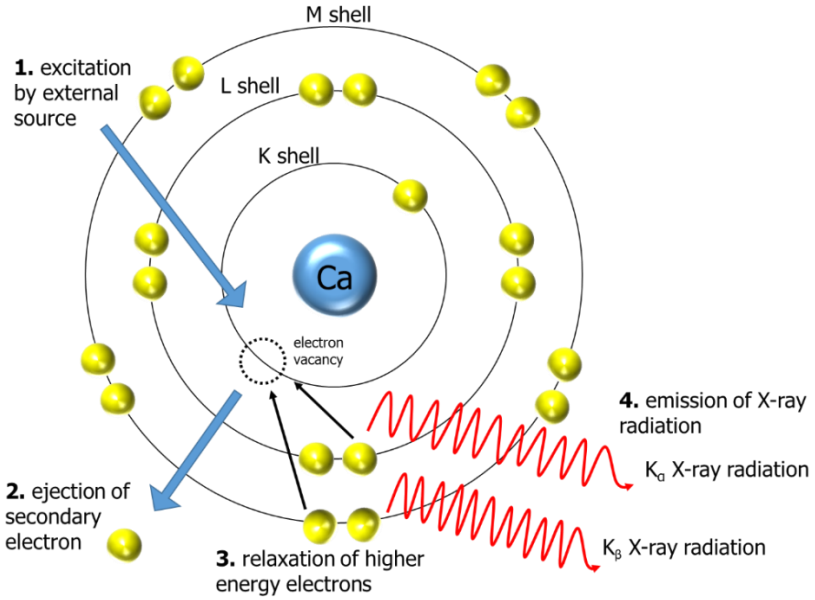


**Figure 3.4.** **Schematic diagram of the mechanism of X-ray generation from an incident excitation. The incident excitation can be electrons or X-ray radiation for use with energy-dispersive X-ray spectroscopy (EDS) and X-ray fluorescence spectroscopy (XRF), respectively.**

## 3.3 X-Ray Fluorescence Spectroscopy

X-ray fluorescence is a non-destructive elemental analysis technique used for determining the Pt content of catalytic materials used in this thesis. Similar to the principles of EDS, this technique utilizes an X-ray source (instead of the focused electron beam used in EDS) to perturb the materials and, subsequently lead to the emission of secondary X-rays (**Figure 3.4**). Materials of different Z numbers will emit distinct X-rays that have energies specific to their elemental composition.[89] Since, the incident excitation utilizes X-rays, the interaction volume of XRF is larger (e.g., at least 20 µm along the Z-axis) when compared to the aforementioned EDS techniques, which achieves a penetration into C films to ~1.20 µm by an electron beam accelerated at 10 kV.[90] The intensities of the emission will, however, still depend on sample Z number, material density (e.g., a continuous film versus a distributed powder), sample thickness, and relative amount of each element in the sample. A typical XRF spectrum of a CCL containing Pt NPs is presented in **Figure 3.5** depicting the various Pt emission lines that were obtained from an XRF analysis (the Cu signals originated from components in the XRF system). To assess the Pt content of the samples, the XRF system was calibrated using commercially purchased standards each with a known Pt content and similar sample thickness. These XRF standards consist of a similar matrix of materials (carbon particles and ionomer binder) and a similar sample thicknesses (from 5 to 50 µm) to those for conventional PEMFC CLs. A calibration curve was constructed by integrating the Pt peak for the most intense Pt $L_{\alpha}$ transition that occurs at 9.442 eV. These peak areas were plotted against the known mass concentrations of Pt in the CLs. Samples containing a mass of Pt that was within the range established by the calibration curve were accurately determined by correlating the determined XRF Pt signal to Pt loadings of the calibration standards. This elemental analysis technique enabled a simple and fast determination of the Pt content within these standard reference materials and within the experimental samples.

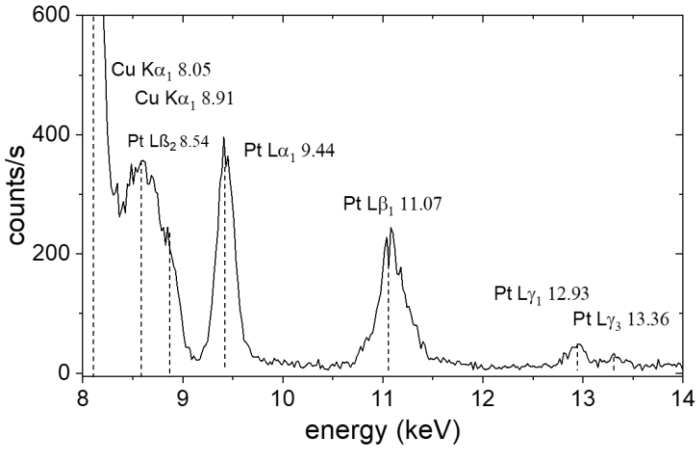


**Figure 3.5. An XRF spectrum of a CCL depicting the different Pt signals that can be detected by the system.**

## 3.4 *Ex situ* Electrochemical Characterizations

### 3.4.1 Three Electrode Electrochemical Techniques

Due to the complexity of the components in PEMFCs, the process of screening for suitable electrocatalytic materials by building PEMFCs is not cost effective due to the large amount of trial-and-error that must be performed for identifying a suitable catalyst material. Therefore, electrochemical analyses for assessing electrocatalysts can be performed *ex situ* in an electrochemical cell with a three-electrode setup (**Figure 3.6**). This electrochemical setup is comprised of a working electrode (WE; containing the material that is being analyzed), a reference electrode [RE; such as a reversible hydrogen electrode (RHE), or silver/silver chloride electrode (Ag/AgCl)] and a counter electrode (CE; such as a Pt mesh or graphite rod).[11] The electrodes are immersed in a conductive electrolyte that is relevant to the reaction under investigation. For example, the ORR is measured in an oxygen saturated solution containing $H_2SO_4$. The electrochemical analysis is performed using a potentiostat. The applied potential, as well as the resulting current, are measured and recorded for further analysis. An array of electrochemical analyses, such as cyclic voltammetry (CV), linear scan voltammetry (LSV), and chronoamperometry (CA) were utilized in these studies to assess the electrochemically active surface area

($\boldsymbol{A}_{ecsa}$), voltage dependent performance of the ORR, and the constant potential or steady state performance of the ORR, respectively, for the samples of interest.[91,92]

For voltammetry techniques used in this thesis, including CV, LSV, and CA, the required voltage setpoints for the analyses were entered into the software that controls the potentiostat. During the experiments, the potential difference between the WE and the RE is maintained to equal the voltage setpoint entered in the software. The potentiostat accomplishes this task through a feedback loop that allows current to flow from the CE to the WE. The details of this setup can be reviewed in **Section 1.3.4** and **15.3** in the Electrochemical Methods textbook written by Bard [11].

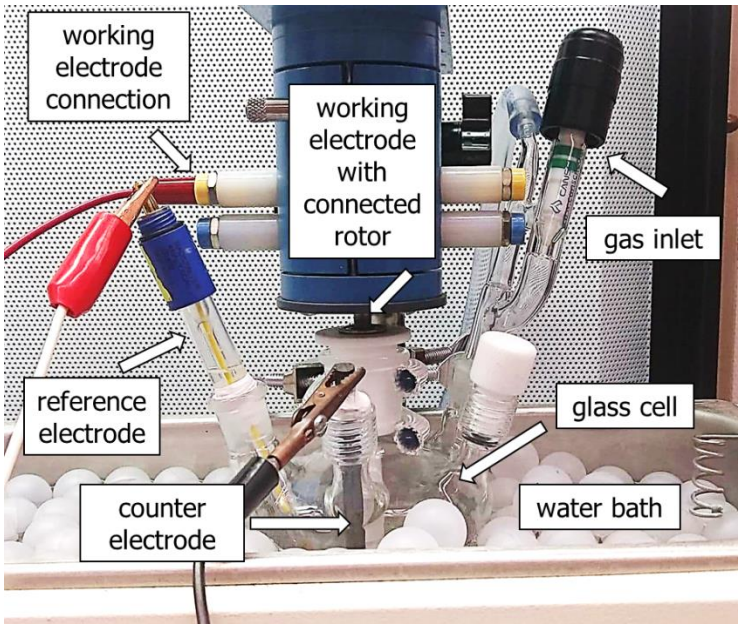


**Figure 3.6. A photograph of the rotating disc electrode (RDE) incorporated into a typical three-electrode setup used for the studies outlined in this thesis. The setup consists of a working electrode, a counter electrode, and a reference electrode. The electrodes are connected to a potentiostat with the electrodes inserted into an electrolyte filled glass cell that is immersed in a temperature controlled water bath.**

## 3.4.2 Cyclic Voltammetry Techniques

The electrochemical CV technique applies a potential between the WE and CE that is scanned linearly between two set points (i.e. $E_1$ and $E_2$ in **Figure 3.7**) at a constant rate of change (measured in mV $s^{-1}$). The current that passes between the WE and CE is

measured by the potentiostat. The CV analysis is useful for assessing different faradaic processes, such as oxidation and reduction reactions, as well as non-faradaic processes (e.g., capacitive currents), such as chemical adsorption and desorption that occur at the electrode/electrolyte interface of the WE electrodes.[11,91,92]

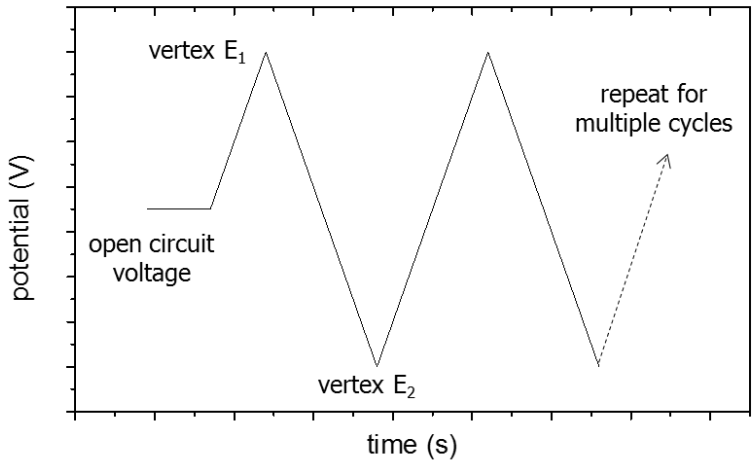


**Figure 3.7. Potential-time relationship for a cyclic voltammetry measurement.**

To assess the $\boldsymbol{A}_{ecsa}$ of the Pt electocatalysts studied in this thesis, a series of CV profiles were obtained between $E_1$ = 0.05 V and $E_2$ = 1.25 V (versus a RHE) in a 0.5 M $H_2SO_4$ electrolyte. The voltages for $E_1$ and $E_2$ are defined by the stability of the electrolyte. At the WE, $H_2$ and $O_2$ gases are produced at potentials that are less than $E_1$ and greater than $E_2$, respectively. These upper and lower potential limits are similar to the potential limits of the cathode under PEMFC operating conditions. A typical CV profile for a polycrystalline Pt WE over this potential range is displayed in **Figure 3.8**. The current measured in this CV analysis results from processes that include double layer charging ($C_{DL}$, non-faradaic capacitive current), underpotential adsorption or desorption of H ($H_{upd}$), and Pt oxide formation or reduction. The $H_{upd}$ adsorption and desorption peaks (~ 0.05 to 0.4 V vs. RHE) are the results of the energy required to displace or adsorb H on different crystalline facets of Pt. In the forward scan, $H_{upd}$ desorption primarily occurs on the (110), (111), and (100) facets at approximate voltage ranges of 0.05 to 0.15 V, 0.15 to 0.25 V, and 0.25 to 0.4 V (vs. RHE), respectively.[93–96] The formation and reduction of Pt begins approximately at 0.85 V and 0.8 V (vs. RHE), in the forward and reverse scans,

respectively, of the applied potential.[93–96] The positive and negative currents observed during the forward and reverse scan in the region between ~ 0.4 to 0.5 V (vs. RHE) are the double layer charging currents for displacing the non-reactive species from the electrode surfaces. This constant $C_{DL}$ current is the energy used for displacing the electrolyte from the surfaces of the working electrode. Generally WE materials with a higher $\boldsymbol{A}_{ecsa}$ will result in a larger $C_{DL}$ current.[92]

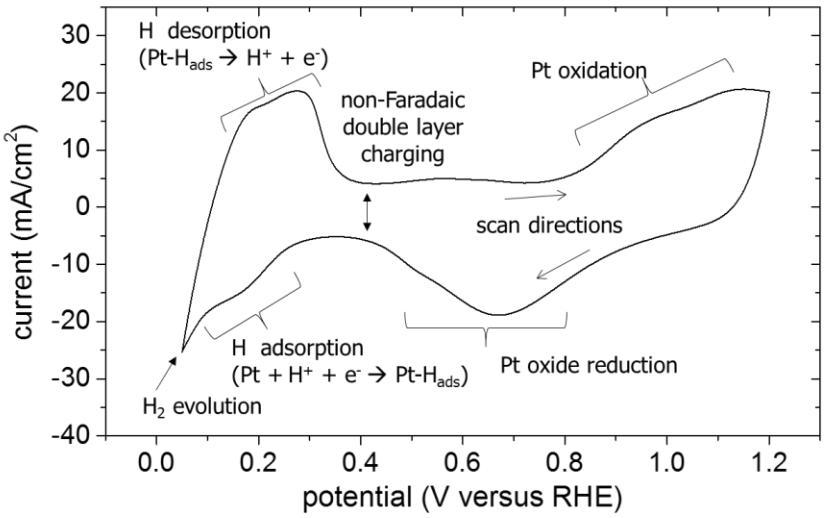


**Figure 3.8. Typical CV profile obtained at 100 mV/s for a PEMFC catalyst layer containing Pt nanocatalysts, carbon nanoparticles, and ionomer. This profile was measured *in situ* within an assembled fuel cell. Each of the respective regions are labelled accordingly.**

To assess the specific activity of a Pt catalyst, the $\boldsymbol{A}_{ecsa}$ of Pt must be determined as accurately as possible. In this thesis, the $\boldsymbol{A}_{ecsa}$ of most of the Pt samples were determined from the CV profiles by using **Equations 3.1** and **3.2**.[94–97] The variables *q* and *I* correspond to charge and current, respectively. The $H_{upd}$ desorption peaks were integrated over 0.05 to 0.4 V (vs RHE) with the baseline corrected to the level of the adjacent $C_{DL}$. This integrated charge was divided by the scan rate of the CV experiment to obtain the $q_H$ ($\mu C \cdot cm^{-2}$). This value is the experimentally measured charge for removing chemically absorbed H from the surfaces of the Pt WE.[92,96] Assuming H is adsorbed as a monolayer onto the Pt surfaces, $q_H$ is divided by $q_S$ (which is the theoretical charge density for removing a monolayer of $H_{UPD}$ from the surfaces of the Pt electrode) to obtain the $\boldsymbol{A}_{ecsa}$ of the Pt WE. It is generally accepted that the Pt surface area can be calculated with a

high degree of accuracy when using 210 μC per $cm^{-2}$ for the value of $q_S$ for the desorption and adsorption of a monolayer of H on the polycrystalline surfaces of Pt in an acidic based electrolyte.[94–97]

$$q = \int I \, dt \tag{3.1}$$

$$\boldsymbol{A}_{ecsa} = \frac{q_H}{q_S} \tag{3.2}$$

### 3.4.3 Rotating Disk Electrode Voltammetry Techniques

For non-reversible reactions that are assessed in a three-electrode electrochemistry cell, the rate of the reaction is often limited by the mass transport of reactants and the diffusion of products to and from the WE surfaces, respectively.[98–100] This limitation is especially apparent when analyzing porous materials, such as the PEMFC catalyst layers. Methods, such as rotating disk electrode (RDE) techniques, create a hydrodynamic convection over the surfaces of the WE for overcoming mass transport limitations of the reaction.[98–100] The LSV experiments were applied to the WE to assess the extent of electrochemical reactions over a range of potentials. For the ORR, the potentials are usually set to scan from where there is little reaction towards the ORR (e.g., 1.0 to 0.9 V versus RHE) to where this reaction occurs readily (e.g., 0.2 to 0.1 V versus RHE). In contrast to non-RDE LSV experiments, the RDE technique enables the assessment of a steady-state current by overcoming the diffusion limitations with a continual flux of electrolyte to the surfaces of the electrode created by the rotation of the electrode. The current response of the reaction reaches a maximum (limiting current) that is directly proportional to the square root of the rotational speeds.[98–100]

To further assess the efficiency of electrocatalyst for the ORR, the reaction mechanism can be investigated by applying the Koutecký–Levich equation to the results of the RDE experiment. For example, the ORR reaction mechanism can be assessed, such as to determine if the reduction of oxygen is occurring through a 2 electron or 4 electron process.[51,101,102] The difference between these two processes is summarized in **Equations 3.3** and **3.4**. The generation of $H_2O_2$ through the 2 electron based ORR process can lead to degradation of the catalyst materials and is, therefore,

undesirable.[51,101,102] These different mechanisms for the ORR are described in further detail in **Section 2.5.**

$$O_2 + 4H^+ + 4e^- \rightarrow H_2O \ (E^0 = 1.229\ V) \quad (3.3)$$

$$O_2 + 2H^+ + 2e^- \rightarrow H_2O_2 \ (E^0 = 0.70\ V) \quad (3.4)$$

This reaction mechanism can be directly assessed using the Koutecký-Levich equation (**Equation. 3.5**).[101–103] In this equation, $j_l$ is the Levich current density [current over the geometric area of the electrode ($cm^2$)], $j_k$ is the kinetic current density, *F* is Faraday's constant, $C$ is the concentration of dissolved oxygen, *D* is the diffusion coefficient of oxygen in the analyte, *v* is the kinematic viscosity of the analyte, and ω is the rotational speed of the electrode (rad $s^{-1}$). The values used for each of the variables in the studies reported in this thesis are presented in **Table 3.1**.[104–106]

**Table 3.1. Different variables and their corresponding values for use in the Koutecký-Levich equation [104–106]**

| variables | definitions | values |
|---|---|---|
| *F* | Faraday's constant | 96485.332 Columb $mol^{-1}$ |
| *C* | concentration of dissolved oxygen | 1.1 x $10^{-6}$ mol $cm^{-3}$ in 0.5 M $H_2SO_4$ at 25 °C and 1 atm |
| *D* | diffusion coefficient of oxygen in the analyte | 1.4 x $10^{-5}$ $cm^2$ $s^{-1}$ in 0.5 M $H_2SO_4$ at 25 °C and 1 atm |
| *v* | kinematic viscosity of the analyte | 0.010 $cm^2$ $s^{-1}$ for dilute aqueous solutions at 25°C and 1 atm |

The value *n* (the number of electrons transferred during the electrochemical reaction) can be calculated upon substitution of all the known values into **Equation 3.6**. The kinetic current density ($j_k$) is related to the rate constant (k) for electron transfer reaction at the catalyst surfaces. This value can be used for assessing and comparing the activities of different catalyst materials. The slope of the Koutecký-Levich plot, constructed by plotting the limiting current densities against the inverse square root of the rotational speed, is inversely proportional to *n*, the number of electrons that participates in the ORR (**Equation 3.5;** and **Figure 3.9 b**). In this thesis, the number of electrons participated in the ORR is an important matric that can give us insights into insights in the long-term stability of the CLs. An *n* value of ~2 could suggest the production of hydrogen production

at the catalytic sites. The production of hydrogen peroxide can lead to the degradation of C and ionomer that is within the CL. An *n* of 4 can infer an reduced production of hydrogen peroxide at the catalytic sites, which could result in improved catalyst stability by minimizing the corrosion of the carbon and ionomer supports.[17] Examples of the LSV plots and a Koutecký-Levich plot for a Pt containing catalyst layer with respect to WE rotational speeds are shown in **Figure 3.9**.[103,107]

$$\frac{1}{j_l} = \frac{1}{j_k} + \frac{1}{0.62nFCD^{2/3}\nu^{-1/6}\omega^{1/2}} \tag{3.5}$$

$$j_k = nFkC \tag{3.6}$$

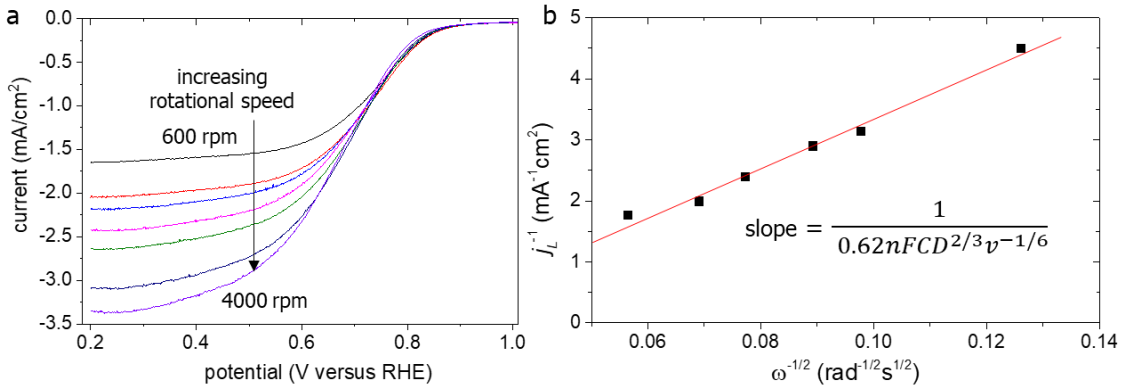


**Figure 3.9. The ORR experimental results of a nanostructured Pt catalyst: (a) LSV plots obtained at different electrode rotational speeds; and (b) a Koutecký-Levich plot obtained by taking the limiting current at 0.2 V at different rotational speeds.**

In summary, RDE methods are valuable for the analysis of electrochemical reactions and for the comparison of the electrocatalytic activity for the ORR of similar electrodes under specific conditions. This setup is especially useful for overcoming the diffusion limitations of PEMFC based CCLs (when used as the WE), which is composed of a porous film containing a mixture of carbon, ionomer, and Pt nanocatalysts. If no electrolyte perturbation was induced, the reactant at the WE can be depleted at a faster rate than it is replenished, leading to a decrease in current density that can occur within a few seconds.[92,100] In a fuel cell, this diffusion limitation is overcome by establishing a steady flow of gases over the CCL. In the RDE setup, the flux of reactant towards the WE is proportional to the rotational speed. This technique not only can reveal insights into the

reaction mechanism, the flux of reactant can also better mimic (to an extent) the reaction dynamics of an operating PEMFC in comparison to a stationary electrode setup.[92,100]

## 3.5 *In situ* PEMFC Characterization

*In situ* PEMFC experiments were performed in this thesis to assess the quality of materials for use as CCLs in PEMFCs. The experimental catalyst materials prepared in this study included patterned CCLs, embossed PEMs, and electrodeposited mesoporous Pt. These materials were incorporated into MEAs and analyzed with a single-cell testing system. Two different types of PEMFC test hardware were used, each accommodating MEAs of a different size. The small and large PEMFC test stations accommodated MEAs with geometric active areas of 5 $cm^2$ and 40 $cm^2$, respectively. Typically, the 40 $cm^2$ cell exhibits less variance related to the errors in preparing the MEAs. The variation of MEAs can arise from the preparation of the MEAs. These influencing factors include variability in CL coatings uniformity (crack or thickness changes), localized catalyst agglomerations, and variability in ionomer distributions, and variable contact between GDLs and the CLs. The limiting current method performed in Chapter 5 (described in **Section 3.5.5**) demonstrated that the variations in current density between two different 40 $cm^2$ MEAs is approximately 12 %. This variation is relatively low compared to the 5 $cm^2$ MEAs, suggesting these localized CL variations are averaged over the larger MEA areas. It is, however, more difficult and costly to prepare experimental materials at the larger scale. As a result, fewer MEAs were tested with the large scale PEMFC station. The 5 $cm^2$ MEAs are easier to prepare. These smaller MEAs are, however, more prone to variability due to the inconsistency in the preparation of the CLs. An example of the error between three different 5 $cm^2$ MEAs is presented in **Figure 7.12**. These different 5 $cm^2$samples were shown with variations in overpotential of as much as 0.3 V when the MEAs were tested at current densities over 500 $mA/cm^2$. To establish confidence in the results, more than 3 sets of samples were tested for each of group of experimental samples in the 5 $cm^2$ fuel cell test station. The two different types of test stations consisted of the same components shown in **Figure 1.1**. Each set of fuel cell analyses consisted of a comparison between standard or reference MEAs (prepared with continuous CCL films) and MEAs containing the experimental materials created as part of this thesis. The reference MEAs consisted

of anode and cathode Pt loadings of 0.05 and 0.4 $mg_{Pt}/cm^2$, respectively. Several analytical methods can be applied to the PEMFCs for investigating the different characteristics of these materials such as the Pt $\boldsymbol{A}_{ecsa}$, fuel cell polarization, ohmic resistance, ionic resistance, and mass transport resistances.

### 3.5.1 Fuel Cell Activation and Pt Surface Area Measurements

When the MEA is first prepared and loaded into the PEMFC, the catalyst activity may be limited due to the following inefficiencies: (i) potential blockage of reactant transport to the catalyst (e.g., due to the presence of ionomer or impurities); (ii) insufficient hydration of the PEM during the initial operation; (iii) reduction of catalyst activity due to impurities introduced during MEA preparation; and (iv) formation of an oxide layer on the catalyst. To overcome these inefficiencies, when an MEA is first loaded into the fuel cell, each MEA was subjected to a series of CV experiments as a means to activate the catalyst materials, as well as to determine the Pt $\boldsymbol{A}_{ecsa}$ of the catalyst.[80,108] The CV experiments were performed as a two electrode system, where the voltages were measured and applied between the WE and CE using a potentiostat. The PEMFCs were maintained at a standard condition of 80 °C and 100 % relative humidity (RH) during the activation procedure.[109] The CV experiments included applying potentials to the MEA from 0.05 V to 0.8 V, while supplying $H_2$ (g) and $N_2$ (g) to the anode and cathode, respectively. Generally, the MEAs required 50 to 200 sequential CV scans to become stable (e.g., to achieve subsequent CV profiles with deviations of <1 μA).[108] Once the CV profile had stabilized, the Pt $\boldsymbol{A}_{ecsa}$ could be determined from the profile as described in **Section 3.4.2**.

### 3.5.2 Fuel Cell Performance Metrics

The PEMFC performance was assessed after the MEAs had been conditioned and had reached equilibrium conditions with respect to the RH and temperature conditions of the operating fuel cell. An LSV technique was applied to the fuel cell to assess its current and power output with respect to the applied potential. A typical PEMFC polarization curve is shown in **Figure 3.10**, where the potential is scanned from open circuit potential (OCV) to 0.1 V.

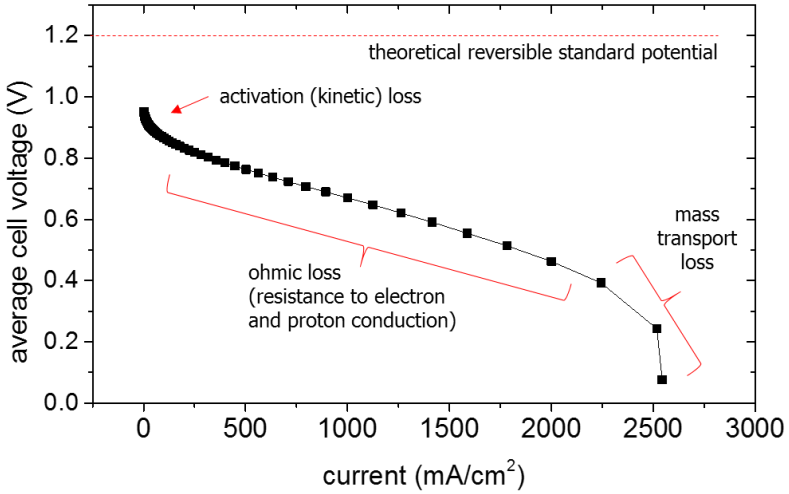


**Figure 3.10. The PEMFC polarization curve of a conventionally prepared Pt ink CCL with labels for the different overpotential losses.**

According to the overall reaction of PEMFC operation ($2H_2 + O_2 \rightarrow 2H_2O$), the theoretical reversible standard potential [$E_{(T,P)}$] of the balanced reaction is 1.23 V.[80,110–112] In a perfect system, the increase in current should not influence the potential of the system. Under real world operation the PEMFCs are, however, influenced by many resistance losses that lower the cell potential at higher current densities and that can ultimately cause a loss of current density that terminates the fuel cell reactions. The fuel cell voltage $V_{fc}$ is predominantly affected by losses due to catalyst activation ($V_{act}$), mass transport ($V_{mt}$), and ohmic ($V_{ohm}$) resistances.[80,110–112] The overall equation for determining the cell voltage is shown in **Equation 3.7**.

$$V_{fc} = E_{(T,P)} - \Delta V_{cross} - \Delta V_{act} - \Delta V_{mt} - \Delta V_{ohm} \quad (3.7)$$

At open circuit voltages, a typical fuel cell would exhibit a mixed potential that is slightly lower than that of the theoretical OCV of PEMFCs. This loss at OCV is predominantly affected by the cross-over of $H_2$ gas ($V_{cross}$) through the membrane from the anode. In the first region of fuel cell polarization, from ~0 to 100 mA/cm$^2$, a sharp drop from the OCV is observed in the polarization curve (**Figure 3.10**). This reduction in potential is predominantly attributed to $\Delta V_{act}$, where the loss is due to slow oxygen reduction kinetics associated with the exchange current density of the ORR electrocatalyst in the cathode. Another gradual decrease in potential is observed in the next region, from

~100 to 500 mA/cm$^2$. This gradual loss of voltage is attributed to $\Delta V_{ohm}$, where it is affected by the electric conductivity and the transport resistance of protons in the MEA. At higher current densities (>500 mA/cm$^2$), another sharp decrease of fuel cell voltage is observed, followed by a loss in current density and the termination of the ORR reaction. This loss in cell voltage is due to $V_{mt}$, which is due to the limitations of the diffusion of $O_2$ through the gas channels and pores within the GDL and CCL, as well as its diffusion through the water and hydrated ionomers within the CCL to the catalytically active sites. Generally, the overall performance of the fuel cell can be assessed by analyzing the LSV and the power curves to determine the performance of the fuel cell.

The power curve for the fuel cell can be calculated using **Equation 3.8**, and plotted against current density as shown in **Figure 3.11**.

$$\text{Power density } (Watt/cm^2) = \frac{I(\text{amperes})V(\text{voltage})}{cm^2(\text{MEA area})} \tag{3.8}$$

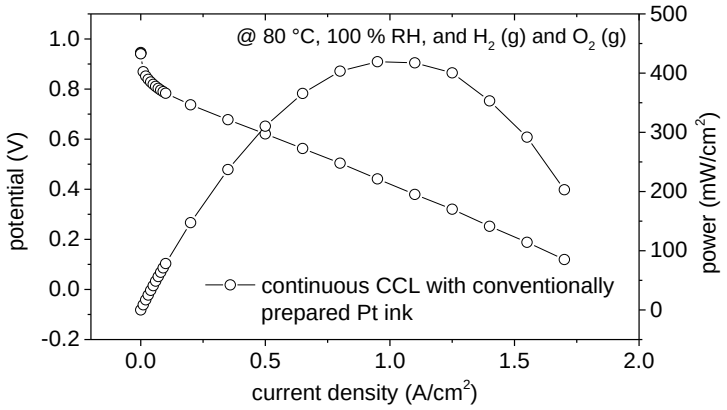


**Figure 3.11. Typical fuel cell polarization and power curves for a PEMFC with respect to applied potentials.**

In this thesis, additional electrochemical measurements were performed under specific fuel cell operating conditions to further investigate the $\Delta V_{ohm}$ and $\Delta V_{mt}$ of the fuel cells. The variation in $\Delta V_{ohm}$ and $\Delta V_{mt}$ when compared to the conventionally prepared reference samples provides further insight into how the interfaces between the various

components (and the structures prepared therein) may affect the overall performance of the fuel cell.

### 3.5.3 Determining Hydrogen Cross-Over and Short-Circuit Currents

After obtaining $\boldsymbol{A}_{ecsa}$ from the CV analyses, the fuel cell's $H_2$ cross-over resistance and ionic resistance can also be determined (at 80 °C and 100 % RH) while supplying the fuel cell with $H_2$ (g) and $N_2$ (g) to the anode and cathode, respectively.[80,112,113] To measure the $H_2$ (g) cross-over, an LSV experiment was setup to scan the cathode from 0 to 0.8 V at a slow scan rate (typically 20 mV/s or slower). When the fuel cell is supplied with $H_2$ (g) and $N_2$ (g) (to the anode and cathode, respectively) all current monitored from the cathode can only originate from $H_2$ (g) that was not oxidized at the anode. The un-oxidized $H_2$ (g) can travel through the PEM membrane, and subsequently oxidize at the cathode. This later oxidation reaction will result in an increase in the observed fuel cell current. A typical MEA should have less than 8 mA/cm$^2$ of $H_2$ cross-over current (**Figure 3.12**).[80,109,112,113] Any increase in $H_2$ cross-over is indicative of issues with the integrity of the membrane, such as membrane damage or a compositional breakdown.

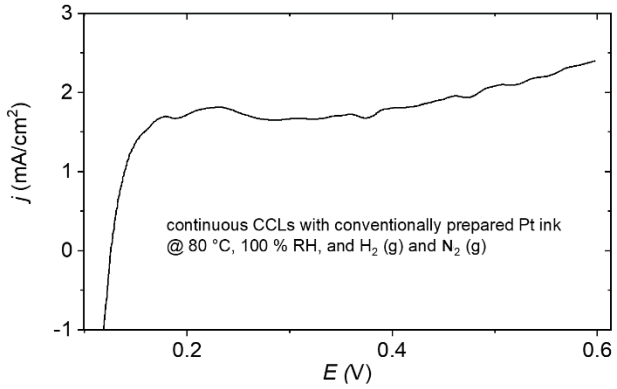


**Figure 3.12. Hydrogen cross-over currents analyzed by LSV for a PEMFC.**

### 3.5.4 Determining Ionic Resistances of MEAs

Under the same fuel cell conditions as used for the determination of $H_2$ cross-over, the resistance of $H^+$ traveling through the CCL can be determined using electrochemical impedance spectroscopy (EIS). This technique applies an oscillating voltage (typically with

an amplitude of 10 mV) at the cathode and measures the current response to determine the impedances of the assembled system. According to the representative CV profile obtained in **Section 2.4.2**, a potential of 0.45 V was chosen for the EIS measurements. at this potential, no Faradaic processes, such as the desorption/adsorption of hydrogen or the oxidation/reduction of Pt, occurs at the cathode. The absence of Faradic processes during the EIS measurement can reduce the complexity of the mathematical fitting for the resulting data. The EIS results were interpreted by fitting the data with a physically meaningful model of similar circuits to determine the contributions from the resistances or capacitances present in the system. Specifically, a de Levie model of a porous electrode was utilized to analyze the EIS results.[53,114–116] This model assumes that the cathode is composed of a single, uniform layer that has a network of cylindrical pores with a homogeneous diameter (shown in inset of **Figure 3.13**). The thickness, ionomer content, and volume specific capacitance of the CL are all assumed to be homogeneous. Although the experimental samples used in this thesis may not have a uniform interface between the CCL and the membrane, this model served as a baseline comparison between the experimental and reference samples. Typical for the MEAs prepared in this thesis, the Nyquist plot (or the real component of the impedance versus the imaginary component of the impedance) follows a 45° line at high frequencies, and transitions to a nearly vertical line at low frequencies (**Figure 3.13**). The high frequency intercept of the plot is attributed to the membrane resistance ($R_{ohm}$) and the electrical and contact resistances of the system. These electrical and contact resistances are, however, considered to be negligible when compared to the membrane resistance.[114–116] The extrapolated x-intercept in the low frequency region ($Z_{Re,l}$) has been shown to be equivalent to the high frequency resistance plus one-third of the ionic resistance ($R_{ion}$) of the catalyst layer as shown in (**Equation 3.8)**.

$$R_{ion} = 3(Z_{Re,l} - R_{ohm}) \tag{3.8}$$

To reduce errors in interpolating non-linear data, the EIS results can be fit with the model described by **Equation 3.9** to estimate their corresponding resistances from the individual components (**Figure 3.12**).

$$Z = j\omega L_{wire} + R_{ohm} + \sqrt{\frac{R_{ion}}{C_{dl}(j\omega)^{\Phi}}}\coth(\sqrt{R_{ion}C_{dl}}(j\omega)^{\Phi} \tag{3.9}$$

The inductance of the hardware cables, the applied angular frequency, resistance of the membrane, resistance of the CLs, double layer capacitance, and the constant phase exponent of the double layer are represented as $L_{wire}$, $\omega$, $R_{Ohm}$, $R_{ion}$, $C_{dl}$, and $\Phi$, respectively.

The electrochemical data in the EIS profiles was fit with a Cronbach's alpha value of > 0.95 (95 % confidence interval). The $R_{ohm}$ and $R_{ion}$ can, therefore, be determined consistently, and with a high level of confidence, among from the different samples.

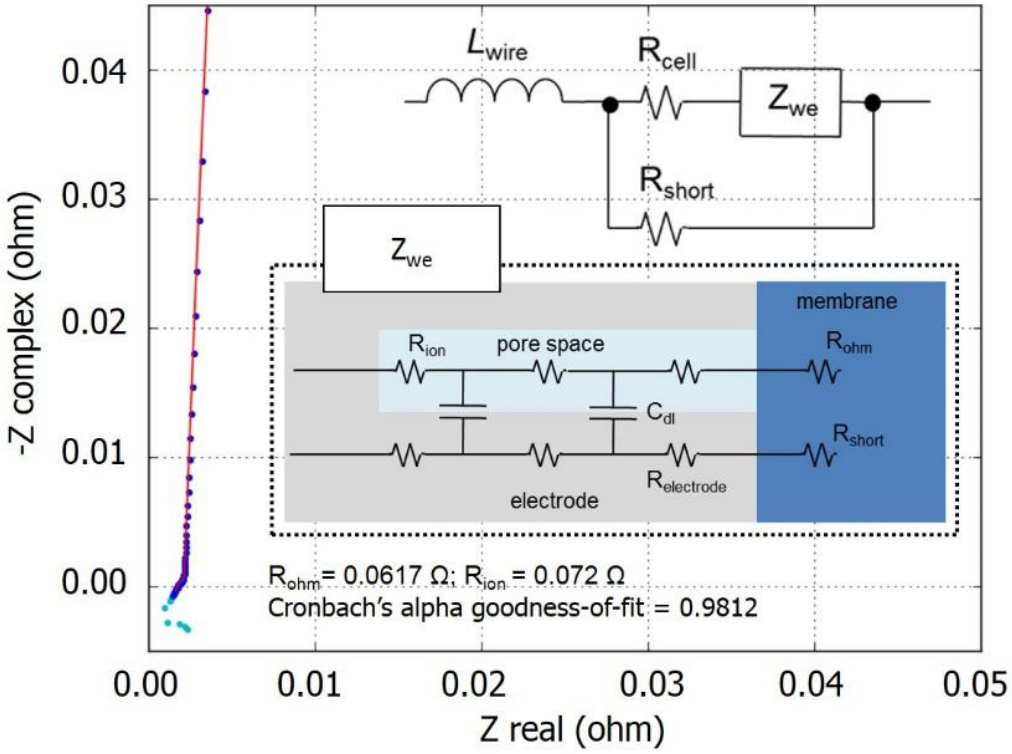


**Figure 3.13. A high frequency EIS profile (in blue) and fit (in red) obtained for a fuel cell containing a microstructured PEM membrane while operating at 70 °C, 100 % RH, and with $H_2$ (g) and $N_2$ pressurized at 2.5 bar to the anode and cathode, respectively. The Cronbach's alpha value of 0.98 indicated a 98 % confidence of fit between the theoretical model and the obtained data.**

### 3.5.5 Baker's Method for Determining Oxygen Resistances in PEMFCs

To further investigate mass transport losses in the MEAs, a Baker's analysis was utilized for separating the pressure dependent and independent oxygen-transport

resistances by measuring the cathode limiting current ($I_{lim}$) at different pressures.[38,114,117] The transport resistance $\Delta V_{mt}$ can be obtained from $I_{lim}$ and separated into a pressure-dependent component ($R_{pd}$) and a pressure-independent component ($R_{id}$). The parameter $R_{pd}$ is associated with oxygen transport in dry channels or pores. The $R_{id}$ is associated with the Knudsen diffusion, namely the transport of oxygen through the ionomer or through the accumulated $H_2O$ (l) present as hydronium ions.[117]

To perform the oxygen resistance measurements, the MEAs should undergo the aforementioned activation cycles and electrochemical analyses with $H_2$ (g) and $N_2$ (g) supplied to the anode and cathode, respectively (**Sections 3.4.2; 3.4.3**). The PEMFC was supplied with $H_2$ (g) and $O_2$ (g) (to the anode and cathode, respectively) for the oxygen resistance measurements. The concentration of the $O_2$ was fixed with inlet pressures of 1.5, 2.0, 2.5, and 3.0 bar, and the cell was allowed to equilibrate for 10 min at each pressure set-point. The cell was then potentio-statically controlled at 400, 300, 200, 150, 125, 100, and 50 mV for 10 mins at each potential to collect the limiting current. This process was repeated for 3 times at each $O_2$ concentration (pressure) and a straight line is fit through the linear region of the current density obtained over the range between 0.1 and 0.4 V. The average current density was recorded as the representative limiting current (**Figure 3.14**).

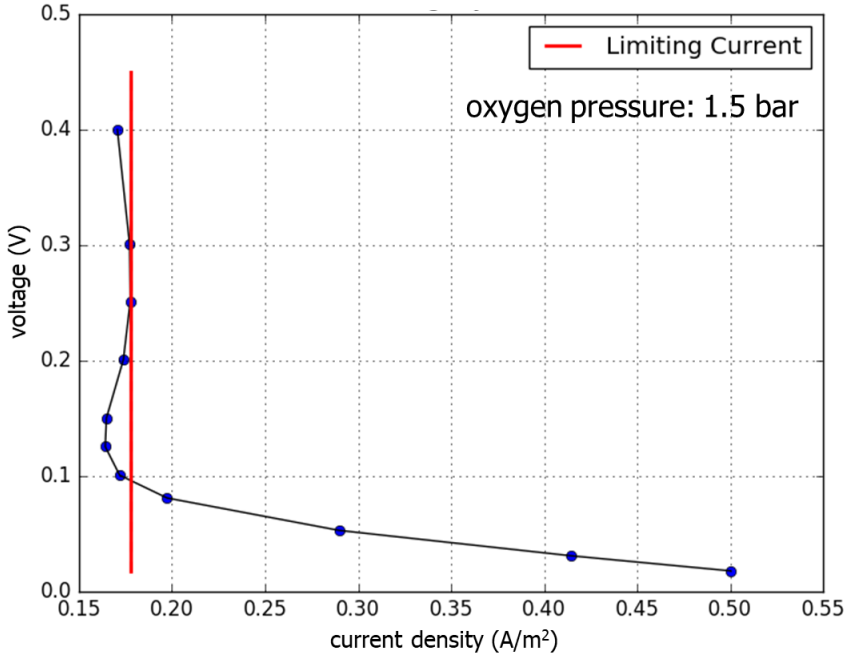


**Figure 3.14. A limiting current profile (in blue) the highest current obtained from the range between 0.1 and 0.4 V indicated by the vertical red line.**

The analysis of the results of these tests yielded the total $O_2$ mass-transfer resistance ($R_{mt}$), which is defined as the change in $O_2$ pressure between the gas channels and the cathode electrode, divided by the average $O_2$ molar flux to the cathode. At $I_{lim}$ conditions, the $O_2$ concentration at the cathode electrode is assumed to be zero, and the $O_2$ molar flux is equal to the measured current divided by the constant value of 4·F (since the ORR is a 4 electron process). Therefore, the relationship between $R_{mt}$ and $O_2$ concentrations can be simplified as **Equation 3.10**.

$$R_{mt} = \frac{4 \cdot F \cdot C_{O2-channel}}{I_{lim}} \tag{3.10}$$

Once $R_{mt}$ is calculated, the different components of the transport resistance can be further determined by constructing a relationship between $R_{mt}$ and $O_2$ pressure. The transport of gaseous oxygen molecules through small gas filled pores (as described by molecular diffusion coefficients) is inversely proportional to the total pressure (P) of $O_2$. This pressure dependent oxygen transport resistance is denoted as $R_{pd}$. It is assumed that the increase in dissolved $O_2$ concentration in the ionomer and water are negligible with

increasing gas pressure for these measurements. The transport of oxygen by diffusion through the ionomer and/or water layers covering the Pt nanoparticles is independent of P. This pressure independent oxygen transport resistance is denoted as $R_{id}$. The PEMFC measurements were set to collect $I_{lim}$ at several different oxygen pressures, and to calculate their respective $R_{mt}$ values. A liner plot of $R_{mt}$ versus P can be obtained, which is described by **Equation 3.11** and presented in **Figure 3.15**.

$$R_{mt} = R_{id} + R_{pd}(P) = Intercept + Slope \cdot P \tag{3.11}$$

The pressure independent transport resistance, $R_{id}$, is the Y-axis intercept of the linear relationship between $R_{mt}$ and P. The pressure dependent transport resistance, $R_{pd}$, is the slope of the same linear relationship of $R_{mt}$ versus P.

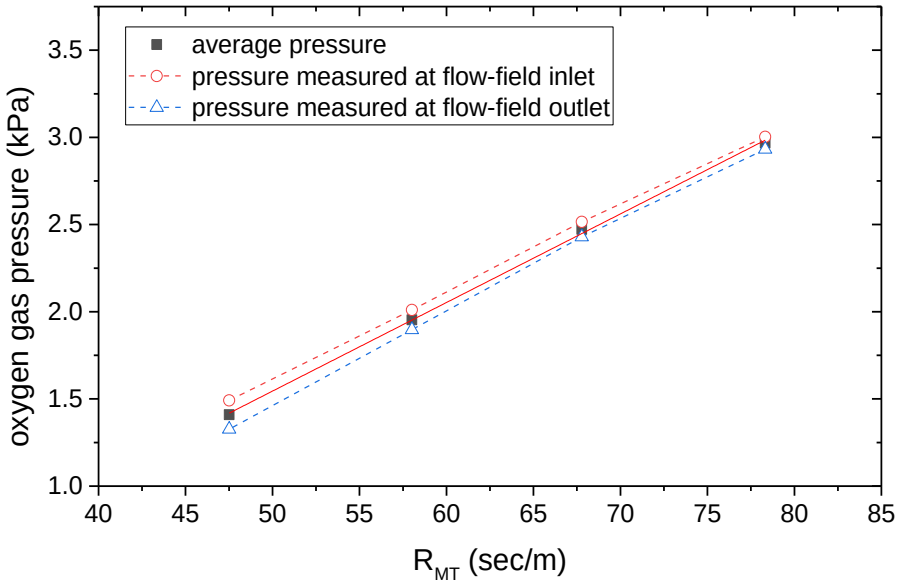


**Figure 3.15. The oxygen pressure to transport response ($R_{mt}$) for a PEMFC operating at 70 °C, 100 % RH, and with $H_2$ (g) and $O_2$ (g) supplied to the anode and cathode, respectively.**

The determination of $R_{id}$ and $R_{pd}$ can be correlated to the structural properties of the MEA components. By understanding the different components of voltage loss (e.g., $H_2$ cross-over, membrane resistance, and pressure independent versus dependent $O_2$ transport resistances) of a MEA when compared to a standard reference sample, we can more efficiently design MEAs to improve the performance of PEMFCs. For example, the design of CLs with increased pressure-dependent transport of oxygen can reduce fuel cell flooding and enhance the operation of PEMFCs at high current densities.

In summary, the combination of characterization methods demonstrated in this chapter were used throughout the work performed in this thesis. These include physicochemical techniques for morphological and elemental analyses of catalyst layers and materials, *ex situ* electrochemical characterization of catalytic materials, and *in situ* PEMFC characterization of materials prepared as MEAs. These studies provided insights into structure to function correlations of the materials in the CCLs or at the PEM and CCL interface with micro- to nanoscale features that were created by design through the techniques described throughout this thesis.

# Chapter 4.

# Patterning Catalyst Layers with Microscale Features for Proton Exchange Membrane Fuel Cells

## 4.1 Acknowledgement

This research was conducted with contributions in part from the Natural Sciences and Engineering Research Council of Canada (NSERC) Discovery Program (Grant No. 1077758), the Mitacs-Accelerate Internship Program (M.T.Y. Paul, Grant No. IT05017), and the Canada Research Chairs Program (B.D. Gates; Grant No. 950-215846). This work made use of 4D LABS (www.4dlabs.ca) and the Centre for Soft Materials shared facilities supported by the Canada Foundation for Innovation (CFI), British Columbia Knowledge Development Fund (BCKDF), Western Economic Diversification Canada, and Simon Fraser University.

## 4.2 Abstract

Microtransfer molding (μTM) and microcontact printing (μCP) techniques were demonstrated for the preparation of platinum based catalysts in hexagonally arranged patterns to achieve microstructured cathode catalyst layers (CCLs). These CCLs were used for improving the performance of proton exchange membrane fuel cells (or PEMFCs). It was demonstrated that CCLs prepared by μTM which contained arrays of microscale cylindrical holes exhibited improved water management characteristics in PEMFCs when compared to CCLs prepared from continuous films. Upon further tuning of the CCL transfer procedures, μCP of CCLs with discrete microscale features were demonstrated to have twice the mass activity of that observed for PEMFCs containing CCLs with uniform thin films. These methods to prepare CCLs are compatible with current manufacturing techniques and could be easily adapted to incorporate other catalyst materials for further improvements in PEMFC performance.

**Graphical Abstract**

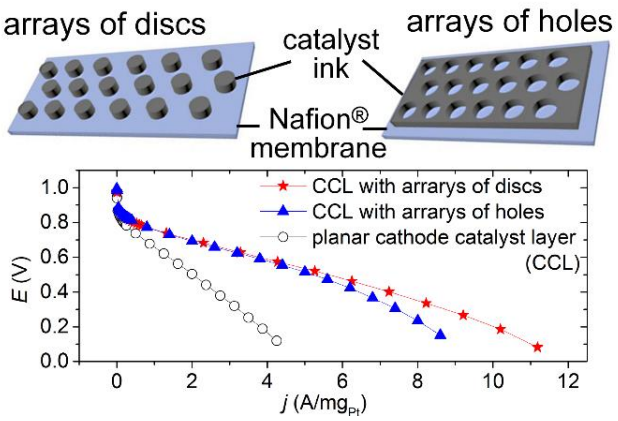


## 4.3 Introduction

The performance of PEMFCs is influenced by proton conductivity through the PEM and the catalyst layers, oxygen gas permeation to the cathode catalysts, and water removal from the cathode catalyst layer (CCL).[63,118,119] These challenges for PEMFC systems are especially prominent during vehicle start-up and prolonged operation of the vehicle under "strained" conditions.[120–125] During vehicle start-up, the temperatures of the fuel cell stack and system humidifier are relatively low. This "start-up" (WUP) condition can lead to an under-hydrated condition for the PEM, which is more resistant to proton conduction at relatively low operating current densities.[124–126] Water produced by the cathodic ORR at these relatively lower cell temperatures are not removed in an efficient manner. The accumulation of water within the CCL can lead to flooding and halting the operation of the PEMFC system. [124–126] Conversely, during vehicle operation under a heavy load, the fuel cell temperature and fuel humidifier temperature can be relatively high in comparison to the WUP condition.[123,127,128] These higher temperatures (HOT) conditions can lead to dry conditions over a range of fuel cell operating voltages (~1 to 0.2 V).[122,123,127,128] Recent advances in PEMFC systems include system design elements to better manage these challenges. These include the use of both dynamic control of fuel cell humidifiers and the incorporation of hydrophobic microporous layer (MPL) coated gas diffusion layers (GDLs) for achieving an optimal balance of water within a PEMFC under a variety of operating conditions.[121,122,129]

It has been reported that, in addition to system designs and GDL modifications, the CCL itself can be modified for managing water that is produced during operation of the PEMFC. The porosity within a CCL has been shown to affect the mass transport efficiencies of the system.[33,49,59,130–134] One study indicated that increasing the hot-bonding pressures applied during the preparation of MEAs can decrease the presence of nanoscale pores (e.g., 30 to 70 nm) within the CCL.[33] This reduction in porosity restricts water formation and can, therefore, result in a decreased performance of the PEMFCs. [33] Other studies have demonstrated that the inclusion of macroscopic pores (pore diameters between 50 nm and 1 μm) can improve the achievable operating current densities of PEMFCs.[49,59,133] It was also demonstrated that ordered macroporous Pt materials (with >500-nm diameter pores) can exhibit improved efficiency for the ORR and fuel cell performance when compared to more conventional cathode materials.[49,59] It has been suggested that macroscopic pores incorporated into the CCL can improve the water management characteristics of these films, which can enhance the overall performance of PEMFCs. These macroscopic pores can assist in collecting and removing water from the surfaces of Pt nanocatalysts, which can enhance transport of reactants and ions to these catalytic sites.[33,129,135] To further improve the water management at scales greater than 1 μm, some studies have shown that while maintaining overall Pt loadings and catalyst layer thicknesses, a CCL that is prepared from two distinct layers of catalyst with an equivalent overall Pt loading can outperform a CCL that consists of a single continuous layer of catalytic material. Tuning the Pt loadings of the CCLs as a function of the thickness (i.e., perpendicular to the PEM) can improve the overall power output of PEMFCs by as much as 13.5 %.[134] However, variations in the Pt loadings in the lateral directions (i.e., within the xy-plane of the MEA) have not been previously investigated due to the difficulties in preparing such catalyst layers.[33]

A goal of this study was to demonstrate the use of soft lithography techniques for preparing CCLs with discrete patterns on the PEM. Microtransfer molding (μTM) and microcontact printing (μCP) techniques were used to pattern films of Pt catalyst materials with hexagonally arranged arrays of cylindrical discs of catalyst or cylindrical holes within the catalyst layer.[136] The dimensions of these features ranged between 20 to 50 μm. The techniques to prepare the CCLs and to transfer these films into MEAs were optimized for preparing patterns with clearly defined features. It is hypothesized that these CCL

patterns, with well-defined and regular regions of varying Pt loadings, could serve to enhance water management within PEMFCs. For example, regions with a minimal, or lower, loading of Pt nanocatalysts could be designed to assist in both lateral and vertical transport of water away from neighbouring regions of a higher Pt loadings. The patterned CCLs were incorporated into MEAs and characterized in PEMFCs under a of WUP, HOT, and NOC operating conditions described in **Section 4.4.6**. The performances of these patterned CCLs were compared to MEAs prepared with continuous CCLs. The results of this study demonstrated that CCLs containing regular arrays of cylindrical holes prepared by μTM exhibited improved water management properties in comparison to CCLs consisting of continuous films. Patterned CCLs containing arrays of either cylindrical discs of catalyst material or holes within the catalyst film as prepared by μCP exhibited an improvement in the overall performance of the PEMFCs.

## 4.4 Materials and Methods

In this study, elastomeric polymer templates were used to create an array of hexagonally arranged microscale features within the catalyst layers of PEMFCs. These features consist of either arrays of cylindrical discs, or perforations (holes) in an otherwise continuous film containing a mixture of Pt and C nanoparticles that make up the cathode catalyst layers (CCLs) coated onto Nafion® 211 membranes. The patterned CCLs were characterized to verify their physical dimensions and the densities of the Pt loadings. These samples were further incorporated into MEAs with a 5 $cm^2$ active area for determining their performance in PEMFCs.

### *4.4.1* Preparation of Elastomeric Templates

In this study, elastomeric templates were used for the microcontact printing and microtransfer molding of catalyst materials onto Nafion® membranes. These elastomeric templates were prepared by curing the elastomeric pre-polymer materials over a series of masters. These masters consisted of photolithographically patterned SU-8 (SU-8 2025, MicroChem, Germany) supported on polished Si (100) wafers (International Wafer Service, Inc., USA). Chromium patterned on borosilicate glass photomasks used in the photolithographic processes were purchased from 4D LABS at Simon Fraser University

(www.4dlabs.ca). Photolithography was performed according to the manufacturer's protocols (http://www.microchem.com/Prod-SU82000.htm; as of April 2018). The photolithographically created features consisted of 50-µm diameter cylindrical pillars or recesses arranged in a hexagonal pattern with a minimum edge-to-edge feature spacing of 25 µm. The SU-8 pillars and recesses were controlled to a thickness of 15, 20, or 25 µm. The general photolithographic process to prepare the masters is shown in **Figure 4.1**

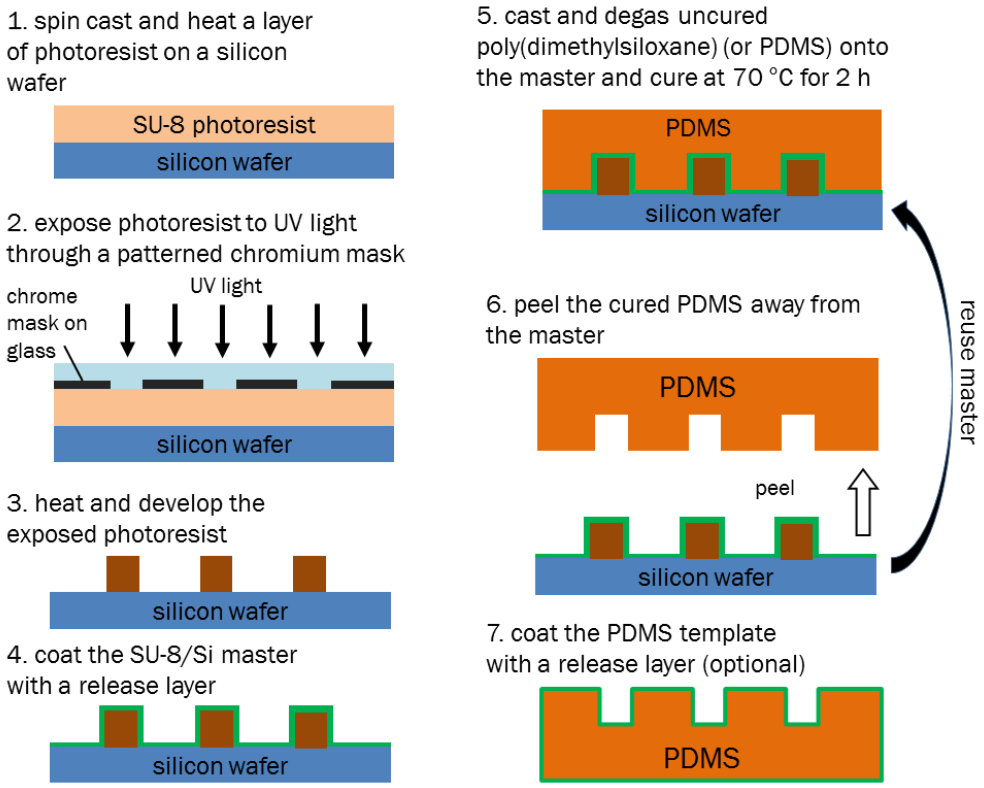


**Figure 4.1. Schematic illustration of the preparation of masters and elastomeric stamps or molds.**

To create the elastomeric templates used for the patterning of CCLs, poly(dimethylsiloxane) (PDMS; Dow Corning Sylgard® 160) were cast and cured against the masters. These hard templates were first treated with a release layer (Alfa Aesar, 1H, 1H, 2H, 2H-perfluorooctyldimethylchlorosilane, 95 %) to minimize adhesion of the PDMS to the masters. The procedure for preparing the release layer coating included the following steps: (i) treatment of the masters with an air-based plasma at ~30 Watts for 5 min; (ii) immersion of plasma treated masters in a 0.1 % (v/v) solution of the perfluoro silane prepared in toluene for 5 min; and (iii) rinsing of the silane coated masters with

isopropanol and drying with a flow of nitrogen gas (99.998 % $N_2$, Praxair, Canada). After treatment with the release layer, the uncured elastomer and the curing agent were mixed according to the manufacturer's protocol and cast onto the release layer treated hard templates. The elastomer covered masters were degassed in a vacuum chamber for at least 15 min. After the removal of gas bubbles from the uncured elastomer by degassing, the elastomer was cured at 70 °C for 2 h. Once cured, the elastomer was peeled from the master for use as an ink patterning template. The elastomeric template was also treated with a release layer [Sigma Aldrich; trichloro(octadecyl) silane (OTS); >90 %] before use in printing or molding of the PEMFC catalyst ink. The release layer assisted with the transfer of ink from the templates onto the Nafion® membranes. Coating of the release layer onto the elastomeric templates was performed in a similar manner to the aforementioned procedures that were used for coating release layers onto the masters. Quality of the release layers on the masters and elastomeric templates were evaluated using a VCA Optima water contact angle (WCA) measurement system (AST Products, MA, United States). These measurements were performed with 1 µL droplets of deionized (DI) water (Barnstead DIamond™ with an output of 18 MΩ·cm), and the average WCA values were obtain using measurements from at least 5 different regions of each substrates. An example of the WCA measurements performed on the elastomeric stamps are presented in **Figure 4.2**

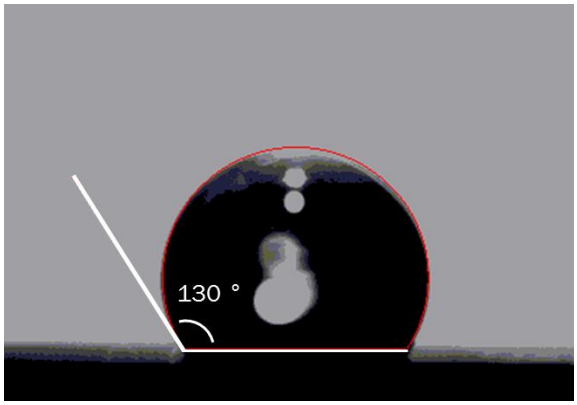


**Figure 4.2. Optical image of a 1 µL droplet of deionized water on an octyldecyltrichlorosilane (OTS) coated elastomeric template with a hexagonally arranged array of cylindrical recesses used for the microtransfer molding of CCLs.**

The elastomeric stamps consisted of hexagonally arranged cylinders (**Figure 4.3**). These circular features are typically easier to prepare through photolithography and soft

lithography due to the absence sharp angles that are present in polygonal shaped features. It was demonstrated by Jeon *et al.* that PEM membranes with hexagonally arranged cylindrical features at the catalyst layer interface exhibited the largest improvement over other patterns such as a square lattice of cylindrical features, a close-packed square features, and a close-packed array of hexagonfeatures.[148] It was suggested that hexagonally arranged circular patterns have the highest feature circumference per geometric area within the prepared MEA. The catalyst layer was prepared from a conventional ink [30 wt % Pt NPs and C particles (1:1 wt/wt; Pt:C), and 30 wt % ionomer].

The Pt loading target specified by the US DOE target of ~0.15 $mg_{Pt}/cm^2$ made with the aforementioned ink formulation would require a continuous CL with thickness of ~5 µm. [35] To achieve this loading with the hexagonally arranged patterns presented in this thesis would require a CL thickness of ~10 µm. In a preliminary investigation into the transfer of catalyst ink from elastomeric stamps. It was determined that the transfer of high aspect ratio (> 1:5; height:width) CLs would be difficult to achieve reproducibly. A decreasing feature sizes also required the preparation of high aspect ratio features, which is also difficult. The mechanical processes of polymer casting and hot-bonding was shown to delaminate the prepared SU-8 patterns with aspect ratios of greater than 1. The patterned CLs of interest for the studies in Chapter 4 were, therefore, focused on hexagonally arranged cylinders. The feature size of 50 µm was also chosen over smaller features sizes. This critical feature size is similar to a previous study that demonstrated catalyst containing 10 to 40 µm cracks (CL free regions) can have beneficial effects in managing water formation within the CL.[8]

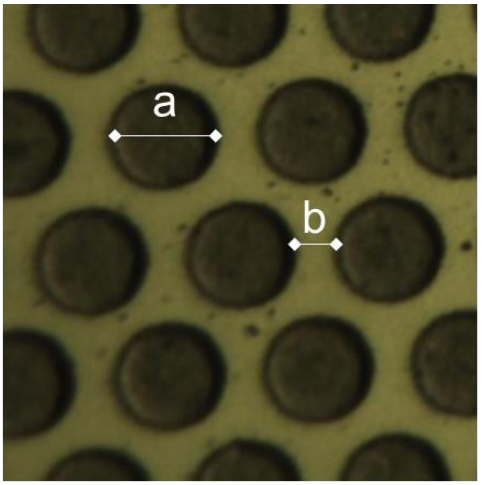


| feature size (a, µm) | 50 | 20 | 10 | 5 |
|---|---|---|---|---|
| feature min. separation (b, µm) | 25 | 10 | 5 | 2.5 |
| target catalyst layer thickness (µm) | 10 | 10 | 10 | 10 |
| catalyst layer aspect ratio | 0.2 | 0.5 | 1 | 2 |
| min. stamp aspect ratio | 0.5 | 1.3 | 3 | 5 |

**Figure 4.3 An illustration of hexagonally arranged features and relevant physical measurements for the relevant features created with these patterns.**

### 4.4.2 Catalyst Ink Preparation

To prepare the microscale patterned CCLs, catalyst ink was coated onto the microstructured PDMS templates and subsequently transferred onto Nafion® 211 membranes. The catalyst ink consisted of a mixture of Pt and C nanoparticles (50 wt % Pt content, TEC10E50E, Tanaka Kikinzoku Kogyo, Japan) that was blended with a 30 wt % loading of ionomer (Nafion® DE2020, Dupont, USA). This prepared catalyst mixture was dispersed in a 3:1 (v/v) solution of 2-propanol (Anachemia, Canada, ACS grade) and DI water (18 MΩ·cm) prepared in different overall volumes to achieve different solid contents of the ink solution as needed for the various coating applications. The ink suspensions were mixed using ultra-sonication applied for intervals of 1 s "on" and 3 s "off" for a total duration of 1 h (and a total of 15 min of sonication during the collective "on" time) using a probe sonicator (Fisher Scientific, USA, Sonic Dismembrator 500) with a 12-mm diameter probe, operating at 40 % maximum power.

### 4.4.3 Ink Coating Procedures

For preparing the CCMs, the CCLs were transferred onto the Nafion® membranes by microtransfer molding or microcontact printing techniques through the use of the elastomeric templates. The elastomeric templates were coated with catalyst materials using techniques that are described in the following sections. After transfer of the CCLs onto the Nafion® 211 membranes, the Pt loadings for each of the samples were verified by XRF techniques using a Niton XL3t system (Thermo Scientific, United States) operating at 40 kV. The XRF system was calibrated with a series of standard Pt samples with loadings in the range of 10 to 400 $\mu g_{Pt}/cm^2$ as prepared by MICROMATTER (Surrey, BC, Canada) for the quantification of the Pt loadings.

For the microtransfer molding of the CCLs, multiple coatings of catalyst ink with a 10 % (wt/wt) solids content were deposited onto the elastomeric templates by a Mayer bar coater. The elastomeric templates were first coated with the ink by a Mayer bar process and the ink was dried on a 50 °C heated stage for 10 min. Once dried, a piece of 3M Magic tape™, which covered the entire area of the elastomeric template, was placed on top of the template. The tape was smoothed over the elastomeric template with a very light pressure, and immediately peeled away from the template with a gentle force. These operations were all performed by hand. The CCLs created by this molding process were determined to have a Pt loading of 0.15 ± 0.01 $mg_{pt}/cm^2$.

For microcontact printing of the CCLs, multiple coatings of a catalyst ink solution with a 2 (wt/wt) % solids content (described in the previous section) were deposited onto the elastomeric templates using an ultrasonic spray coater (ExactaCoat, Sono-Tek, USA). The elastomeric templates were placed on a heated vacuum stage (held at 80 °C) in the spray coating chamber for fast drying between each coat of the catalyst ink onto the elastomeric templates. An air shaping parameter of 0.6 (arbitrary unit), and a spray flow rate of 0.2 mL/min were used for coating the elastomeric templates. The spray coater was programmed with four repeating serpentine patterns that were each perpendicular to the pattern of ink deposited in the previous layer. A dwell time of 30 s was used between each layer of the catalyst to ensure an even drying and the formation of a uniform coating on top of the elastomeric templates. The printed CCLs, with arrays of hexagonally arranged

cylindrical discs and holes, were determined to have Pt loadings ~80 ± 5 $\mu g_{Pt}/cm^2$ and ~130 ± 5 $\mu g_{Pt}/cm^2$, respectively.

For the comparative study of the CCLs, control CCLs were prepared with a continuous film was coated onto sheets of poly(ethylene-co-tetrafluoroethylene) (ETFE) films using a Mayer bar coater. A 20% (wt/wt) solids content of catalyst ink was used with the Mayer bar coater to achieve a continuous catalyst film with a Pt loading of 0.15 ± 0.01 $mg_{Pt}/cm^2$ with a single pass of the Mayer bar. The coated ETFE were placed on a 50 °C heated stage for 10 min for drying of the ink. Continuous films with a Pt loading of 0.05 ± 0.01 $mg_{Pt}/cm^2$ were also coated onto ETFE using the same technique, but for use as the anode catalyst layers (ACLs). These ACLs were used in all of the samples for the preparation of the MEAs.

### 4.4.4 Physical Characterization of Templates and MEAs

The morphologies of the elastomeric templates and the transferred CCLs were characterized by a series of techniques that included laser profilometry, optical microscopy, and SEM. To verify the morphologies of the elastomeric templates, scanning laser profilometry was performed using a Keyence VK series 3D laser scanning confocal microscope. The laser based profilometry was used to determine the aspect ratios of the hexagonally arranged cylindrical pillars or recesses on the elastomeric templates. The morphologies of the transferred CCLs were verified by SEM and optical microscopy. The optical images were obtained using a Zeiss Axio M1m optical microscope operating under a bright field mode. The SEM analyses were performed using an FEI Helios SEM/ focused ion beam (FIB) dual beam system operating at 10 kV. Furthermore, SEM images of sample cross-sections were also obtained by epoxy impregnation of the MEAs, and polishing the embedded samples to reveal materials in a cross-sectional manner. Cross-sections of all samples in Chapter 4 and 5 were obtained both before and after electrochemical and/or fuel cell testing to verify the integrity of the CCL microstructures. The MEAs were impregnated with an EpoxyCure™ 2 (Buehler, Illinois Tool Works Inc., United States) epoxy according to the manufacturer's specifications (https://www.buehler.ca/epoxy-mounting-systems.php, as of April, 2018), degassed in a vacuum chamber for 30 min, and cured overnight at room temperature. The epoxy

embedded samples were polished using an EcoMet™ 300 polisher (Buehler, Illinois Tool Works Inc., United States) with a series of Buehler brand silicon carbide sand papers (P280, P400, P800, P1200) to reveal the cross-sections of the epoxy embedded samples. The exposed surfaces were finely polished by a series of MetaDi Supreme ™ and MasterPrep™ (Buehler, Illinois Tool Works Inc., United States) polishing suspensions (diameters of 9 µm, 3 µm, 1 µm, and 0.05-µm). The finely polished epoxy embedded samples were coated with a 1-nm thick layer of carbon using a Leica EM ACE600 high vacuum deposition system (Leica Microsystems, Germany) prior to imaging with the SEM to reduce sample charging. Examples of the MEA cross-sections are presented in **Figure 4.4**.

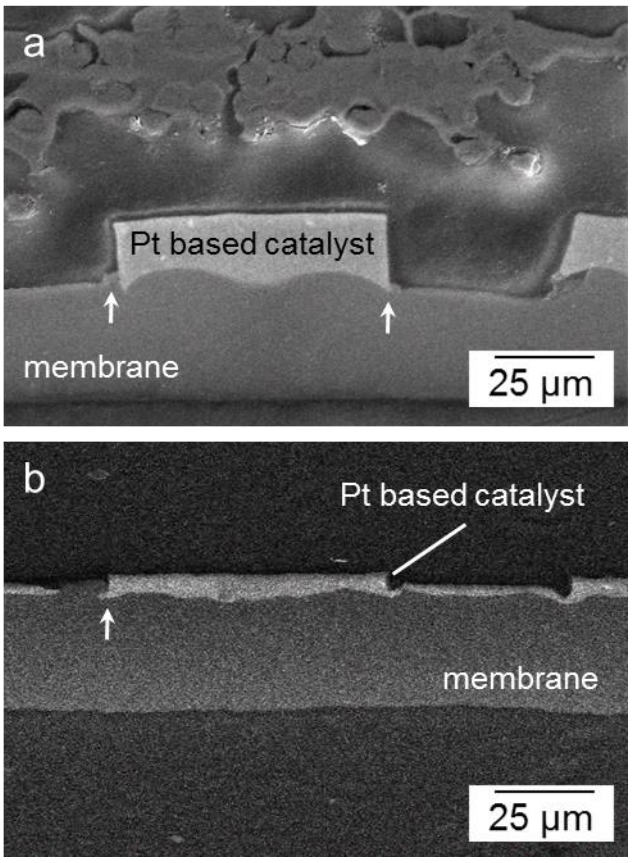


**Figure 4.4. Cross-sections of MEAs with patterned CCLs, prepared as outlined in Section 4.4.4, after PEMFC testing were imaged by scanning electron microscopy (SEM). These cross-sections were prepared by embedded the sample in epoxy and imaged by SEM operating at 15 kV using a backscattered electron detector. (a) An example of a catalyst ink molded onto a Nafion® membrane after removal of the catalyst skin layer. Note that the edges of the patterned ink exhibited relatively sharp features that was indicative of deformation to the Nafion® membrane, which resulted from the molding process (see arrows). (b) An example of a catalyst ink molded on Nafion® membrane without the removal of a 3-µm thick catalyst skin layer that was present on the elastomeric template before fuel cell testing.**

### 4.4.5 Preparation of MEAs

Patterned and control CCLs were used to prepare a series of CCMs, which were incorporated into MEAs and analyzed for their performance in PEMFCs. The catalyst ink coated materials (including ETFE and microstructured elastomer templates) were hot-bonded with a proton exchange membrane (PEM) to form the CCMs. All CCM anodes were prepared by hot-bonding a piece of catalyst ink coated ETFE (Pt loading of 0.05

$mg_{Pt}/cm^2$) to the Nafion® 211 membrane (NRE 211, DuPont, United States). To form the CCLs, either a catalyst ink coated elastomeric template (for either the microtransfer molding or microcontact printing processes), or a continuous catalyst ink coated ETFE film (Pt loading of 0.15 $mg_{Pt}/cm^2$) were used during the hot-bonding procedure. For microtransfer molding of the cathodes, the cathode and anodes catalyst layers were bonded to the Nafion® membrane at 4 bar/$cm^2$ of pressure and 150 °C for 5 min using a Carver® 25 ton hydraulic unit (Carver Inc., United States). The hot bonding temperature of 150 °C is required for the Nafion® to reach its glass transition temperature that would enable the contact between the membrane and the ink in the recesses of the stamp. [113,142] For microcontact printing of CCLs, the bonding pressure was reduced to 1 bar/$cm^2$, while all of the other parameters were unchanged as previously described. The control samples for each of the different CCLs were prepared with identical hot-bonding conditions for an equivalent comparison between the patterned and control samples. During the hot-bonding process, a sheet of 0.05-mm thick polytetrafluoroethylene (PTFE; Teflon®) was placed on top of the layered CCM materials, followed by a sheet of 2-mm thick polyurethane rubber. This layered set of materials was used to ensure an even distribution of the bonding pressure across the CCMs. After 2 min of bonding, the layered CCM materials were immediately removed from the Teflon® sheet and cooled to room temperature for at least 10 min. The ETFE films and elastomeric templates were gently removed by hand when the assembly was cooled sufficiently. A schematic of the CCM hot-bonding procedure is shown in **Figure 4.5**.

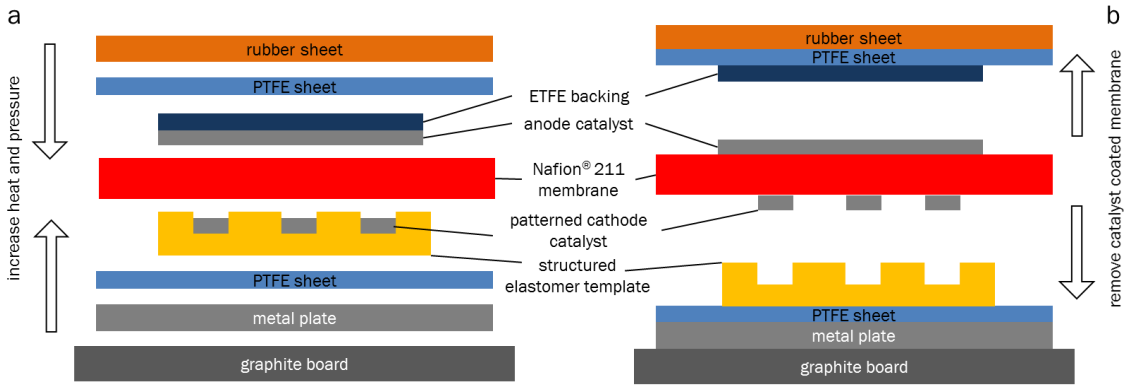


**Figure 4.5. Illustration of the hot-bonding process for preparing the CCMs: (a) the assembly and hot-bonding of various components for CCMs; and (b) the bonded CCMs after removal of the backing materials and other components of the support. PDMS: polydimethylsiloxane; ETFE: poly(ethylene-co-tetrafluoroethylene); and PTFE: polytetrafluoroethylene.**

The MEAs were prepared by hot-bonding the CCM with a 5 $cm^2$ square section of a macroporous layer (MPL) coated gas diffusion layer (GDL) (Freudenberg Fuel Cell Components, Germany), and a piece of G10 gasket (Saint-Gobain Performance Plastics Corporation, NH, USA) with a square opening in the center (5 $cm^2$). The same MPL/GDL and G10 gaskets materials were used for both the anode and cathode of the CCMs. The hot-bonding was performed with the same procedure as the one outlined for the preparation of the CCMs, with 4 bar/$cm^2$ of pressure at 150 °C for 2 min. Additional Mylar® gaskets (DuPont Teijin Films, UK) were used to adjust the thickness of the gaskets to induce a 25 % compression of the MPL/GDL materials when assembled into the PEMFCs. The fuel cell assembly pressure was adjusted by a manual process during a pre-assembly procedure with the use of a piece of Fuji prescale® pressure sensitive film (Super Low 0.5-2.5 MPa, LLW, Fujifilm, Japan).

### 4.4.6 Fuel Cell Testing of MEAs

The MEAs were analyzed as PEMFCs for comparing the performance of the patterned CCLs in contrast to the continuous CCLs. Fuel cell testing was performed using equipment provided by the Centre for Soft Materials in 4D LABS at SFU. These analyses were performed with a 50 W, Teledyne Medusa/Scribner systems (United States). Graphite plates with parallel gas flow-fields and landings were used in the assembly of the

single stack fuel cells. The active cell size was 5 $cm^2$ and a maximum backpressure of 5 psi applied to both the anode and cathode. The gas flow rates for the cathodes and anodes were set to 1 L/min (maximum set-point of the system). Electrochemical analyses, such as CV conditioning, assessment of the electrochemically active surface area ($A_{ecsa}$), and hydrogen cross-over analyses, were performed using a VersaSTAT 4 potentiostat (Princeton Applied Research, USA) operating in a two electrode configuration. The CV conditioning and $A_{ecsa}$ determination were performed at a scan rate of 100 mV/s with a sweep range from 0 to 1.2 V. The hydrogen cross-over was analysed by LSV performed over the range of 0.05 to 0.6 V at a scan rate of 5 mV/s. These electrochemical experiments were performed while the fuel cell was held at 80 °C with 100 % relative humidity (RH), and with $H_2$ (99.95 %, Praxair Canada) and $N_2$ (99.999 %, Praxair Canada) supplied to the anode and cathode, respectively. The microtransfer molded CCLs were analyzed under conditions that included conditions similar to the United States Department of Energy (US DOE) standard fuel cell test conditions (e.g., a cell temperature of 80 °C, at 100 % RH, 5 psi of backpressure, and with $H_2$ and air supplied to the anode and cathode, respectively), WUP conditions (e.g., a cell temperature of 65 °C, at 100 % RH, 5 psi of backpressure, and with $H_2$ and air supplied to the anode and cathode, respectively), and HOT conditions (e.g., a cell temperature of 90 °C, at 100 % RH, 5 psi of backpressure, and with $H_2$ and air supplied to the anode and cathode, respectively).[109] The microtransfer molded CCLs were polarized under potentio-static conditions at a series of potentials that included an open circuit potential (OCV), 0.8, 0.6, 0.4, 0.2, and 0.1 V with a 10 min dwell time at each set-point voltage.

The microcontact printed CCLs were also analyzed at a cell temperature of 80 °C, 100 % RH, without backpressure, and with $H_2$ and $O_2$ supplied to the anode and cathode, respectively. The microcontact printed CCLs were conditioned by LSV from 0.95 to 0.1 V, with the voltage stepped in 50 mV increments, and a 60 s dwell time per voltage step. A total of 12 LSV experiments were performed to condition the MEAs while aiming to achieve a deviation in fuel cell current densities of less than 0.5 $mA/cm^2$ for 3 consecutive LSV scans. A gradual increase and stabilization of the peak current produced by the fuel cell can be observed in **Figure 4.6**. After the LSV plots reached stabilization, 3 additional scans were performed, averaged, and analyzed to assess the fuel cell performance for each of the MEAs (e.g., **Figure 4.6**). The microcontact printed features were analyzed

through the preparation of duplicate samples, whereas the microtransfer molded CCLs were analyzed through the preparation of triplicate samples.

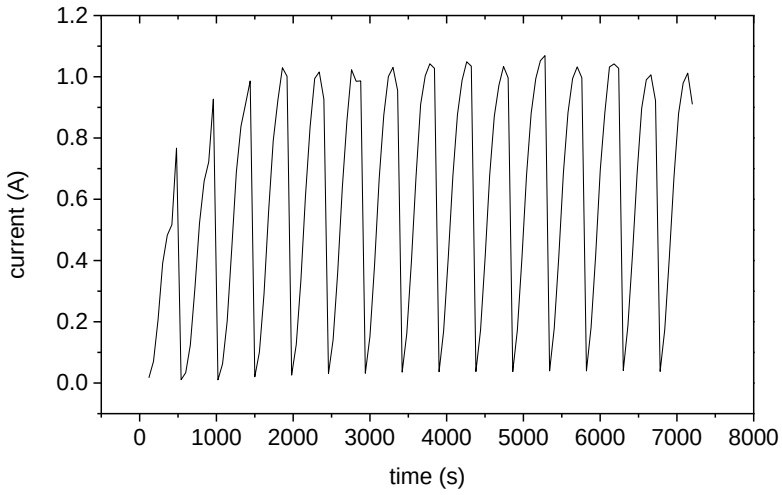


**Figure 4.6. A series of fuel cell polarization profiles, from 0.95 V to 0.1 V, which were used to condition the MEAs. The profiles demonstrated here were from a reference sample (200 $\mu g_{Pt}/cm^2$), which was conditioned at 80 °C, 100 % relative humidity (RH), and with $H_2$ (g) and $O_2$ (g) supplied at 1 L/min to the anode and cathode, respectively**

## 4.5 Results and Discussion

In this study, templates were prepared from a poly(dimethylsiloxane) (or PDMS) elastomer for the μTM and μCP processes for the patterning of Pt based inks. These patterned inks were used as CCLs for PEMFCs to seek improved catalyst layer designs that enhance their performance in comparison to continuous CCLs. The techniques for preparing these templates are outlined in detail in **Section 4.4.1**. The PDMS templates were prepared with hexagonally arranged arrays of 50-μm diameter cylindrical pillars or recessed features with a minimum edge-to-edge spacing of 25 μm between the features (**Figure 4.6c**). Microstructured CCLs were prepared through μTM and μCP techniques and transferred onto PEMs through a hot-bonding procedure. The hot-bonding procedures were optimized for each of the μTM and μCP techniques. Optical microscopy, SEM, and SEM cross-sectional imaging techniques were used to verify the morphologies, regularity,

and dimensions of the transferred CCLs. The CL coated membranes were further incorporated into MEAs and their performance analyzed using a series of fuel cell tests.

### 4.5.1 Treatment of Elastomeric Templates

The elastomeric templates used for molding and printing of catalyst inks also required a surface treatment to improve the transfer of the catalysts from the templates to the PEMs. Different surface coatings were evaluated for their ability to prepare patterned CCLs with a high fidelity of the features and to transfer them efficiently onto PEMs. Prior to pattern transfer, the elastomeric templates were coated with a slurry of catalyst ink that was composed of Pt nanoparticles on Vulcan C particles (50:50, wt/wt, Pt:C), along with a mixture of ionomer solution (Nafion® DE2020, 20 wt/wt % solids content), isopropyl alcohol (IPA), and DI water. The mass ratio of ionomer (Nafion DE2020) to Pt and C catalyst was maintained at 1:1 (w/w). The ratio of IPA to DI water was kept at 3:1 (v/v). The catalyst coated templates were hot-bonded with Nafion membranes (NRE211), which transferred the patterned CCLs from the templates to these membranes.

The surface chemistries of the templates were tuned to achieve both a uniform coating of the inks and an ease of their transfer to the PEMs. Coatings including trichloro (octadecyl) silane (OTS), perfluorosilane, and tartaric acid were grafted or adhered to the surfaces of different templates. The wettability of each release layer was assessed by water contact angle (WCA) measurements. The OTS, perfluoro silane, and tartaric acid coated templates exhibited WCAs of ~130°, ~150°, and ~30°, respectively.

The templates with a perfluoro silane release layer exhibited an optimal release of ink from the templates to the membranes. The ink did, however, not form a uniform layer upon drying while in contact with the templates. Due to the relatively high degree of hydrophobicity of the perfluoro silane coating, the catalyst ink formed discontinuous islands with large cracks between each of these islands upon drying. The tartaric acid coated template exhibited an excellent uniformity of the ink coating with no apparent cracks in the ink coatings even after drying. After the hot-bonding process the elastomeric templates will, however, bond irreversibly to the Nafion® membrane.

The OTS coated templates exhibited the best balance between uniformity of these coatings and release of the patterned inks. These templates exhibited an improved release of the ink, but also a smoother coating of the inks when compared to the results from the tartaric acid and perfluoro silane coated templates, respectively. The OTS surface coatings were robust enough to withstand three complete repeats of the processes for ink coating, hot-bonding, and cleaning of the templates. The cleaning process included soaking the template in IPA for 30 s and rinsing with IPA, followed by rinsing with water using a pressurized stream of DI water from a hand-held rinse bottle. After three successive uses of the templates in the hot-bonding procedure, the templates should be re-coated with OTS. The templates could otherwise start to exhibit adhesion with the PEM during the subsequent hot-bonding processes. The coating procedures used for coating of inks onto the templates are described in the following sections for their specific use in either μTM or μCP of the patterned CCLs.

### 4.5.2 Microtransfer Molding of CCLs

In this study, μTM techniques were used to prepare CCLs that contained hexagonal arrays of cylindrical holes for enhancing mass transport efficiencies of reagents and products in PEMFCs. A schematic of the molding process is illustrated in **Figure 4.7a**.

Details of these CCL transfer processes to transfer CCLs are described in the **Section 4.4.5**. In brief, microstructured elastomeric templates were coated with the catalyst ink using a metering bar (Mayer bar) coater. The catalyst ink used to prepare these coatings on the templates were diluted by 50 % (v/v) with the IPA and DI water mixture to prepare the necessary ink suspension, which was more dilute than conventionally prepared inks used for Mayer bar preparation of standard, continuous CCLs on poly(ethylene-co-tetrafluoroethylene) (ETFE) films. The reduced solid content of the diluted inks increased their fluidity over that of the more conventional ink formulations. The diluted inks were beneficial for their ease of filling into the recessed features of the templates without trapping air bubbles. After drying the ink, a process for the selective removal of the top, skin layer of ink was achieved using an adhesive tape. After removing the skin layer, the ink transferred from these templates resulted in the formation of CCL films with well-defined features within the otherwise continuous ink layer (**Figure 4.4b**).

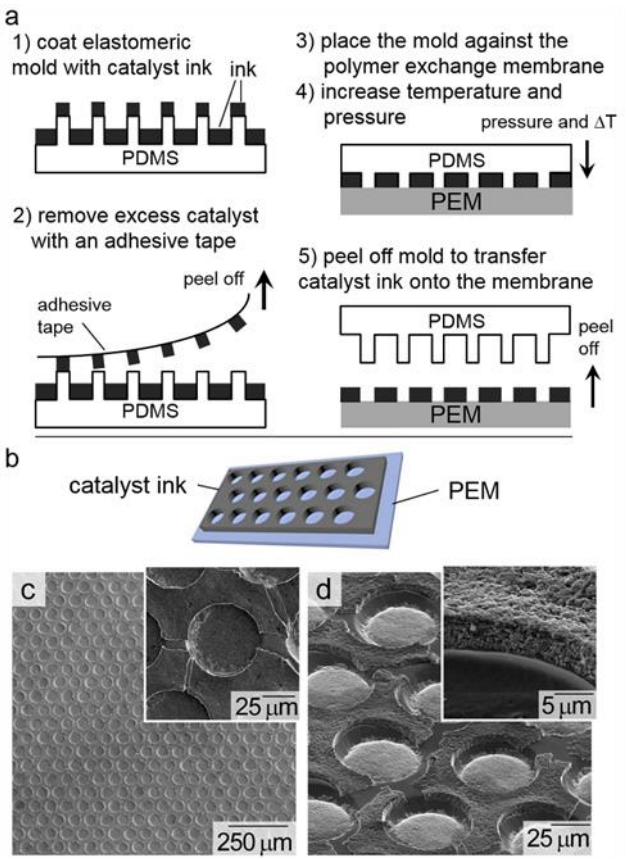


**Figure 4.7. (a) Schematic of the process to fill catalyst inks into the recesses of a poly(dimethylsiloxane) (or PDMS) template, and the transfer this patterned ink to a proton exchange membrane (PEM). (b) A three-dimensional representation of a patterned catalyst on a Nafion® membrane depicting an array of hexagonally arranged holes in the catalyst film. (c, d) The SEM images depict the patterned catalyst inks that were transferred to the Nafion® 211 membrane. Inset images depict: (c) a magnified top-down view; and (d) a side view of the patterned catalyst ink when imaged at a tilt angle of 52°.**

Cross-sectional SEM images indicated that CCLs prepared without removal of the skin layer of ink would retain a ~3-μm thick layer of catalyst covering the transferred features (**Figure 4.3b**). The patterned CCLs had a thickness ranging between 10 to 20 μm, whereas standard reference CCL films of a continuous ink had a thickness of ~5 μm. The transferred features consisted of hexagonally arranged arrays of 50-μm diameter cylindrically shaped holes that were separated by a minimum edge-to-edge spacing of 25 μm (**Figures 4.6b to 4.6d**).

The patterned CCL consisted of catalyst free holes within an otherwise continuous film of Pt ink. The holes covered ~40 % of the geometric active surface area of the MEA. It was proposed that these cylindrical holes, where catalyst is absent, could act as reservoirs for the collection and removal of water that is produced during the operation of the PEMFCs. The Pt loading within the CCLs was tuned to 0.15 $mg_{Pt}/cm^2$ as set as a target established by the United States Department of Energy (US DOE) for the desired Pt loadings in 2020.[139] The loadings of Pt within the catalyst coated templates, as well as within the CCMs, were measured by XRF spectroscopy. The patterned CCLs, with Pt loadings adjusted to 0.15 $mg_{Pt}/cm^2$, were incorporated into MEAs and characterized in PEMFCs under various operating conditions. The performances of these patterned CCLs were compared to that of MEAs prepared with continuous CCLs.

### 4.5.3 Performance of Molded CCLs for PEMFCs

The MEAs prepared in this study were analyzed in PEMFCs with active geometric areas of 5 $cm^2$. The detailed preparation of the MEAs and fuel cell testing procedures are provided in **Sections 4.4.4 and 4.4.5**. The molded CCLs were conditioned under standard conditions for PEMFCs [i.e. 80 °C and 100 % relative humidity (RH)], and analyzed for their performance under both WUP and HOT conditions. Details of these conditions are outlined in **Section 4.4.6**. The CV based analyses demonstrated that the patterned CCLs created by the described molding techniques had ~45 % less Pt electrochemically active surface area (Pt $A_{ecsa}$) than that in the reference samples with continuous CCLs (**Figure 4.7a**).

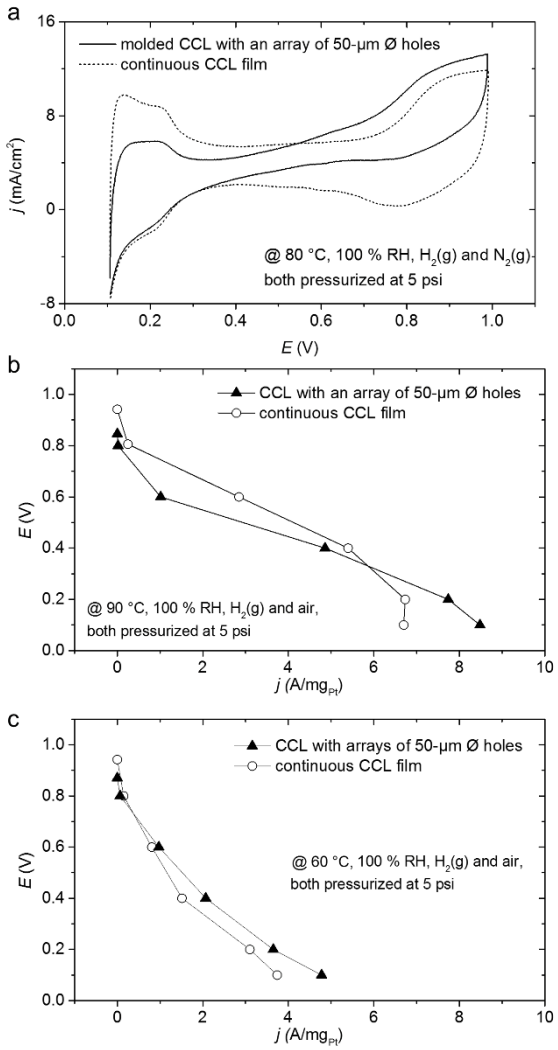


**Figure 4.8. (a) Cyclic voltammetry traces for cathode catalyst layers (CCLs) prepared as a continuous film or a patterned film containing an array of hexagonally arranged holes with 50-μm diameters. The patterned ink was transferred from a PDMS template by a microtransfer molding process. (b-c) Fuel cell polarization curves for both the continuous and patterned CCLs when operated under either (b) HOT or (c) WUP fuel cell conditions. The fuel cell operating conditions, RH, and the types of fuel used in these experiments are indicated on each of the plots.**

The Pt $A_{ecsa}$ for the molded and continuous CCLs were 42.4 $cm^2$ and 75.8 $cm^2$, respectively. This reduction in Pt $A_{ecsa}$ for the molded CCLs correlated with its reduced geometric surface area (i.e., 40 % less versus the continuous CCLs). The molded CCLs also had an increased thickness in comparison to that of the reference sample. The CV profiles for the molded CCLs also exhibited a tilted baseline at higher cell potentials. This

distortion in the CV profile indicated short-circuiting of the catalyst layer in the PEMFCs.[108] It is possible that the hot-bonding procedure used for the preparation of the MEAs caused the GDL to penetrate into the Nafion® membrane in the areas that were not covered by the catalyst inks. Compromised membranes with penetrating GDL fibers can induce a short-circuit current in PEMFCs.[140,141] A higher $H_2$ cross-over current was also observed for the molded CCLs (**Figure 4.8**).

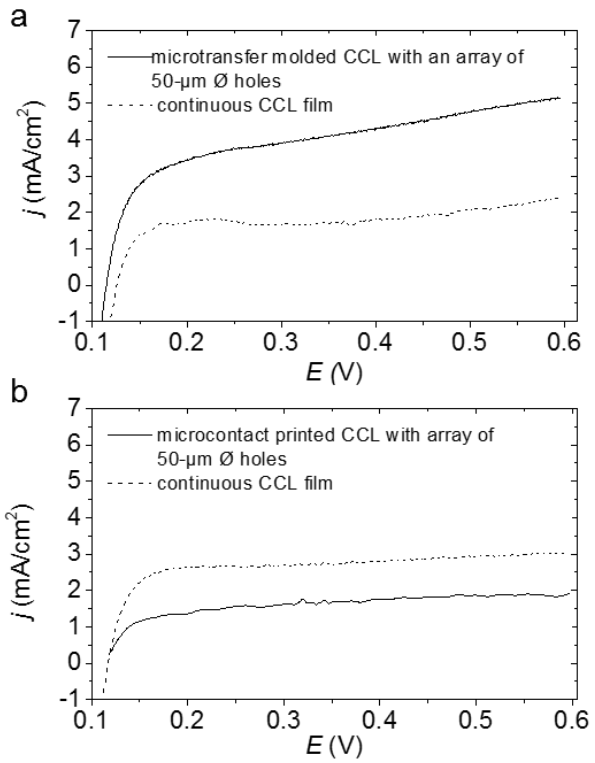


**Figure 4.9. Hydrogen cross-over currents for MEAs prepared from (a) microtransfer molded CCLs and (b) microcontact printed CCLs in comparison to control samples with continuous, unpatterned CCLs. These hydrogen cross-over currents were obtained at a cell temperature of 80 °C, 100 % RH, and with $H_2$ (g) and $N_2$ (g) supplied to the anode and cathode, respectively. The MEAs in (a) were tested under 5 psi of gas pressure to the anode and the cathode. The MEAs in (b) were unpressurized during this test.**

The μTM technique required a hot-bonding temperature of 150 °C, which is above the glass transition temperature of the Nafion® membrane. This temperature softened the membrane and enabled it to come into contact with the catalyst ink that was coated into the recesses of the stamps. It is possible that the hot-bonding temperature and pressure

for transferring CCLs onto the Nafion® could also result in membrane damage that leads to a higher degree of hydrogen cross-over.[113,142] Furthermore, significant membrane deformation occurred in the initial samples prepared with molded CCLs. An optimization of the hot-bonding process was investigated to eliminate the deformation of the PEM during the molding process. However, the balance of parameters for preparing the enhanced CCLs by molding and transfer to the PEM still resulted in ~1 µm deformations in the CCMs.

The MEAs were analyzed for performance under WUP and HOT fuel cell operating conditions. The resulting fuel cell polarization curves are presented in **Figures 4.7b** and **4.7c**. Under HOT fuel cell conditions, the reference CCLs had a higher current density than the molded CCLs over the potential range from 1.0 to 0.4 V. The molded CCLs did, however, exhibit an improved performance relative to the reference CCL over a potential range from 0.3 to 0.1 V. It is possible that despite the hot conditions, the increased water production at higher current densities (i.e., lower voltages) can lead to flooding of the reference CCL,[123,127] whereas the molded CCLs were able to better manage the water formation by expelling water into the recesses of the CCL patterns.[33,59,143]

In contrast, under the WUP conditions, the reference CCLs exhibited better performance than the molded CCLs in the potential range of 1.0 to 0.8 V. Also under WUP conditions, but from 0.6 to 0.1 V, the molded CCLs exhibited an increase in mass activity of at least 500 $mA/mg_{Pt}$ over that of the reference CCLs. Within this potential range, water can easily accumulate within the CCLs and lead to flooding of the PEMFCs due to the relatively low operating temperatures of the system.[123,144] The molded CCLs were determined to have a higher mass specific performance than the continuous CCLs under these conditions that can lead to flooding.

The results demonstrated for flooding under HOT and WUP conditions agreed with our hypothesis that CCLs with hexagonally arranged cylindrical holes within an otherwise continuous catalyst film can enhance the removal of excess water within the CCLs for improving the performance of PEMFCs. These µTM techniques for preparing CCLs and MEAs can, however, lead to membrane degradation and deformation. The damaged membrane can result in an increase of hydrogen cross-over and electrical shorting of the

MEAs, which can lead to an overall decrease in PEMFC performance for the patterned CCLs under standard fuel cell operating conditions. Further investigations into the patterning of CCLs by other techniques were, therefore, performed with the aim of reducing membrane damage and improving the overall performance of the patterned CCLs under standard fuel cell operating conditions.

### 4.5.4 Microcontact Printing of CCLs

In addition to μTM, another method for the preparation of patterned CCLs was investigated with the goal of improving PEMFC performance under standard conditions through reducing damage to the PEM. The μCP techniques utilize the top surfaces (e.g., highest features) of the elastomeric templates for creating a patterned CCL that is subsequently transferred to the PEM. This printing process enabled lower applied pressures (1 versus 4 bar/cm$^2$) and temperatures to be used during the CCL transfer than those used with the molding process. The CCL patterns were printed at a hot-bonding pressure of 1 bar/cm$^2$. Higher printing pressures can result in the transfer of ink from the recesses of the stamp. The transfer of ink from the stamp recesses would reduce the definition of the patterns or could even yield continuous CCL films over some regions. These milder CCL transfer conditions could minimize damage to the PEM, and improve the PEMFC performance for these patterned materials.

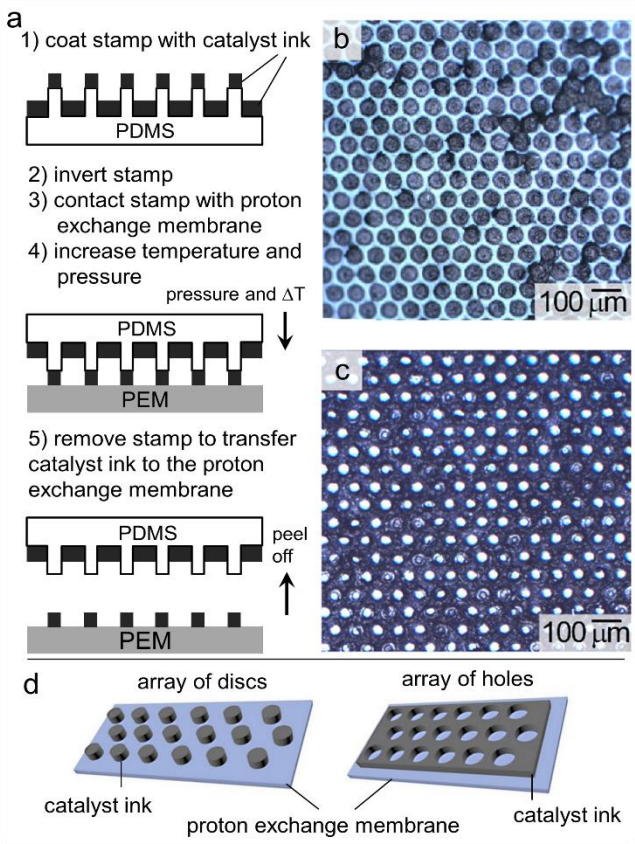


**Figure 4.10. (a) Schematic depiction of a microcontact printing (μCP) process used to prepare patterned CCLs. Representative optical microscopy images demonstrate the regularity of patterned CCLs consisting of hexagonally organized arrays of (b) discs of catalyst, or (c) holes within the catalyst film. (d) Three-dimensional representations of the patterned CCLs after transfer to the Nafion® 211 membranes. Examples are included to depict arrays of either discrete disc-like islands of catalyst or holes in an otherwise continuous catalyst film.**

The μCP procedures are illustrated in **Figure 4.9a**, and the detailed methods are described in the **Section 4.4.3**. Two different types of patterned CCLs were investigated for assessing their influence on the performance of PEMFCs. These patterns included arrays of hexagonally arranged cylindrical holes within an otherwise continuous film of catalyst ink, as well as catalyst ink arranged in a hexagonal array of discrete cylindrical discs (**Figures 4.9b and 4.9c**).

An ultrasonic spray coating method was used to deposit the ink on top of the elastomeric templates for the printing process. The spray coating conditions were tuned to deposit catalyst ink that dried relatively quickly after deposition onto the templates in

comparison to the conditions used for the Mayer bar coating of the templates. Because of capillary effects, the catalyst ink deposited onto the templates will collect primarily within the recesses of the microstructures when too much liquid remains in the ink after the coating process. By spray coating an ink that dries relatively quickly, the top surfaces of the template can be effectively coated with catalyst ink while only partially filling the recesses of the template.

The discontinuity that resulted in the films of catalyst ink between the top surfaces of the templates and their recesses ensured that only the ink on the ridges was transferred onto the PEM during the printing (hot-bonding) process. The μCP techniques were, however, limited to producing patterned CCLs with a reduced thickness. The reduced thickness of catalyst ink on the templates was necessary to achieve the desired discontinuity in the ink films between the ridges and the recesses of the stamp. A more uniform film of ink deposited onto the templates resulted in the printing of a continuous CCL film instead of a CCL with distinct patterns.

A series of elastomeric templates with different aspect ratios were prepared with the intention of increasing the discontinuity between the ridges and the recesses of the templates. The elastomeric templates consisted of arrays of 50-μm diameter cylindrical pillars or recesses patterned in a hexagonal arrangement and a minimum edge-to-edge spacing of 25 μm. The heights of the features were tuned to 15, 20, or 25 μm. All of the printed CCLs with discretely defined features were found with similar maximum loadings of catalyst regardless of the height of the template used for the transfer of the CCL films. The maximum Pt loadings for these arrays of catalyst patterned as discrete cylindrical discs or as films containing cylindrical holes were ~80 $\mu g_{Pt}/cm^2$ and ~130 $\mu g_{Pt}/cm^2$, respectively.

The μCP was also performed using elastomeric templates containing 20-μm diameter cylindrical features with a minimum edge-to-edge spacing of 7 μm. The elastomeric templates with these features of reduced dimensions were demonstrated to be unsuccessful in transferring CCLs to the PEMs with distinct patterns. These results suggested that the thickness of the printed CCLs was limited by the lateral spacing

between the distinct feature within the template and not by the aspect ratio of these features.

To prepare MEAs with CCMs that contained the μCP CCLs, the hot-bonding of the CCM to the GDL was skipped to reduce the possibility for short-circuiting the MEAs. These μCP CCLs were subsequently analyzed in PEMFCs under standard operating conditions and compared to the performance of standard samples containing continuous, non-patterned CCLs.

### 4.5.5 Performance of PEMFCs with Printed CCLs

The CCLs patterned by μCP were incorporated into MEAs, and their PEMFC performance evaluated against standard samples. The standard samples consisted of continuous CCL films with loadings of either 200 or 400 $\mu g_{Pt}/cm^2$. The microstructured CCLs were electrochemically conditioned using standard PEMFC operating conditions, and were analyzed for their performance under standard operating conditions as outlined by the US DOE.[145] The detailed procedures for MEA preparation and testing are described in detail in the **Section 4.4.5**. Representative CV and polarization profiles for these samples are presented in **Figure 4.10**.

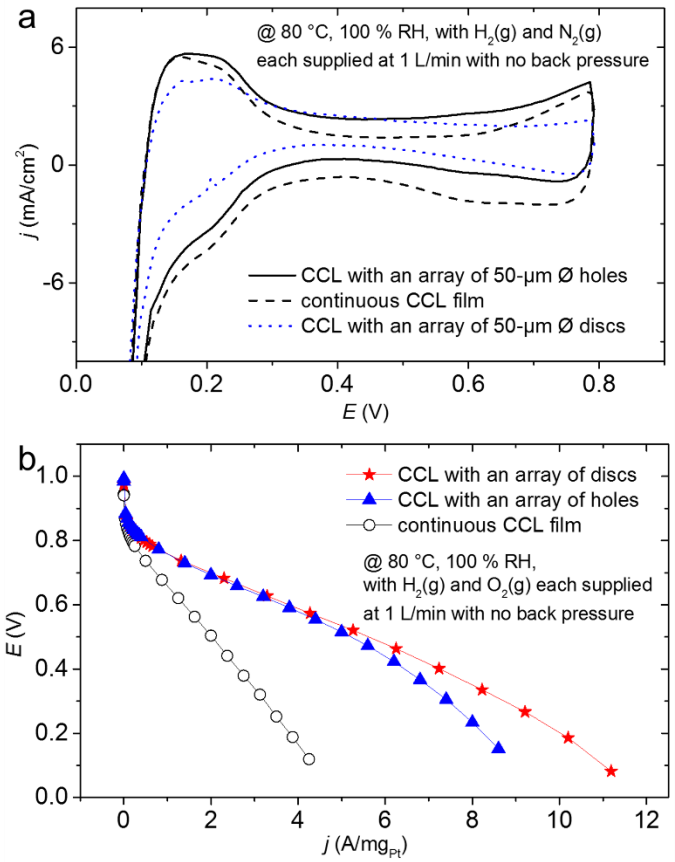


**Figure 4.11. Electrochemical and fuel cell characteristics of CCLs that contain either continuous films or microcontact printed films with arrays of hexagonally arranged cylindrical features that were 50-µm in diameter. This data includes (a) cyclic voltammetry profiles and (b) fuel cell polarization curves for these CCLs. The operating conditions of the fuel cells are indicated on each of the plots.**

The CV profiles of the samples containing patterned CCLs exhibited no short-circuiting characteristics, in contrast to the observations for the molded CCLs. The absence of a short-circuit current may be the result of eliminating the hot-bonding step for the GDL to the CCM. Both types of patterned CCLs (i.e., hexagonal arrays of either cylindrical discs of ink or holes within an otherwise continuous film) exhibited at least 2 times the Pt $A_{ecsa}$ when compared to the reference CCLs (**Figure 4.10a**). This increase in $A_{ecsa}$ could result from the difference in thickness between the CCLs. The thicker CCLs prepared for the standard, continuous films of ink may impede the infiltration of protons to the catalytic sites resulting in a reduced Pt $A_{ecsa}$.

In terms of fuel cell performance, the standard samples prepared with either a loading of 200 or 400 $\mu g_{Pt}/cm^2$ exhibited similar mass specific activities in comparison to the patterned CCLs despite the difference in thickness between these samples. The standard samples with 400 and 200 $\mu g_{Pt}/cm^2$ had a thickness of at least 5 and 10 µm, respectively. The 400 $\mu g_{Pt}/cm^2$ samples also exhibited a drastic mass transport loss at 0.2 V when compared to the samples with lower Pt mass loadings (**Figure 4.12a**). This increase in mass transport loss could be correlated to the increased thickness of the CCL, which could hinder the removal of water produced from the ORR.[143] Both of the patterned CCLs exhibited at least twice the mass activity of the reference CCLs (**Figure 4.10b**). It is possible that under the relatively low maximum backpressure (5 psi) of our fuel cell test station that only a fraction of the reactants were able to penetrate into the CCLs with their increased thickness.[123] The patterned CCLs did, however, also exhibit an improved specific current density in comparison to the standard sample with a loading of 200 $\mu g_{Pt}/cm^2$ (**Figure 4.12b**).

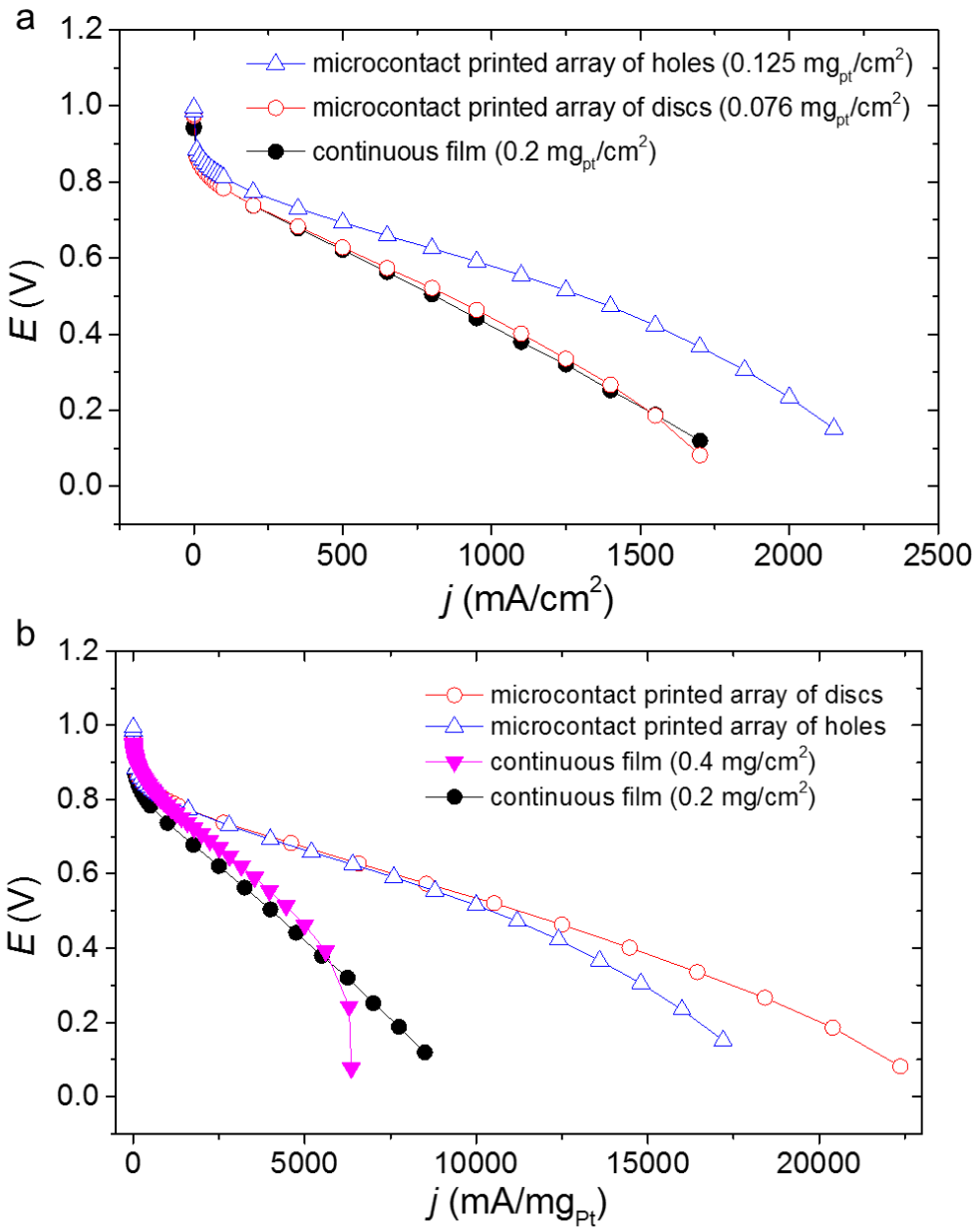


**Figure 4.12. Fuel cell polarization profiles of microcontact printed CCLs containing arrays of hexagonally arranged discs of ink or holes in comparison to reference samples with continuous CCL films. The polarization curves were normalized against the (a) geometric surface areas and (b) Pt weight as determined by XRF techniques. These polarizations were collected with fuel operating conditions of 80 °C, 100 % RH, and with $H_2$ (g) and $O_2$ (g) supplied at 1 L/min to the anode and cathode, respectively.**

The above result suggests that these patterned CCLs may also improve proton conductivities and their transport due to the inclusion of catalyst-free regions in contrast to CCLs with a continuous catalyst layer. Both types of patterned catalyst layers exhibited a similar performance from 0.8 to 0.5 V. From 0.6 to 0.1 V, the CCLs containing the hexagonal arrays of disc-like regions of catalyst ink exhibited a slight improvement over the CCLs with arrays of cylindrical holes in the catalyst films. This improved performance of the patterned CCLs with disc-like features at higher current densities may correspond to an improved water management, which could correlate to the higher percentage (60 vs 40 %) of catalyst-free geometric area within the hexagonal arrays of disc-like catalyst ink in contrast to the catalyst films containing an array of holes. This observation further supports the hypothesis that an increase in the void spaces within the catalyst layers can increase the volume in which water can move more freely under conditions resulting in a higher level of hydration. This increase in void space in the CCLs resulted in an enhanced performance of these CCLs at higher current densities, which correspond to an increased production of water within the fuel cells.

## 4.6 Conclusions

In this study, CCLs with arrays of hexagonally organized cylindrical features were prepared and analyzed for their performance in PEMFCs. These patterned CCLs were prepared by μTM and μCP techniques with the use of PDMS elastomeric templates. A surface coating of OTS was applied to the templates to achieve a uniform catalyst ink coating and an optimal transfer of this catalyst ink from the templates to Nafion® membranes.

When compared to standard samples containing unpatterned or continuous CCLs, the μTM CCLs exhibited a higher fuel cell performance under conditions that lead to a higher water content in the CCLs. These conditions included operation of the PEMFCs at higher current densities (0.2 to 0.1 V) under HOT fuel cell conditions, as well as over a range of current densities (0.7 to 0.1 V) under WUP conditions for fuel cells. A high degree of hydrogen cross-over and short-circuiting of the MEAs were, however, observed for these CCLs. These deficiencies may be a result from deformation of the membranes during the μTM process, and the intrusion of GDL materials into the membrane.

A further optimization of the transfer process for creating patterned CCLs was performed by pursuing μCP of the catalyst inks. The μCP process was performed at lower bonding pressures and temperatures for transferring the patterned CCLs to the Nafion® in comparison to the μTM process. These printed CCLs were assembled into MEAs without bonding to the GDLs. The samples of printed CCLs included arrays of hexagonally organized discs of catalyst ink or cylindrical holes in an otherwise continuous film. These patterned CCLs created by μCP exhibited at least twice the mass activity of the samples containing continuous CCLs when tested under standard fuel cell operating conditions. The PEMFCs containing patterned CCLs with arrays of cylindrical discs also exhibited a higher performance at relatively high current densities when compared to the samples containing the regular arrays cylindrical holes. This improvement in performance could be attributed to the higher percentage of catalyst-free space within the CCLs for the samples with discrete cylindrical discs of catalyst ink when compared to samples with cylindrical holes in an otherwise uniform film of catalyst ink.

The methods for patterning of the CCLs to improve their mass transport are compatible with existing CCL materials. These processes could also be extended to additional CCL materials and alternative patterns in the future to further optimize the performance of PEMFCs. Additional optimization of this technique for reducing hydrogen cross over and short circuits within the MEAs should be further investigated by utilizing different techniques for producing patterned CCLs. Catalyst-free carbon and ionomer coatings could also be used for planarizing the patterned CCLs and to further improve water management within the CCLs. Furthermore, future investigations will also include a further tuning of the dimensions of the cylindrical features and their spacing for additional optimization of the PEMFC performance.

# Chapter 5.

# Microstructured Membrane for Improving Proton Transport Resistance in Proton Exchange Membrane Fuel Cells

## 5.1 Acknowledgement

This research was conducted with contributions in part from the Natural Sciences and Engineering Research Council of Canada Discovery Program (Grant No. 1077758), the Mitacs-Accelerate Internship Program (M.T.Y. Paul, Grant No. IT05017), and the Canada Research Chairs Program (B.D. Gates; Grant No. 950-215846). This work made use of 4D LABS (www.4dlabs.ca) and the Centre for Soft Materials shared facilities supported by the Canada Foundation for Innovation (CFI), British Columbia Knowledge Development Fund (BCKDF), Western Economic Diversification Canada, and Simon Fraser University.

## 5.2 Abstract

Proton exchange membrane fuel cells have been identified as a renewable energy system for use in automotive applications. However, due to the wide range of weather conditions around the world, the PEMFCs must be stable for operating under these variable conditions. One of the inefficiencies of PEMFCs in automotive applications is during cold-start conditions where the low hydration level within the PEMFC can lead to a low performance of the fuel cell. In this study, a proton exchange membrane (PEM) was prepared with regular microstructures containing a range of aspect ratios. These microstructured membranes were incorporated into MEAs and analyzed for their membrane, proton, and oxygen transport resistances. These fuel cells were tested under different conditions to simulate vehicle WUP, NOC conditions, and hot operating conditions. It was determined that microstructured PEMs improved performance over planar PEMs under both the WUP and HOT conditions. Despite the improved performance of the microstructured PEMs, a high hydrogen cross-over and short-circuit current were

also observed for these samples. Adjusting the preparation techniques and tuning the dimensions of the microstructures should be investigated in the future for further optimizing of the performance of the PEMFCs.

**Graphical Abstract**

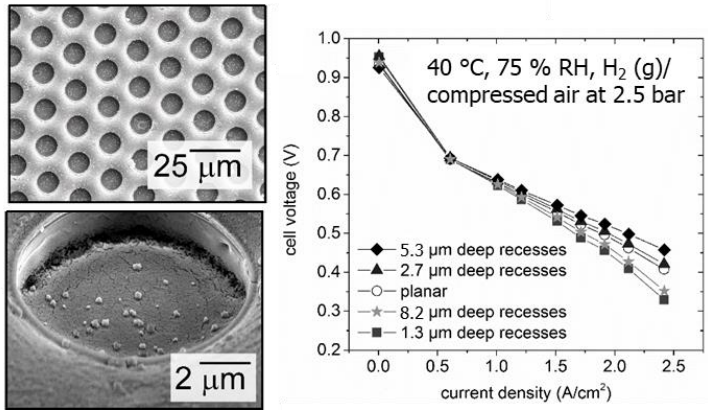


## 5.3 Introduction

At the heart of a PEMFCs is the CCM. The CCM contains the most expensive materials used in the PEMFCs (i.e., ionomer and Pt based catalyst). Researchers since the 1960s have used nanoscale Pt catalyst and catalyst support materials for reducing the cost of the system by maximizing the surface area to weight ratio of the catalyst.[41,51] These improvements essentially achieved a reduction in Pt loading densities from 4 $mg_{pt}/cm^2$ to 0.4 $mg_{pt}/cm^2$ from the catalysts in the first Gemini project to the current standards for commercial catalysts, respectively. In addition, methods for increasing the surface area of the PEM is less investigated due to processing challenges for preparing micro- and nanostructured interfaces.[146–148]

Compared to a synthetic approach to tuning catalyst surface areas (i.e., most solution based reactions), a reproducible modification of membranes with microscale patterns can utilize methods developed from the semiconductor industry. For example, Si-based materials can be prepared with regular patterns of cylindrical or pyramidal structures with high aspect ratios.[149] These Si-based materials can then be used for patterning the PEMs for use in PEMFCs. Only a few studies to date have investigated the use of thermal imprint lithography[146,147], micro-molding[148,150], electron beam lithography[151],

and molding with nanostructured metal oxide templates[152] for preparing microstructured PEMs for use in PEMFCs.

It was demonstrated by Aizawa *et al.* that PEM with microscale pillars (feature sizes of 10 µm), could be created by casting a solution of the membrane against a microstructured master. These patterned PEMFC exhibited an improvement in performance at low relative humidity (RH) levels (i.e., <50 % RH) over that of planar membranes by improving proton conduction of the PEMs.[146,147] The improvement in proton conduction was attributed to the increase in PEM to cathode catalyst layer (CCL) interface. Without modifying the PEM morphology, these improvements were previously achieved only by increasing the ionomer content in the CCL.[21,24] This microscale pattern is an attractive alternative to improve PEMFC performance under low humidity levels (vehicle cold-start conditions). Increasing the ionomer content within the CCL is not desired as it can impact the electrochemically active surface area of the Pt catalysts.[22]

A study by Bae *et al.* have investigated the hot-embossing of Nafion® membranes with both micro- and nanoscale parallel line structures.[153] It was determined that PEMs with microscale (>1 µm) features is advantageous over nanoscale (<110 nm) features due an improved interface with larger sized agglomerates that are present in the catalyst ink solution.[153] These PEMs were only tested under standard operating conditions, yet, with improved performance over planar PEMs.

Another study performed by Jeon *et al.* investigated additional ordered patterns of recesses in the PEMs (i.e., cylindrical, square, hexagonal features). It was determined that a cylindrical pattern exhibited the highest improvement in the performance for PEMFCs.[148] In this previous study, the aspect ratio (height/width) was, however, kept relatively low (0.5), and it was suggested that a higher aspect ratio features could further improve the performance of microstructured PEMs.

Furthermore, these aforementioned studies focused only on either normal operating conditions or conditions at low RH levels. The fuels in this study were tested under cold conditions, as well as hot conditions to simulated vehicle WUP and HOT operating conditions to further determine the improvements of these microstructured PEMs over planar membranes.

Our study aimed to prepare PEMs with microscale cylindrical features with different aspect ratios. A series of PEMs containing different microstructures were assessed for their PEMFC performance at NOC, WUP, and HOT operating conditions. The operating conditions of the fuel cell tests consisted of WUP (40 °C), NOC (70 °C), and HOT (90 °C) operating conditions. We hypothesized that an increase in surface area at the PEM and CCL interface could further improve PEMFC performance under unfavourable conditions, such as WUP and HOT. A detailed analysis was performed to further understand oxygen transport phenomena within MEAs containing microstructured interfaces between the PEM and CCL.

## 5.4 Materials and Methods

In this study, lithographically prepared templates were used to create an array of hexagonally arranged microscale features between the cathode catalyst layers (CCLs) and proton exchange membrane (PEMs; Nafion® 211). The microstructured interfaces were created by imprinting the PEM with a master containing arrays of cylindrical features to create a PEM surface with arrays of cylindrical recesses. After obtaining the microstructured PEMs, an ink mixture of Pt nanoparticles (NPs), carbon NPs, and ionomer (Nafion® DE2020, Dupont, USA) were coated on top of the PEM to create the CCMs. The patterned PEMs and CCMs were characterized to verify their physical dimensions and the densities of their Pt loadings. These patterned CCLs were incorporated into MEAs with a 40 $cm^2$ active area to determine their performance in PEMFCs.

### 5.4.1 Preparation of Templates for Use in the Hot-Embossing of PEMs

Microscale PEM to CCL (half-CCM) interfaces were created by hot-embossing PEMs with photolithographically prepared templates. These templates were prepared from photolithographically patterned SU-8 (SU-8 2025, MicroChem, Germany) supported on polished Si (100) wafers (International Wafer Service, Inc., USA). Chromium patterned on borate-glass photomasks used in the photolithographic processes were purchased from 4D LABS at Simon Fraser University (www.4dlabs.ca). Photolithography was performed according to the manufacturer's protocols (http://www.microchem.com/Prod-

SU82000.htm). The photolithgraphically created features consisted of 10-µm diameter circular pillars arranged in a hexagonal pattern with a minimum edge-to-edge feature spacing of 5 µm. The SU-8 pillars and recesses were controlled to a thickness of 10 µm. The general photolithographic process to prepare the masters is shown in **Figure 4.1**. Because the templates were used to directly hot-emboss patterns into PEMs. A release layer coating is required for removing the PEM from the template after the embossing process. The release layer coating procedure includes the following steps: (i) treatment of the templates with an air-based plasma at ~30 Watts for 5 min; (ii) immersion of plasma treated templates in a 0.1 % (v/v) solution of the 1H, 1H, 2H, 2H-perfluorooctyldimethylchlorosilane (Alfa Aesar, 95 %; referred to herein as prefluorosilane) prepared in toluene (v/v) for 5 min; and (iii) the silane coated templates were rinsed with isopropanol and dried under a flow of nitrogen gas (99.998 % $N_2$, Praxair, Canada). The qualities of the release layer coatings were evaluated by a VCA Optima water contact angle (WCA) measurement system (AST Products, MA, United States). The measurements were performed with droplets of 1 µL of deionized (DI) water (Barnstead DIamond™ with an output of 18 MΩ·cm), averaged over 5 different regions on the prepared masters. An average WCA of ~150° was achieved for the release layer coated microstructured templates.

### 5.4.2 Preparation and Coating of Catalyst Ink

To prepare the microscale half-CCM interfaces, catalyst ink was coated directly onto the microstructured PEMs. The catalyst ink used in these studies consisted a mixture of Pt and C nanoparticles (50 wt/wt % of Pt content, TEC10E50E, Tanaka Kikinzoku Kogyo, Japan) that was blended with a 30 wt/wt % loading of ionomer (Nafion® DE2020). This mixture was dispersed in a 3:1 (w/w), 2-propanol (Anachemia, Canada, ACS grade) to DI water solution to achieve a 20 % solid content (wt/wt %) solution. The ink suspensions were mixed with ultra-sonication using intervals of 1 s "on" and 3 s "off" for a total duration of 1 h (and a total of 15 min of sonication during the collective "on" time) using a probe sonicator (Fisher Scientific, USA, Sonic Dismembrator 500) with a 12-mm diameter probe, operating at 40 % of its maximum power. A Mayer bar coater was used for coating the hot-embossed PEM with the prepared ink solution. The Mayer bar coater was used to achieve a continuous catalyst film with an average Pt loading of 0.15 $mg_{Pt}/cm^2$

with a single pass of the Mayer bar. The Pt loadings for the samples were verified by XRF techniques using a Niton XL3t system (Thermo Scientific, United States) operating at 40 kV. The XRF system was calibrated with a series of standard Pt samples with loading ranging from 10 to 400 $\mu g/cm^2$ prepared by MICROMATTER (Surrey, BC, Canada) for the quantification of Pt loading. After Mayer bar coating, the half-CCMs were dried at room temperature overnight. To create the anode catalyst layer (ACL) laminates, poly(ethylene-co-tetrafluoroethylene) films were coated with continuous films at a Pt loading of 0.05 $mg_{Pt}/cm^2$. The coated ETFE were placed on a 50 °C heated stage for 10 min to dry the ink. These ACLs were subsequently hot-bonded to the half-CCMs during the MEA preparation process. For comparative studies, the same amount of CCL inks were coated onto a planar PEM that was hot-embossed with a silane treated, polished Si wafer.

### 5.4.3 Preparation of the MEAs

To prepare MEAs for fuel cell testing, the Mayer bar coated half-CCMs were bonded with ACLs, followed by their incorporation into MEAs. The ACL laminates (ETFE backed ACLs) were first hot-bonded to the half-CCL at 10 bars of pressure and 150 °C for 2 min using a Carver® 25 ton hydraulic unit (Carver Inc., United States). During the hot-bonding process, a sheet of 0.05-mm thick polytetrafluoroethylene (PTFE; Teflon®, DuPont, USA) was placed on either side of the layered ACL laminate and half-CCM, followed by a sheet of 2-mm thick polyurethane rubber. This layered set of materials was used to ensure an even distribution of the bonding pressure across the CCMs. After 2 min of bonding, the layered CCM materials were immediately removed from the Teflon® sheet and cooled to room temperature for at least 10 min. The ETFE films were gently removed by hand after the assembly was cooled to room temperature. A schematic of the CCM hot-bonding procedure is outlined in **Figure 5.1**.

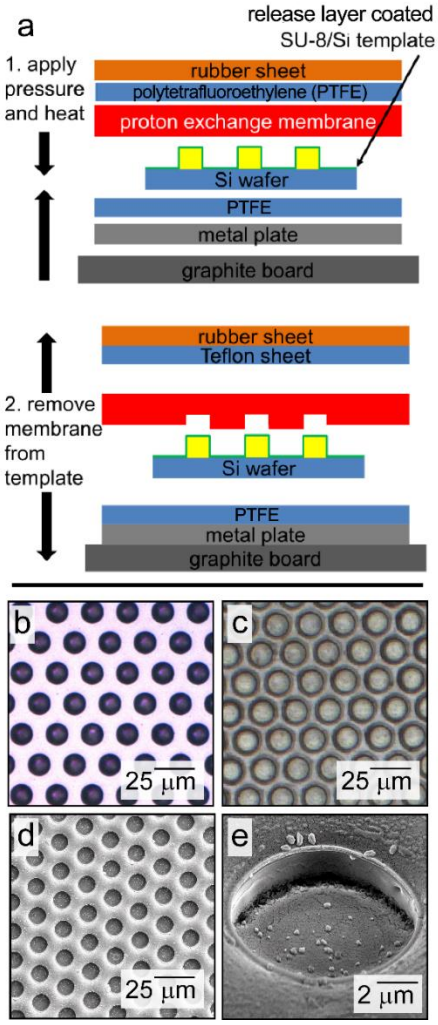


**Figure 5.1.** **(a) A schematic illustration of the different components used in the hot embossing process. (b-c) Bright field optical microscopy bright field images of (b) a photolithographically prepared SU-8/Si master, and (c) an embossed Nafion® membrane with arrays of hexagonally arranged recesses. (d-e) Scanning electron microscopy images of the embossed Nafion® membrane shown in (c) at (d) a lower magnification, and (e) a higher magnification with the sample tilted at 45°.**

The MEAs were prepared by hot bonding the CCM with two pieces of polyimide based gasket frames and macroporous layer (MPL) coated gas diffusion layer (GDL) (proprietary and separately optimized for the cathode and anode by Automotive Fuel Cell Corporation (AFCC; Burnaby BC, Canada) leaving a 4 cm by 10 cm exposed MEA surface area for PEMFC testing. The heat and pressures were only applied to the polymer frame using a handheld soldering iron with the assistance of an alignment jig. No additional

gaskets were needed during fuel cell testing to achieve a 25 % compression of the MPL/GDL materials when assembled into the PEMFCs.

### 5.4.4 Physical Characterization of the Templates and MEAs

The morphologies of the hot-embossing templates and the microstructured PEMFCs were characterized by a series of techniques that included laser profilometry, optical microscopy, and SEM. To verify the morphologies of the hot-embossed PEMs, laser profilometry was performed using a Keyence VK series 3D laser scanning confocal microscope. The laser profilometry was used to determine the aspect ratios of the hexagonally arranged pillars on the hot-embossing templates. The morphologies of the hot-bonded PEMs were verified by SEM and optical microscopy. The optical images were obtained using a Zeiss Axio M1m optical microscope operating under bright field mode. The SEM analyses were performed using an FEI Helios SEM/focused ion beam (FIB) dual beam system operating at 5 kV. Prior to imaging the microstructured PEM, a ~5-nm thick gold coating was sputtered (Hummer 6.2, Anatech USA) onto the polymeric sample for providing electron conductivity during the SEM analysis. Furthermore, SEM sample cross-sectional images were also obtained by epoxy impregnation of MEAs, and polishing the embedded samples to reveal materials in a cross-sectional manner. The MEAs were impregnated with an EpoxyCure™ 2 (Buehler, Illinois Tool Works Inc., United States) epoxy according to the manufacturer's specifications (https://www.buehler.ca/epoxy-mounting-systems.php), degassed in a vacuum chamber for 30 min, and cured overnight at room temperature. The epoxy embedded samples were polished using an EcoMet™ 300 polisher (Buehler, Illinois Tool Works Inc., United States) with a series of Buehler brand silicon carbide sand papers (P280, P400, P800, P1200) to reveal the material cross-sections from the epoxy embedded samples. The exposed surfaces were further finely polished by a series of MetaDi Supreme ™ and MasterPrep™ (Buehler, Illinois Tool Works Inc., United States) polishing suspensions (diameters of 9 µm, 3 µm, 1 µm, and 0.05-µm). The finely polished epoxy embedded samples were coated with 1-nm thick carbon using a Leica EM ACE600 high vacuum thin film deposition system (Leica Microsystems, Germany) prior to imaging with the SEM to reduce sample charging.

### 5.4.5 Fuel Cells Testing of MEAs

The MEAs were analyzed as PEMFCs for comparing the performance of the microstructured CCLs to PEM interfaces with different feature aspect ratios in contrast to the planar CCL to PEM interface. Fuel cell testing was performed using equipment at AFCC. These analyses were performed with a 100 W, LEANCAT systems (LEANCAT, Jablotron Group, Czech Republic). The active cell size was 40 $cm^2$ with a maximum backpressure of 2.5 bar applied to both the anode and cathode. The fuel cell assemblies were compressed with a pneumatic bladder set at 20 psi. The electrochemical and fuel cell characterization were each performed over a period of 48 h with a computer controlled pre-set program.

Electrochemical analyses, such as CV, carbon monoxide stripping, and hydrogen cross-over analyses, were performed using the potentiostat that is integrated in the LEANCAT system. The CV conditioning and $A_{ecsa}$ determination was performed at a scan rate of 100 mV/s with a sweep range from 0 to 1.2 V. The hydrogen cross-over was analysed by LSV performed over the range of 0.05 to 0.6 V at a scan rate of 5 mV/s. These electrochemical experiments were performed while the fuel cells were held at 78 °C, 100 % relative humidity (RH), and with $H_2$ and $N_2$ gases supplied to the anode and cathode, respectively.

The MEAs were analyzed under the following conditions: (i) NOC conditions (a cell temperature of 70 °C, 75 % RH, 2.5 bar of backpressure, and with $H_2$ and compressed air supplied to the anode and cathode, respectively); (ii) WUP conditions (a cell temperature of 40 °C, 75 % RH, 2.5 bar of backpressure, and with $H_2$ and compressed air supplied to the anode and cathode, respectively); and (iii) HOT conditions (a cell temperature of 90 °C, 75% RH, 2.5 bar of backpressure, and with $H_2$ and compressed air supplied to the anode and cathode, respectively). The MEAs were polarized with LSV under galvanostatic conditions for a series of current densities that included 0, 0.6, 1.2, 1.5, 1.7, 1.9, 2.1, and 2.4 $A/cm^2$ with a 10 min dwell time at each current set-point.

To determine the oxygen transport resistances of the MEAs. A limiting current method with variable oxygen gas pressure was used to determine the oxygen transport resistances of the MEAs.[117] The concentration of the $O_2$ was fixed with inlet pressures of

1.5, 2.0, 2.5, and 3.0 bar, and the cell was allowed to equilibrate for 10 min at each pressure set-point. The cell was then potentio-statically controlled at 400, 300, 200, 150, 125, 100, and 50 mV for 10 mins at each potential to collect the limiting current. For more details of this analysis please refer to **Section 3.5.5.**

## 5.5 Results and Discussion

The goal of this study is to create microstructured proton exchange membranes (PEMs) and to study the relationship between microscale features and their performance in PEMFCs. These microstructured PEMs were prepared by physical embossing of hexagonally arranged cylindrical patterns into the membranes using a hard template. The aspect ratios of the embossed features were controlled by varying both the hot-embossing temperature and pressure. The resulting features in the membrane were analyzed by laser profilometry to determine their aspect ratios. These microstructured membranes were subsequently coated with Pt based catalysts and incorporated into MEAs for use in PEMFCs. The electrical and proton resistances of these MEAs were determined by EIS utilizing a porous catalyst layer model. A limiting current method with variable oxygen gas pressure was also used to determine the oxygen transport resistances of the MEAs.[117] Finally, these MEAs containing microstructured PEMs with features of different aspect ratios were analyzed under an array of conditions to determine their performance characteristics. These conditions simulated WUP, NOC, and HOT vehicle operating conditions.

### 5.5.1 Preparation of Hot-Embossing Templates

To create microstructured PEMs, a series of hot-embossing templates were prepared with regular patterns using photolithographic techniques. Microstructured templates were prepared with a negative tone photoresist (2000 series SU-8 from Microchem®, Germany) supported on polished silicon (100) wafers (International Wafer Service, Inc., USA). The detailed methods of the template preparation are presented in **Section 5.4.1**. In brief, the photolithography process was performed according to the manufacture's specifications. An additional post-exposure thermal treatment at a reduced temperature (65 °C for 5 mins) was, however, required to prepare mechanically stable SU-

8 features with high aspect ratios higher than 1. Without this additional thermal treatment, the SU-8 features could peel off from the Si substrate during the hot-embossing process. A schematic representation of the photolithography process is presented in **Figure 5.1**.

### 5.5.2 Hot-Embossing of PEM Membranes

Prior to hot-embossing of the PEM membranes with the prepared templates, a release layer was needed to prevent irreversible adhesion between the PEM and the templates. Details of the preparation of the release layer on the templates are presented in the **Section 5.4.1**. A fluorinated release was used in this study (1H, 1H, 2H, 2H-perfluorooctyldimethylchlorosilane; Alfa Aesar, USA, 95 %). The hot-embossing procedures could be repeated up to 3 times with each template, at which point the release layer coating needed to be replenished to prevent unwanted adhesion between the template and the PEM.

### 5.5.3 Hot-Pressing Procedures

To create the microstructured PEMs, the release layer coated templates were hot-embossed against a Nafion® 211 membrane while tuning the applied temperature and pressure. The detailed hot-pressing procedures are reported in the **Section 4.4.5**. Many different layers of materials were used during the hot-embossing process to enhance the uniformity of the resulting features in the PEMs. A schematic depiction of the materials used during the hot-embossing process is presented in **Figure 5.1a**. Optical and SEM images of the templates and embossed features are presented in **Figures 5.1b to 5.1e**. These embossed features contained hexagonally arranged arrays of recesses each covering an area of 50 $cm^2$. The recesses consisted of cylindrical features with 10-µm diameters and a minimum feature edge-to-edge spacing of 5 µm. These feature sizes were chosen due to the ease of their preparations, and the similarity of their dimensions to previous literature on microstructured PEMs (10 to 2-µm diameters). The feature depth in this current study ranges from 1.3 to 8.2 µm, which is deeper than those previously reported (i.e., 1 µm). Membranes with microstructured recesses of different depths were prepared by tuning the hot-embossing conditions. These features were also assessed for their impact on the performance of PEMFCs.

For the procedures for hot-embossing of the PEMs, a hot-bonding time of >5 min was required to achieve uniformly embossed features in the PEMs across the 50 $cm^2$ area regardless of the embossed feature dimensions and aspect ratios. To create regular hexagonally arranged arrays of recesses in the PEMs, hexagonally arranged arrays of 10-µm tall cylindrical pillars of SU-8 on polished Si wafers were prepared as the hot-embossing template. To tune the aspect ratio of the embossed features, incremental increases to the applied pressure in steps of 0.02 bar/$cm^2$ above 0.4 bars/$cm^2$ resulted in a corresponding stepwise increase of ~1 µm to the feature heights at a bonding temperature of 135 °C (**Figure 5.2**).

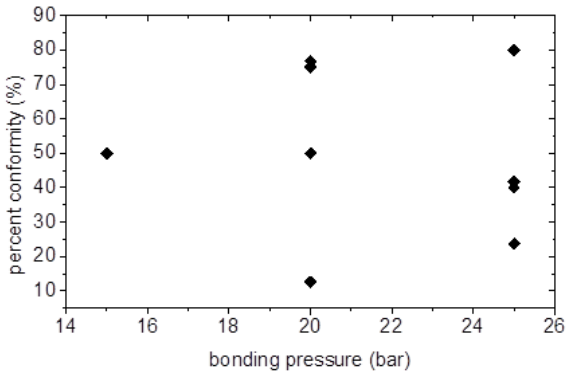


**Figure 5.2. The ratios between SU-8/Si template feature heights and the resulting depths of features in the embossed Nafion® membranes at constant embossing temperatures with varying bonding pressures. The depths of the features were correlated with the height of the features on the embossing templates (Equation 5.1)**

$$\text{percent conformity} = \frac{\text{embossed NRE feature depth}}{\text{hard template feature height}} \times 100 \qquad \textbf{(Equation 5.1)}$$

It was determined that variations in temperature can also be used to control the depth of the embossed features (**Figure 5.3**). For the purpose of this study, all samples prepared for testing in PEMFCs were prepared by varying the applied pressure, while keeping the temperature constant at 135 °C. This constant temperature approach was sought to avoid changes in the molecular composition and/or structure of the membrane materials, which could happen during hot-embossing processes at high temperatures.

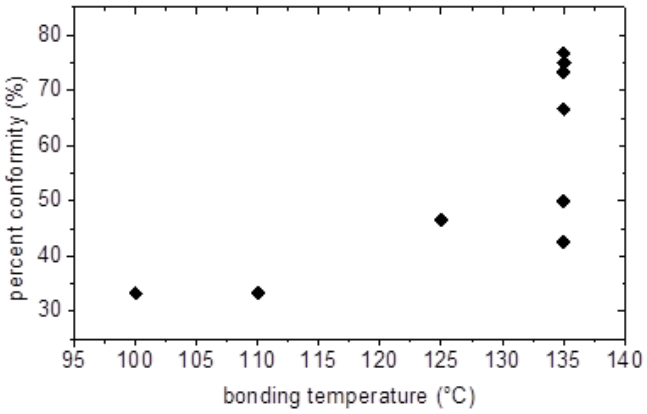


**Figure 5.3. The ratios between SU-8/Si template feature heights and the resulting depths in the embossed Nafion® membrane at constant embossing pressures of 4 bar/cm$^2$ with varying bonding temperatures. The depths of the features were correlated with the height of the features on the embossing templates (Equation 5.1).**

A maximum depth of 8.2 µm was achieved through these processes. This limitation may be due in part to trapped air within the recessed features of the templates and the relatively low hot-embossing temperatures. Initial hot-bonding attempts with templates prepared on borosilicate glass substrates (3 mm in thickness) resulted in a broken substrate during their second use at 0.4 bar/cm$^2$. The polished Si wafer based templates were tested for applied pressures up to 0.8 bar/cm$^2$ without observing fractures or other damages of the substrates.

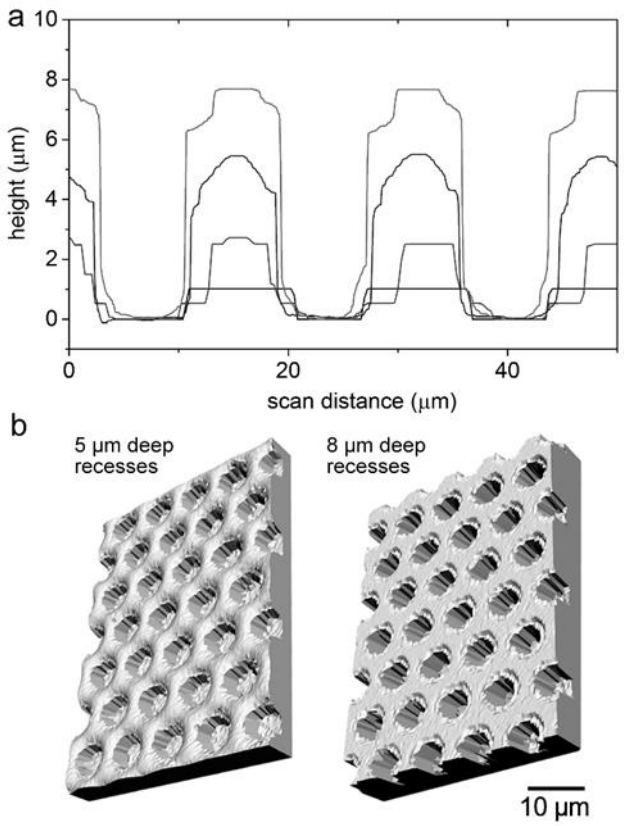


**Figure 5.4. (a) Laser profilometry measurements of samples with different depths of recessed features ranging from 8 to 1 μm. (b) Rendered, 3D images depicting the morphologies of the embossed Nafion® membranes.**

The membrane features were verified by scanning laser profilometry (Keyence VK series) after hot-embossing (**Figure 5.4**). This process was determined to be reliable after a correlative study between a probe-based profilometer (Bruker Dektak XT, USA) and the laser system. The feature depths were determined at 5 different locations of the embossed membranes (middle, and at ~1 cm diagonally from each of the corners). The formation of these microstructures increases the surface area of the interface between the PEMs and the CCLs. For example, an interfacial surface area increase of as much as 129 % calculated for PEMs with 8.2-μm deep recesses (**Figure 5.5**). The increase in membrane to catalyst layer interface could result in an increase to the performance of the fuel cell by increasing proton conduction across the anode and cathode catalyst layers.[146–148,153] These membranes with increased interfacial surface area were incorporated into MEAs for further characterization in PEMFCs.

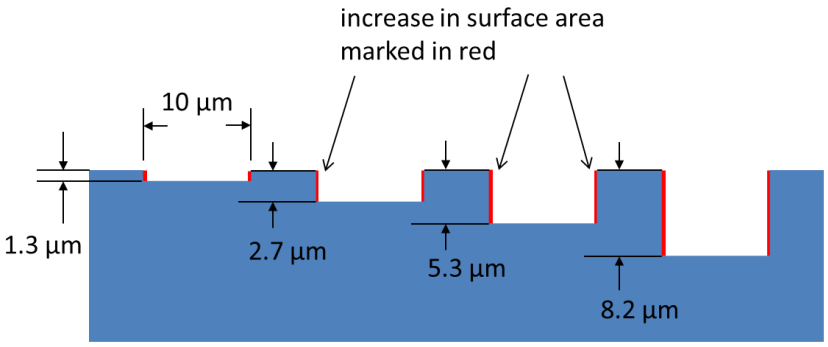


| feature feight (± 0.5 µm ) | 1.3 | 2.7 | 5.3 | 8.2 |
|---|---|---|---|---|
| surface area increase (%) | 21 | 44 | 81 | 130 |

**Figure 5.5. Theoretical calculation of the increase in PEM surface area after the formation of microstructured recesses. The various feature depths were obtained by averaging the results from laser profilometry at 5 different locations on the hot-embossed PEMs.**

### 5.5.4 Preparation of MEAs

Microstructured PEMs with different patterns were coated with a Pt based catalyst ink, and incorporated them into MEAs for analysis in PEMFCs. The procedures for preparing the CCMs are described in detail in the **Section 5.4.2**. The microstructured interface of the PEM were coated for use as the CCL in the PEMFCs. The CCLs were prepared with a loading of 0.15 $mg_{Pt}/cm^2$. The anodes were prepared as laminates with a loading of 0.05 $mg_{Pt}/cm^2$. The anodes were hot-bonded from the laminate to the CCL coated half CCMs. The final CCMs were sandwiched between 2 microporous layer coated gas diffusion layers and a polymer frame that had a 10 cm by 4 cm window in the center for accessing the MEA performance under fuel cell testing conditions.

### 5.5.5 Basic Characteristics of the MEAs

The MEAs containing microstructured PEMs were analyzed by a LEANCAT system (LEANCAT Fuel Cell Technology, Czech Republic) with a 40 $cm^2$ cell. The fuel cell testing procedures are presented in detail in **Section 5.4.5**. Prior to this assessment, the MEAs underwent 200 complete CV scans from 0.05 V to 1.2 V. The fuel cell was held 70

°C, 100 % RH, and with $H_2$ and $N_2$ pressurized to 2.5 bar to the anode and cathode, respectively. These conditions were maintained for 8 h to equilibrate the environment within the fuel cells. The fuel cells were characterised for their membrane resistances, proton resistances, electrochemically active surface areas ($A_{ecsa}$), and $H_2$ cross-over with $H_2$ and $N_2$ gases supplied to the anode and cathode, respectively.

The ohmic resistance (membrane, or $R_{ohm}$) and proton resistance ($R_{ion}$) of the fuel cells were measured by electrochemical impedance spectroscopy (EIS) at baseline conditions. The EIS measurement protocols were described in detail in **Section 3.5.4**. In brief, the EIS response of the MEA was measured at baseline levels and the data were fit with an equivalent circuit consisting of a wire inductor, short-circuit and fuel cell resistors, and a Warburg element ($Z_{we}$) that describes a De Levie porous electrode model (**Figure 3.13**).[50,53] The wire inductance and of the fuel cell resistance were assumed to be negligible compared to the other parameters in the circuit. The resistances of the membranes slightly decreased with increases to the depth of the recesses in the membrane. This reduction in membrane resistance may be due to the reduced membrane thickness within the recessed features.

The Nafion® 211 membrane had an original thickness of ~25 µm. After the formation of the microstructured recesses, which accounts for 44 % of the projected surface area, the membrane thickness decreases to ~17 µm within the recesses. The thinner regions of the membrane could be attributed to the overall reduction in membrane resistance (**Figure 5.6a**).[154–156] The ionic resistance of the MEAs also decreased with an increase in the depth of the embossed recesses. In comparison to planar membranes, the membrane with 8-µm deep recesses exhibited a 10 times increase in proton conductivity (**Figure 5.6a**). This increase in proton conductivity may be attributed to the increased interfacial surface area between the CCL and the PEM. Alternatively, proton conductivity can be improved by increasing the ionomer content in the CCL, while maintaining similar MEA hydration conditions.[157] The increase in ionomer content within the CCL can, however, lead to swelling of the CCL under a high level of hydration.[21,44,158] The increase in ionomer content can also inevitably reduce $A_{ecsa}$ by blocking Pt surface area.[44,158] The increase in PEM surface area demonstrated in this study could achieve similar properties to these previous studies without increasing the ionomer content within the CCLs.

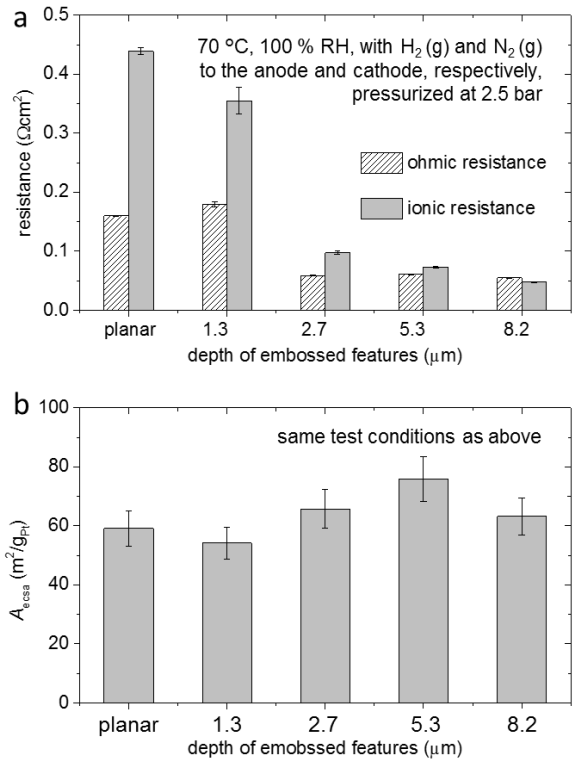


**Figure 5.6. Characteristics of the MEAs with features of different depths embossed into membranes at the CCL interface: (a) total ohmic resistance of the MEA (ohmic resistance) and proton resistance of the cathode catalyst layer (ionic resistance); and (b) electrochemically active Pt surface areas ($A_{ecsa}$). The error bars represented a standard deviation of +/- 1σ from the calculated means as obtained from the average of 3 different electric impedance spectroscopy (EIS) measurements for (a), and of 5 cyclic voltammetry (CVs) and of 2 CO stripping measurements for (b).**

The $A_{ecsa}$ of the CCLs in the microstructured MEAs are presented in **Figure 5.6b**. To provide a fair assessment of $A_{ecsa}$ for the MEAs, the reported values were averaged with results from the CO stripping experiments, as well as assessing the total charge under the respective hydrogen adsorption and desorption peaks in the cyclic voltammogram (**Figure 5.7**). The CO stripping experiment was performed according to a published procedure, while assuming the charge required for removing a monolayer of CO on the Pt surface is 0.210 mC/cm$^2$.[159] All of the microstructured MEAs exhibited similar $A_{ecsa}$ values, within 15 % of one another. This result was expected since all of the CCMs were coated

with a similar ink and evaluated under similar conditions. The mass specific $A_{ecsa}$ determined for the MEAs are each within the range of the reported values for Pt and C nanoparticle based catalyst layers.

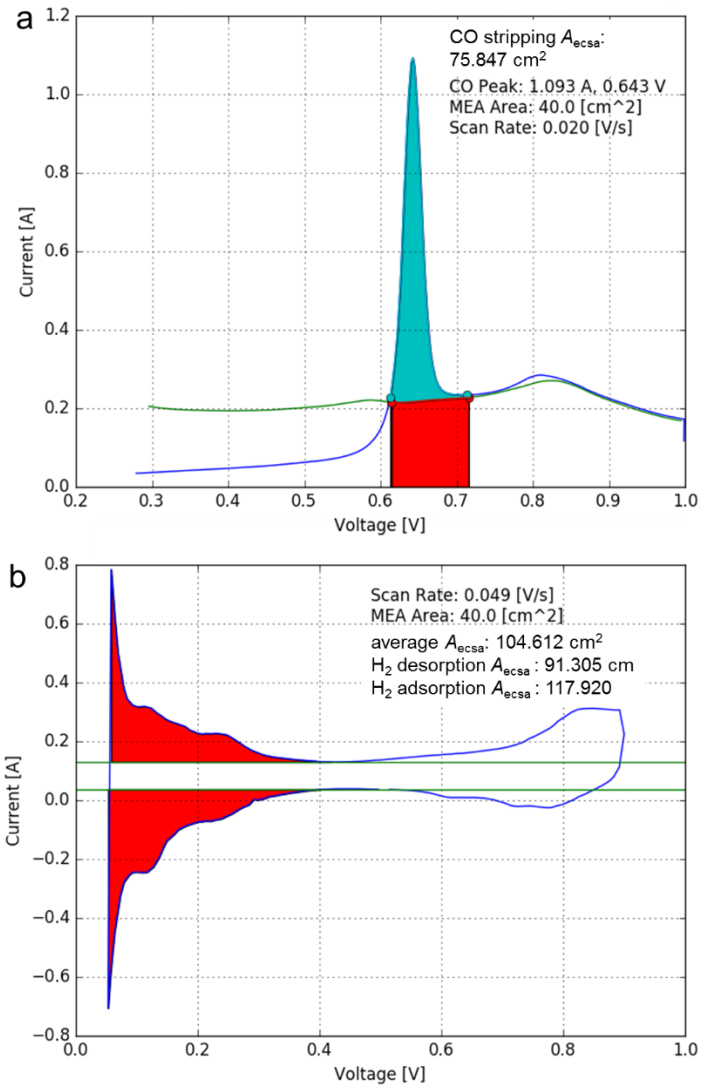


**Figure 5.7. The electrochemically active $A_{ecsa}$ profiles of MEAs containing 5-µm deep recesses, obtained by (a) CO stripping experiment; and (b) cyclic voltammetry in a PEMFC at 70 °C, 100 % RH, and $H_2$ and $N_2$ gas supplied to the anode and cathode, pressurized at 2.5 bar. The red and green regions in (a) represented the background and integrated peak area, respectively. The red regions in (b) represented the integrated peak areas.**

The hydrogen cross-over current density ($j_{H2}$) of the MEAs were also assessed under fuel cell operating conditions (with $H_2$ and $N_2$ gases). The MEAs exhibited a trend of increasing $H_2$ gas cross-over currents with increasing depth of the embossed membrane features (**Figure 5.8**).

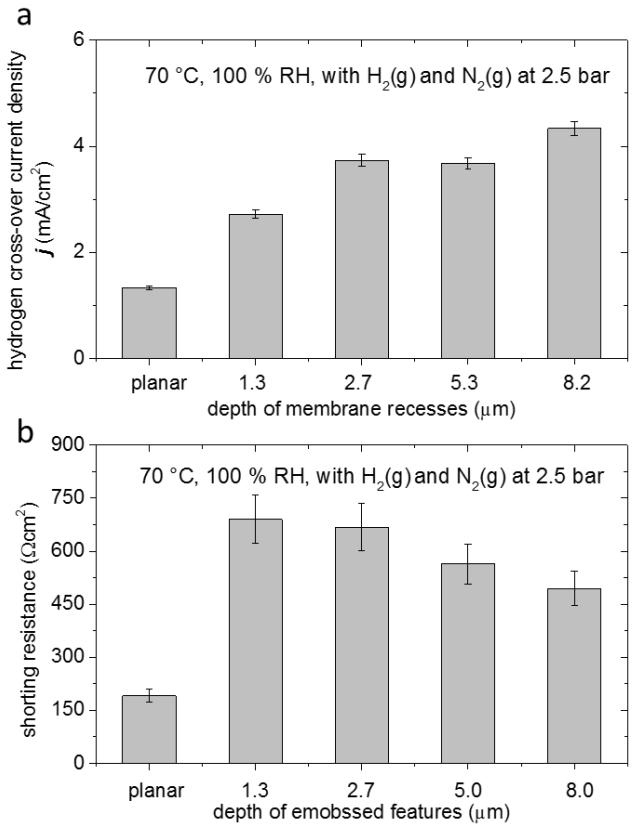


**Figure 5.8. Characteristics of the MEAs with different depths of features in the embossed membranes at the CCL interface: (a) hydrogen cross-over current densities; and (b) shorting resistances. The error bars represent a standard deviation of +/- 1σ from the calculated means obtained from the average values obtained from 3 different $H_2$ cross-over measurements for (a), and from 3 different EIS measurements for (b).**

The membranes with 8-µm deep features exhibited more than twice the cross-over currents than the membranes without microstructures. All membranes were hot-embossed under the same temperatures. The planar membrane was hot-embossed with a flat Si wafer coated with the same release layer used for embossing with the templates. Therefore, the variations in $H_2$ cross-over are most likely a result of the membrane microstructures. As mentioned previously, the increase in depth of the recesses in the

membranes can reduce the thickness of the membrane in some regions. A thinner membrane could contribute to a higher degree of $H_2$ cross-over. It is also possible that the mechanical processes involved in deforming the membrane could create microscopic damage in the membrane and increase the cross-over current.[142,160] Furthermore, the shorting resistance ($R_{short}$) of the MEAs were also calculated by determining the slope of the $j_{H2}$ (**Figure 5.8**). The observed increases in shorting resistance was proportional to the depth of the embossed features. This correlation further implies that significant physical damage and thinning of the membrane could result from the hot-embossing process.

### 5.5.6 Oxygen Mass Transport Resistance of the MEAs

After conditioning and performing an initial assessment of the characteristics of the MEAs, the $N_2$ supplied to the cathode was switched to a compressed air source. A series of limiting current methods were performed under NOC to determined oxygen transport resistances ($R_{mt}$) of the MEAs at the different operating conditions. Detailed testing procedures are presented in the **Section 3.5.5**. In short, each MEAs were pressurised with 1.5, 2.0, 2.5, and 3.0 bar, at both the cathode and anode. The fuel cells were held for 10 min at each of the set point voltages (0.4, 0.3, 0.25, 0.2, 0.15, 0.125, and 0.1 V) to determine the averaged limiting current of the fuel cells. The total oxygen (RH $R_{mt}$ were directly related to the limiting current of the fuel cells at a constant oxygen pressure (averaged between inlet and outlet pressures). A linear plot between pressure and $R_{mt}$ was then constructed, where the slope and Y intercept of the curve represented the pressure dependent ($R_{pd}$) and pressure independent ($R_{id}$) components of $R_{mt}$. The $R_{pd}$ transport is related to the intermolecular diffusion of oxygen within “open spaces.” For example, large pores within the catalysts that is not filled with liquid water. The $R_{id}$ is related to the Knudsen diffusion or the transport of oxygen through the ionomer/liquid water layers. The $R_{pd}$ and $R_{id}$ of the MEAs are presented in **Figure 5.9**.

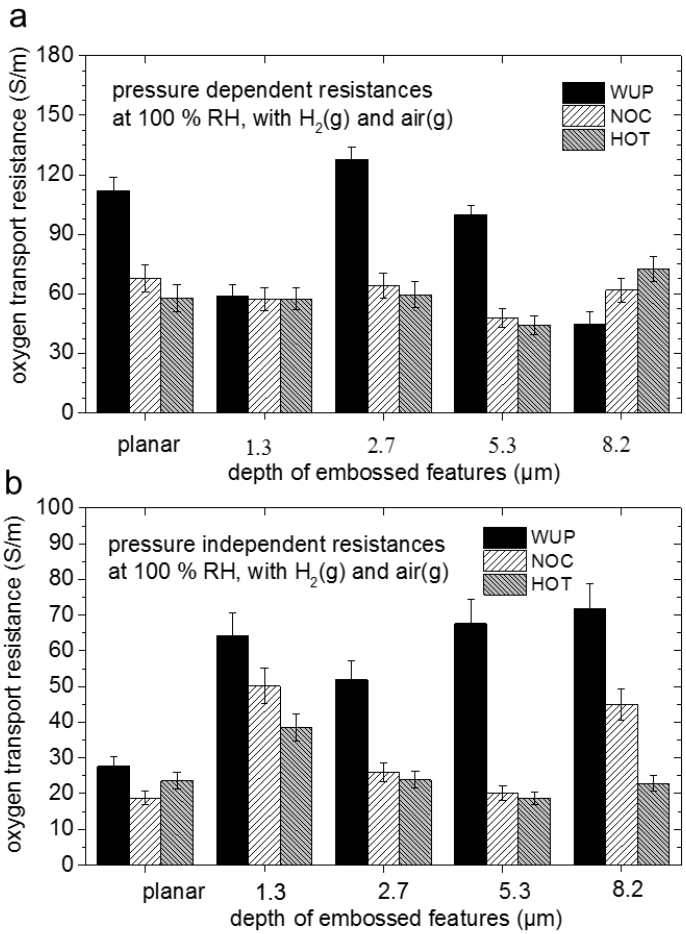


**Figure 5.9. The (a) pressure dependent and (b) pressure independent oxygen transport resistance characteristics of the MEAs with different depths of features in the embossed membranes at the CCL interface under warm-up operating conditions (WUP), normal operating conditions (NOC), and hot operating conditions (HOT).**

Since the $R_{mt}$ calculation assumes a uniform CCL and PEM morphology, the absolute values of the experiment may not be as relevant since the microstructured PEMs contained a non-uniformity in both the PEM and CCL morphologies.[23,117] Therefore, the relative transport distributions were calculated, and these are presented in **Figure 5.10** for each of the MEAs under the different operating conditions.

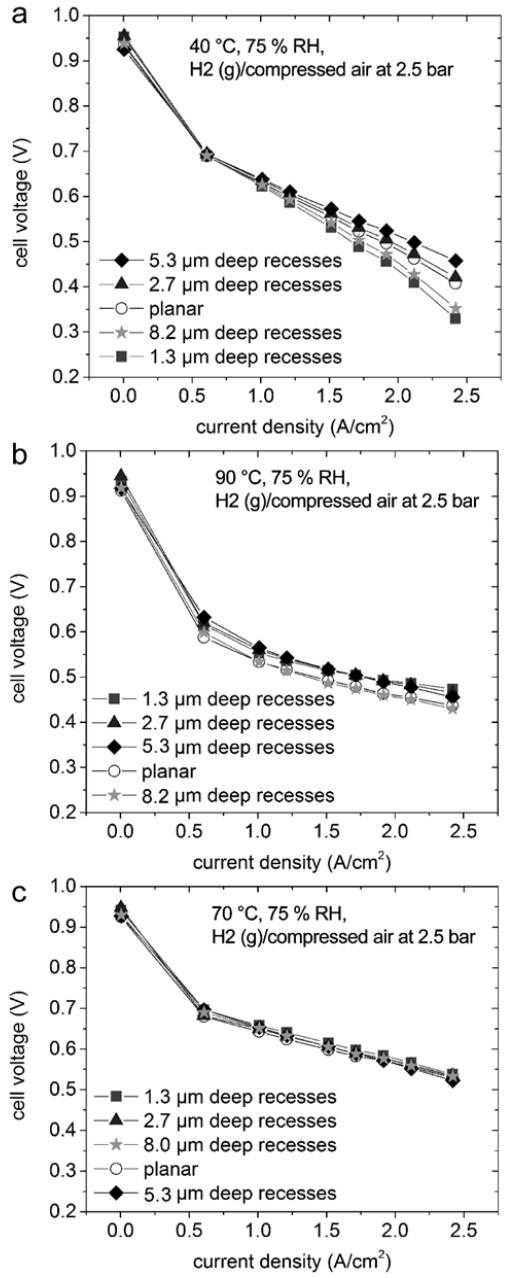


**Figure 5.10. Fuel cell polarizations for samples with hexagonally arranged cylindrical recesses of different depth evaluated under different operating conditions. (a) Fuel cells under WUP at 40 °C, 75 % RH, and $H_2$ (g)/ compressed air at the anode/cathode each pressurized at 2.5 bar. (b-c) Fuel cells under different operating cell temperatures emulating (b) HOT 90 °C, and (c) NOC at 70 °C while maintaining consistent settings for all other parameters.**

Under WUP conditions, all of the MEAs containing microstructured PEMs exhibited a higher percentage of $R_{id}$ transport than MEAs with planar PEMs. An increase in the depth of the microstructures is correlated with an increase in $R_{id}$. The increase in $R_{id}$ indicated that more water was retained in the MEA. This result agrees with prior literature, which determined that PEMs with nanostructures are able to self-regulate its hydration levels.[147,157] Furthermore, the fuels cells were tested under different operating conditions including WUP, NOC, and HOT conditions, which corresponded to cell temperatures of 40 °C, 70 °C, and 90 °C, respectively. The relationship that was previously observed between the $R_{id}$ and microstructure was observed under WUP and NOC. Under HOT conditions all of the oxygen transport resistances were, however, similar for all of the samples (within a deviation of 10 %). The $R_{mt}$ values gave a rough estimation of how each of the MEAs behaved with respect to the depth of their microstructures. The actual fuel cell performance will, however, largely depend on the balance between all relevant operating parameters, such as $H_2$ cross-over, shorting resistance, proton resistance, membrane resistance, and $R_{mt}$.

### 5.5.7 Performance of the MEAs in PEMFCs

The MEAs were analyzed under a range operating conditions, including NOC, WUP, and HOT, with $H_2$ and compressed air supplied to the cathode and anode, respectively. The detailed testing conditions are described in detail in **Section 5.4.5**. The PEMFCs were held galvanostatically at an open circuit potential (~0 A/cm$^2$), as well as at set-points of 0.6, 1, 1.2, 1.5, 1.7, 1.9, 2.2, and 2.4 A/cm$^2$ for 10 min at each set-point. Despite the increased $H_2$ cross-over and shorting current of the MEAs that contained microstructured PEMs, some of these MEAs exhibited an increased PEMFC performance over MEAs containing planar PEMs. It was determined that under WUP conditions, the membrane with 5.3-µm deep features exhibited the best overall performance, followed by the sample with 2.7-µm deep features (**Figure 5.10a**). The MEAs with 5.3-µm deep PEM features exhibited a 50 mV (15 %) improvement over MEAs with a planar PEM at 2.4 A/cm$^2$. Under this condition, water is easily condensed within the MEA due to the lower cell temperatures.[8,38,155] This water accumulation is more severe at higher current densities where a lot of water molecules are being produced at the CCL. A generalized simulation of the migration front of a liquid against a permeable material with structured

and planar surfaces were prepared using Solidworks™ (Solidworks 2016, Dassault Systems, France) and the results are presented in **Figure 5.11**.

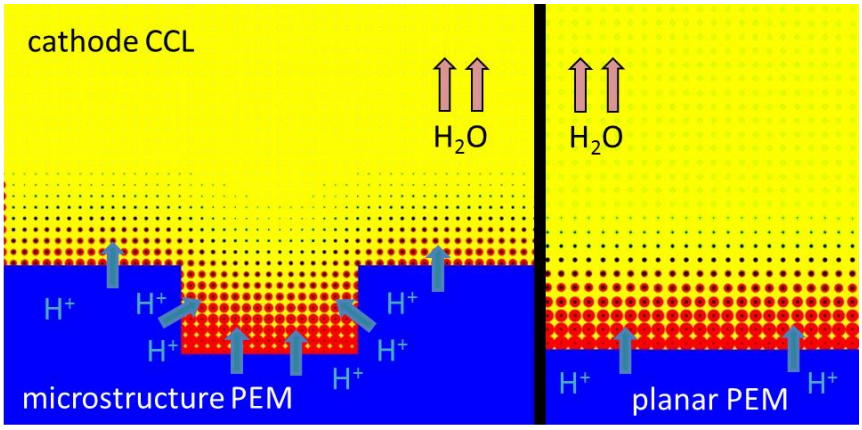


**Figure 5.11. Schematic representation of the gradient of the concentration of water in a microstructured membranes, simulated by Solidworks® (version 2016, Dassault Systems, France) as a migrating solution front against a structured or planar interface.**

It is suggested that the interface between the microstructured PEM and the CCL can result in differences in the water distribution and, therefore, may reduce the flooding of the CCL. This result is similar to those simulations presented in the study by Aizawa *et al.*[146] Under HOT conditions, most of the microstructured PEMs (1.3, 2.7, and 5.3-µm deep features) exhibited an increase in PEMFC performance of ~30 mV over planar PEMs across all current ranges (**Figure 5.10b**). It is hypothesized that under HOT conditions, the PEMFCs have a limited proton conduction due to the formation of overly dry membranes.[20,155] The microstructured PEM and CCL interfaces may improve proton conduction by creating an increased surface area of contact, as well as reducing the thickness of the membrane in certain areas.[146–148,161] The PEMs with 8.2-µm deep features exhibited only a slightly lower performance than the planar membranes. It is possible that the increase in $H_2$ cross-over and the shorting current outweighed the benefits of the increased interfacial surface area between the PEM and the CCL. Under NOC conditions, all MEAs performed similarly, with a <5 mA difference between all of the MEAs over the range of tested current densities (**Figure 5.10c**). It is likely that under this operating condition, the benefits and detriments cancel out each other, resulting in similar PEMFC performances for all of the MEAs. Each of the MEAs were also analyzed by SEM cross-

section analyses to determine if the cylindrical features were retained following the fuel cell testing (**Figure 5.12**).

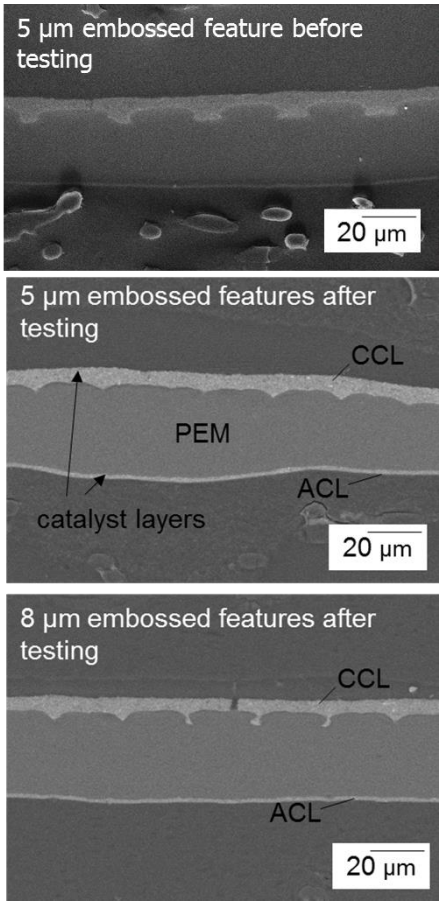


**Figure 5.12. Scanning electron microscopy cross-sectional images obtained at end of life for the MEAs with different embossed features in Nafion® 211 membranes.**

It was determined that, on average, the samples retained about ~50 % of their original feature heights. All of the previous studies did not show any after fuel cell testing cross-sections of the MEAs. Therefore, retention of the microstructures prepared by hot-embossed versus casted membrane requires further investigation. The total duration of the fuel cell tests for each of the MEAs was about 48 h. Longer-term retention of these microstructures will require further analyses. A similar study utilized elastomeric materials for casting microstructured PEMs.[148] The microstructured PEMs were subsequently laminated onto planar PEMs for testing. These prior studies have created membranes with microstructures of low aspect ratios (~ 0.5 and lower) with improved PEMFC performance at normal operating conditions. However, no analyses of the stability of these features

were reported in literatures. Casted PEMs may also exhibit lower $J_{H2}$ and $R_{short}$ than hot-embossed membranes. These previous studies demonstrated improved performance for the microstructured PEMs at NOC or with lower humidity levels. A future area of investigation could include the use of flexible templates for the ease of casting and releasing membranes with complex features. Additional features, such as hierarchically arranged microstructures, could be further investigated for enhancing the performance of PEMFCs.

## 5.6 Conclusions

In this study, hexagonally arranged cylindrical features were hot-embossed against Nafion® membranes to achieve features with different depths. These microstructured PEMs were incorporated into MEAs and analyzed in PEMFCs with active catalyst areas of 40 $cm^2$. The membrane resistances such as $R_{ohm}$ and $R_{ion}$ were demonstrated to decrease with respect to increase in the depth of the hot-embossed features. The parameters associated with membrane damage, such as $j_{H2}$ and $R_{short,}$ also increased with respect to the depth of the hot-embossed features. These MEAs containing microstructured PEMs exhibited improved performance at WUP and HOT fuel cell conditions. Under NOC, all MEAs exhibited similar PEMFC performance. It is possible that the performance of these microstructured PEMs could be further improved by a solution casting technique and a more complex hierarchical morphology. The process of preparing such membranes will require further investigation.

# Chapter 6.

# Template Assisted Preparation of High Surface Area Macroporous Supports with Uniform and Tunable Nanocrystal Loadings

## 6.1 Acknowledgement

Financial support for this work was provided in part by the Natural Sciences and Engineering Research Council (NSERC) of Canada Discovery Program (Grant No. 1077758), CMC Microsystems (MNT Grant No. 2152), Canada Research Chairs Program (B.D. Gates; Grant No. 950-215846), and the Engineered Nickel Catalysts for Electrochemical Clean Energy project administered from Queen's University and supported in part by Grant No. RGPNM 477963-2015 from the NSERC of Canada Discovery Frontiers Program. This work made use of 4D LABS (www.4dlabs.ca) and the Centre for Soft Materials shared facilities supported by the Canada Foundation for Innovation (CFI), British Columbia Knowledge Development Fund (BCKDF), Western Economic Diversification Canada, and Simon Fraser University.

## 6.2 Abstract

The incorporation of catalytic nanocrystals into macroporous support materials has been very attractive due to their increased catalyst mass activity. This increase in catalytic efficiency is attributed in part to the increased surface area to volume ratio of the catalysts and the use of complementary support materials that can enhance their catalytic activity and stability. A uniform and tunable coating of nanocrystals on porous matrices can be difficult to achieve with some techniques such as electrodeposition. More sophisticated techniques for preparing uniform nanocrystal coatings include atomic layer deposition, but it can be difficult to reproduce these processes at commercial scales required for preparing catalyst materials. In this study, catalytic nanocrystals supported on three dimensional (3D) porous structures were prepared. The demonstrated technique utilized scalable approaches for achieving a uniform surface coverage of catalysts through the use of

polymeric sacrificial templates. This template assisted technique was demonstrated with a good control over the surface coverage of catalysts, support material composition, and porosities of the support material.

A series of regular porous support were each prepared with a uniform coating of nanocrystals, such as $NaYF_4$ nanocrystals supported by a porous 3D lattice of $Ti_{1-x}Si_xO_2$, Pt nanocrystals on a 3D porous support of $TiO_2$, Pd nanocrystals on Ni nanobowls, and Pt nanocrystals on 3D assemblies of $Au/TiO_2$ nanobowls. The template assisted preparation of high surface area macroporous supports can be utilized for optimizing the use of catalytic materials in chemical, electrochemical, and photochemical reactions through increasing their catalytic efficiency and stability.

**Graphical Abstract**

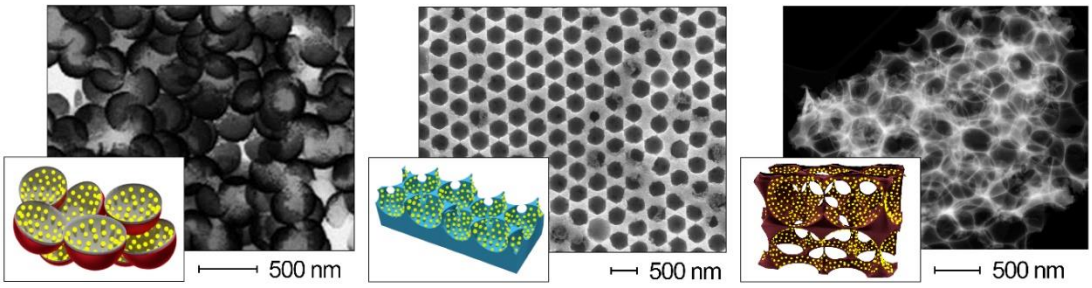


## 6.3 Introduction

This study describes a series of methods for creating uniform and tunable coatings of nanocrystals supported on the surfaces of custom built macroporous materials with two dimensional (2D) or 3D structures. These techniques can be used to prepare supports with a desired porosity, catalytic activity, and chemical stability. Catalytic nanocrystals are widely utilized in chemical reactions due to the significant increase in surface area to volume ratio of these systems relative to larger particles or agglomerates.[162–164] This increased surface area to volume ratio can improve the catalyst mass activity, increase catalyst utilization, and reduce the cost of the systems that incorporate these nanocrystals.[165–167]

Systems designed for the generation of renewable energy, which include PEMFCs and direct methanol fuel cells (DMFCs), utilize nanocrystals such as Pt and Pd.[165–168] To optimize the delivery of reagents to and removal of products from these or similar catalytic systems, materials can be prepared with a tunable porosity using pore forming agents or templates. The preparation of inverse opaline (IO) structures provides access to ordered, close-packed, and interconnected pores, which have been pursued for both fundamental studies in fluid dynamics and an enhanced performance as porous electrodes.[169,170] For example, cathode electrodes in PEMFCs composed of Pt IOs can improve the oxygen reduction reaction (ORR) activities.[49,59] This improvement in catalyst efficiency was attributed to the macroporous IO structure for its influence on the mass transport of reactants and products to and from the surfaces of this catalyst.[49,171–174]

The current study seeks to extend these studies by demonstrating a series of these nanocrystals coated onto the surfaces of various support materials each with a targeted morphology. The morphologies pursued here include IOs, dimpled surfaces, and randomly packed nanobowls. These studies demonstrate methods to create a variety of macroporous supports that incorporate uniform and tunable coatings of nanocrystals, which enables the targeted material to be adjusted to the needs of the intended catalytic reaction.

Many studies have indicated the composition of support materials can improve the electrochemical activity and thermal stability of the supported nanocrystals. These synergistic effects with multiple materials compositions is referred to as a strong metal-support interaction.[57,175] Currently, the loading of nanocrystals onto the surfaces of a structured support is often performed by nanoparticle powder processing, nanoparticle suspension/solution casting, electrodeless and electrochemical deposition techniques, and atomic layer deposition (ALD) methods.[172,173,176–178]

Powder processing and solution casting of nanocrystals are often used to achieve uniform, planar coatings of materials. These techniques may, however, result in the formation of nanocrystal agglomerates due to the of processing conditions.[176,179] This agglomeration can reduce the overall mass efficiency of the nanocrystals by reducing their surface area to volume ratio.[173,176]

Macroporous materials can be created to replace powder based catalyst supports to reduce the possible aggregation of the nanoparticles. It is, however, difficult to coat the inner surfaces of a 3D macroporous support with nanocrystals by powder processing and solution casting techniques.[61,180,181] For improving the uniformity of nanocrystal coatings in macropores, electrochemical deposition can be used to prepare nanocrystals that exhibit limited agglomeration and increased catalyst mass activity.[182–184] This technique is limited to precious metal based support materials because the solutions used for the electroless and electrodepositon of precious metal catalysts are typically corrosive to less noble metals through processes of galvanic replacement.[178,180]

Solutions of Pd and Pt salts for these processes are often prepared at a low pH to improve their stability.[180] The low pH of these electroless and electrodeposition processes can easily damage the nano- and microscale features of a macroporous support prepared from less noble metals. Furthermore, electrodeposition can result in a relatively non-uniform deposition of material within a 3D macroporous support due to diffusion based limitations imposed by concentration gradients, proximity of neighboring deposition sites, and shape of the electric field lines.[184]

For improving the uniformity of nanoscale catalysts within 3D macroporous supports, techniques such as ALD can be used for effectively infiltrating metal precursors into the pores.[172,177] This deposition technique is, however, very time consuming. A deposition rate of 1 to 2 nm of material per hour is commonly observed, but it can be as slow as <1 nm/h.[172] These relatively long processing times, the relatively small sample sizes, and the necessity to place the support materials under vacuum during this process, make ALD a relatively expensive technique in comparison to the aforementioned methods.

As mentioned previously, the characteristics of nanocrystals can be enhanced or complemented by the presence of the support material or the interface between the catalyst particles and the supports. For example, niobium oxide or silicon dioxide supported Pt nanocrystals can exhibit improved electrochemical or thermal stabilities, respectively.[185,186] In a second example, the (117) facet of an α-$(NiCu)_2Pd$ alloy can achieve three times the catalytic activity of the Pd (111) facet.[187] Catalytically active alloys, such as these can be formed at the interface between a nanocrystal and its support.[49,57]

To take advantage of these interactions between nanocrystals and their supports requires alternative processing methods. It is also desired that these methods can overcome nanocrystal agglomeration, non-uniform coverage of the supports, and to address other challenges with processing these materials.

A series of relatively simple methods are discussed here that can achieve a uniform surface coverage of nanocrystals within 2D and 3D macroporous supports. These methods are scalable, compatible with a variety of materials, and utilize relatively mild processing conditions.

Nanocrystals of a range of compositions were loaded onto the surfaces of macroporous supports while achieving both a uniform interparticle spacing, a tunable loading of catalyst particles, and controlled interactions between the nanocrystals and their support. Compositions of the support materials were also tuned to demonstrate the preparation of macroporous metals, semiconducting metal oxides, and insulating ceramics. Our preparation technique combined the assembly of these nanocrystals onto spherical sacrificial templates, the self-assembly of nanocrystal covered templates, the formation of a support matrix within the interstitial spaces among the assembled templates, and the selective removal of the sacrificial templates to create the macroporous products. The self-assembly of nanoparticles onto spherical templates was previously demonstrated, but with limited success in controlling the uniformity of the loading, and extending the process to a diverse range of materials.[78,188]

These procedures have been fine tuned to prepare uniform loadings of nanocrystals on the surfaces of spherical polymer templates while also achieving a tunable surface coverage.[171,174,189] These processes relied on controlling the surface chemistries of both the nanocrystals and the polymer spheres. The refined process was used here to coat nanocrystals of different sizes, shapes, and compositions onto polymer spheres with uniform and tunable surface coverages. These coatings included nanocrystals of $NaYF_4$ (diameter, ø = 26 ± 4 nm), Pt (ø = 3.4 ± 0.5 nm), and Pd (ø = 13 ± 2 nm), which were chosen for their desirable catalytic properties and/or their utility in the generation of renewable energy.[165–167]

To create the macroporous materials, with average pore diameters of 1 μm to 50 nm, in this study, NP coated polymeric templates were self-assembled into ordered arrays with similar procedures that have been previously pursued for creating photonic band gap materials.[169,190,191] Spherical templates coated with either the $NaYF_4$, Pt, or Pd nanocrystals were used here to create macroporous supports whose inner surfaces were uniformly covered with nanocrystals. The nanocrystal coated spherical templates were first organized into close-packed arrays by self-assembly at an air-water interface. These close-packed layers of the templates were lifted from the air-water interface in a finely controlled, layer-by-layer fashion, to produce 2D or 3D crystalline assemblies.[49]

The formation of ordered support matrices was achieved by infiltrating the interstitial spaces among these assembled templates with the desired precursors. For example, metal alkoxide solutions or solutions of metal salts were used for the formation of metal oxides by sol-gel techniques or the preparation of metals by electrodeposition, respectively.[49,59,178,192] The support materials deposited or grown around the nanocrystal coated templates can partially encapsulate the nanocrystals and immobilize them within the support matrix. After the nanocrystals were partially immobilized in the support, the polymer templates were selectively removed by thermal degradation or solvent dissolution to create the macroporous supports coated with uniform layers of nanocrystals. Macroporous supports with randomly arranged interconnecting pores were also prepared using the same spherical templates. Nanobowls were created by physical vapor deposition (PVD) of thin film(s) onto assemblies of the polymer templates followed by the selective removal of these templates and subsequent assembly of the isolated bowls into randomly packed structures.

A range of supporting metals and metal oxides were created in this study, each prepared by a different technique as a demonstration of the versatility of this approach to produce nanocrystal coated macroporous supports. The techniques to deposit or grow the support material included PVD, electrodeposition, and sol-gel processes for preparing metal and metal oxide films, metallic matrices, and metal oxide matrices, respectively. The diameters of the templated features were precisely controlled through the choice of templates (e.g., diameter of the spherical polymer templates). The diameter of the pores, surface coverage of nanocrystals, and other structural features within the supports were

confirmed by SEM, TEM, and EDS techniques. These studies demonstrated a series of approaches to preparing and tuning structural supports coated with nanocrystals. The resulting materials can have tuned chemical, electrochemical, and photochemical properties, including an increased catalytic efficiency and improved chemical, electrochemical, and thermal stabilities. A precise control over the thickness and porosity of the support, the composition of the support and its nanocrystals, and surface coverage of these nanocrystals will enable researchers to tune and optimize the formation of macroporous catalytic materials for an array of applications.

## 6.4 Materials and Methods

### 6.4.1 Experimental Overview

The general procedure for preparing macroporous supports with uniform coatings of nanocrystals involved the following four steps: (1) preparation of nanocrystal loaded onto spherical polymer templates; (2) self-assembly of these spherical templates; (3) deposition or growth of support materials within these assembled templates; and (4) selective removal of the sacrificial polymer templates. Schematic depictions of the three types of porous structures that were prepared in this study are shown in **Figure 6.1**. Detailed procedures for their preparation are outlined below.

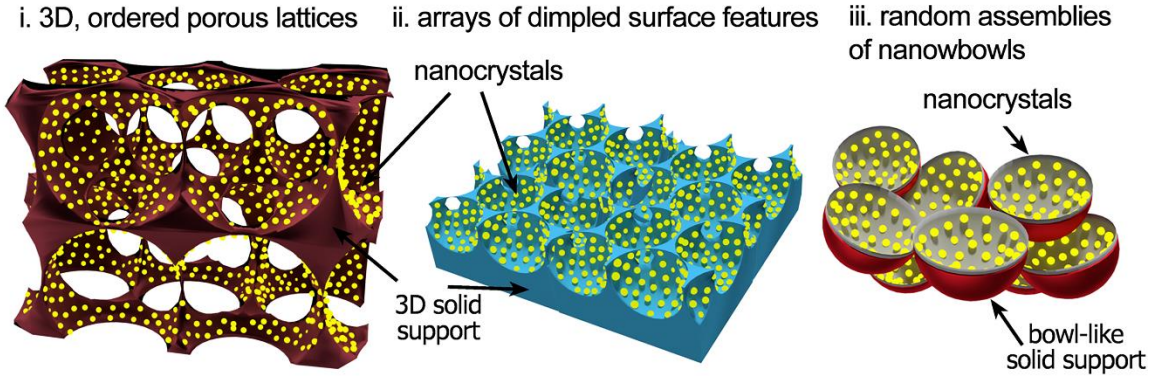


**Figure 6.1. Schematic depictions of three approaches to preparing nanocrystal coated supports: (i) an ordered 3D porous lattice; (ii) a 2D array of dimpled features with a tunable surface roughness; and (iii) a lattice assembled from nanobowls.**

### 6.4.2 Preparation of Nanocrystal Coated Spherical Polymer Templates

The preparation of nanocrystals supported in a 2D or 3D porous matrix began with the coating of nanocrystals onto spherical colloidal templates. Polyvinylpyrrolidone ($M_w$ ~55,000; Sigma-Aldrich, USA) surfactant stabilized Pt and Pd nanocrystals were each synthesized by a hydrothermal process.[193,194] The $NaYF_4$ photon upconverting nanoparticles were prepared via a thermal decomposition method.[195] The procedures for coating these nanocrystals onto polymer spheres were adopted from previously published methods.[171,174,189] A variety of nanocrystals with a range of compositions and diameters can be coated onto spherical polystyrene (PS) templates (Polybead® Amino Microspheres, Polysciences, Inc., UK). The coating process involved tuning the interactions between the spherical templates and the nanocrystals. Attractive interactions between the nanocrystals and templates included a combination of van der Waals interactions, and electrostatic interactions.[78] By preparing nanocrystals with complementary surface charges or surface energies, nanocrystals of different compositions and sizes can be uniformly coated onto the spherical templates. A precise control over the nanocrystal coatings on the templates can be used to tailor their composition as needed for various catalytic applications. For example, Pt nanocrystals can be incorporated with their dimensions optimized for the ORR in PEMFCs, and Pd nanocrystals can be incorporated that are optimized for catalyzing methanol oxidation in DMFCs.[165–167] In the subsequent step, spherical polymer templates with uniform coating of these nanocrystals were self-assembled into 2D or 3D ordered lattices.

### 6.4.3 Self-Assembly of Nanocrystal Coated Spherical Templates

The assembly of nanocrystal coated spherical templates into an ordered structure is desirable for producing matrices with interconnecting pores of regular dimensions, and for the preparation of structurally sound porous supports. The morphology, pore dimensions, and thickness of the final form of these porous materials can be adjusted as required by the desired application, such as for their influences on the mass transport of reactants and products in catalytic processes. The nanocrystal coated polymer spheres can be assembled into ordered lattices by a variety of techniques as demonstrated in previous literature.[95,171,189,196–200] These self-assembled templates can range from

monolayers of hexagonally close-packed spheres to ordered multilayer assemblies. In this study, hexagonally close-packed monolayers were obtained by assembling the nanocrystal coated templates at an air-water interface, followed by selectively transferring these assemblies to a planar substrate.[49] This precise procedure can be repeated as necessary to prepare multiple layers of the close-packed templates in a finely controlled manner. For a faster process of self-assembly when preparing multi-layered crystalline templates, convective evaporation was also used for preparing relatively thick layers of self-assembled nanocrystal coated templates.[201] The interstitial spaces within the assembled arrays of spherical templates, with their homogeneous coatings of nanocrystals, were subsequently infiltrated with support materials by vapor or solution-phase techniques. The creation of a solid support matrix surrounding the templates resulted in the immobilization of the nanocrystals and the formation of a bicontinuous network of support materials and sacrificial templates.

### 6.4.4 Support Material Preparation and Template Removal

Support materials were deposited onto, or grown within the interstitial spaces of the templates. These materials covered the surfaces of the templates, immobilized the nanocrystals, and created stable structures that supported the nanocrystals within a macroporous framework after the removal of the polymeric templates.[49,196,202] Removal of the polymer templates generated either 3D porous structures or textured surfaces with nanoscale relief features. In this study, three strategies were used to prepare structured porous support materials with final compositions ranging from metals, to semiconducting metal oxides, to insulating ceramics. Details of the specific techniques used to prepare these materials, along with the corresponding methods for template removal are provided in the following sections.

### 6.4.5 Sol-Gel Formation of Porous Supports — 3D $Ti_{1-x}Si_xO_2$ Supported $NaYF_4$ Nanocrystals

A multilayered 3D porous matrix of $Ti_{1-x}Si_xO_2$ supporting a uniform coating of $NaYF_4$ nanocrystals were prepared by sol-gel processing. Ordered assemblies of spherical PS templates coated with $NaYF_4$ nanocrystals were prepared on polished Si

(International Wafer Service Inc.; $N_p$ <100>) wafers using convective evaporation techniques.[169,196] The nominal diameters, as determined by TEM, of the $NaYF_4$ nanocrystals and that of the PS templates were ~26 nm and ~320 nm, respectively. The sol-gel process began with spin casting multiple aliquots of a dilute sol-gel solution over the ordered assemblies of the nanocrystal coated polymer spheres. The spin casting method allowed a thin layer of sol-gel solution to be deposited within the interstitial spaces of the assembled templates. Multiple coatings of the dilute solution were used to improve the uniformity of the coatings. The sol-gel coated sacrificial templates were thermally treated to sinter the metal oxide precursors and create a continuous structural support, as well as to decompose the polymer templates and isolate the desired porous structure. The sol-gel recipe was modified from a previously reported method to prepare films of $TiO_2$.[203]

In this study, a $TiO_2/SiO_2$ sol-gel solution was prepared with 1.6 mL of trifluoroacetic acid (TFA; reagent grade, Caledon Laboratory Chemicals, Canada), 2 mL of titanium (IV) ethoxide (99.5 %, Sigma-Aldrich, United States), and 0.4 mL of HCl (36.5-38 %, high purity, ACP Chemicals, Canada). This mixture was shaken for 20 min, followed by the addition of 1 mL of tetraethylorthosilicate (TEOS, 98 %, Sigma-Aldrich, United States). This final mixture was diluted 150-fold by volume with anhydrous ethanol (Commercial Alcohols, Canada). The dilute sol-gel solution was spin cast at 800 rpm for 1.5 min per step (Brewer Science, United States) onto the ordered assemblies of $NaYF_4$ nanocrystal coated polymer spheres. A 10 µL aliquot of the sol-gel solution was drop cast with each step, and a total of 20 aliquots were cast onto the substrates to ensure an even and optimal coverage of the sol-gel solution within the interstitial spaces of the assembled templates. The sol-gel coated templates were subsequently heated while exposed to air in a furnace (Model 48000 Furnace, Barnstead Thermolyne, United States) at 450 °C to sinter the mixture of silica and titania, as well as to thermally decompose the templates and isolate the macroporous supports. The heating ramp rate was 112.5 °C/h, with a 48 h dwell at 450 °C, and a slow cool down to room temperature over at least 6 h. At this temperature, most of the $TiO_2$ would be formed in the anatase phase.[205-209, 214, 215] The anatase phase of $TiO_2$ is more conductive when compared to the rutile phase of $TiO_2$. This phase of TiO2 is, therefore, more suitable for use in photocatalysis and electrochemical applications. These samples were directly characterized by a series of techniques

including focused ion beam (FIB) milling and selective lift-out of thin sections of the sample for further analysis by TEM techniques.

### 6.4.6 Sol-Gel Formation of Porous Supports — 3D Porous Network of $TiO_2$ Supported Pt Nanocrystals

Ordered porous $TiO_2$ supports coated with Pt nanocrystals were prepared in a similar manner as the ordered porous $TiO_2/SiO_2$ supports for the $NaYF_4$ nanocrystals (**Section 6.4.5**). A series of spherical PS templates were coated with an increasing surface coverage of Pt nanocrystals. The surface coverage of Pt nanocrystals was controlled by dilution of the Pt nanocrystals relative to the concentration of PS templates in solution during the preparation of the nanocrystal coatings. Three different mixtures were prepared: (i) a relatively low surface coverage from a 90 v/v % diluted solution; (ii) a medium surface coverage from a 60 v/v % diluted solution; and (iii) a relatively high surface coverage from an undiluted, as-synthesized nanocrystals solution. This study sought to determine if the coverage of nanocrystals in the resulting macroporous matrices corresponded to the initial nanocrystal loadings on the PS templates. All other preparations were identical to the procedures for creating the ordered porous $TiO_2/SiO_2$ supports of $NaYF_4$ nanocrystals, except that the $TiO_2$ sol-gel solution was prepared without the addition of TEOS. Once the porous materials were obtained after the high temperature treatment, the samples were physically fractured, and removed from the surfaces of the polished Si wafer through the use of a razor blade. The fragments from the sample were collected in a centrifuge tube containing 100 µL of DI water (18 MΩ·cm), and 10 µL of this suspension was drop cast onto a Formvar/carbon coated TEM grid and dried overnight under ambient conditions (01753-F, Formvar/carbon support film, Ted Pella Inc., United States).

### 6.4.7 Electrodeposition of Dimpled Supports —Hexagonally Close-packed Arrays of Dimpled Ni Supporting Pd Nanocrystals

Hexagonally close-packed arrays of dimpled features in Ni with the surfaces of these recessed features coated with Pd nanocrystals were prepared by self-assembly and electrodeposition methods. To prepare these ordered arrays of Pd nanocrystals supported on dimpled Ni, a single close-packed layer of PS templates coated with the Pd

nanocrystals were prepared by assembly at an air-water interface followed by transfer to a piece of Ni coated Si wafer (International Wafer Service Inc.; $N_p$ <100>). The 150-nm thick Ni (99.98 % Ni pellets, purchased from Kurt J. Lesker, United States) was deposited by thermal evaporation onto 10 nm of Cr (99.95 % Crpellets, Kurt J. Lesker, United States) that served as an adhesion layer between the Si wafer and the Ni coating. These materials were deposited using a custom built thermal evaporator in 4D LABS at SFU. The template coated Ni substrate was air dried and used as the working electrode in a two-electrode, electrochemical deposition setup (Bio-Logic Science instruments SP150, United States). A platinum wire (0.6-mm diameter, 99.98 % Pt, Alfa Aesar, United States) was used as the counter electrode. The electrodes were immersed in a Watts plating bath solution (Transene Company, United States) and Ni was electrochemically deposited within the voids of the polymer templates at a current density of ~0.3 A/cm$^2$ for 1 min. The extent of Ni deposition and the final structure of the arrays were verified by SEM prior to template removal. After Ni electrodeposition, the PS template was selectively removed by Soxhlet extraction with a 50:50 (v/v) mixture of toluene and acetone for at least 12 h. The arrays of dimpled Ni coated with Pd nanocrystals were evaluated using electrochemical techniques, as well as electron microscopy analyses.

### 6.4.8 Physical Vapor Deposition of Nanobowl Supports — Random Assemblies of Au/$TiO_2$ Nanobowls Covered with Pt Nanocrystals

Random assemblies of nanobowls were created using PVD of metal or metal oxide thin films on top of assemblies of Pt nanocrystal coated polymer spheres. Close-packed monolayers of Pt coated PS templates were assembled on polished Si substrates. These self-assembled structures were dried overnight in a vacuum desiccator to remove residual moisture. The template coated substrates were loaded into a Kurt J. Lesker PVD 75 system, and 20 nm of $TiO_2$ (99.9 % purity, 3" diameter x 0.125" thick sputter target, purchased from Kurt J. Lesker) was deposited on top of the assembly using radio frequency (RF) sputtering. This $TiO_2$ coated sample was transferred to another PVD 75 system for the deposition of 20 nm of Au (99.9990 % purity, 1/8" evaporation pellets, purchased from Materion) by electron beam (e-beam) evaporation. The PS templates coated with this multilayer film were removed from the substrate by ultrasonication while

immersed in a 20 mL glass scintillation vial containing 10 mL of a 50:50 (v/v) toluene to acetone solvent mixture. The suspension was transferred into a 100 mL round bottom flask and more of this solvent mixture was added to bring the total solution volume to 20 mL. This suspension of polymer spheres with the $TiO_2$, Au, and Pt nanocrystal coatings were heated at reflux for 5 h. This solution was decanted, and fresh solvent added every 60 min during this selective removal of PS templates. The suspension of nanobowls was purified twice with ethanol (centrifugation at 10,000 rpm for 10 min, decanting the supernatant, adding fresh solvent, sonicating for 5 min, and repeating this process) and twice again with water. A portion of these suspensions were drop cast onto a Formvar/carbon coated TEM grid for analysis by TEM. Another portion of the sample was prepared by mixing the purified sample with 100 µL of Nafion® DE2020 solution (20 wt/wt %, Dupont, United States) and drop cast onto a substrate for focused ion beam milling to prepare cross-sections that were analyzed by SEM.

### 6.4.9 Details of the Electron Microscopy Characterization

Electron microscopy techniques, such as SEM and TEM, were used at each stage of the sample preparation for: (i) verifying the loading of nanocrystals on the PS templates; (ii) verifying the assemblies prepared from the nanocrystal coated polymer spheres; (iii) verifying the deposition or growth of the support materials; and (iv) identifying the structural morphology and elemental composition of the final material after removal of the polymer templates. The SEM analyses were performed using an FEI Helios NanoLab 650 SEM/FIB dual beam system operating at 5 kV for imaging samples with the presence of polymeric materials and at 10 kV for samples without polymers. Cross-sections of some samples were prepared using a focused Ga ion beam (Tomahawk™ ion column). Layers of platinum with a thickness of ~ 500 nm to 1 µm were deposited onto the samples as a protective coating prior to ion milling to preserve the surface morphology of the samples. Sections of some samples were lifted out for further analysis by TEM. Sections measuring about 4 µm in length by 1 µm in depth and with a width of ~100 nm were milled, lifted from the samples, and transferred onto PELCO® FIB Lift-Out TEM grids (Ted Pella Inc., United States) for analysis by TEM, STEM, and EDS. All of the TEM related analyses were performed using an FEI Osiris X-FEG S/TEM operating at 200 kV. The EDS analyses were performed with a Super-X EDS detection system as a part of the TEM analysis.

### 6.4.10 Electrochemical Oxidation of Methanol Catalyzed with Ni Supported Pd Nanocrystals

Electrochemical experiments were performed to investigate the utility of the ordered arrays of dimpled Ni that supported Pd nanoparticles as a high surface area electrode. The measurements were performed with a Biologic Science Instruments SP-150 potentiostat. Electrochemical data was collected using the EC-Lab data analysis software (V10.18). The customized electrodes were each incorporated as the working electrode into a typical three electrode set-up using a custom glass electrochemistry cell with a single junction, 10-mm diameter, Ag/AgCl reference electrode, and a Pt wire (0.6-mm diameter; 99.98 %; Alfa Aesar) counter electrode. The electrochemical solution, consisting of 10 mM of methanol (99.9 %, Fisher Chemical, United States) and 0.5 mM of KOH (85 %, Macron Fine Chemicals, United States), were purged with $N_2$ gas (99.98 %, Praxair, Canada) for at least 30 min prior to the commencement of the experiments. A positive $N_2$ gas pressure was maintained in the head space of the electrochemical cell throughout the experiments. CV measurements of methanol oxidation were performed at a scan rate of 20 mV/s, with a sweep range from −0.8 to 0.3 V, at 21 ± 0.2 °C, and without perturbation of the solution. The potential applied to the sample was repeatedly scanned until reaching stabilization of the peak current for methanol oxidation (<10 μA deviation in current). The stabilized CV scan profiles were normalized against Pd $\boldsymbol{A}_{ecsa}$. This normalization enabled a comparison of the Pd mass activity for the Pd NPs supported on dimpled Ni to the planar (100 nm of Pd on 10 nm of Cr) Pd electrodes created by electron beam deposition (93 %, Pd pellets, Kurt J. Lesker, PVD75, United States). The Pd ECSAs were estimated from the integrated area for the Pd oxide reduction peak in the CV profiles, assuming the charge associated with the reduction of the oxygen monolayer is 420 $\mu C/cm^2$.[204]

## 6.5 Results and Discussion

In this study, a series unique macroporous structures were prepared using different combinations of support materials and nanocrystals. These materials were created using techniques that included: (i) preparation of nanocrystal coated spherical polymer templates; (ii) self-assembly of these spherical templates; (iii) deposition or growth of

support materials onto, or within these assembled templates; and (iv) selective removal of the sacrificial polymer templates. The resulting materials included ordered 3D macroporous supports with $NaYF_4$ particles for optoelectric applications, regular 3D macroporous supports with Pt particles for chemical and photochemical catalysis, arrays of dimpled supports with Pd particles for applications in DMFCs, and random assemblies of nanobowl supports with Pt particles for flow-through catalytic applications. These methods enable a range of tunable parameters, such as adjusting the composition and surface coverage of nanocrystals, as well as altering the composition, pore diameter, structural morphology, and overall thickness of the macroporous supports. These materials can be adjusted as needed to optimize their performance for specific purposes. For example, the loading densities of nanocrystals and porosity of the support can be simultaneously tuned for their influence on mass transport of reagents and products, and the overall catalytic efficiency.[59,184,204] Each set of materials were analyzed by a series of electron microscopy techniques to verify their porosity, surface coverage of nanocrystals, and material compositions.

### 6.5.1 Ordered Macroporous Supports for Photocatalytic Applications

Ordered macroporous $Ti_{1-x}Si_xO_2$ supports coated with $NaYF_4$ nanocrystals were prepared for photocatalytic applications. The presence of $NaYF_4$ nanocrystals can enhance the photocatalytic activities of the mixed $TiO_2$ and $SiO_2$ porous support material.[205–208] The sol-gel technique for preparing the porous oxide supports is described in the experimental section. A thin section of this sample was lifted out with assistance by FIB milling and analyzed by TEM. The structure of the macroporous $Ti_{1-x}Si_xO_2$ supports for the $NaYF_4$ nanocrystals is shown in **Figure 6.2** with corresponding EDS spectrum presented in **Figure 6.3**. This section of the multi-layered porous metal oxide portrays the ordered structure containing pores with uniform diameters of 320 ± 30 nm. The structures contained interconnected pores within a 3D framework. The HAADF-STEM analyses of the sample indicated the presence of nanoparticles composed of higher atomic number elements that were supported by the oxide matrix. The position of these nanoparticles was further confirmed by EDS mapping, which resolved the atomic composition of elements within these macroporous supports. The overlaid EDS map with the HAADF-STEM image

indicated the presence of Y at discrete locations, indicating the successful transfer of the $NaYF_4$ nanocrystals from the polymer templates onto the sintered oxide support.

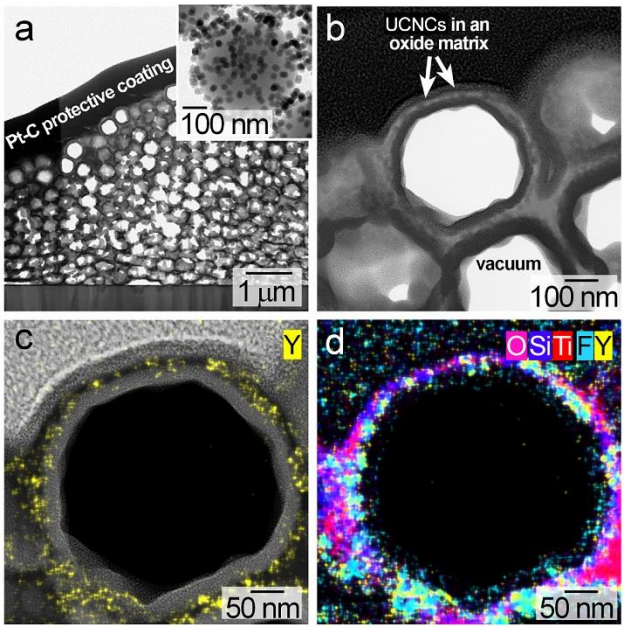


**Figure 6.2.** **Transmission electron microscopy (TEM) analyses of $NaYF_4$ upconverting nanocrystals (UCNCs) with a diameter (ø) of 26 ± 4 nm that were transferred from spherical polystyrene templates into a porous metal oxide lattice with a pore ø of 320 ± 30 nm. (a) The STEM image of a section of this porous structure prepared by focused ion beam (FIB) assisted lift-out; (a, inset) UCNCs loaded onto the colloidal polystyrene templates. (b) High magnification STEM image from a section of the sample in (a) depicting the $NaYF_4$ nanocrystals within the metal oxide support. (c) An EDS map of yttrium overlapped on a HAADF-STEM image to depict the locations of the $NaYF_4$ nanocrystals within the support matrix. (d) Overlapping EDS maps of the majority of elements present in the nanostructured support.**

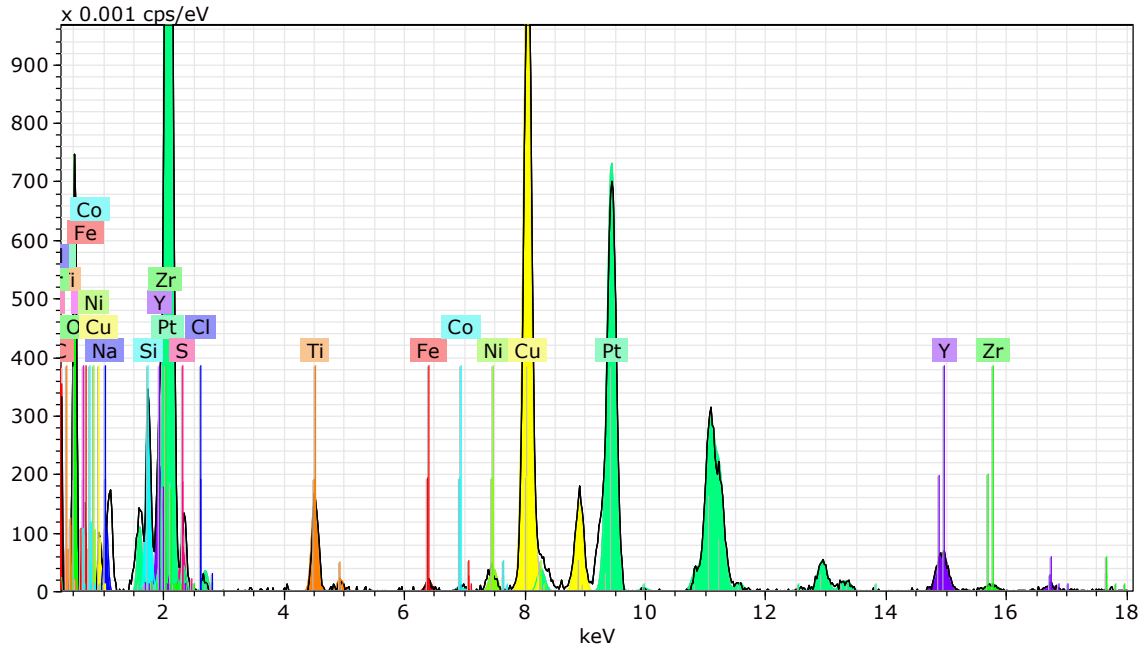


**Figure 6.3. Deconvoluted spectrum obtained by TEM using an EDS analysis of a UCNC coated porous metal oxide.**

Recent studies used $NaYF_4$ nanocrystals supported on $TiO_2$ nanocrystals for improving their photocatalytic performance.[205] It has also been shown that by using $TiO_2$ as a support for these upconverting nanocrystals, their emission intensities can be enhanced by more than five times.[209] These enhancements in upconversion efficiency can be further utilized by dye sensitized solar cells, where improvements in the efficiency of up to 37 % have been demonstrated for converting solar radiation to electrical power by utilizing $TiO_2$ supported upconverting nanocrystals along with photosensitive dyes.[210] Future studies may utilize the tunable macroporous framework, such as that depicted in **Figure 6.2**, for either accommodating photosensitive dyes within its open lattice for further improving its solar conversion efficiencies or as an open porous support for seeking enhanced photocatalytic materials. The ordered arrays of textured surfaces prepared in this study, with features that ranged from ~30 nm to 300 nm, could exhibit plasmonic and anti-reflective properties across the visible light spectrum that can further improve photovoltaic efficiencies of the supported materials.[168,211] Future investigations could utilize the methods outlined in this study for preparing photocatalytic or otherwise photosensitive materials with precisely tuned surface features, porosity, and composition to optimize their optical properties. The techniques demonstrated in this study provide a

platform for preparing high surface area materials with a fine tuned and uniform surface coverage of cataytically and/or optoelectronically active nanocrystals for customization to a variety of photovoltaic or photocatalytic systems.

### 6.5.2 Ordered Macroporous Supports for Pt Based Catalysis

Porous materials with a tuned loading of Pt, as well as a finely adjusted pore size and morphology of the support matrix, could enhance the mass transport efficiencies of catalyzed reactions. A series of materials with an adjusted loading of Pt nanocrystals were prepared on ordered porous $TiO_2$ supports as a demonstration of a technique to directly prepare well-tuned porous catalytic supports. The resulting ordered porous $TiO_2$ supports exhibited a uniform surface coverage of Pt nanocrystals within these 3D matrices (**Figure 6.4**).

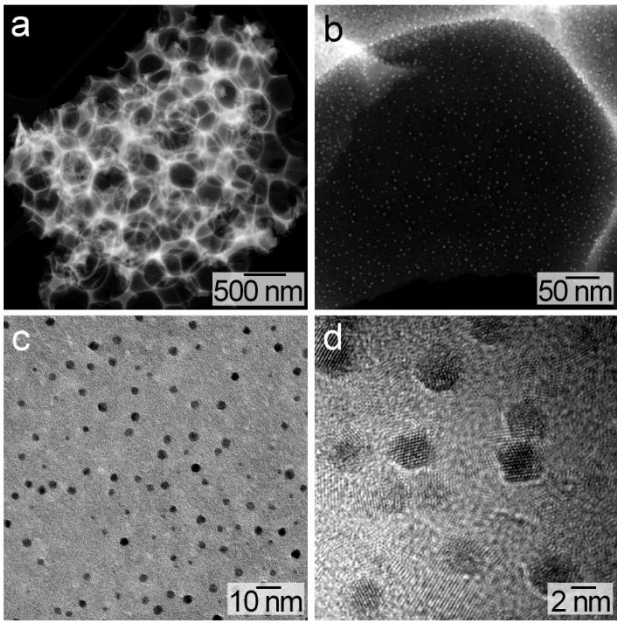


**Figure 6.4. Transmission electron microscopy and STEM images of Pt nanocrystals (ø = 3.4 ± 0.5 nm) supported on a porous frame work of $TiO_2$ (ø = 400 ± 38 nm) after sintering at 450 °C for >48 h : (a) HAADF-STEM image of a section of the nanostructured support; (b) a higher magnification HAADF-STEM image from a region in (a) depicting the Pt nanocrystals supported on the titania; (c) higher magnification bright field TEM image of the same sample; and (d) high resolution TEM (HRTEM) image depicting lattice fringes of the Pt nanocrystals on the $TiO_2$ support. See Figure 6.5 for a detailed analysis of the lattice fringes in the high resolution TEM images.**

The combination of Pt and $TiO_2$ can be used in a number of catalytic applications, such as methanol oxidation reactions, aldehyde and ketone hydrogenation reactions, photocatalytic hydrogen evolution, and the ORR.[212–219] The $TiO_2$ can exhibit an increased photocatalytic activity in the presence of Pt, reduced Pt agglomeration under high temperature conditions, and increased Pt catalytic activity by serving as a surface that promotes the adsorption of organic molecules in proximity to the Pt surfaces. [212–219] The TEM analyses of these materials indicated the formation of ordered multilayers of porous $TiO_2$ containing uniform and interconnected pores with an average diameter of 400 ± 40 nm. These pores were covered with a uniform coating of Pt nanocrystals (4 ± 0.5 nm in diameter), which were evenly spaced with an interparticle separation of 10 ± 3 nm. The high resolution TEM analysis of this material indicated the presence crystalline Pt nanocrystals with a lattice fringe spacing corresponding to the Pt (111) facet (**Figure 6.5**).

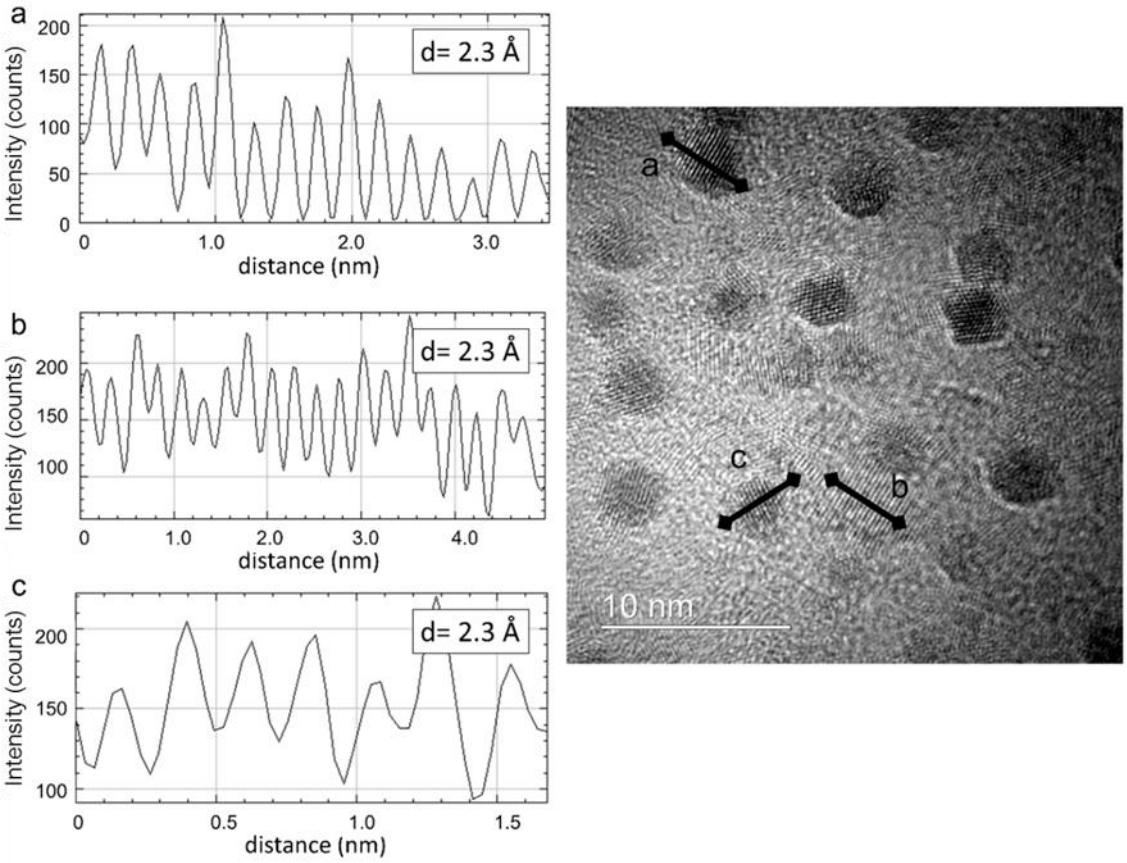


**Figure 6.5. High resolution transmission electron microscopy (HRTEM) images of Pt nanoparticles (NPs) depicting their lattice fringes. The lines a, b, and c correspond to the intensity profiles in the associated plots. These results indicated the lattice fringes had an average spacing of 2.3 Å. This d-spacing corresponds to that expected for the Pt (111) facets.**

The transfer of the Pt nanocrystals from the PS templates to the oxide support was further tuned to demonstrate the versatility of this preparation method. Samples were prepared with three different surface coverages of Pt nanocrystals (**Figure 6.6**). These materials were created by decorating a series of colloidal polymer templates each with a different surface coverage of Pt nanocrystals. Through the TEM analyses, the coverage of Pt nanocrystals on the polymer templates was shown to correlate with the loading of Pt nanocrystals on the $TiO_2$ supports (**Figure 6.7**). This result demonstrated that controlling the initial coverage of Pt nanocrystals on the pore-forming spherical templates can produce support materials with a similar and tunable loading of Pt nanocrystals. Samples prepared with a high, medium, and low surface coverage of Pt nanocrystals were

determined to have average interparticle spacings of 9 ± 2 nm, 11 ± 3 nm, and 17 ± 6 nm, respectively. These Pt loadings are higher than that achieved within a commercially available Pt/C powdered catalyst, which had an average spacing of 27 ± 7 nm between the Pt nanocrystals (**Figure 6.8**).

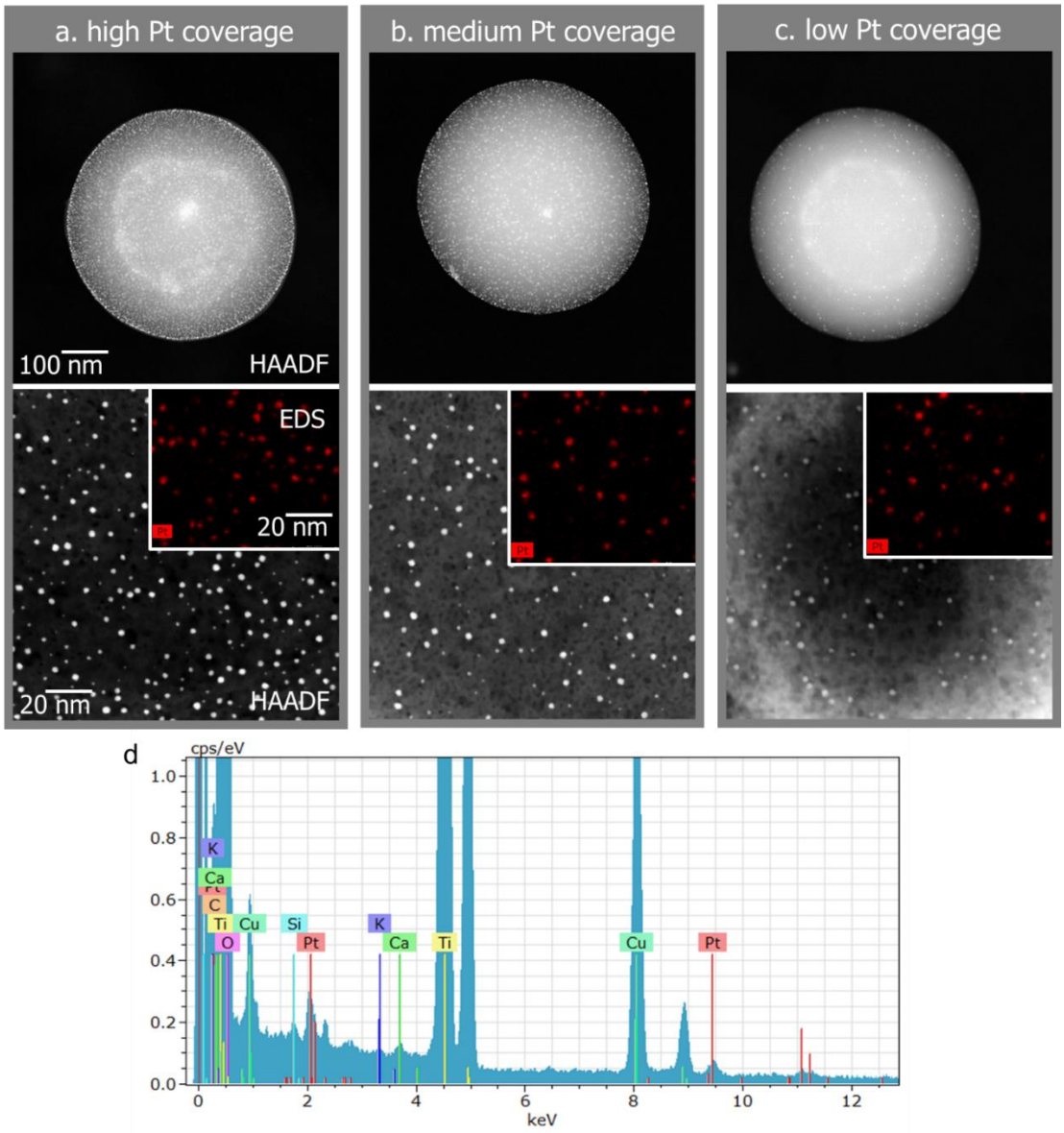


**Figure 6.6.** **Images of polystyrene (PS) spheres with high, medium, and low coverages of Pt NPs and their corresponding transfer onto a porous $TiO_2$ support are shown in column a to c, respectively. The top image of each column is the HAADF TEM image of a representative loading of Pt NPs loaded on the spherical templates. The bottom images consist of HAADF TEM images of Pt NPs immobilized on a $TiO_2$ support, and the inset images are the EDS elemental maps of the Pt NPs on the $TiO_2$ support. A representative EDS spectrum of Pt on $TiO_2$ is shown in (d).**

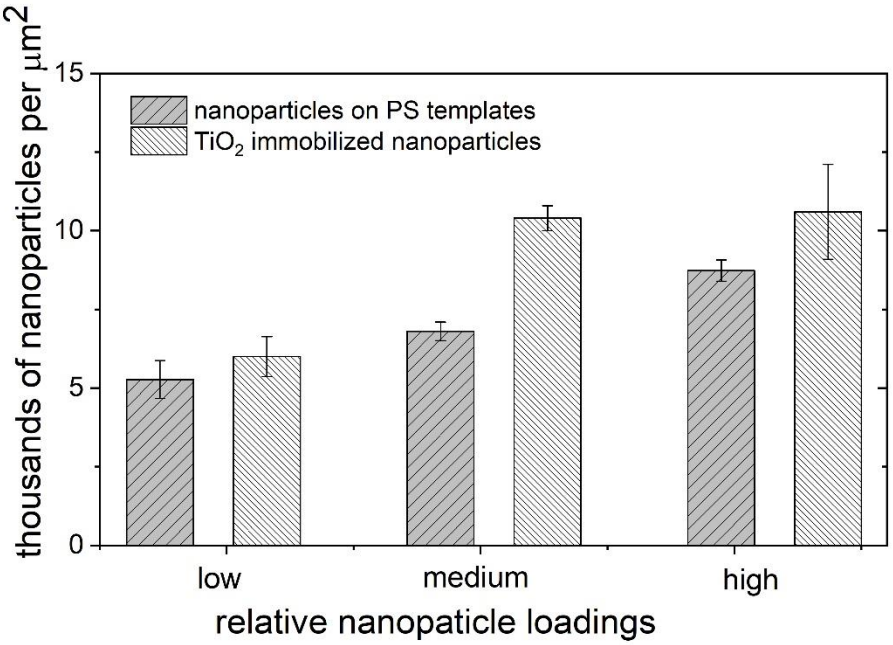


**Figure 6.7.** **Statistical analysis of the number of Pt NPs loaded onto the spherical PS templates, and the number of Pt NPs immobilized on the porous $TiO_2$ supports after further processing of these templates. A total of ~5,000 NPs were manually counted for each of the samples. The error bars represent a standard deviation of +/- 1σ from the calculated means obtained from the average values for each of the samples.**

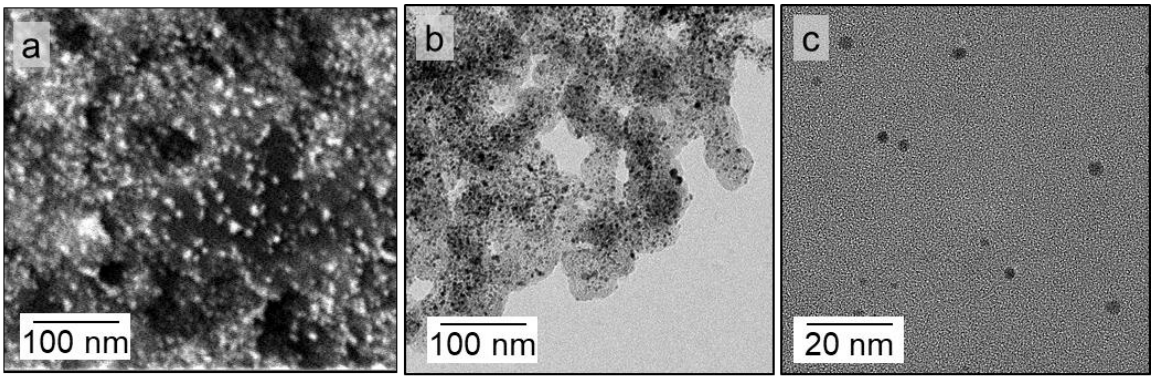


**Figure 6.8.** **Electron microscopy images of a mixture of Pt and carbon nanoparticles (Tanaka Holdings Corp., Ltd.; TEC10E50E); (a) a SEM image using a concentric back scatter detector to highlight the locations of the Pt NPs within this mixture; (b) a similar magnification TEM image of the sample in (a); and (c) a relatively high magnification TEM image of the sample depicting the spacing between the Pt nanocatalysts.**

The control over surface coverage and interparticle spacing of the Pt nanocrystals is especially important for applications that include PEMFCs and chemical sensing. For these applications the density of catalyst loading needs to be optimized for tuning localized reaction turnover rates as this influences the overall mass transport efficiencies of the corresponding reactions.[16,220] In addition, more traditional catalysts for PEMFCs prepared using Pt nanocrystals and carbon particles have been shown to easily agglomerate during the process of catalyst preparation.[221–224] This agglomeration can prevent reactants from effectively reaching all of the surfaces of these catalysts.

The TEM analyses of the Pt nanocrystal coated porous supports presented here indicated that the catalyst particles were fixed in position by the support and did not form clusters within these samples. These well-dispersed catalysts could exhibit higher Pt mass activities than those with agglomeration of their catalyst particles. This lack of agglomerates in the macroporous material is attributed in part to the formation of uniform coatings of nanocrystals on the polymer templates (**Figures 6.6 and 6.9**). The attractive interactions between the polymer template and the nanocrystals is balanced by the electrostatic repulsion between the nanocrystals. This balance of interacting forces can limit the formation of nanocrystal agglomerates on the polymeric template .[77] The uniform distribution of nanocrystals on the PS templates can be further tuned by adjusting the surfactants used to stabilize both the nanocrystals and the PS colloids during the initial assembly process, such as to screen the electrostatic repulsion between individual nanocrystals.[189,217,225] It is anticipated that these finely tuned materials will have higher mass activities than commercial catalysts for PEMFCs. Platinum remains one of the optimal catalysts for PEMFC cathodes for its catalytic activity and stability.[179] It is, however, also one of the most expensive precious metals in the world.[226] The use of ordered macroporous supports for these and related nanocrystals could further optimize their utilization and reduce the overall costs for preparing catalyst materials.

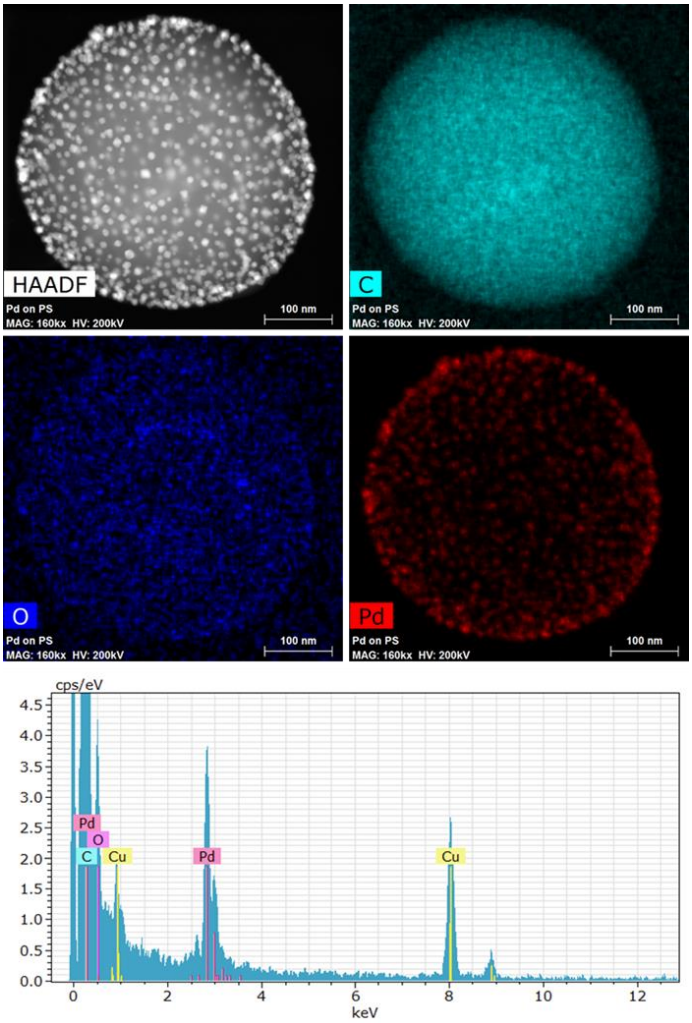


**Figure 6.9.** **A series of TEM images including a HAADF analysis and EDS elemental maps of Pd NPs (13 ± 2 nm ø) coated onto spherical PS templates (~400-nm ø), which were used for the preparation of hexagonally close-packed arrays of dimpled Ni that supported the Pd NPs as a structured electrocatalyst. The corresponding EDS spectrum of the sample is presented at the bottom of the images.**

### 6.5.3 Hexagonally Close-packed Arrays of Dimpled Features for Electrochemical Applications

Ordered arrays of dimpled Ni were prepared with a uniform coating of Pd nanocrystals with diameters of 13 ± 2 nm and an interparticle (edge-to-edge) spacing of 10 ± 4 nm for use in alcohol oxidation reactions. When assuming the Pd nanocrystals were immobilized onto the surface of hemispherical Ni dimples, the Pd to Ni atomic ratio was determined to be about 1:1.5. This Pd to Ni atomic ratio is within the optimal range in the

literature for methanol oxidation, and could be further tuned by varying the Pd nanocrystal concentrations during the aforementioned template coating procedure.[227,228]

These materials, prepared by a combination of the self-assembly processes and Ni electrodeposition, were analyzed for their catalytic efficiency towards the electrochemical oxidation of methanol. There are a number of other electrochemical reactions that also rely on nanocrystals to improve mass activity and reaction efficiency, which could benefit from these structured catalyst supports. Additional applications include the ORR, and the oxygen evolution reaction (OER). These reactions are commonly used in renewable energy generation systems, such as DMFCs, PEMFCs, and metal-air fuel cells.[229–234] Electrodepositon is a tunable process for preparing highly conductive metals of different compositions, and can be used to form a variety of 3D porous supports. Metal deposited by PVD techniques is, in contrast, unable to coat all of the surfaces within a 3D porous support. Sophisticated techniques, such as ALD, are significantly more expensive and difficult for scaling-up the production of materials in contrast to electrodeposition techniques.

The electrocatalytic performance of supported nanocrystals can also arise from the interfaces between two different materials, such as the Pd to Ni interface demonstrated herein. In the alcohol oxidation reaction, the carbon of the alcohol molecule will associate with the Pd surfaces (due to the extraordinary affinity of Pd for carbon), and the alcohol group can be readily oxidized by the neighboring oxygen rich surfaces of the electrochemically active Ni oxides. [229,235–240] Some approaches to preparing the porous supports, such as through the use of ALD, would encapsulate all of the exposed surfaces of the Pd nanocrystal. A continuous coating of Pd over the entire surface of the Ni would, however, eliminate the electrochemically exposed interfacial regions between Pd and Ni. This loss of interfacial regions can lose strong metal support interactions between the Pd and nickel oxide support, and could decrease the overall catalyst activities of these materials. The Pd nanocrystals were, therefore, transferred to the dimpled Ni surfaces using electrodeposition techniques (**Figure 6.10**).

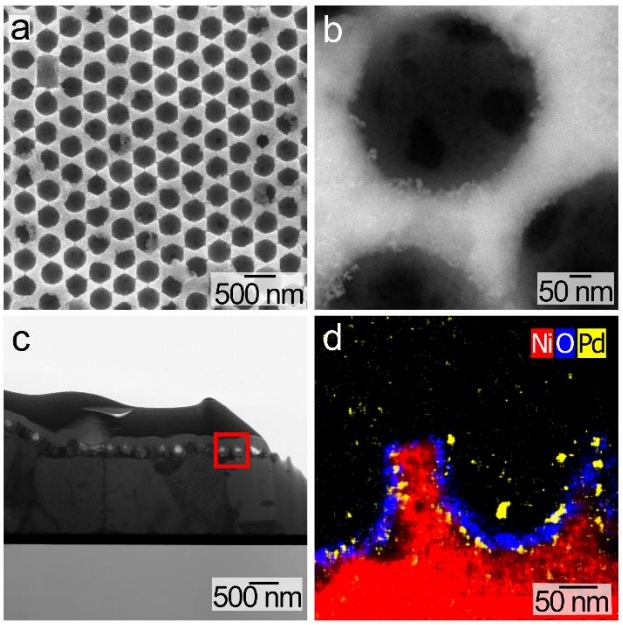


**Figure 6.10. The SEM and TEM images of Pd nanocrystals (ø = 13 ± 2 nm) supported within an array of dimpled Ni features with a periodicity of ~340 nm: (a) lower magnification image obtained using a secondary electron detector (SED) to analyze the array of close-packed features within the dimpled Ni; (b) higher magnification image using concentric backscattered electron detector indicating the presence of Pd nanocrystals on the Ni surfaces as visualized by the contrast in electron density of these elements; and (c) bright field STEM image from a section of the sample prepared by FIB milling and lift-out. The red box in (c) indicates the location associated with (d), which depicts the EDS combined elemental maps confirming the presence of Pd nanocrystals on the surfaces of the structured Ni support.**

The conductive Ni support was deposited from an aqueous electrolyte solution into the interstitial spaces within the assemblies of PS spheres, which had been coated with a controlled loading of Pd nanocrystals (**Figure 6.9**). The rate of nickel deposition was finely controlled, and the thickness of the Ni support monitored to avoid covering all of the templates with Ni. For example, the surface features were tuned to approximately 2/3 and 1/2 of the height of the polymer templates as verified by FIB prepared cross-sections of the dimpled arrays (**Figure 6.11**). These arrays of dimpled Ni demonstrated the ability to fine tune the surface morphology of the catalyst support.

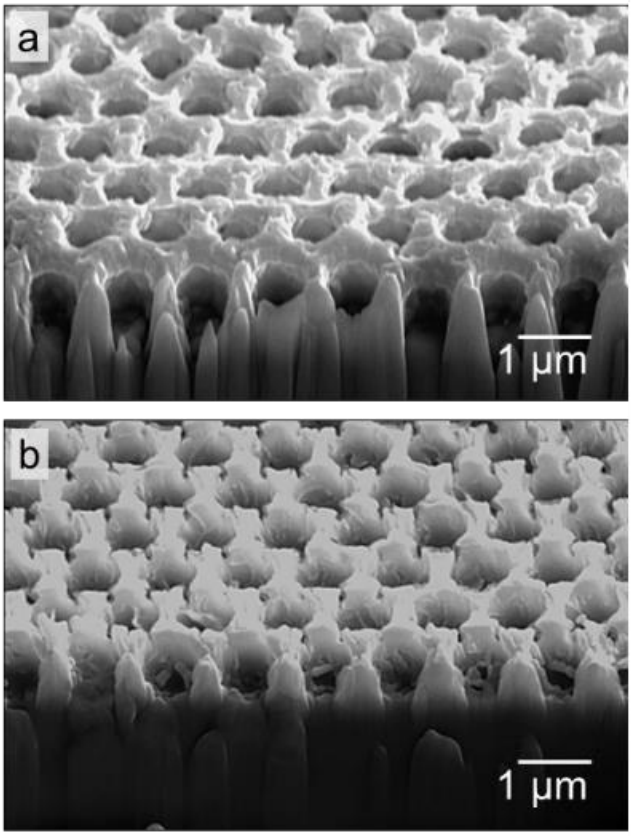


**Figure 6.11. Cross-sectional SEM images of dimpled features in Ni after template removal: (a) Ni electrodeposited to cover approximately 2/3 of the height of the polymer templates; and (b) Ni electrodeposited to cover approximately 1/2 of the height of the polymer templates.**

Arrays of Ni supported Pd nanocrystals are a relatively low cost and stable catalyst for alcohol oxidation reactions performed under alkaline conditions.[229,235–240] The structured arrays of dimpled Ni supporting Pd nanocrystals were evaluated for their use in methanol oxidation reactions (**Figure 6.12**). A detailed description of these experiments is presented in **Section 6.4.10**.

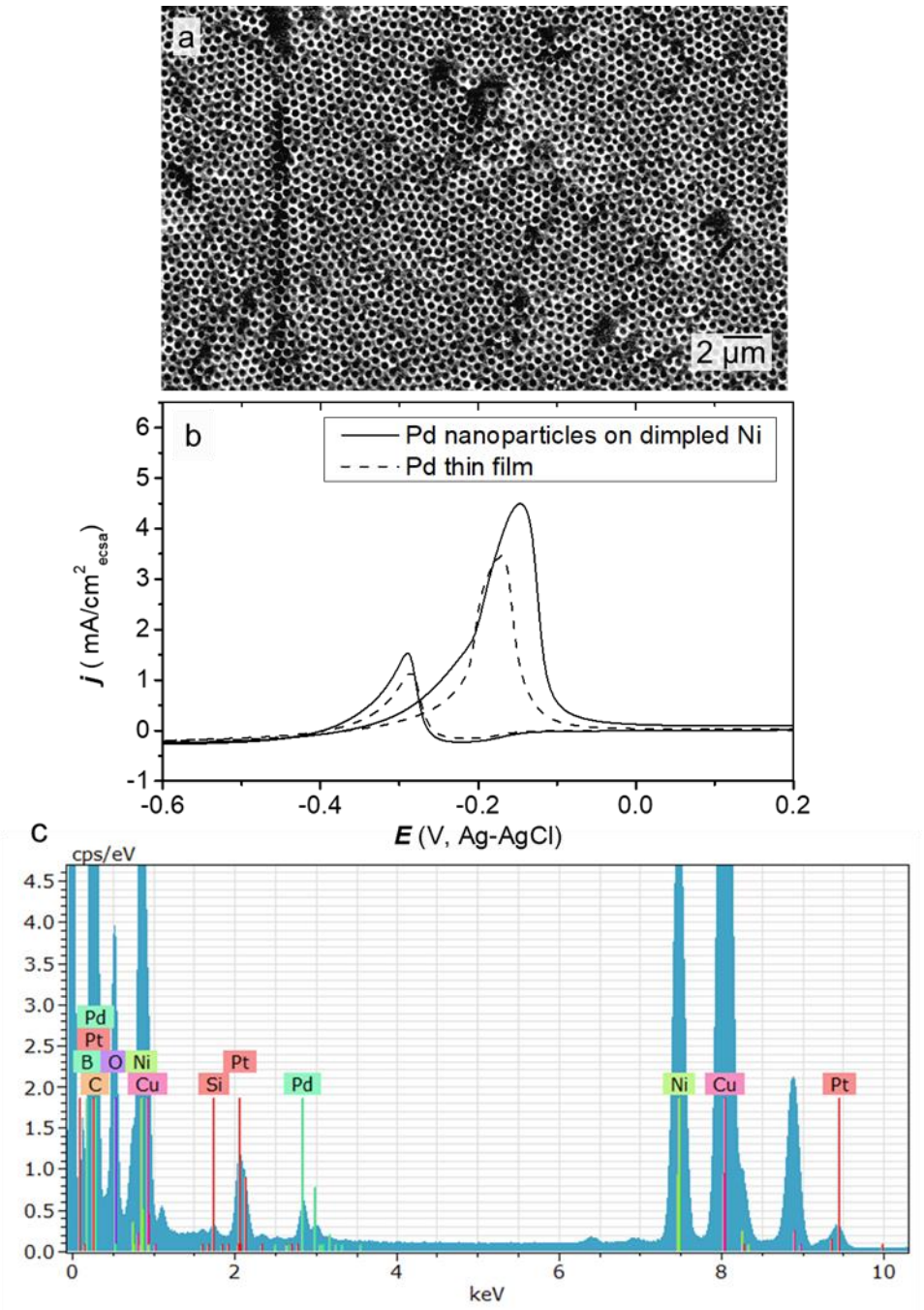


**Figure 6.12.** **(a) The SEM image of a working electrode used for methanol oxidation, which contained Pd NPs supported on dimpled Ni. (b) Specific current density (normalized against Pd ECSA) of methanol oxidation for a planar Pd electrode and Pd NPs loaded onto regular, dimpled features (200-nm ø) in Ni. (c) An EDS spectrum of the Pd nanocatalyst coated Ni dimples where the Pt signal originated from the protection layer used during the FIB milling of the Pd coated Ni.**

These experiments determined that the dimpled electrode coated with nanocrystals had a 30 % higher specific activity than a planar polycrystalline Pd film. At the end of the electrochemistry experiments, a cross section of the sample was prepared by FIB techniques for TEM and EDS analyses (**Figure 6.10**). These analyses indicated that the Ni support retained the Pd nanocrystals and contained a thin surface layer of nickel oxide. This oxide layer acts as a barrier that limits the oxidation of the underlying Ni metal. This oxide layer was stable at the applied potentials required for the electrochemical oxidation of methanol. [229,235–240] This tunable templating technique could be used to prepare customized electrodes that are further optimized with respect to its overall thickness, dimensions of the pores, electrode surface morphology, and composition towards catalyzing different electrochemical alcohol oxidation reactions. It is hypothesized that similarly porous materials with a further fine-tuned pore size and surface coverage of the nanocrystals may exhibit an enhanced performance towards additional alcohol containing species. The optimization of these porous materials could be customized to account for differences in the diffusion coefficients and steric hindrance of each reaction.[241]

### 6.5.4 Randomly Assembled Nanobowls for Flow-through catalytic Applications

Random assemblies of nanobowls, each coated with Pt nanocrystals (3 ± 1 nm in diameter) were prepared to demonstrate additional material deposition techniques commonly used on a commercial scale, such as PVD used in the production of nanostructured and/or conductive films. These nanobowls of $Au/TiO_2$ (~60 nm in total thickness) supporting Pt nanocrystals can be easily deposited as an ink, and dried as a layer with interconnecting pores for flow-through applications. One of these application can be found in PEMFCs as a structured catalyst layers that are subjected to the influx and removal of fuel and products.[229–234] These pore spaces created by the curvatures of the nanobowls could influence mass transport characteristics, such as to further improve the efficiency of the ORR. The sol-gel processes described herein can be easily scaled to produce commercially relevant quantities of materials. The sol-gel process is, however, most often used in the production of semi-conducting or ceramic materials. The demonstrated electrodeposition techniques utilize a solution-based process, where

precise control over deposition conditions (i.e., bath concentration, circuit conductivity and impedance) is required for the formation of uniform nanometer-scale continuous thin films. Controlling these parameters for the reproduction of nanoscale features can be more challenging at commercial scales when compared to the throughput of PVD techniques.[242,243] The PVD process can be extended to create a variety of thin film materials, such as metals, metal oxides, and ceramic materials. These are scalable processes that provide an ease of controlling both material purity and thickness. Physical vapour deposition techniques can also deposit materials onto non-conductive substrates, and have been used in decal transfer and related commercial scale processes.[73] Our study utilized PVD to prepare both metal and metal oxide coatings on assemblies of nanocrystal coated PS templates. This process effectively immobilized the nanocrystals in the deposited thin films. Nanobowls were prepared with immobilized nanocrystals, which were isolated from the templates by sonication in a 50:50 (v/v) mixture of toluene and acetone. Suspensions of these nanobowls were cast as assemblies of randomly organized, 3D porous supports (**Figure 6.13**).

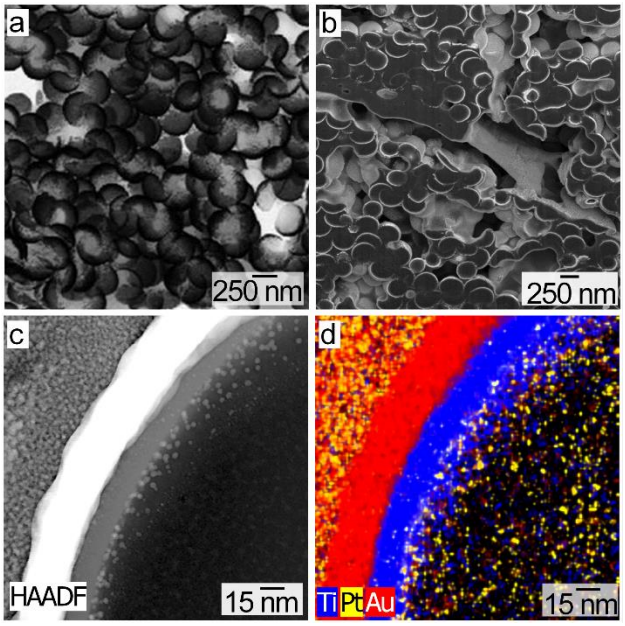


**Figure 6.13. Scanning electron microscopy and TEM images of Pt nanocrystals (ø = 2.8 ± 0.5 nm) supported on the surfaces of nanobowls prepared from a composite of Au and $TiO_2$ (ø = ~350 nm): (a) bright field TEM image of the Pt nanocrystals supported on a randomly assembled structure prepared from these nanobowls; (b) SEM image collected using a SED of a FIB prepared cross-section of the same sample of nanobowls that was also mixed with a DuPont™ DE2020 ionomer; (c) HAADF-STEM image from a cross-section of a single nanoshell; and (d) combined image of the Ti, Pt, and Au EDS elemental maps for the nanostructure shown in (c).**

The Au and $TiO_2$ multilayer compositions were chosen in part to demonstrate the flexibility of using PVD techniques to create structures containing both metals and metal oxides that are not achievable by either sol-gel or electrodeposition alone. This material combination can also be used to prepare substrates that are active in photocatalytically induced hydrogen evolution and the ORR.[216–219,221,225,231] The Pt nanocrystals supported by these nanobowl structures were clearly identifiable in the HAADF-STEM images and EDS maps **Figure 6.13c** and **Figure 6.13d**). The preparation of this material demonstrated that the procedures for preparing the nanocrystal coatings on PS and their transfer to a support are compatible with commercially relevant PVD processes while retaining nanostructured features. When compared to the other techniques demonstrated in this study, PVD techniques can be used to prepare unique nanostructures that can be further assembled into 3D structures using conventional powder processing techniques.

## 6.6 Conclusion

This study demonstrated a number of tunable approaches to preparing porous supports containing uniform coatings of nanocrystals. It was shown that the loadings of nanocrystals on spherical polymer templates can be fine-tuned with respect to the composition, size, and surface coverage of the catalyst. Subsequent procedures transferred these nanocrystals to the surfaces of a series of macroporous support materials. Different techniques to deposit or grow the support material were used to demonstrate the preparation of materials for a range of applications. Ordered 3D macroporous supports of $Ti_{1-x}Si_xO_2$ with coatings of upconverting nanocrystal were prepared by sol-gel techniques for photocatalytic or other photonic applications. Ordered porous $TiO_2$ supporting uniform layers of Pt nanocrystals were prepared for catalytic reactions that include alcohol oxidation and hydrogenation reactions. By adjusting the loading of nanocrystals on the spherical polymer templates, porous $TiO_2$ samples were prepared with a uniform and well-tuned coverage of Pt nanocrystals. The interparticle spacing can be controlled for optimizing the specific needs of Pt based catalytic reactions.

Efforts of incorporating these metal oxide supported Pt NPs into testing fuel cells were unsuccessful. The CL comprised of macroporous $TiO_2$ supported Pt were found to be too resistive for use in the fuel cells with a drastically increased activation voltage loss. These macroporous CLs also exhibited increased mass-transport losses (flooding) that would result in the loss of power at increased fuel cell current density. Further improvements of these materials can include additional dopants in the metal oxide to increase the conductivity of the CLs. The flooding issue could also be improved by the investigation of MPLs and GDLs that are tuned for removing water from these macroporous CLs.

Hexagonally close-packed arrays of dimpled Ni features with Pd nanocrystal coatings were prepared for the electrochemical oxidation of alcohols. This structure exhibited higher specific current densities towards the electrochemical oxidation of methanol than planar films of polycrystalline Pd. Nanobowls containing a multilayer of Au and $TiO_2$ coated with Pt nanocrystals were prepared by PVD techniques and assembled into randomly packed 3D structures to demonstrate an extension of these techniques to

relevant commercial processes for producing nanostructured materials for fuel cell applications. The use of these modular techniques can be utilized to produce nanostructured materials with a tunable porosity and structure, as well as finely adjusted nanocrystal loadings and catalysts-support interactions for enhancing chemical, electrochemical, and photochemical processes. The ability to tune each of these properties can increase the catalytic efficiency and stability of the nanocrystals, optimize the utilization of nanocrystals, create synergistic effects at disparate interfaces, and reduce consumption of precious metals and other valuable materials.

# Chapter 7.

# Mesoporous Platinum Prepared by Electrodeposition for Ultralow Loading Proton Exchange Membrane Fuel Cells

## 7.1 Acknowledgement

This research was financially supported in part by the Natural Sciences and Engineering Research Council (NSERC) Discovery Program (Grant No. 1077758), CMC Microsystems (MNT Grant No. 4440), and the Canada Research Chairs Program (B.D. Gates; Grant No. 950-215846). This work made use of 4D LABS (www.4dlabs.ca) and the Centre for Soft Materials shared facilities supported by the Canada Foundation for Innovation (CFI), British Columbia Knowledge Development Fund (BCKDF), Western Economic Diversification Canada, and Simon Fraser University.

## 7.2 Abstract

Platinum (Pt) is a commonly used catalyst for PEMFCs due to its high catalytic activity, selectivity for the oxygen reduction reaction (ORR), and resistivity to chemical and electrochemical degradation under fuel cell operating conditions.[10,244] To increase the competitiveness of PEMFCs in contrast to internal combustion engines (ICEs) for automotive applications, the mass of Pt used in PEMFCs must be reduced to lower the cost of these systems.[179,245] Researchers have demonstrated the use of electrodeposition as a superior method for creating catalysts with a higher Pt utilization than the Pt nanoparticle-based powdered catalysts that are widely adopted by current PEMFC manufacturing techniques.[61,180,246]

To the best of our knowledge, this study describes the first demonstration of a commercially viable PEMFC catalyst with an ultra-low loading of Pt and a high degree of mesoporosity as prepared by electrodeposition. The prepared material was analyzed by both ex-situ electrochemical and in-situ fuel cell techniques. Most notably, when utilizing

the electrodeposited mesoporous Pt as cathode catalyst in PEMFCs the maximum mass specific power density was 0.114 $g_{Pt}$/kW, which is at least 3 times the value achieved with a conventional Pt nanoparticle-based catalyst. The results of this study demonstrated that the electrodeposited mesoporous catalyst also had a higher utilization of Pt. We anticipate that other platinum group catalysts could be prepared by the electrodeposition technique demonstrated here for use in other electrochemical systems to reduce system costs and improve catalytic efficiencies.

**Graphical Abstract**

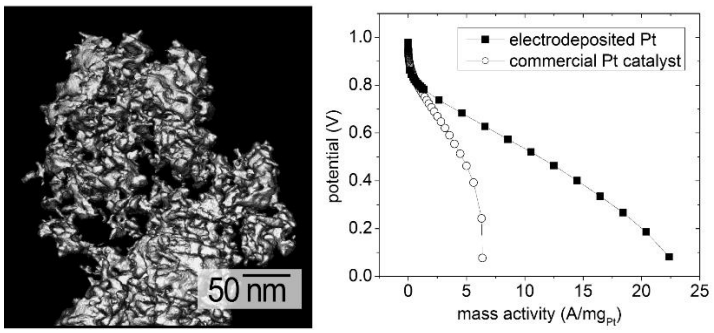


## 7.3 Introduction

Current manufacturing practices aim to increase Pt mass activity and reduce system costs by utilizing Pt nanoparticles (NPs) that maximize the surface area to volume ratios of these catalysts.[165,179,255] During catalyst preparation, these Pt NPs are mixed with support materials that consist of conductive carbon NPs and a non-electrically conductive perfluorosulfonate containing proton conductive ionomer.[40] The carbon particles and ionomer conduct electrons and protons, respectively, to the Pt surfaces for the catalysis of the ORR. The processing of these catalyst and catalyst support materials can, however, result in agglomeration of the carbon particles that can impede the infiltration of oxygen gas, and the ionomer can coat the conductive particles and insulate them from the conductive pathways within the catalyst layers (CLs).[179,256] A large amount (ranging from 30 to 80 %) of the Pt NPs incorporated into the powder processed, particle-based CLs can be inactive due to the formation of these agglomerates.[31,47,257] Many investigations have implemented specific engineering controls, such as the ultrasonic dispersion of carbon particles and ionomer for creating catalyst layer inks with reduced aggregation and

increased utilization of Pt.[30] In Chapter 4 and 5, the modification to the interface between the CCL and PEM were demonstrated with improved PEMFC performance. However, these improved CL designs still utilized the conventionally prepared catalyst ink. Therefore, the issues that plague powder processed materials can still impact their performance. To further improve Pt utilization, we believe a fundamentally different approach is necessary for the preparation of CLs for PEMFCs.

Theoretically, Pt nanocatalysts prepared by electrodeposition are superior to those prepared by processing of particle-based inks. Electrodeposition techniques deposit the Pt materials onto regions with sufficient ionic and electrical conductivity.[183,258,259] The benefits of preparing custom built catalyst materials by electrodeposition was demonstrated in a recent study through the formation of porous Pt on planar glassy carbon substrates created by a pulsed electrodeposition technique.[246] The resulting bicontinuous structure of Pt and void spaces with dimensions of <10 nm are more commonly achieved through the selective removal of lesser noble metals from Pt alloys.[175,245,260,261] These electrodeposited porous Pt structures were determined to have relatively moderate material porosities (25 %) and a low overall surface coverage (1.6 %).[246] They demonstrated an ORR mass activity that was at least 9 fold higher than reference catalysts prepared with Pt NPs.[246] These materials were, however, only evaluated through small scale *ex situ* tests in a solution-based electrochemical cell.

## 7.4 Materials and Methods

### 7.4.1 Substrate Preparation

Mesoporous Pt catalysts were prepared by electrodeposition onto both planar and porous substrates to characterize the deposition process. The electrochemical activities of these nanostructures for the ORR were compared to commercial catalysts of Pt nanoparticles. The performances of these catalysts were evaluated through a series of tests in electrochemical RDE and PEMFC setups.

A planar conductive Pt substrate was initially used to identify appropriate surfactants for use in the electrodeposition process and to assess the current densities

required for the formation of mesoporous Pt. A p-type <001> Si wafer was coated with a 5-nm thick Cr adhesion layer and a 150-nm thick layer of Pt, which was used as a planar substrate for the electrodeposition processes. These Cr and Pt metal films were sequentially deposited by thermal evaporation, without breaking vacuum, using a custom built physical vapor deposition (PVD) system in 4D LABS (Simon Fraser University).

Mesoporous Pt was also deposited onto glassy carbon electrodes that were coated with a layer of Vulcan XC-72 (Cabot Corporation, United States) carbon particles and ionomer (Nafion® DE2020, Dupont, United States) — referred to as the C and ionomer films in the main text. This layer catalyst free C and ionomer film was prepared similarly (as described in **Section 4.4.2**) to the reference cathode catalyst layers (CCLs). The similarities in CL preparation and layer thickness allowed a fairer comparison of the electrochemical performance of these mesoporous Pt catalysts to conventional CCLs prepared with Pt nanoparticles. The glassy carbon electrodes (5-mm in diameter) were inserted into a ChangeDisk electrode holder (Pine Research Instrumentation; NC, United States) and used as the working electrodes to support the Pt nanostructures during their electrochemical analyses by RDE techniques. The glassy carbon electrodes were each sequentially polished using a suspension of 300-nm and 50-nm diameter alumina particles (Buehler, IL, United States) to create a mirror-like finish.

The polished carbon was coated with an ~10-µm thick layer of Vulcan XC-72 carbon nanoparticles mixed with a 30 wt/wt % loading of ionomer (Nafion® DE2020, Dupont, United States). This layer of carbon particles and ionomer was prepared by spin casting this ink mixture at 500 rpm for 5 min prior to Pt electrodeposition to mimic the structure and composition of conventional CCLs in PEMFCs. Prior to spin coating, the suspension of carbon and ionomer were dispersed in a 3:1 (w/w) mixture of 2-propanol (Anachemia, Canada, ACS grade) and DI (18 MΩ·cm) water to achieve a 0.3 w/w % (solid/liquid) solution. All DI water, used to prepare the necessary solutions and for rinsing of the electrodes, was filtered with a Barnstead DIamond™ deionizing water system with an output of 18 MΩ·cm. An aliquot of 20 mL of the dilute ink solution was placed into a glass vial. The vial containing the ink solution was chilled by placing it into an ice filled container and sonicated using a process of 1 s "on" and 3 s "off" for a total duration of 1 h (and a total of 15 min of sonication during the collective "on" time) using a probe sonicator

(Fisher Scientific, United States, Sonic Dismembrator 500). A 12-mm diameter sonication probe was immersed ~1 cm into the solution, and operated at 40 % of the maximum power (the maximum power was ~500 Watts).

Large area glassy carbon electrodes were also coated with the layer of carbon particles and ionomer upon which the electrodeposited mesoporous Pt were prepared and transferred to MEAs for fuel cell testing. To prepare these films containing a layer of mesoporous Pt, a 3-mm thick and 5-cm by 5-cm wide, square glassy carbon plate (SPI Supplies, United States) was first spin coated (at 500 rpm for 30 min) with the layer of carbon particles and ionomer, and subsequently loaded into a custom electrodeposition cell (shown in **Figure 7.1**).

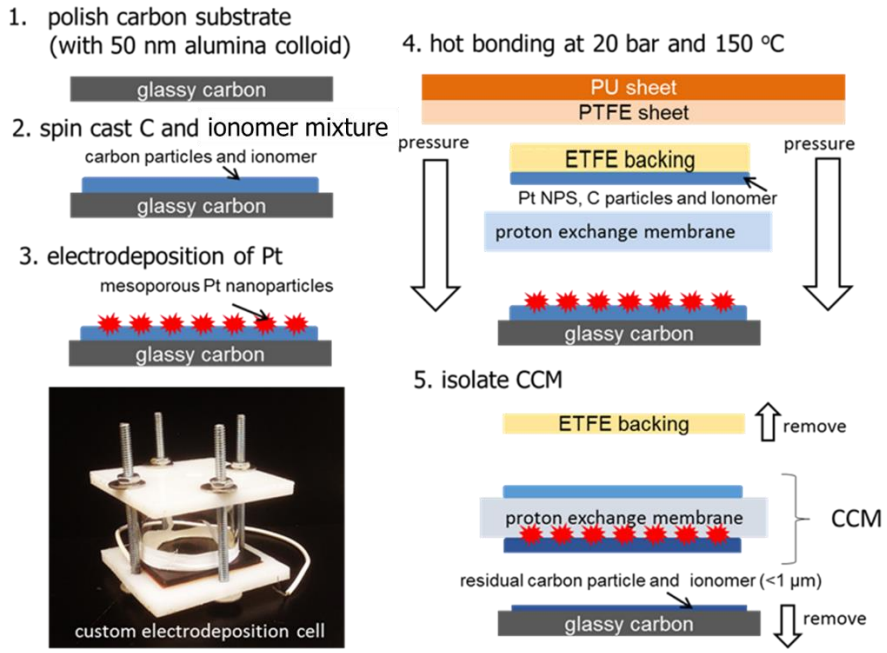


**Figure 7.1. Schematic diagram of the preparation of mesoporous Pt by electrodeposition and its transfer onto proton exchange membranes for the evaluation of these assemblies as custom cathode catalysts layers (CCLs) in PEMFCs. Bottom left picture: the custom electrochemical cell used to prepare the mesoporous Pt on a film of C particles and ionomer coated onto a polished glassy carbon plate. Abbreviations: PU = polyurethane; PTFE = polytetrafluoroethylene [IUPAC: poly(1,1,2,2-tetrafluoroethylene)]; ETFE = ethylene tetrafluoroethylene [IUPAC: poly(1,1,2,2-tetrafluorobutane-1,4-diyl)]; and CCM = catalyst coated membrane.**

### 7.4.2 Electrodeposition of Mesoporous Pt

Planar Pt electrodes, C and ionomer coated glassy carbon RDE electrodes, and C and ionomer coated large area glassy carbon electrodes were each separately used as the working electrode during the electrodeposition of mesoporous Pt. A series of surfactants, such as polyethylene glycol (PEG; average $M_n$ ~400; Sigma Aldrich, United States), ethylenediaminetetraacetic acid (EDTA; Sigma Aldrich, ACS Grade, United States), hexadecyltrimethylammonium bromide (CTAB; ≥96 % [AT]; Sigma Aldrich, United States), and polyoxyethylene (30) cetyl ether (Brij-30; Sigma Aldrich, United States) were each evaluated for their influence on creating mesoporous Pt. Following this initial screening process, a series of mesoporous Pt were prepared by electrodeposition from an aqueous solution of 5 mM $H_2PtCl_6$ (Sigma Aldrich, ACS Grade, United States), 0.2 M $H_2SO_4$ (Caledon Laboratories Ltd, ACS Grade, Canada), and 1.0 % (v/v) polyethylene glycol *p*-(1,1,3,3-tetramethylbutyl)-phenyl ether (Triton™ X-100; Sigma Aldrich, Laboratory Grade, United States). Each of the prepared solutions were stored in the dark at room temperature for at least 24 h prior to use in the electrodeposition processes to ensure all of the respective reagents were in equilibrium with one another. Electrodeposition of Pt onto each of the desired conductive substrates was performed using a SP-150 potentiostat (BioLogic Science Instruments, France). The electrodeposition processes were performed galvanostatically at 5 mA/cm$^2$ for 30 s, 3 min, or 10 min with a graphite rod (part #: MPGRR250; Pine Research Instrumentation, NC, United States) as the counter electrode in a two electrode electrochemical setup.

### 7.4.3 Electron Microscopy Characterization

Electron microscopy techniques, such as SEM and TEM, were used to verify the surface coverage, morphology, and crystalline nature of the electrodeposited Pt. The SEM analyses were performed using an FEI Helios SEM/ focused ion beam (FIB) dual beam system operating at 10 kV. This system was also equipped with an EDAX EDS detector for elemental mapping of the materials. At the end of a series of electrochemical tests the electrode materials were sacrificed for preparing cross-sections. The experimental procedures for these electrochemical tests consisted of the following series of techniques: (i) 1,500 complete CV scans at 100 mV/s from 0 to 1.2 V [versus a reversible hydrogen

electrode (or RHE)]; (ii) LSV measurements at 1 mV/s from 1.2 to 0.2 V (versus RHE) at a series of different electrode rotational speeds; and (iii) 5 complete CV scans at 50 mV/s from 0 to 0.8 (versus RHE) after each LSV measurement. These tests required at least 12 h while continuously holding the electrode of interest under an applied potential. Cross-sections of the samples for SEM analysis were obtained by lifting out sections of the catalyst films through the assistance of small sections of adhesive carbon tape (Ted Pella, Inc., CA, United States). For TEM analyses, sections of the electrodeposited samples were physically removed from the Pt or carbon electrodes using a plastic spatula. These sections of each sample were collected into centrifuge tubes containing 50 µL of DI water. A 10 µL portion of each suspension was drop cast onto Formvar/carbon coated 300 mesh copper TEM grids (PELCO®, Ted Pella Inc., United States) for analysis by TEM and EDS techniques. All of the TEM related analyses were performed using an FEI Osiris X-FEG S/TEM operating at 200 kV. The TEM was equipped with a Super-X EDS detection system and a Fischione single tilt holder (advanced tomography holder Model 2020, Fischione Instruments, Inc.; United States). The TEM tomography analyses were prepared from a series of images obtained at tilt angles from +70° to -65° with 3° increments between each image. The series of tomography images were processed by Inspect 3D Express (FEI, Thermo Fisher Scientific, United States) for tilt correction, alignment, and volume reconstruction of the data. The reconstructed volumes were rendered by Amira Version 6.0 (FEI, Thermo Fisher Scientific, United States).

### 7.4.4 Electrochemical Characterization

A series of electrochemical experiments were performed to determine the electrochemically active surface area ($A_{ecsa}$) of the samples, to condition the electrodes for the ORR experiments, and to determine the ORR efficiency of each electrode by CV and LSV techniques. These experiments were performed using a BioLogic Science Instruments SP-150 potentiostat in addition to using an analytical rotating disk electrode (RDE) system (Modulated Speed Rotator, Pine Research Instrumentations, PA, United States). Electrochemical data was collected using EC-Lab data analysis software (V10.18). The as-prepared electrodes were incorporated as the working electrode into a typical three electrode setup using a custom built glass electrochemistry cell with a custom made Pt reversible hydrogen reference electrode, and a Pt gauze counter electrode (100

mesh woven from 0.0762-mm diameter; 99.9 %; Alfa Aesar, United States). All electrochemical experiments were performed in a 0.5 M $H_2SO_4$ solution that was purged with ultra high purity $N_2$ gas (99.999 %, Praxair, Canada) for at least 30 min prior to the commencement of the experiments. A positive $N_2$ pressure was maintained in the head space of the electrochemical cell throughout the experiments unless otherwise noted. The CV measurements were performed without rotation at a scan rate of 100 mV/s from 0 to 1.2 V (versus RHE) while at ambient temperatures (measured to be 22.1 ±0.2 °C). Prior to the ORR analyses, a series of CV scans were performed on each electrode to optimize their ORR activities and to remove any adsorbed organic molecules from the Pt surfaces (e.g., from the electrodeposition process or carbon contaminating species from the atmosphere). A total of 1,500 complete CV scans were performed to condition the electrodes to maximize the ORR performance of the electrodes and ensure consistency of the ORR performance between different CLs. Prior to the ORR experiments, $O_2$ gas (99.993 %, Praxair, Canada) was bubbled through the electrolyte for at least 30 min to saturate the solution with dissolved oxygen. The subsequent LSV experiments for the ORR were performed with the same electrochemical set-up, but at a series of electrode rotational speeds and with potentials scanned from 1.2 to 0.2 V (versus RHE) at a scan rate of 1 mV/s. The range of rotational speeds included 200, 600, 1000, 1200, 1600, 2000, 3000, 4000, and 5000 rpm. These parameters were chosen to assess the catalytic efficiencies of the samples towards the ORR while immersed in the sulfuric acid solutions. Furthermore, the number of electrons that was involved in the process of ORR was investigated using Koutecký-Levich plot (current density versus inverse square root of rotation speed in rad/s) generated from the RDE experiments for each of the electrodes. A representative analysis is presented in **Figure 3.9**.

For the determining the $A_{ecsa}$ of the electrode, a total of five CV scans at 50 mV/s were performed, from 0 to 0.8 V versus RHE, between each consecutive LSV measurement as part of the ORR analysis to ensure a consistency of the Pt catalysts. The CV profiles were also used to assess the $A_{ecsa}$ of the Pt for each of the electrodes (e.g., **Figure 7.8**). The $A_{ecsa}$ of Pt was calculated from the area under the hydrogen desorption peaks assuming that the charge associated with the formation of a monolayer of hydrogen on the Pt surfaces is approximately 210 μC/cm$^2$.[60,179,256] The $A_{ecsa}$ per gram of Pt was determined following the series of electrochemical analyses. This series of

electrochemical tests, which were performed over a continuous period of at least 12 h, were followed by XRF and inductively coupled plasma mass spectrometry (ICP-MS). This order of experiments was adopted due to the destructive nature of the ICP-MS analyses.

### 7.4.5 Preparation of Catalyst Coated Membranes

A series of MEAs were prepared and tested to characterize the electrodeposited mesoporous Pt for its performance in PEMFCs. To compare these materials with conventional cathode catalysts for PEMFCs, MEAs were prepared using cathode catalysts containing a mixture of commercially available Pt nanoparticles (TEC10V50E, Tanaka Kikinzoku Kogyo, Japan), C particles (Vulcan® XC-72), and ionomer (Nafion® DE2020). A series of MEAs were also prepared using mesoporous Pt electrodeposited onto films of carbon particles mixed with ionomer. The standard anode and cathode catalyst inks were prepared according to the same procedures outlined in the section providing details on the preparations of the substrates. The same procedures outlined therein for preparing the solutions of C particles and ionomer were also used to create supporting materials for the electrodeposition of mesoporous Pt.

These anode and cathode catalysts were hot-bonded with a proton exchange membrane to form catalyst coated membranes (CCMs) by a process of decal transfer.[262] These catalyst materials were transferred from the substrate used in the electrodeposition process and/or from catalyst coated polymer decals to the membranes through a process of hot-bonding. The standard cathode and anode catalysts were prepared for decal transfer by coating thin films of ethylene tetrafluoroethylene [ETFE; poly(ethene-co-tetrafluoroethene)] with the ink solutions using a generic Mayer bar coater operated at a roller speed of 8 m/min. The catalyst films were dried on a heated vacuum stage at 50 °C for approximately 10 min. The Pt loading and thickness of the cathode and anode catalyst films were controlled using Mayer bar rollers of different sizes. The anode loadings were consistently prepared at 0.1 $mg_{Pt}/cm^2$. The thicknesses of the cathodes containing Pt NP-based catalyst were varied to prepare Pt loadings of 0.2 $mg_{Pt}/cm^2$ and 0.4 $mg_{Pt}/cm^2$. The CCMs were prepared with mesoporous Pt supported on a film of carbon particles and ionomer (itself supported on a glassy carbon plate) as the cathode layer and the Pt NP based catalyst coated on an ETFE decal as the anode layer. These catalyst layers were

both decal transferred at the same time onto the Nafion® membrane at 20 bar of pressure and 150 °C for 5 min with a use of a Carver® 25 ton hydraulic unit (Carver Inc., United States). The reference samples were each prepared by the same hot-bonding conditions for both the cathode catalysts and anode catalysts, which were prepared using the Pt NP containing ink coated onto ETFE decals. The different components used in the hot-bonding process are depicted in **Figure 7.1**. A sheet of 0.05-mm thick Teflon® was placed on top of the layered CCMs, followed by a sheet of 2-mm thick polyurethane rubber prior to hot bonding to ensure an even distribution of the bonding pressure. After 5 min of bonding, the layered CCMs were immediately removed from the Teflon® sheet and allowed to cool to room temperature for at least 10 min. The ETFE and glassy carbon plate were gently removed by hand after the CCM assembly was sufficiently cooled. The MEAs were prepared by hot bonding the CCMs, with of macroporous layer (MPL) coated gas diffusion layer (GDL) (Sigracet® gas diffusion layers, SGL Group, Germany) and adding a piece of G10 gasket on either side of the CCM. The hot bonding procedure was identical to the one outlined above for the preparation of the CCMs except that the bonding time was reduced from 5 min to 2 min. Additional Mylar® gaskets (DuPont Teijin Films, UK) were used to adjust the overall thickness of the gaskets as necessary to induce a 25 % compression of the MPL/GDL materials when assembled for testing in the fuel cell.

### 7.4.6 Fuel Cell Testing

The MEAs were analyzed in a single stack test setup for PEMFCs to compare the performance of the mesoporous Pt serving as CCLs versus CCLs prepared from inks containing Pt NP based catalysts. Fuel cell testing was performed using equipment provided by the Centre for Soft Materials in 4D LABS at SFU. These tests used a 50 W, Teledyne Medusa/Scribner system (Teledyne Technologies Inc., United States). The single stack fuel cells were assembled using graphite plates with parallel flow-field landings. The active area of the MEA exposed in each of the fuel cells was 5 $cm^2$. Maximum backpressures were maintained at 5 psi for both the anode and cathode. Gas flow rates for the cathodes and anodes were set at 1 L/min (maximum of the system). Electrochemical experiments on the MEAs, such as CV conditioning and the $A_{ecsa}$ determination, were performed using a VersaSTAT 4 potentiostat (Princeton Applied Research, United States). These experiments were performed with a scan rate of 100

mV/s with a scan range from 0 to 1.2 V (verses anode). The cell conditions were maintained at the standard conditions outlined by the United States Department of Energy (US DOE) [cell temperatures of 80 °C with $H_2$ (99.95 %, Praxair Canada) and $N_2$ (99.999 %, Praxair Canada) gases supplied to the anode and cathode, respectively, at 100 % relative humidity (RH)].[40,109] The MEAs were further tested under similar conditions to these electrochemical experiments, except $O_2$ (99.998 %, Praxair Canada) was supplied instead of $N_2$ (99.999 %, Praxair Canada) at the cathode. The LSV polarizations were performed under potentiostatic conditions from 0.95 to 0.1 V while stepped at 0.05 V increments with a 10 min dwell time at each voltage set-point. A total of 12 LSV experiments were performed to condition the MEAs for obtaining stable fuel cell polarization curves. The MEAs were deemed to be stable when at least three consecutive LSV experiments exhibited an overall deviation of < 0.5 $mA/cm^2$. After the LSV measurements had reached stabilization, 3 additional LSV experiments (100 mV/s; 0 to 1.2 V versus RHE) were performed, the results averaged, and analyzed to assess the fuel cell performance for each of the MEAs.

### 7.4.7 Analysis of Elemental Composition

Quantitative elemental analysis techniques were used to compare the Pt loadings of the samples. The Pt loading of the samples were initially verified by XRF spectroscopy (Themo Scientific, Niton XL3t, United States; operating at 50 kV), which was calibrated with a series of Pt thin film standards (ranging from 10 $\mu g_{Pt}/cm^2$ to 400 $\mu g_{Pt}/cm^2$ in 50 $\mu g_{Pt}/cm^2$ increments) made by nanoXRF (UHV Technologies, Inc., United States). For a more accurate determination of the Pt loadings, the Pt samples were digested at 80 °C in a solution of aqua regia and analyzed by ICP-MS. The aqua regia solutions were prepared as 3:1 (v/v) solutions of hydrochloric acid (36.5 – 38.0 % in water; Anachemia, Canada) and nitric acid (68 to 70 % in water; Anachemia, Canada). *CAUTION: Aqua regia solutions are extremely corrosive. These solutions should be handled with extreme care.* The ICP-MS measurements were performed using an Agilent 7700x quadrupole system maintained by the Department of Chemistry at the University of British Columbia.

## 7.5 Result and Discussion

In this study, we demonstrated an improved electrodeposition technique that produces mesoporous Pt with relatively high porosities (~60 %) and a high surface coverage (>95 %). This electrodeposition process was first performed on planar Pt substrates to determine the optimal surfactant system to assist in creating highly porous Pt nanostructures. Surfactants including polyethylene glycol (PEG), polyethylene glycol hexadecylether (Brij-30), ethylenediaminetetraacetic acid (EDTA), and hexadecyltrimethylammonium bromide (CTAB) were individually evaluated as additives (1.0 % v/v) in the solutions of Pt salt used for the electrodeposition process (**Table 7.1**).

**Table 7.1 Physical properties of some surfactants utilized in evaluating the preparation of mesoporous Pt by electrodeposition techniques (data obtained from Sigma Aldrich, Canada).**

| molecule | average molecular weight (g/mol) | density ($g/cm^3$) | type of surfactant |
|---|---|---|---|
| CTAB | 364 | 0.39 | ionic |
| PEG-400 | 400 | 1.13 | non-ionic |
| Triton™ X-100 | 625 | 1.07 | non-ionic |
| Brij-30 | 363 | 0.95 | non-ionic |
| EDTA | 363 | 0.86 | ionic |

Abbreviations:
CTAB = cetyltrimethylammonium
PEG 400 = polyethylene (400) glycol
Triton™ X-100 = polyethylene glycol tert-octylphenyl ether
Brij-30 = polyoxyethylene (30) cetyl ether
EDTA = ethylenediaminetetraacetic acid

### 7.5.1 Electrodeposition of Mesoporous Pt on Planar Substrates

A constant current technique was used for the electrodeposition process to ensure that the production of the mesoporous Pt catalysts could be easily achieved with commonly available industrial equipment. The Pt electrodeposited in the presence of Triton X-100 exhibited the highest surface coverage (>95 %) and the formation of needle-like nanostructures (**Figures 7.2a** and **7.2b**), while the other surfactants yielded poorly covered surfaces or feature-less films (**Figure 7.3**).

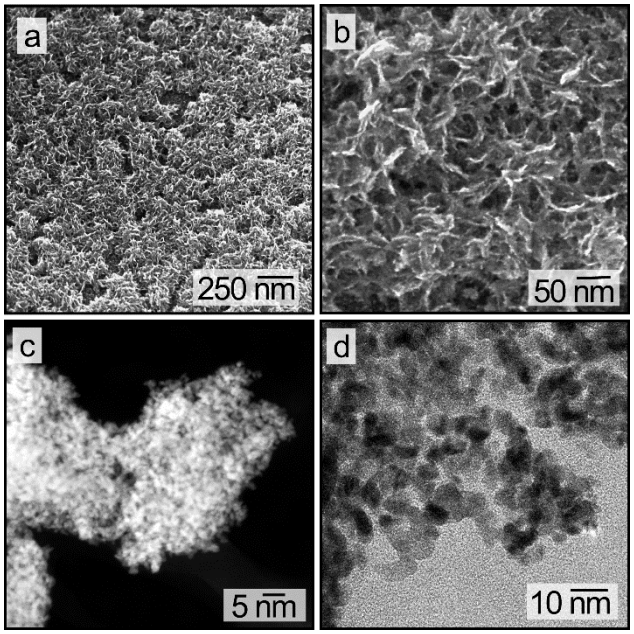


**Figure 7.2.** **Electron microscopy analyses of mesoporous Pt prepared by electrodeposition. (a) The SEM image of a surface covered with mesoporous Pt, which was created by electrodeposition for 10 min at 5 mA/cm$^2$. (b) A higher magnification SEM image of the sample in (a). (c) Scanning transmission electron microscopy (STEM) analysis using a HAADF detector for a section of the mesoporous Pt, and (d) a high resolution TEM (HRTEM) analysis of the same sample.**

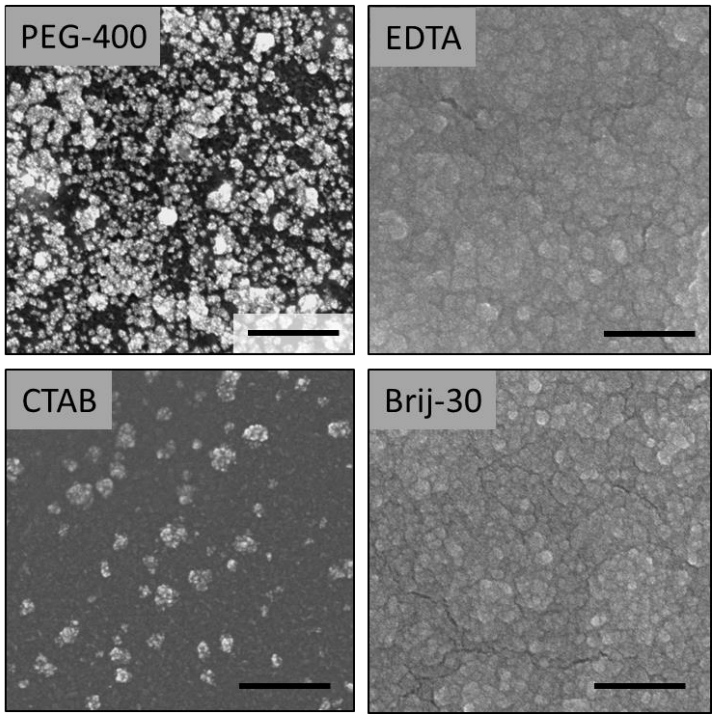


**Figure 7.3. The SEM images of Pt nanostructures created by electrodeposition from a solution of 0.5 M $H_2SO_4$ and 5 mM $H_2PtCl_6$, in the presence of different surfactants at concentrations of 1.0 % (v/v). These structures were electrodeposited onto electrodes prepared from Pt thin films on polished Si wafers. The surfactant used to facilitate the formation of the electrodeposited Pt structures are indicated on each of the images. The scale bars in each of the images is 200 nm in length.**

The Triton X-100 molecule has a distinct hydrophobic structure (a 4-tert-octylphenol group) that is covalently linked to a PEG sidechain. The Triton X-100 molecules can exhibit both metal to surfactant interactions (e.g., charge-transfer between the metal surfaces and oxygen atoms within the molecular structure of Triton X-100) and intra-surfactant interactions (e.g., π-stacking of phenol groups and van der Waals forces between alkyl chains) that result in the formation of hydrophobic pockets in solution that are inaccessible to metal ions.[263] The combination of these discrete structures and the relatively high current densities used for Pt electrodeposition (i.e., resulting in a rapid depletion of local concentrations of metal ions) can promote the formation of anisotropic Pt nanostructures.[183,264]

The porous structure of the electrodeposited Pt prepared in the presence of Triton X-100 was visualized using high resolution transmission electron microscopy (TEM) techniques (**Figures 7.2c** and **7.2d**). These TEM analyses indicated that the electrodeposited Pt contained a mesoporous structure of bicontinuous void spaces (with minimum diameters of ~2 nm) and Pt protrusions (with maximum diameters of ~3 nm). The high-resolution TEM analysis of the mesoporous Pt indicated a predominantly (111) surface faces (**Figure 7.4**) with an d-spacing of 0.23 nm that is similar to the properties of spherical Pt nanoparticles.[183]

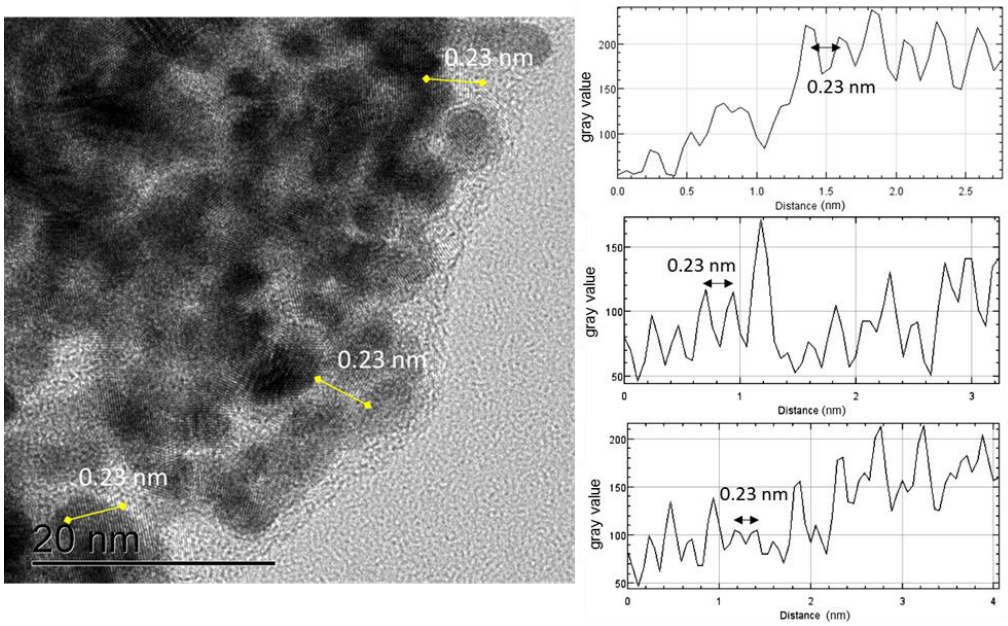


**Figure 7.4. High resolution transmission electron microscopy (HRTEM) analysis of mesoporous Pt depicting lattice fringes that correspond to the spacing of Pt (111) crystal planes.**

The average dimensions of the Pt protrusions within these mesoporous structures is similar to the dimensions of Pt NPs commonly used to prepare CLs in PEMFCs.[179,256,265] Three dimensional representations of the mesoporous Pt were prepared using data obtained from TEM tomographic analyses (**Figure 7.5a**). By taking cross-sectional slices from the center of the 3D datasets, the porosity of the mesoporous Pt was determined to be 59 ± 2 % (**Figure 7.5b**). This porosity is about 2 to 4 times higher than the porosities reported for nanoporous Pt created by other electrodeposition techniques (e.g., porosities up to 30 %, but with average values of 15 %).[60,264]

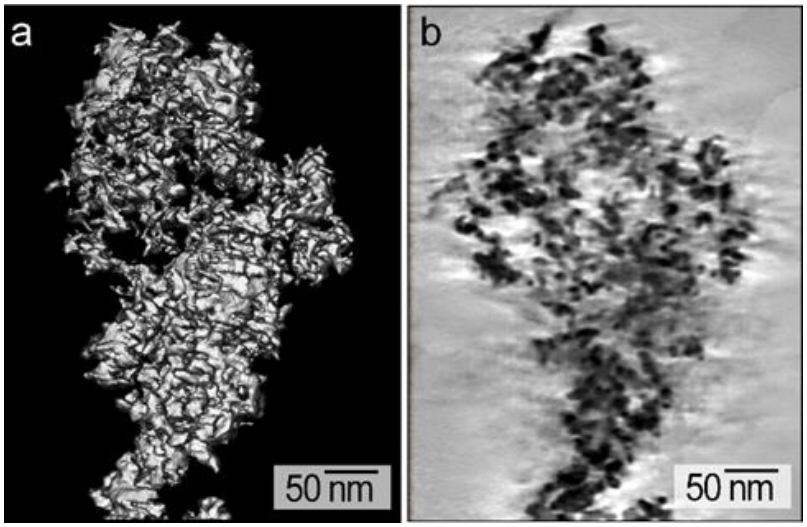


**Figure 7.5. Analysis of the mesoporous Pt obtained by tomographic TEM techniques: (a) a 3D rendered image obtained from a reconstruction of the tomography results; and (b) a reconstructed TEM orthoslice in the XY plane of the mesoporous Pt structure in (a).**

Theoretical studies suggest that cathode CLs containing a porosity of 40 to 50 % should exhibit ideal conditions for the mass transport of reagents and products as necessary to optimize the performance of PEMFCs.[266–268] This mesoporous Pt prepared by surfactant assisted electrodepositon was, therefore, a promising material to be incorporated into PEMFCs and evaluated for its overall performance.

### 7.5.2 Electrodeposition of Mesoporous Pt on a Layer of C particles and Ionomer

To create mesoporous Pt that can be easily incorporated into PEMFCs, the electrodeposition process was carried out on glassy carbon electrodes coated with a film of Vulcan XC-72 carbon particles and Nafion® DE2020 ionomer. Morphology of the electrodeposited Pt supported on the film of C and ionomer were confirmed by TEM analyses to retain their mesoporous structure (**Figure 7.6**).

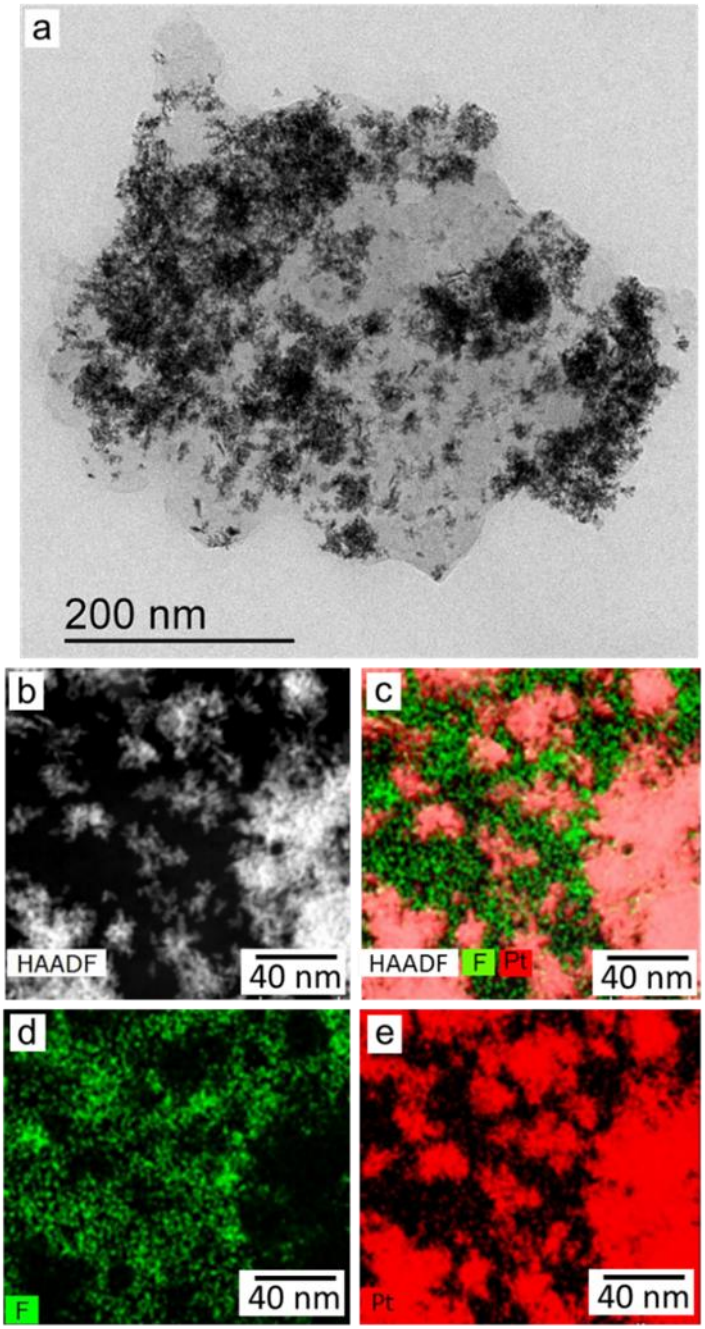


**Figure 7.6.** **Electron microscopy images of mesoporous Pt that was prepared by electrodeposition on a substrate of carbon and ionomer: (a) transmission electron microscopy (TEM) image of a section of the carbon and ionomer supported mesoporous Pt; (b) A HAADF image from a section of the sample in (a); (c) overlaid EDS elemental maps corresponding to F and Pt; (d) EDS elemental map for F; and (e) EDS elemental map for Pt corresponding to the sample in (b).**

To investigate the effects of altering the duration of the electrodeposition process on the resulting Pt morphologies, a series of different samples were prepared by electrodeposition of Pt for 30 s, 3 min, and 10 min (**Figure 7.7**). These C and ionomer supported Pt structures were analyzed for their ORR activity through a series of electrochemical studies to determine their potential use for enhancing the performance of PEMFCs.

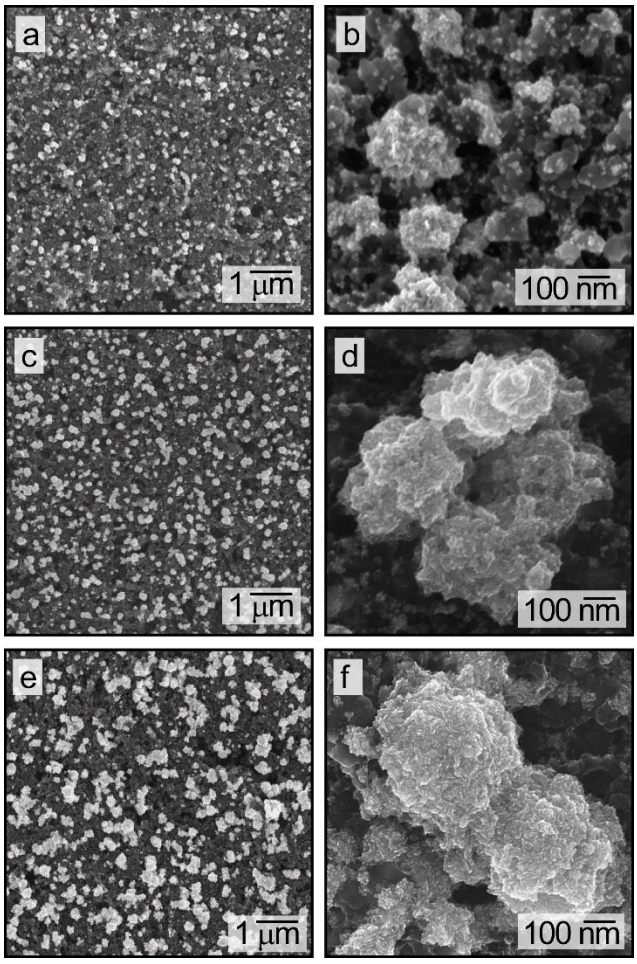


**Figure 7.7. A series of SEM images of mesoporous Pt prepared by electrodeposition onto films containing a mixture of carbon particles and ionomer. The mesoporous Pt were prepared by electrodeposition for: (a, b) 30 s; (c, d) 3 min; and (e, f) 10 min.**

### *7.5.3 Ex situ* Electrochemical Analyses of Electrodeposited Mesoporous Pt

The mesoporous Pt were assessed for the ORR by loading each of these glassy carbon supported layers into a rotating disc electrode setup. These substrates were used as the working electrode in a typical three electrode electrochemical system. The properties of each electrode for the ORR were compared to those of a commercially available catalyst prepared with a Pt NP loading of 0.2 $mg_{Pt}/cm^2$ and a CL thickness of ~10 µm. The CV profiles of the electrodeposited Pt had well defined peaks associated with the hydrogen desorption and adsorption processes on the Pt (111) and Pt (100) surfaces at ~0.1 and 0.3 V [versus a reversible hydrogen electrode (or RHE)], respectively.[159] These features in the CV profiles were more distinct for the mesoporous Pt than for the standard Pt NP based catalyst (**Figure 7.8**). [49,269]

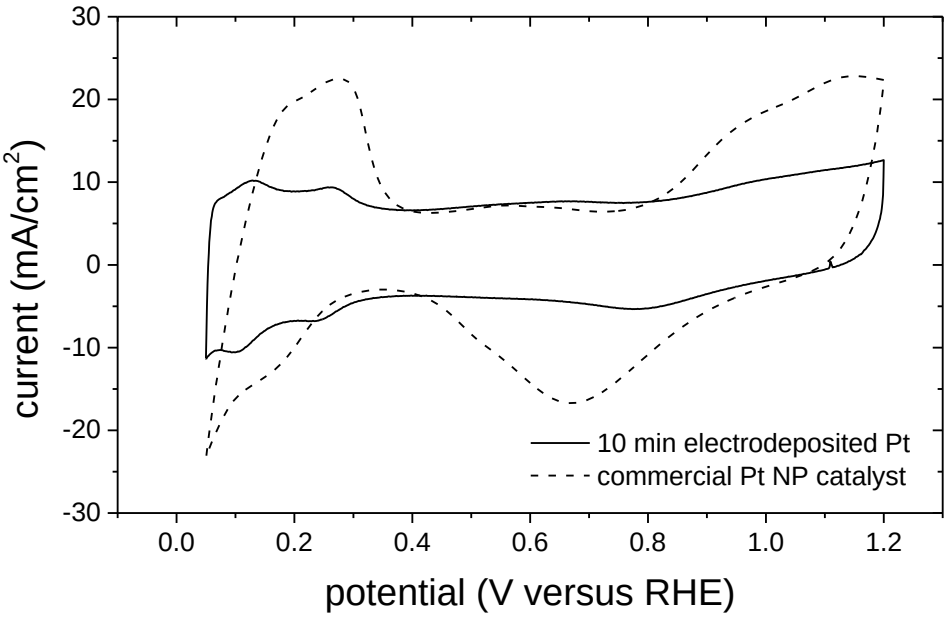


**Figure 7.8. The CV profiles for a film prepared from a standard commercial Pt NP based catalyst (containing a mixture of Pt nanoparticles, C particles, and ionomer), and for a sample of mesoporous Pt prepared by 10 min of electrodeposition on top of a film prepared from a mixture of carbon particles and ionomer. These samples were each analyzed in a degassed solution of 0.5 M $H_2SO_4$ at a scan rate of 100 mV/s.**

The CV results presented in **Figure 7.8** suggest that the surfaces of electrodeposited Pt were more exposed and had fewer adverse interactions with the non-Pt materials within the CLs. For example, the Pt surfaces can be covered by carbon NPs or ionomer that impede the transport of electrolyte to catalytic sites. After conditioning the electrodes with a series of CV scans, the electrolyte — initially purged with $N_2$ (g) — was saturated with $O_2$ (99.998 %) over a period of 20 min. The efficiency of each electrode for the ORR was determined through a series of LSV experiments. The ORR efficiencies of the mesoporous Pt prepared by electrodeposition for 30 s and 3 min exhibited at least a two-fold increase in mass activity in comparison to Pt NP based catalysts. These samples of mesoporous Pt maintained a higher activity at all electrode rotational speeds (**Figure 3.9**). The Pt prepared by electrodeposition for 10 min exhibited a lower efficiency than the standard catalyst prepared from a mixture of Pt NPs, C particles, and ionomer. This result indicated that the degree of mesoporosity can decrease with an extended period of electrodeposition, which decreases the ability of the electrolyte to infiltrate the porous Pt structure.

The electrodeposited Pt samples were also assessed for their electrochemical stability. A series of XRF measurements were obtained at the beginning of test (BOT) and end of test (EOT) time points (**Figure 7.9**). The series of electrochemical tests performed for each sample included 1,500 complete CV scans obtained at 100 mV/s, 9 LSV traces obtained at 1 mV/s for a series of different rotational speeds, and 5 complete CV scans obtained at 50 mV/s following each LSV measurement. These tests required at least 12 h to complete. Throughout this period, the electrode of interest was kept under an applied potential. The XRF measurements obtained at the BOT and the EOT indicated a decrease of Pt content by ~10 % (**Figure 7.9**), which may correspond to the dissolution of Pt or a growth in the dimensions of Pt particles that can increase shielding of the XRF detector from emitted X-ray signals.[270]

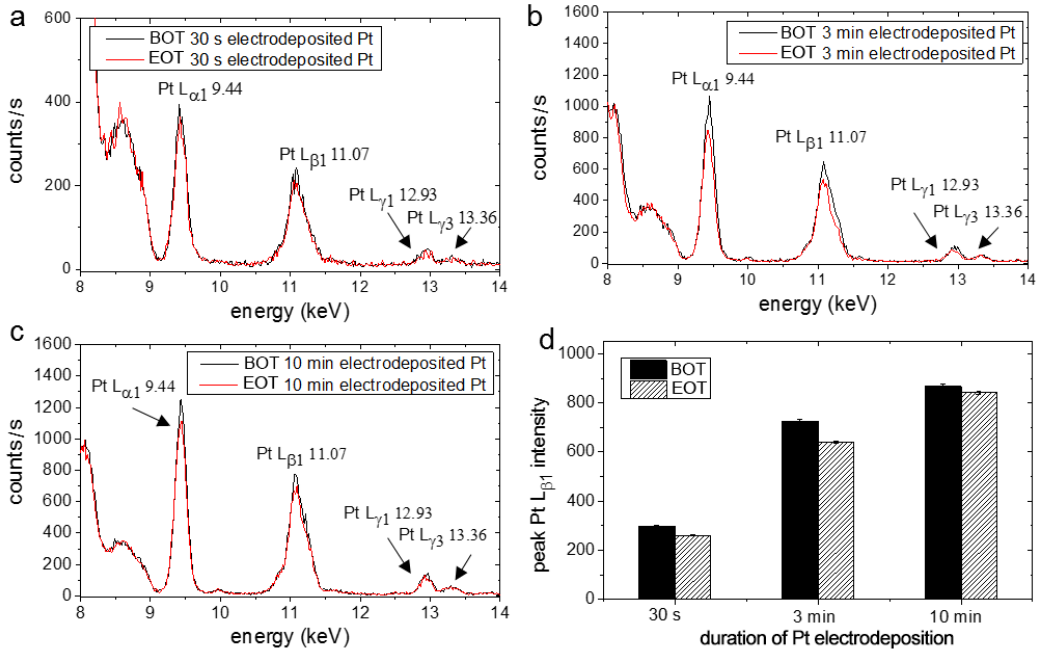


**Figure 7.9. Assessment of the durability of electrodeposited mesoporous Pt before and after electrochemical testing. (a-c) Results from the XRF spectroscopy analyses of the mesoporous Pt samples before and after the series of electrochemical tests performed for each sample over a period of at least 12 h. (d) The average peak Pt $L_{\beta1}$ intensity for each of the samples shown in (a-c) with error bars corresponding to one standard deviation from the mean values. Abbreviations: BOT: beginning of test; and EOT: end of test.**

Cross-sectional SEM analysis of the electrodeposited Pt was performed at the EOT for samples initially prepared by electrodeposition for 3 min (**Figures 7.10a**, **7.10b**). The electrodeposited Pt beneath the outermost surfaces of this sample at the EOT still retained relatively small particles of Pt with overall dimensions of ~100 nm. The TEM analysis of these mesoporous Pt at the EOT indicated that their porosity is retained after the electrochemical tests (**Figure 7.10c**).

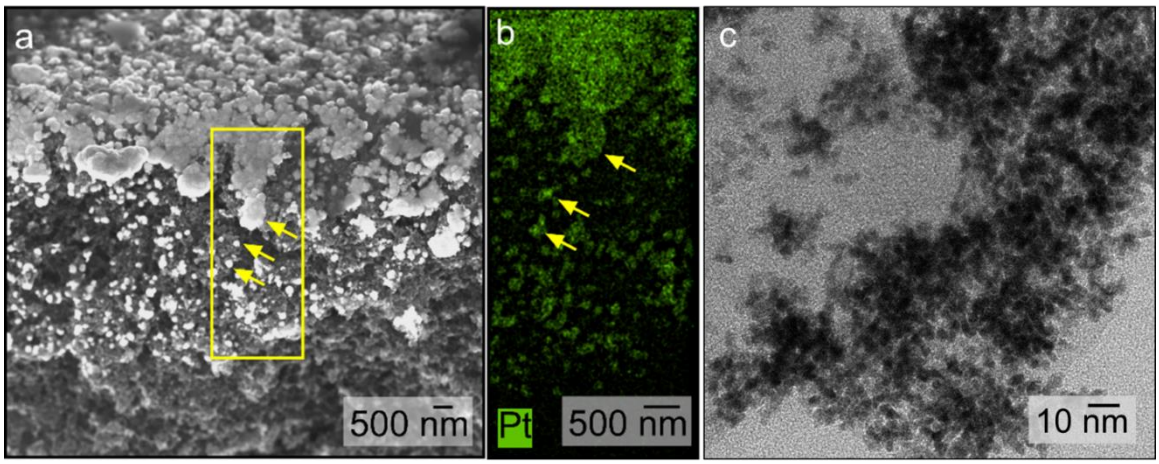


**Figure 7.10. Scanning electron microscopy image of (a) a cross-section obtained at the end of the electrochemistry experiments for mesoporous Pt supported on a layer of carbon particles and ionomer. (b) An EDS map corresponding to the region of interest outlined with a yellow box in (a) with arrows pointing to examples of corresponding features in the two images. (c) A TEM analysis for a sample of Pt, carbon particles, and ionomer obtained from the materials in (a). This TEM study confirmed the presence of the mesoporous Pt structure after the series of electrochemical tests.**

The electrochemically active surface area ($A_{ecsa}$) per gram of Pt was determined for each sample using CV profiles obtained at the EOT in combination with their Pt content as determined from ICP-MS analyses at the EOT. Mesoporous Pt samples prepared by electrodeposition for 30 s, 3 min, and 10 min had mass specific surface areas ($A_{ecsa}/g_{Pt}$) at the EOT of 32.9, 25.6, and 8.45 $m^2/g_{Pt}$. The TEM tomography analysis and 3D reconstruction for the 3 min sample also indicated that the surface area to weight ratio is about 22.8 $m^2/g_{Pt,}$ which is in good agreement to the electrochemical measurements. The Pt NP based CLs exhibited a mass specific surface area of 68.0 $m^2/g_{Pt}$, which is similar to the values reported in the literature.[179,268] It was previously determined that $A_{ecsa}/g_{Pt}$ would need to be ~40 $m^2/g_{Pt}$ for ultra-low loadings of Pt in the cathode CLs of PEMFCs to be commercially viable for automotive applications.[40] That assessment took into account the relatively high oxygen transport resistances that can arise from the interactions of the ionomer with the Pt NPs. Analyses by high resolution elemental mapping indicated that the C and ionomer supported mesoporous Pt exhibited distinct regions for the Pt and fluorine (i.e., ionomer) signals (**Figure 7.6**). The clear segregation of the Pt and F signals suggests that the mesoporous Pt were only deposited onto the exposed surfaces of the C

particles that were largely free of ionomer. Although the mesoporous Pt prepared by electrodeposition for 30 s and 3 min achieved only 60 to 80 % of the $A_{ecsa}/g_{Pt}$ target previously reported for ultra-low loadings of Pt in PEMFCs, the surfaces of the mesoporous Pt were largely free of ionomer. These mesoporous structures could, therefore, still be a viable catalyst for use in PEMFCs.

Samples prepared using 30 s and 3 min of electrodeposition in the presence of Triton X-100 exhibited the 1st and 2nd highest mass activities for the ORR, respectively, of the samples evaluated in this study. In contrast, the commercially available Pt NP catalyst had the highest mass specific $A_{ecsa}$, but had a lower mass activity towards the ORR than the mesoporous samples prepared using 30 s and 3 min of electrodeposition. These results suggest a higher Pt utilization for these mesoporous Pt samples than for the Pt NP based catalysts. It is likely that a portion of the Pt within the sample prepared from the Pt NPs is electrochemically inactive during the ORR.[179,256,265] Cross-sections at the EOT prepared from the mesoporous sample, originally created by the 3 min electrodeposition process, also indicated the presence of mesoporous Pt at depths of 3 to 5 µm into the film of C and ionomer (**Figure 7.10**). A gradient of Pt coverage was observed with the highest loading of Pt on the outermost surfaces of the C and ionomer, which would be in contact with the membrane when assembled into the membrane electrode assembly (MEA). In comparison, the reference catalysts contained a more uniform distribution of Pt NPs throughout the 10-µm thick CLs. This difference in Pt distribution can improve Pt utilization, proton conduction, and mass transport characteristics for the mesoporous catalysts.[36] For example, this CL design could enable a more efficient delivery of gaseous reactants to and removal of water produced at the Pt catalysts.[134] This non-uniform distribution of Pt could result in a better overall performance of the electrodeposited samples for the ORR, when compared to Pt NP based catalyst materials.

### 7.5.4 *In situ* Characterization of Mesoporous Pt in a PEMFC Test Station

Based on these initial electrochemical measurements, mesoporous Pt were prepared on films of C and ionomer by electrodeposition for 3 min and evaluated for their performance in PEMFCs. This electrodeposition time was selected in an attempt to

maximize the mass specific surface area of the mesoporous Pt samples, while also maintaining an overall Pt loading that is directly comparable to that used for the Pt NP-based catalysts.[16,40,271] Furthermore, the RDE analysis of the electrode indicated that the 3 min sample exhibited a 4 electron transfer ORR when compared to all other samples (2.0, 1.3, and 2.3 for the 10 min, 30 s, and reference samples). When compared to the 2 electron transfer ORR, the 4 electron transfer process can be less corrosive to the CCLs due to the reduced production of $H_2O_2$ within the CCLs.[51,102] This result suggests that the porosity and the distribution of Pt in the 3 min could be the most balanced among all prepared CCLs. Mesoporous samples were prepared using a custom built large area electrochemical cell (**Figure 7.1**). Films containing the mesoporous Pt were incorporated into MEAs as the cathode CLs by a process of decal transfer (**Figure 7.1**).

Membrane electrode assemblies containing the Pt NP- based catalysts were prepared as reference materials using two different Pt loadings (i.e., 0.2 and 0.4 $mg_{Pt}/cm^2$). The PEMFCs were prepared with a 5 $cm^2$ active surface area for each CL. The fuel cells were tested under standard operating conditions as outlined by the United States Department of Energy (US DOE).[109] At least two different MEAs were prepared and tested for each type of the CL (e.g., mesoporous Pt versus Pt NPs) evaluated in these measurements. The average polarization curve for the MEAs prepared with cathode CLs containing the mesoporous Pt exhibited at least a two-fold increase in Pt mass activity at 0.7 V (cell voltage) when compared to the MEAs containing cathode CLs prepared from Pt NP based catalysts (**Figure 7.11a**).

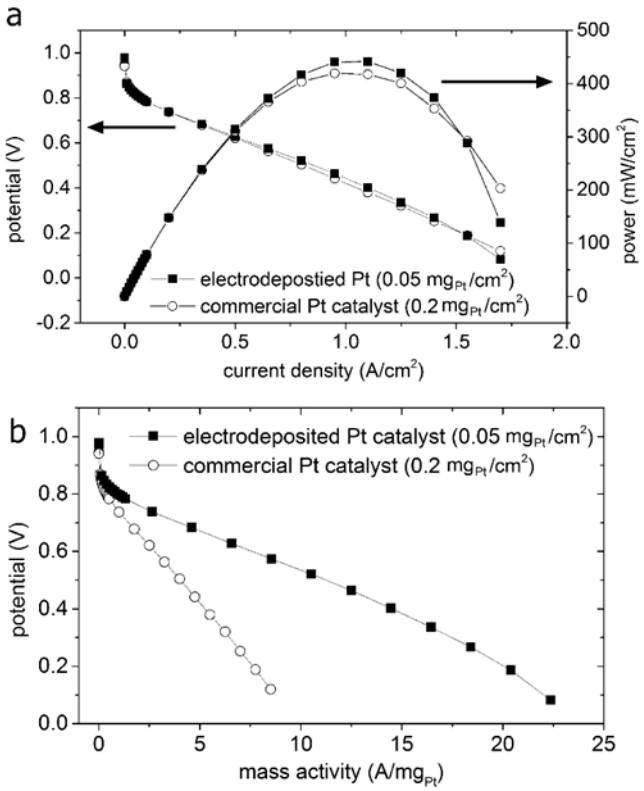


**Figure 7.11. Polarization profiles for proton exchange membrane fuel cells (PEMFCs) prepared with catalysts layers containing either the mesoporous Pt or commercially available Pt NPs. (a) Polarization profiles and power curves for the mesoporous Pt or Pt NPs in the cathode catalyst layers after normalization against the fuel cell active surface area. (b) The same polarization profiles in (a) after when normalization against the mass of Pt in each catalyst as determined by XRF.**

The mass activities observed for each of the MEAs containing the Pt NP-based catalysts were similar despite the two different Pt loadings (i.e., adjusted by tuning the CL thickness). These results suggest that any differences in the thickness of the cathode CLs between the various samples may not play a significant role in their observed fuel cell performance (**Figure 7.12a**). The calculated values of power per $mg_{Pt}$ were also similar for the Pt NP based catalysts prepared with Pt loadings of 0.4 and 0.2 mg/cm$^2$ (e.g., 0.36 $g_{Pt}$/kW and 0.43 $g_{Pt}$/kW, respectively) (**Figure 7.12b**). Without correcting for Pt mass activity, the ultra-low loading CLs containing the mesoporous Pt (0.05 $mg_{Pt}/cm^2$) demonstrated a similar PEMFC performance when compared to the Pt NP based catalysts prepared with a Pt loading of 0.2 $mg_{Pt}/cm^2$ (**Figure 7.11b**).

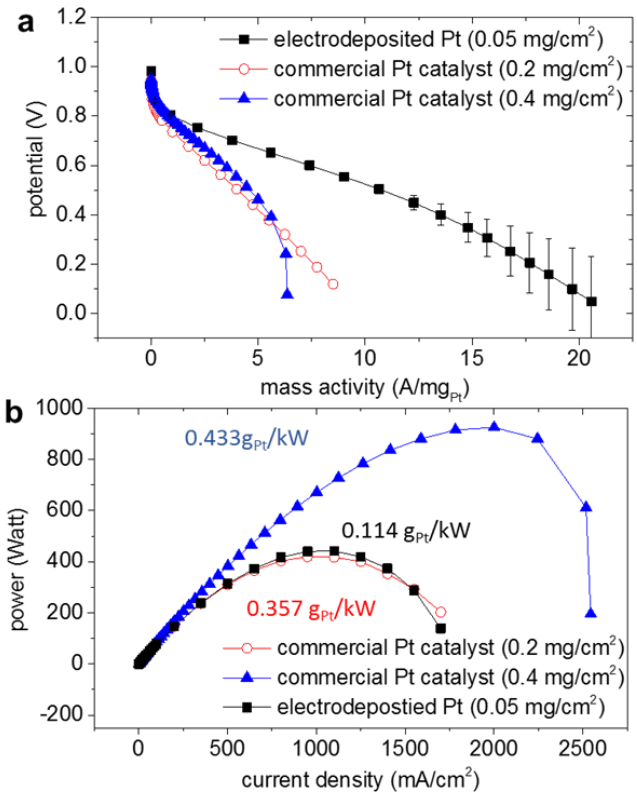


**Figure 7.12. The PEMFC performance using cathodes prepared from the electrodeposited mesoporous Pt in comparison to cathodes prepared from standard Pt nanoparticle based catalysts. (a) Average PEMFC polarization curves plotted as a function of Pt mass activity for the mesoporous Pt (n = 3 samples) and standard commercial catalysts prepared at two different Pt loadings. The respective Pt loadings are included in the legend. (b) Power curves plotted as a function of current density (current versus MEA geometric surface area) for cathodes prepared with mesoporous Pt or commercial Pt nanoparticle based catalysts. The Pt nanoparticle based catalysts were prepared with loadings of 0.4 mg$_{Pt}$/cm$^2$ or 0.2 mg$_{Pt}$/cm$^2$ as noted in the legend.**

The MEAs containing mesoporous Pt had an average mass specific power that was at least a 3 times improvement (0.11 g$_{Pt}$/kW) over the PEMFCs containing only CLs prepared from commercial Pt NPs. The mesoporous Pt catalyst exceeds the US DOE target for 2020 of 0.125 g$_{Pt}$/kW.[247] These results collectively demonstrate that mesoporous Pt created by electrodeposition onto a film of C and ionomer can be directly incorporated into PEMFCs as cathode CLs, and can exhibit higher Pt mass specific activities and powers than observed for Pt NP based catalysts.

## 7.6 Conclusion

In conclusion, it was demonstrated that mesoporous Pt can be created by a one-step electrochemical process under constant current conditions with the addition of appropriate surfactants into the electroplating solution. Evaluation of these mesoporous Pt structures as cathode catalysts in PEMFCs demonstrated that these materials had at least a 3 times higher mass specific activity than for Pt NP based catalysts. The results demonstrated that direct electrodeposition of Pt onto C and ionomer, followed by decal transfer to prepare MEAs can provide a superior method for preparing electrocatalysts and improving Pt utilization than powder processing methods. Future analyses of the mesoporous Pt for PEMFCs will include an evaluation of their impact on ionic and oxygen mass transport, stability to extensive corrosion cycles, and incorporation into larger area MEAs (>40 $cm^2$) to further verify the suitability of these materials and methods to prepare cathode catalysts for PEMFCs. The results of these initial studies suggest that the electrochemical deposition of electrocatalysts warrants a further investigation by the fuel cell industry as a method to increase Pt utilization and to reduce system costs. The preparation of mesoporous Pt materials could also be applied to other electrochemical systems, such direct methanol and metal-air fuel cells.

# Chapter 8.

# Summary and Outlook

In this thesis, we demonstrated methods for tuning the morphologies of fuel cell catalysts and catalyst interfaces for improving the performances of PEMFC systems. The future investigations, with respect to the techniques presented in each chapter, were discussed at the end of each chapter. In summary:

In Chapter 4, the performances of CCLs with cylindrical patterns were investigated. A limitation of this study is the high $R_{short}$ that could arise from the GDL penetrating the non-CL covered PEM surfaces. A planarization (low to no Pt content) could be applied on top of the patterns to potentially mitigate this penetration of GDL into the PEM. Furthermore, different catalyst patterns (i.e., line structures that are parallel or perpendicular to the gas flow-field) should be investigated.

In Chapter 5, the performances of PEMFCs were improved with the use of a microstructured PEM. The improvements of these microstructured PEM were attributed to an increase in the interface between the PEM and the CCL. Future investigations should employ methods, such as hot-extrusion to produce PEMs with high aspect ratio features or even nanowire type morphologies, to further increase the CCL to PEM interfacial areas for further improving the performance of the PEMFCs.

Chapter 6 presented a range of methods for preparing nanostructured catalyst materials. Future investigations could be focused on preparing these materials in larger quantities, incorporating them into MEAs, and analyzing these MEAs with a PEMFC testing station.

Chapter 7 described electrodeposition as an improved method for preparing PEMFC CCLs with significantly enhanced Pt mass activities. A follow-up study should be performed to prepare these CCLs over larger areas (i.e., 40 $cm^2$) and analyzed for their long-term stability (i.e., the retention of the mesoporous structure). Electrodeposition is known to be a relatively simple method for preparing a range of materials with different

elemental compositions by simply adjusting the relative concentrations of the reagents in the electrodeposition solution. Catalysts with different compositions other than Pt, while maintaining similar activity of the ORR and stability within PEMFC, could also be investigated to further reduce the Pt content within these CCLs.

In this thesis we observed that a microstructured CCL can improve water management of the PEMFC, while electrodeposition was identified as an improved method in comparison to powder processed CCLs. A new CCL design is proposed to combine all of the learning outcomes from this thesis (**Figure 8.1**).

Mesoporous Pt can be electrodeposited onto the microstructured CL with a target loading of 0.05 $mg_{Pt}/cm^2$. This loading was determined with the highest mass activity and optimized conditions for electrodeposition. The electrodeposited Pt can greatly enhance the mass activity in comparison to a powder processed Pt catalyst.

The supporting microstructured CCL can contain a mix of Pt NPs and C particles that is to be prepared by an optimized µTM method. The microstructured CL was shown to improve water removal by creating offsets in catalyst loadings. The CCL pattern can be prepared with a feature size between 20 to 50 µm as identified in the literature as the relevant range of dimensions for water management.[8] The catalyst loading of this layer should be kept to a minimum, for example, 0.1 $mg_{Pt}/cm^2$ to achieve a total Pt loading of 0.15 $mg_{Pt}/cm^2$. This catalyst loading is a good target as indicated in the US DOE 2007 report (for 2020).[35]

A planarizing layer with only C particle and ionomer can be used to fill in the top of the prepared CL microstructure. This layer can prevent the GDL from contacting the PEM. The elimination of contact between the GDL PEM can reduce the short-circuit current of the fuel cell. The porosity of this planarizing layer can be tuned for optimizing the water management of the fuel cell. A starting point of >1 µm pore dimensions should be investigated for the planarizing layer as suggested by the literature.[47] The inverse opaline materials demonstrated in Chapter 5 may also be used for introducing metal oxide materials with defined porosities into this planarizing layer.

As demonstrated herein, the combination of techniques demonstrated in this thesis allows a creative approach of creating alternate CCL designs. These designs enable a range of tunability over conventionally prepared CCLs in terms of the micro- and nanostructure of the catalyst, finely controlled layer porosity, and composition of the materials therein. The established CCL design with improved mass activity and water management can further improve PEMFC technologies to become a primary renewable energy system as an alternative to petroleum-based systems.

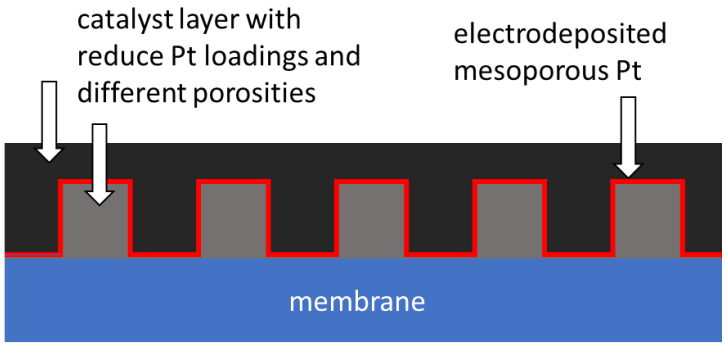


**Figure 8.1** **Illustration of a proposed CCL design that combines all of the improvements demonstrated in this thesis. The designer CCL consists of microstructured catalyst support, electrodeposited mesoporous Pt, and a planarizing over layer. The microstructured catalyst support and the planarizing layer can consist of Pt nanoparticles, C particles, and ionomer at different Pt loading densities with different porosities to optimize the performance of the PEMFC.**

# References


(1) Pellow, M. A.; Emmott, C. J. M.; Barnhart, C. J.; Benson, S. M. Hydrogen or Batteries for Grid Storage? A Net Energy Analysis. *Energy Environ. Sci.* **2015**, *8* (7), 1938–1952.

(2) Kousksou, T.; Bruel, P.; Jamil, A.; El Rhafiki, T.; Zeraouli, Y. Energy Storage: Applications and Challenges. *Solar Energy Materials and Solar Cells*. **2014**, pp 59–80.

(3) Chen, H.; Cong, T. N.; Yang, W.; Tan, C.; Li, Y.; Ding, Y. Progress in Electrical Energy Storage System: A Critical Review. *Prog. Nat. Sci.* **2009**, *19* (3), 291–312.

(4) Barbir, F. PEM Electrolysis for Production of Hydrogen from Renewable Energy Sources. *Sol. Energy* **2005**, *78* (5), 661–669.

(5) Lee, H. F.; Huang, Y. C.; Wang, P. H.; Lee, C. C.; Hung, Y. S.; Gopal, R.; Holdcroft, S.; Huang, W. Y. Synthesis of Highly Sulfonated Polyarylene Ethers Containing Alternating Aromatic Units. *Mater. Today Commun.* **2015**, *3*, 114–121.

(6) Zhang, J.; Gasteiger, H. A.; Gu, W. Electrochemical Measurement of the Oxygen Permeation Rate. **2013**, *160* (6), 616–622.

(7) Sui, S.; Wang, X.; Zhou, X.; Su, Y.; Riffat, S.; Liu, C. A Comprehensive Review of Pt Electrocatalysts for the Oxygen Reduction Reaction: Nanostructure, Activity, Mechanism and Carbon Support in PEM Fuel Cells. *J. Mater. Chem. A* **2017**, *5* (5), 1808–1825.

(8) Karst, N.; Faucheux, V.; Martinent, A.; Bouillon, P.; Simonato, J. P. Improvement of Water Management in Polymer Electrolyte Membrane Fuel Cell Thanks to Cathode Cracks. *J. Power Sources* **2010**, *195* (16), 5228–5234.

(9) Das, P. K. Transport Phenomena in Cathode Catalyst Layer of PEM Fuel Cells, PhD thesis in MEchanical Engineering presented to the University of Waterloo, **2010**, 224.

(10) Holton, O. T.; Stevenson, J. W. The Role of Platinum in Proton Exchange Membrane Fuel Cells. *Platin. Met. Rev.* **2013**, *57* (4), 259–271.

(11) Bard, a; Faulkner, L. Allen J. Bard and Larry R. Faulkner, Electrochemical Methods: Fundamentals and Applications, New York: Wiley, 2001. *Russ. J. Electrochem.* **2002**, *38* (12), 1505–1506.

(12) Song, C.; Zhang, J. Electrocatalytic Oxygen Reduction Reaction. *PEM Fuel Cell Electrocatal. Catal. Layers* **2008**, 89–134.

(13) Genorio, B.; Strmcnik, D.; Subbaraman, R.; Tripkovic, D.; Karapetrov, G.; Stamenkovic, V. R.; Pejovnik, S.; Marković, N. M. Selective Catalysts for the Hydrogen Oxidation and Oxygen Reduction Reactions by Patterning of Platinum with calix[4]arene Molecules. *Nat. Mater.* **2010**, *9* (12), 998–1003.

(14) Strmcnik, D.; Tripkovic, D.; van der Vliet, D.; Stamenkovic, V.; Marković, N. M. Adsorption of Hydrogen on Pt(1 1 1) and Pt(1 0 0) Surfaces and Its Role in the HOR. *Electrochem. commun.* **2008**, *10* (10), 1602–1605.

(15) Holton, O. T.; Stevenson, J. W. The Role of Platinum in Proton Exchange Membrane Fuel Cells. *Platinum Metals Review*. **2013**, pp 259–271.

(16) Owejan, J. P.; Owejan, J. E.; Gu, W. Impact of Platinum Loading and Catalyst Layer Structure on PEMFC Performance. *J. Electrochem. Soc.* **2013**, *160* (8), F824–F833.

(17) Malczewski, R. M.; Jahn, D. A.; Schoenherr, W. J. Peroxide or Platinum ? Cure System Considerations for Silicone Tubing Applications. *Dow Corning* **2003**, 5.

(18) Steele, B. C.; Heinzel, A. Materials for Fuel-Cell Technologies. *Nature* **2001**, *414* (November), 345–352.

(19) Ball, M.; Weeda, M. The Hydrogen Economy - Vision or Reality? *Int. J. Hydrogen Energy* **2015**, *40* (25), 7903–7919.

(20) Liu, Y.-L. Developments of Highly Proton-Conductive Sulfonated Polymers for Proton Exchange Membrane Fuel Cells. *Polym. Chem.* **2012**, *3* (6), 1373.

(21) Afsahi, F.; Mathieu-Potvin, F.; Kaliaguine, S. Impact of Ionomer Content on Proton Exchange Membrane Fuel Cell Performance. *Fuel Cells* **2016**, *16* (1), 107–125.

(22) He, Q.; Suraweera, N. S.; Joy, D. C.; Keffer, D. J. Structure of the Ionomer Film in Catalyst Layers of Proton Exchange Membrane Fuel Cells. *J. Phys. Chem. C* **2013**, *117* (48), 25305–25316.

(23) Novitski, D.; Holdcroft, S. Determination of O2 Mass Transport at the Pt | PFSA Ionomer Interface under Reduced Relative Humidity. *ACS Appl. Mater. Interfaces* **2015**, *7* (49), 27314–27323.

(24) Suzuki, A.; Sen, U.; Hattori, T.; Miura, R.; Nagumo, R.; Tsuboi, H.; Hatakeyama, N.; Endou, A.; Takaba, H.; Williams, M. C.; Miyamoto, A. Ionomer Content in the Catalyst Layer of Polymer Electrolyte Membrane Fuel Cell (PEMFC): Effects on Diffusion and Performance. *Int. J. Hydrogen Energy* **2011**, *36* (3), 2221–2229.

(25) Williams, M. V.; Begg, E.; Bonville, L.; Kunz, H. R.; Fenton, J. M. Characterization of Gas Diffusion Layers for PEMFC. *J. Electrochem. Soc.* **2004**, *151* (8), A1173.

(26) Aiyejina, A.; Sastry, M. K. S. PEMFC Flow Channel Geometry Optimization: A Review. *J. Fuel Cell Sci. Technol.* **2012**, *9* (1), 11011.

(27) Stern, S. A.; Trohalaki, S. Fundamentals of Gas Diffusion in Rubbery and Glassy Polymers. *Symp. A Q. J. Mod. Foreign Lit.* **1990**, *2* (2), 22–59.

(28) Spiegel, C. Modeling the Gas Diffusion Layers. *PEM Fuel Cell Model. Simul. Using Matlab* **2008**, 197–241.

(29) Park, C. H.; Lee, C. H.; Guiver, M. D.; Lee, Y. M. Sulfonated Hydrocarbon Membranes for Medium-Temperature and Low-Humidity Proton Exchange Membrane Fuel Cells (PEMFCs). *Progress in Polymer Science (Oxford)*. **2011**, pp 1443–1498.

(30) Soboleva, T.; Malek, K.; Xie, Z.; Navessin, T.; Holdcroft, S. PEMFC Catalyst Layers: The Role of Micropores and Mesopores on Water Sorption and Fuel Cell Activity. *ACS Appl. Mater. Interfaces* **2011**, *3* (6), 1827–1837.

(31) Eikerling, M. H.; Kourosh, M.; Wang, Q. *PEM Fuel Cell Electrocatalysts and Catalyst Layers: Fundamentals and Applications*; Springer, **2008**.

(32) Song, D.; Wang, Q.; Liu, Z.; Navessin, T.; Eikerling, M.; Holdcroft, S. Numerical Optimization Study of the Catalyst Layer of PEM Fuel Cell Cathode. *J. Power Sources* **2004**, *126* (1–2), 104–111.

(33) Yim, S. D.; Sohn, Y. J.; Park, S. H.; Yoon, Y. G.; Park, G. G.; Yang, T. H.; Kim, C. S. Fabrication of Microstructure Controlled Cathode Catalyst Layers and Their Effect on Water Management in Polymer Electrolyte Fuel Cells. *Electrochim. Acta* **2011**, *56* (25), 9064–9073.

(34) Xie, Z.; Song, C.; Wilkinson, D. P.; Zhang, J. Catalyst Layers and Fabrication. *Prot. Exch. Membr. Fuel Cells* **2010**, 61–105.

(35) Zlotorowicz, A.; Jayasayee, K.; Dahl, P. I.; Thomassen, M. S.; Kjelstrup, S. Tailored Porosities of the Cathode Layer for Improved Polymer Electrolyte Fuel Cell Performance. *J. Power Sources* **2015**, *287*, 472–477.

(36) Ye, L.; Gao, Y.; Zhu, S.; Zheng, J.; Li, P.; Zheng, J. P. A Pt Content and Pore Structure Gradient Distributed

Catalyst Layer to Improve the PEMFC Performance. *Int. J. Hydrogen Energy* **2017**, *42* (10), 7241–7245.

(37) Mezzavilla, S.; Cherevko, S.; Baldizzone, C.; Pizzutilo, E.; Polymeros, G.; Mayrhofer, K. J. J. Experimental Methodologies to Understand Degradation of Nanostructured Electrocatalysts for PEM Fuel Cells: Advances and Opportunities. *ChemElectroChem*. **2016**, 3 (10), 1524–1536.

(38) Srouji, A. K.; Zheng, L. J.; Dross, R.; Aaron, D.; Mench, M. M. The Role of Water Management on the Oxygen Transport Resistance in Polymer Electrolyte Fuel Cell with Ultra-Low Precious Metal Loading. *J. Power Sources* **2017**, *364*, 92–100.

(39) Garland, N.; Benjamin, T.; Kopasz, J. DOE Fuel Cell Program: Durability Technical Targets and Testing Protocols. In *ECS Transactions*; **2007**; 11, pp 923–931.

(40) Kongkanand, A.; Mathias, M. F. The Priority and Challenge of High-Power Performance of Low-Platinum Proton-Exchange Membrane Fuel Cells. *Journal of Physical Chemistry Letters*. **2016**, 7, 1127–1137.

(41) Wilson, M. S. High Performance Catalyzed Membranes of Ultra-Low Pt Loadings for Polymer Electrolyte Fuel Cells. *J. Electrochem. Soc.* **1992**, *139* (2), L28.

(42) Becker, W. L.; Braun, R. J.; Penev, M.; Melaina, M. Design and Technoeconomic Performance Analysis of a 1 MW Solid Oxide Fuel Cell Polygeneration System for Combined Production of Heat, Hydrogen, and Power. *J. Power Sources* **2012**, *200*, 34–44.

(43) Srinivasan, S.; Ticianelli, E. a.; Derouin, C. R.; Redondo, a. Advances in Solid Polymer Electrolyte Fuel Cell Technology with Low Platinum Loading Electrodes. *J. Power Sources* **1988**, *22*, 359–375.

(44) Cho, M. K.; Park, H.-Y.; Lee, S. Y.; Lee, B.-S.; Kim, H.-J.; Henkensmeier, D.; Yoo, S. J.; Kim, J. Y.; Han, J.; Park, H. S.; Sung, Y.-E.; Jang, J. H. Effect of Catalyst Layer Ionomer Content on Performance of Intermediate Temperature Proton Exchange Membrane Fuel Cells (IT-PEMFCs) under Reduced Humidity Conditions. *Electrochim. Acta* **2017**, *224*, 228–234.

(45) Shao, Y.; Yin, G.; Zhang, J.; Gao, Y. Comparative Investigation of the Resistance to Electrochemical Oxidation of Carbon Black and Carbon Nanotubes in Aqueous Sulfuric Acid Solution. *Electrochim. Acta* **2006**, *51* (26), 5853–5857.

(46) Park, S.; Shao, Y.; Wan, H.; Rieke, P. C.; Viswanathan, V. V.; Towne, S. A.; Saraf, L. V.; Liu, J.; Lin, Y.; Wang, Y. Design of Graphene Sheets-Supported Pt Catalyst Layer in PEM Fuel Cells. *Electrochem. commun.* **2011**, *13* (3), 258–261.

(47) Marquis, J.; Coppens, M. O. Achieving Ultra-High Platinum Utilization via Optimization of PEM Fuel Cell Cathode Catalyst Layer Microstructure. *Chem. Eng. Sci.* **2013**, *102*, 151–162.

(48) Saha, M. S.; Paul, D. K.; Peppley, B. A.; Karan, K. Fabrication of Catalyst-Coated Membrane by Modified Decal Transfer Technique. *Electrochem. commun.* **2010**, *12* (3), 410–413.

(49) Kinkead, B.; van Drunen, J.; Paul, M. T. Y.; Dowling, K.; Jerkiewicz, G.; Gates, B. D. Platinum Ordered Porous Electrodes: Developing a Platform for Fundamental Electrochemical Characterization. *Electrocatalysis* **2013**, *4* (3), 179–186.

(50) Jang, J. H.; Jeon, S.; Cho, J. H.; Kim, S.-K.; Lee, S.-Y.; Cho, E.; Kim, H.-J.; Han, J.; Lim, T.-H. Complex Capacitance Analysis of Ionic Resistance and Interfacial Capacitance in PEMFC and DMFC Catalyst Layers. *J. Electrochem. Soc.* **2009**, *156* (11), B1293.

(51) Gottesfeld, S. Oxygen Reduction Kinetics on a Platinum RDE Coated with a Recast Nafion Film. *J. Electrochem. Soc.* **1987**, *134* (6), 1455.

(52) Roen, L. M.; Paik, C. H.; Jarvi, T. D. Electrocatalytic Corrosion of Carbon Support in PEMFC Cathodes.

*Electrochem. Solid-State Lett.* **2004**, *7* (1), A19.

(53) Young, A. P.; Stumper, J.; Gyenge, E. Characterizing the Structural Degradation in a PEMFC Cathode Catalyst Layer: Carbon Corrosion. *J. Electrochem. Soc.* **2009**, *156* (8), B913.

(54) Sasaki, K.; Zhang, L.; Adzic, R. R. Niobium Oxide-Supported Platinum Ultra-Low Amount Electrocatalysts for Oxygen Reduction. *Phys. Chem. Chem. Phys.* **2008**, *10* (1), 159–167.

(55) Song, Z.; Wang, B.; Cheng, N.; Yang, L.; Banham, D.; Li, R.; Ye, S.; Sun, X. Atomic Layer Deposited Tantalum Oxide to Anchor Pt/C for a Highly Stable Catalyst in PEMFCs. *J. Mater. Chem. A* **2017**, *5* (20), 9760–9767.

(56) Meier, J. C.; Katsounaros, I.; Galeano, C.; Bongard, H. J.; Topalov, A. A.; Kostka, A.; Karschin, A.; Schüth, F.; Mayrhofer, K. J. J. Stability Investigations of Electrocatalysts on the Nanoscale. *Energy Environ. Sci.* **2012**, *5* (11), 9319.

(57) Lewera, A.; Timperman, L.; Roguska, A.; Alonso-Vante, N. Metal–Support Interactions between Nanosized Pt and Metal Oxides (WO3 and TiO2) Studied Using X-Ray Photoelectron Spectroscopy. *J. Phys. Chem. C* **2011**, *115* (41), 20153–20159.

(58) Song, Z.; Wang, B.; Cheng, N.; Yang, L.; Banham, D.; Li, R.; Ye, S.; Sun, X. Atomic Layer Deposited Tantalum Oxide to Anchor Pt/C for a Highly Stable Catalyst in PEMFCs. *J. Mater. Chem. A* **2017**, *5* (20), 9760–9767.

(59) Kim, O.-H.; Cho, Y.-H.; Kang, S. H.; Park, H.-Y.; Kim, M.; Lim, J. W.; Chung, D. Y.; Lee, M. J.; Choe, H.; Sung, Y.-E. Ordered Macroporous Platinum Electrode and Enhanced Mass Transfer in Fuel Cells Using Inverse Opal Structure. *Nat. Commun.* **2013**, *4*, 2473.

(60) Tajabadi, M. T.; Sookhakian, M.; Zalnezhad, E.; Yoon, G. H.; Hamouda, A. M. S.; Azarang, M.; Basirun, W. J.; Alias, Y. Electrodeposition of Flower-like Platinum on Electrophoretically Grown Nitrogen-Doped Graphene as a Highly Sensitive Electrochemical Non-Enzymatic Biosensor for Hydrogen Peroxide Detection. *Appl. Surf. Sci.* **2016**, *386*, 418–426.

(61) Saibuathong, N.; Saejeng, Y.; Pruksathorn, K.; Hunsom, M.; Tantavichet, N. Catalyst Electrode Preparation for PEM Fuel Cells by Electrodeposition. In *Journal of Applied Electrochemistry*; 2010; 40, 903–910.

(62) Fofana, D.; Natarajan, S. K.; Hamelin, J.; Benard, P. Low Platinum, High Limiting Current Density of the PEMFC (Proton Exchange Membrane Fuel Cell) Based on Multilayer Cathode Catalyst Approach. *Energy* **2014**, *64*, 398–403.

(63) Debe, M. K. Electrocatalyst Approaches and Challenges for Automotive Fuel Cells. *Nature* **2012**, *486* (7401), 43–51.

(64) Lorenz, H.; Laudon, M.; Renaud, P. Mechanical Characterization of a New High-Aspect-Ratio near UV-Photoresist. *Microelectron. Eng.* **1998**, *41(42)*, 371–374.

(65) Kowalczyk, K.; Spychaj, T.; Krala, G. High-Build Alkyd Urethane Coating Materials with a Partially Solvolyzed Waste Polyurethane Foam. *Polym. Eng. Sci.* **2015**, *55* (9), 2174–2183.

(66) Dektar, J. L.; Hacker, N. P. Photochemistry of Triarylsulfonium Salts. *J. Am. Chem. Soc.* **1990**, *112* (16), 6004–6015.

(67) Chang H., Kim Y.: UV-LIGA for high aspect ratio structure using stress barrier and C-shaped etch hole. *Sensors and Actuators*, **2000**, 84, 342-350.

(68) LaBianca, N.; Delorme, J. High Aspect Ratio Resist for Thick Film Applications. *Proc. SPIE* **1995**, *2438*, 846–852.

(69) Shaw, J. M.; Gelorme, J. D.; LaBianca, N. C.; Conley, W. E.; Holmes, S. J. Negative Photoresists for Optical Lithography. *IBM J. Res. Dev.* **1997**, *41* (1.2), 81–94.

(70) Stafie, N.; Stamatialis, D. F.; Wessling, M. Effect of PDMS Cross-Linking Degree on the Permeation Performance of PAN/PDMS Composite Nanofiltration Membranes. *Sep. Purif. Technol.* **2005**, *45* (3), 220–231.

(71) Oulad Hammouch, S.; Beinert, G. J.; Herz, J. E. Contribution to a Better Knowledge of the Crosslinking Reaction of Polydimethylsiloxane (PDMS) by End-Linking: The Formation of Star-Branched PDMS by the Hydrosilylation Reaction. *Polymer (Guildf).* **1996**, *37* (15), 3353–3360.

(72) Johnston, I. D.; McCluskey, D. K.; Tan, C. K. L.; Tracey, M. C. Mechanical Characterization of Bulk Sylgard 184 for Microfluidics and Microengineering. *J. Micromechanics Microengineering* **2014**, *24* (3), 35017.

(73) Childs, W. R.; Nuzzo, R. G. Decal Transfer Microlithography: A New Soft-Lithographic Patterning Method. *J. Am. Chem. Soc.* **2002**, *124* (45), 13583–13596.

(74) Alam, A. U.; Howlader, M. M. R.; Deen, M. J. The Effects of Oxygen Plasma and Humidity on Surface Roughness, Water Contact Angle and Hardness of Silicon, Silicon Dioxide and Glass. *J. Micromechanics Microengineering* **2014**, *24* (3).

(75) Tan, S. H.; Nguyen, N. T.; Chua, Y. C.; Kang, T. G. Oxygen Plasma Treatment for Reducing Hydrophobicity of a Sealed Polydimethylsiloxane Microchannel. *Biomicrofluidics* **2010**, *4* (3).

(76) Sakurai, A.; Saito, A.; Habuka, H. Surface and Gas Phase Reactions Induced in a trichlorosilane–SiHx System for Silicon Film Deposition. *Surf. Coatings Technol.* **2015**, *272*, 273–277.

(77) Qian, W.; Zhaoqun, W.; Xuanfeng, K.; Xiaodan, G.; Gi, X. A Facile Strategy for Controlling the Self-Assembly of Nanocomposite Particles Based on Colloidal Steric Stabilization Theory. *Langmuir* **2008**, *24* (15), 7778–7784.

(78) Lee, J. M.; Jun, Y. D.; Kim, D. W.; Lee, Y. H.; Oh, S. G. Effects of PVP on the Formation of Silver-Polystyrene Heterogeneous Nanocomposite Particles in Novel Preparation Route Involving Polyol Process: Molecular Weight and Concentration of PVP. *Mater. Chem. Phys.* **2009**, *114* (2–3), 549–555.

(79) Gasteiger, H. A.; Marković, N. M. Just a Dream—or Future Reality? *Science (80-. ).* **2009**, *324* (5923), 48–49.

(80) Zhang, J. *PEM Fuel Cell Electrocatalysts and Catalyst Layers: Fundamentals and Applications*, Springer-Verlag London, **2008**.

(81) Jinnouchi, R. New Insight into Microscale Transport Phenomena in Pefc by Quantum Md. *Microscale Thermophys. Eng.* **2003**, *7* (1), 15–31.

(82) Nørskov, J. K.; Rossmeisl, J.; Logadottir, A.; Lindqvist, L.; Kitchin, J. R.; Bligaard, T.; Jónsson, H. Origin of the Overpotential for Oxygen Reduction at a Fuel-Cell Cathode. *J. Phys. Chem. B* **2004**, *108* (46), 17886–17892.

(83) Borup, R.; Meyers, J.; Pivovar, B.; Kim, Y. S.; Mukundan, R.; Garland, N.; Myers, D.; Wilson, M.; Garzon, F.; Wood, D.; Zelenay, P.; More, K.; Stroh, K.; Zawodzinski, T.; Boncella, J.; McGrath, J. E.; Inaba, M.; Miyatake, K.; Hori, M.; Ota, K.; Ogumi, Z.; Miyata, S.; Nishikata, A.; Siroma, Z.; Uchimoto, Y.; Yasuda, K.; Kimijima, K. I.; Iwashita, N. Scientific Aspects of Polymer Electrolyte Fuel Cell Durability and Degradation. *Chemical Reviews*. **2007**, 3904–3951.

(84) Williams, D. B.; Carter, C. B. *Transmission Electron Microscopy: A Textbook for Materials Science*, Springer-Verlag US, **2009**; 1–4.

(85) Wilkinson, A. J.; Hirsch, P. B. Electron Diffraction Based Techniques in Scanning Electron Microscopy of Bulk Materials. *Micron* **1997**, *28* (4), 279–308.

(86) Egerton, R. F. *Physical Principles of Electron Microscopy*, Springer-Verlag US, **2005**; 8.

(87) Amelinckx, S.; Van Dyck, D.; Van Landuyt, J.; Van Tendeloo, G. *Electron Microscopy: Principles and Fundamentals*, VCH Verlagsgesellschaft mbH, **2007**.

(88) Nakanishi, N.; Yamazaki, T.; Rečnik, A.; Čeh, M.; Kawasaki, M.; Watanabe, K.; Shiojiri, M. Retrieval Process of High-Resolution HAADF-STEM Images. *J. Electron Microsc. (Tokyo).* **2002**, *51* (6), 383–390.

(89) Cesareo, R. X-Ray Physics: Interaction with Matter, Production, Detection. *Riv. del Nuovo Cim.* **2000**, *23* (7), 1–183.

(90) Sharon, L.; Hua, Y.; Zhao, S.; Mo, Z. Studies on Electron Penetration versus Beam Acceleration Voltage in Energy-Dispersive X-Ray Microanalysis. In *IEEE International Conference on Semiconductor Electronics, Proceedings, ICSE*; **2006**; 610–613.

(91) Inesi, A. Instrumental Methods in Electrochemistry. *Bioelectrochemistry Bioenerg.* **1986**, *15* (3), 531.

(92) Schmickler, W.; Santos, E. *Interfacial Electrochemistry*, Springer-Verlag Berlin Heidelberg, **2010**.

(93) Jerkiewicz, G.; Vatankhah, G.; Lessard, J.; Soriaga, M. P.; Park, Y.-S. Surface-Oxide Growth at Platinum Electrodes in Aqueous H2SO4. *Electrochim. Acta* **2004**, *49* (9–10), 1451–1459.

(94) Canullo, J. C.; Triaca, W. E.; Arvia, A. J. Electrochemical Faceting of Single Crystal Platinum Electrodes. *J. Electroanal. Chem.* **1986**, *200* (1–2), 397–400.

(95) Kinkead, B.; van Drunen, J.; Paul, M. T. Y.; Dowling, K.; Jerkiewicz, G.; Gates, B. D. Platinum Ordered Porous Electrodes: Developing a Platform for Fundamental Electrochemical Characterization. *Electrocatalysis* **2013**, *4* (3), 179–186.

(96) Jerkiewicz, G. Electrochemical Hydrogen Adsorption and Absorption. Part 1: Under-Potential Deposition of Hydrogen. *Electrocatalysis* **2010**, *1* (4), 179–199.

(97) Rand, D. A. J.; Woods, R. Determination of the Surface Composition of Smooth Noble Metal Alloys by Cyclic Voltammetry. *J. Electroanal. Chem. Interfacial Electrochem.* **1972**, *36* (1), 57–69.

(98) Hsueh, K. L.; Chin, D. T.; Srinivasan, S. Electrode Kinetics of Oxygen Reduction. A Theoretical and Experimental Analysis of the Rotating Ring-Disk Electrode Method. *J. Electroanal. Chem. Interfacial Electrochem.* **1983**, *153* (Copyright (C) 2013 American Chemical Society (ACS). All Rights Reserved.), 79–95.

(99) Xing, W.; Yin, G.; Zhang, J. *Rotating Electrode Methods and Oxygen Reduction Electrocatalysts*, Elsevier **2014**.

(100) Paulus, U. A.; Schmidt, T. J.; Gasteiger, H. A.; Behm, R. J. Oxygen Reduction on a High-Surface Area Pt/Vulcan Carbon Catalyst: A Thin-Film Rotating Ring-Disk Electrode Study. *J. Electroanal. Chem.* **2001**, *495* (2), 134–145.

(101) Garsany, Y.; Baturina, O. A.; Swider-Lyons, K. E.; Kocha, S. S. Experimental Methods for Quantifying the Activity of Platinum Electrocatalysts for the Oxygen Reduction Reaction. In *Analytical Chemistry*; **2010**; 82, 6321–6328.

(102) Du, C.; Sun, Y.; Shen, T.; Yin, G.; Zhang, J. Applications of RDE and RRDE Methods in Oxygen Reduction Reaction. In *Rotating Electrode Methods and Oxygen Reduction Electrocatalysts*; **2014**; 231–277.

(103) Xu, S.; Kim, Y.; Higgins, D.; Yusuf, M.; Jaramillo, T. F.; Prinz, F. B. Building upon the Koutecky-Levich Equation for Evaluation of Next-Generation Oxygen Reduction Reaction Catalysts. *Electrochim. Acta* **2017**, *255*, 99–108.

(104) Kim, D. S.; Kim, C.; Kim, J. K.; Kim, J. H.; Chun, H. H.; Lee, H.; Kim, Y. T. Enhanced Electrocatalytic Performance due to Anomalous Compressive Strain and Superior Electron Retention Properties of Highly Porous Pt Nanoparticles. *J. Catal.* **2012**, *291*, 69–78.

(105) Mazumder, V.; Chi, M.; More, K. L.; Sun, S. Core/Shell Pd/FePt Nanoparticles as an Active and Durable Catalyst for the Oxygen Reduction Reaction. *J. Am. Chem. Soc.* **2010**, *132* (23), 7848–7849.

(106) Wang, D.; Xin, H. L.; Hovden, R.; Wang, H.; Yu, Y.; Muller, D. A.; Disalvo, F. J.; Abruña, H. D. Structurally Ordered

Intermetallic Platinum-Cobalt Core-Shell Nanoparticles with Enhanced Activity and Stability as Oxygen Reduction Electrocatalysts. *Nat. Mater.* **2013**, *12* (1), 81–87.

(107) Treimer, S.; Tang, A.; Johnson, D. C. A Consideration of the Application of Koutecký-Levich Plots in the Diagnoses of Charge-Transfer Mechanisms at Rotated Disk Electrodes. *Electroanalysis*. **2002**, 165–171.

(108) Wu, J.; Yuan, X. Z.; Martin, J. J.; Wang, H.; Zhang, J.; Shen, J.; Wu, S.; Merida, W. A Review of PEM Fuel Cell Durability: Degradation Mechanisms and Mitigation Strategies. *Journal of Power Sources*. **2008**, 104–119.

(109) Garland, N.; Benjamin, T.; Kopasz, J. DOE Fuel Cell Program: Durability Technical Targets and Testing Protocols. In *ECS Transactions*; **2007**; 11, 923–931.

(110) Sense, V. Electrochemical Impedance Spectroscopy ( EIS ): A Powerful and Cost- Effective Tool for Fuel Cell Diagnostics. *Cell* **1990**, *35*, 1–5.

(111) Forrai, A.; Funato, H.; Yanagita, Y.; Kato, Y. Fuel-Cell Parameter Estimation and Diagnostics. *IEEE Trans. Energy Convers.* **2005**, *20* (3), 668–675.

(112) Zaidi, S. M. J.; Rauf, M. A. Fuel Cell Fundamentals. In *Polymer Membranes for Fuel Cells*, Springer Science **2009**; pp 1–6.

(113) Francia, C.; Ijeri, V. S.; Specchia, S.; Spinelli, P. Estimation of Hydrogen Crossover through Nafion?? Membranes in PEMFCs. *J. Power Sources* **2011**, *196* (4), 1833–1839.

(114) Cooper, K. R.; Smith, M. Electrical Test Methods for on-Line Fuel Cell Ohmic Resistance Measurement. *J. Power Sources* **2006**, *160* (2 SPEC. ISS.), 1088–1095.

(115) Ogihara, N.; Itou, Y.; Sasaki, T.; Takeuchi, Y. Impedance Spectroscopy Characterization of Porous Electrodes under Different Electrode Thickness Using a Symmetric Cell for High-Performance Lithium-Ion Batteries. *J. Phys. Chem. C* **2015**, *119* (9), 4612–4619.

(116) Lasia, A. Impedance of Porous Electrodes. *J. Electroanal. Chem.* **1995**, *397* (1–2), 27–33.

(117) Baker, D. R.; Caulk, D. A.; Neyerlin, K. C.; Murphy, M. W. Measurement of Oxygen Transport Resistance in PEM Fuel Cells by Limiting Current Methods. *J. Electrochem. Soc.* **2009**, *156* (9), B991.

(118) Liu, X.; Guo, H.; Ma, C. Water Flooding and Two-Phase Flow in Cathode Channels of Proton Exchange Membrane Fuel Cells. *J. Power Sources* **2006**, *156* (2), 267–280.

(119) El Hannach, M.; Prat, M.; Pauchet, J. Pore Network Model of the Cathode Catalyst Layer of Proton Exchange Membrane Fuel Cells: Analysis of Water Management and Electrical Performance. *Int. J. Hydrogen Energy* **2012**, *37* (24), 18996–19006.

(120) Debe, M. K. Electrocatalyst Approaches and Challenges for Automotive Fuel Cells. *Nature* **2012**, *486* (7401), 43–51.

(121) Wu, B.; Matian, M.; Offer, G. J. Hydrogen PEMFC System for Automotive Applications. *Int. J. Low-Carbon Technol.* **2012**, *7* (1), 28–37.

(122) Hogarth, W. H. J.; Benziger, J. B. Dynamics of Autohumidifed PEM Fuel Cell Operation. *J. Electrochem. Soc.* **2006**, *153* (11), A2139.

(123) Rohendi, D.; Majlan, E. H.; Mohamad, A. B.; Daud, W. R. W.; Kadhum, A. A. H.; Shyuan, L. K. Effects of Temperature and Backpressure on the Performance Degradation of MEA in PEMFC. *Int. J. Hydrogen Energy* **2015**, *40* (34), 10960–10968.

(124) Jiao, K.; Li, X. Cold Start Analysis of Polymer Electrolyte Membrane Fuel Cells. *Int. J. Hydrogen Energy* **2010**, *35* (10), 5077–5094.

(125) Jiao, K.; Alaefour, I. E.; Karimi, G.; Li, X. Cold Start Characteristics of Proton Exchange Membrane Fuel Cells. *Int. J. Hydrogen Energy* **2011**, *36* (18), 11832–11845.

(126) Jiao, K.; Li, X. Effects of Various Operating and Initial Conditions on Cold Start Performance of Polymer Electrolyte Membrane Fuel Cells. *Int. J. Hydrogen Energy* **2009**, *34* (19), 8171–8184.

(127) Mckahn, D. A.; Liu, X. Comparison of Two Models for Temperature Observation of Miniature PEM Fuel Cells Under Dry Conditions. *Ieee Trans. Ind. Electron.* **2015**, *62* (8), 5283–5292.

(128) Alink, R.; Haußmann, J.; Markötter, H.; Schwager, M.; Manke, I.; Gerteisen, D. The Influence of Porous Transport Layer Modifications on the Water Management in Polymer Electrolyte Membrane Fuel Cells. *J. Power Sources* **2013**, *233*, 358–368.

(129) Eikerling, M. E.; Kulikovsky, A. *Polymer Electrolyte Fuel Cells Physical Principles of Materials and Operation*; Taylor & Francis Group, LLC, **2015**.

(130) Debe, M. K.; Hendricks, S. M.; Vernstrom, G. D.; Meyers, M.; Brostrom, M.; Stephens, M.; Chan, Q.; Willey, J.; Hamden, M.; Mittelsteadt, C. K.; Capuano, C. B.; Ayers, K. E.; Anderson, E. B. Initial Performance and Durability of Ultra-Low Loaded NSTF Electrodes for PEM Electrolyzers. *J. Electrochem. Soc.* **2012**, *159* (6), K165.

(131) Kongkanand, a.; Owejan, J. E.; Moose, S.; Dioguardi, M.; Biradar, M.; Makharia, R. Development of Dispersed-Catalyst/NSTF Hybrid Electrode. *J. Electrochem. Soc.* **2012**, *159* (11), F676–F682.

(132) Sinha, P. K.; Gu, W.; Kongkanand, A.; Thompson, E. Performance of Nano Structured Thin Film (NSTF) Electrodes under Partially-Humidified Conditions. *J. Electrochem. Soc.* **2011**, *158* (7), B831.

(133) Zhang, Y.; Ma, C.; Zhu, Y.; Si, R.; Cai, Y.; Wang, J. X.; Adzic, R. R. Hollow Core Supported Pt Monolayer Catalysts for Oxygen Reduction. *Catal. Today* **2013**, *202* (1), 50–54.

(134) Kim, G.; Eom, K.; Kim, M.; Yoo, S. J.; Jang, J. H.; Kim, H. J.; Cho, E. Design of an Advanced Membrane Electrode Assembly Employing a Double-Layered Cathode for a PEM Fuel Cell. *ACS Appl. Mater. Interfaces* **2015**, *7* (50), 27581–27585.

(135) Friedmann, R.; Van Nguyen, T. Optimization of the Microstructure of the Cathode Catalyst Layer of a PEMFC for Two-Phase Flow. *J. Electrochem. Soc.* **2010**, *157* (2), B260–B265.

(136) Odom, T. W.; Love, J. C.; Wolfe, D. B.; Paul, K. E.; Whitesides, G. M. Improved Pattern Transfer in Soft Lithography Using Composite Stamps. *Langmuir* **2002**, *18* (13), 5314–5320.

(137) Lee, M. V.; Husseini, G.; Sautter, K.; Linford, M. R. Gas Phase Deposition of Trichloro(1H,1H,2H,2H-Perfluorooctyl)silane on Silicon Dioxide, by XPS. *Surf. Sci. Spectra* **2010**, *17* (1), 87–92.

(138) Parvais, B.; Pallandre, A.; Jonas, A. M.; Raskin, J. P. Liquid and Vapor Phase Silanes Coating for the Release of Thin Film MEMS. In *IEEE Transactions on Device and Materials Reliability*; **2005**; 5, 250–254.

(139) US. Department of Energy. The Department of Energy Hydrogen and Fuel Cells Program Plan, published on https://www.energy.gov/eere/fuelcells/downloads/department-energy-hydrogen-and-fuel-cells-program-plan (as of April 2018) **2011**, September, 1–105.

(140) Andersen, S. M.; Dhiman, R.; Larsen, M. J.; Skou, E. Importance of Electrode Hot-Pressing Conditions for the Catalyst Performance of Proton Exchange Membrane Fuel Cells. *Appl. Catal. B Environ.* **2015**, *172–173*, 82–90.

(141) Glassman, M.; Omosebi, A.; Besser, R. S. Repetitive Hot-Press Approach for Performance Enhancement of Hydrogen Fuel Cells. *J. Power Sources* **2014**, *247*, 384–390.

(142) Schoemaker, M.; Misz, U.; Beckhaus, P.; Heinzel, A. Evaluation of Hydrogen Crossover through Fuel Cell Membranes. In *Fuel Cells*; **2014**; 14, pp 412–415.

(143) Eikerling, M., Kulikovsky, A., Catalyst Layer Structure and OperationChapter 3, Taylor & Francis Group, **2015**.

(144) Khajeh-Hosseini-Dalasm, N.; Kermani, M. J.; Moghaddam, D. G.; Stockie, J. M. A Parametric Study of Cathode Catalyst Layer Structural Parameters on the Performance of a PEM Fuel Cell. *Int. J. Hydrogen Energy* **2010**, *35* (6), 2417–2427.

(145) Partnership, U. S. D. Fuel Cell Technical Team Roadmap Hydrogen Storage Technologies Roadmap, published on https://www.energy.gov/sites/prod/files/2014/02/f8/fctt_roadmap_june2013.pdf (as of April 2018) **2013**, June.

(146) Aizawa, M.; Gyoten, H.; Salah, A.; Liu, X. Pillar Structured Membranes for Suppressing Cathodic Concentration Overvoltage in PEMFCs at Elevated Temperature/Low Relative Humidity. *J. Electrochem. Soc.* **2010**, *157* (12), B1844.

(147) Aizawa, M.; Gyoten, H. Effect of Micro-Patterned Membranes on the Cathode Performances for PEM Fuel Cells under Low Humidity. *J. Electrochem. Soc.* **2013**, *160* (4), F417–F428.

(148) Jeon, Y.; Kim, D. J.; Koh, J. K.; Ji, Y.; Kim, J. H.; Shul, Y. G. Interface-Designed Membranes with Shape-Controlled Patterns for High-Performance Polymer Electrolyte Membrane Fuel Cells. *Sci. Rep.* **2015**, *5* (May), 1–11.

(149) Liu, X.; Coxon, P. R.; Peters, M.; Hoex, B.; Cole, J. M.; Fray, D. J. Black Silicon: Fabrication Methods, Properties and Solar Energy Applications. *Energy Environ. Sci.* **2014**, *7* (10), 3223–3263.

(150) Deshmukh, A. B.; Kale, V. S.; Dhavale, V. M.; Sreekumar, K.; Vijayamohanan, K.; Shelke, M. V. Direct Transfer of Micro-Molded Electrodes for Enhanced Mass Transport and Water Management in PEMFC. *Electrochem. commun.* **2010**, *12* (11), 1638–1641.

(151) Omosebi, A.; Besser, R. S. Electron Beam Patterned Nafion Membranes for DMFC Applications. *J. Power Sources* **2013**, *228*, 151–158.

(152) Chi, W. S.; Jeon, Y.; Park, S. J.; Kim, J. H.; Shul, Y. G. Fabrication of Surface-Patterned Membranes by Means of a ZnO Nanorod Templating Method for Polymer Electrolyte Membrane Fuel-Cell Applications. *Chempluschem* **2014**, *79* (8), 1109–1115.

(153) Bae, J. W.; Cho, Y. H.; Sung, Y. E.; Shin, K.; Jho, J. Y. Performance Enhancement of Polymer Electrolyte Membrane Fuel Cell by Employing Line-Patterned Nafion Membrane. *J. Ind. Eng. Chem.* **2012**, *18* (3), 876–879.

(154) Paul, D. K.; Mccreery, R.; Karan, K. Proton Transport Property in Supported Nafion Nanothin Films by Electrochemical Impedance Spectroscopy. *J. Electrochem. Soc.* **2014**, *161* (14), 1395–1402.

(155) Eikerling, M.; Kornyshev, A.; Spohr, E. Proton-Conducting Polymer Electrolyte Membranes: Water and Structure in Charge. *Fuel Cells I* **2008**, No. April, 15–54.

(156) Han, B.; Mo, J.; Kang, Z.; Zhang, F.-Y. Modeling of Interfacial Resistance Effects on the Performance and Efficiency for Electrolyzer Energy Storage. *13th International Energy Conversion Engineering Conference*; AIAA Propulsion and Energy Forum, **2015, 3915**.

(157) Park, C. H.; Lee, S. Y.; Hwang, D. S.; Shin, D. W.; Cho, D. H.; Lee, K. H.; Kim, T. W.; Kim, T. W.; Lee, M.; Kim, D. S.; Doherty, C. M.; Thornton, A. W.; Hill, A. J.; Guiver, M. D.; Lee, Y. M. Nanocrack-Regulated Self-Humidifying Membranes. *Nature* **2016**, *532* (7600), 480–483.

(158) Kim, S.; Han, J.; Kwon, Y.; Lee, K. S.; Lim, T. H.; Nam, S. W.; Jang, J. H. Effect of Nafion Ionomer and Catalyst in Cathode Layers for the Direct Formic Acid Fuel Cell with Complex Capacitance Analysis on the Ionic Resistance. *Electrochim. Acta* **2011**, *56* (23), 7984–7990.

(159) Vidaković, T.; Christov, M.; Sundmacher, K. The Use of CO Stripping for in Situ Fuel Cell Catalyst Characterization. *Electrochim. Acta* **2007**, *52* (18), 5606–5613.

(160) Kocha, S. S.; Yang, J. D.; Yi, J. S. Characterization of Gas Crossover and Its Implications in PEM Fuel Cells. *AIChE J.* **2006**, *52* (5), 1916–1925.

(161) Bae, J. W.; Cho, Y.-H.; Sung, Y.-E.; Shin, K.; Jho, J. Y. Performance Enhancement of Polymer Electrolyte Membrane Fuel Cell by Employing Line-Patterned Nafion Membrane. *J. Ind. Eng. Chem.* **2012**, *18* (3), 876–879.

(162) Raimondi, F.; Scherer, G. G.; Kötz, R.; Wokaun, A. Nanoparticles in Energy Technology: Examples from Electrochemistry and Catalysis. *Angewandte Chemie - International Edition*. **2005**, 2190–2209.

(163) Aricò, A. S.; Bruce, P.; Scrosati, B.; Tarascon, J.-M.; van Schalkwijk, W. Nanostructured Materials for Advanced Energy Conversion and Storage Devices. *Nat. Mater.* **2005**, *4* (5), 366–377.

(164) Liu, C.; Burghaus, U.; Besenbacher, F.; Wang, Z. L. Preparation and Characterization of Nanomaterials for Sustainable Energy Production. *ACS Nano* **2010**, *4* (10), 5517–5526.

(165) Antoine, O.; Bultel, Y.; Durand, R. Oxygen Reduction Reaction Kinetics and Mechanism on Platinum Nanoparticles inside Nafion (R). *J. Electroanal. Chem.* **2001**, *499* (1), 85–94.

(166) Sun, Z. P.; Zhang, X. G.; Liang, Y. Y.; Li, H. L. Highly Dispersed Pd Nanoparticles on Covalent Functional MWNT Surfaces for Methanol Oxidation in Alkaline Solution. *Electrochem. commun.* **2009**, *11* (3), 557–561.

(167) Waszczuk, P.; Solla-Gullón, J.; Kim, H.-S.; Tong, Y. Y.; Montiel, V.; Aldaz, A.; Wieckowski, a. Methanol Electrooxidation on Platinum/Ruthenium Nanoparticle Catalysts. *J. Catal.* **2001**, *203* (1), 1–6.

(168) Nozik, A. J. Nanoscience and Nanostructures for Photovoltaics and Solar Fuels. *Nano Lett.* **2010**, *10* (8), 2735–2741.

(169) Johnson, N. .; McComb, D. .; Richel, A.; Treble, B. .; De La Rue, R. . Synthesis and Optical Properties of Opal and Inverse Opal Photonic Crystals. *Synth. Met.* **2001**, *116* (1–3), 469–473.

(170) Schroden, R. C.; Al-Daous, M.; Blanford, C. F.; Stein, A. Optical Properties of Inverse Opal Photonic Crystals. *Chem. Mater.* **2002**, *14* (8), 3305–3315.

(171) Paul, M. T. Y.; Kinkead, B.; Gates, B. D. Ordered Porous Gold Electrodes to Enhance the Sensitivity of Enzyme-Based Glucose Sensors. *J. Electrochem. Soc.* **2014**, *161* (2), B3103–B3106.

(172) Lei, Y.; Lu, J.; Luo, X.; Wu, T.; Du, P.; Zhang, X.; Ren, Y.; Wen, J.; Miller, D. J.; Miller, J. T.; Sun, Y. K.; Elam, J. W.; Amine, K. Synthesis of Porous Carbon Supported Palladium Nanoparticle Catalysts by Atomic Layer Deposition: Application for Rechargeable Lithium-$O_2$ Battery. *Nano Lett.* **2013**, *13* (9), 4182–4189.

(173) Long, N. V.; Thi, C. M.; Nogami, M.; Ohtaki, M. Novel Issues of Morphology, Size, and Structure of Pt Nanoparticles in Chemical Engineering: Surface Attachment, Aggregation or Agglomeration, Assembly, and Structural Changes. *New J. Chem.* **2012**, *36* (6), 1320–1334.

(174) Pilapil, B. K.; van Drunen, J.; Makonnen, Y.; Beauchemin, D.; Jerkiewicz, G.; Gates, B. D. Ordered Porous Electrodes by Design: Toward Enhancing the Effective Utilization of Platinum in Electrocatalysis. *Advanced Functional Materials*. *Adv. Funct. Mater.* **2017**, 27, 1703171

(175) Luc, W.; Jiao, F. Synthesis of Nanoporous Metals, Oxides, Carbides, and Sulfides: Beyond Nanocasting. *Acc. Chem. Res.* **2016**, *49* (7), 1351–1358.

(176) Maillard, F.; Schreier, S.; Hanzlik, M.; Savinova, E. R.; Weinkauf, S.; Stimming, U. Influence of Particle Agglomeration on the Catalytic Activity of Carbon-Supported Pt Nanoparticles in CO Monolayer Oxidation. *Phys. Chem. Chem. Phys.* **2005**, *7* (2), 385–393.

(177) Park, M. H.; Kim, K.; Kim, J.; Cho, J. Flexible Dimensional Control of High-Capacity Li-Ion-Battery Anodes: From 0D Hollow to 3D Porous Germanium Nanoparticle Assemblies. *Adv. Mater.* **2010**, *22* (3), 415–418.

(178) Teranishi, T.; Hosoe, M.; Tanaka, T.; Miyake, M. Size Control of Monodispersed Pt Nanoparticles and Their 2D Organization by Electrophoretic Deposition. *J. Phys. Chem. B* **1999**, *103* (19), 3818–3827.

(179) Latsuzbaia, R.; Negro, E.; Koper, G. Synthesis, Stabilization and Activation of Pt Nanoparticles for PEMFC Applications. *Fuel Cells* **2015**, *15* (4), 628–638.

(180) Rao, C. R. K.; Trivedi, D. C. Chemical and Electrochemical Depositions of Platinum Group Metals and Their Applications. *Coordination Chemistry Reviews*. **2005**, 613–631.

(181) Hsueh, Y.-C.; Wang, C.-C.; Kei, C.-C.; Lin, Y.-H.; Liu, C.; Perng, T.-P. Fabrication of Catalyst by Atomic Layer Deposition for High Specific Power Density Proton Exchange Membrane Fuel Cells. *J. Catal.* **2012**, *294*, 63–68.

(182) Baumgartner, B. M. E.; Raub, C. J. The Electrodeposition of Platinum and Platinum Alloys. *Platin. Met. Rev.* **1988**, *32* (4), 188–197.

(183) Ustarroz, J.; Altantzis, T.; Hammons, J. A.; Hubin, A.; Bals, S.; Terryn, H. The Role of Nanocluster Aggregation, Coalescence, and Recrystallization in the Electrochemical Deposition of Platinum Nanostructures. *Chem. Mater.* **2014**, *26* (7), 2396–2406.

(184) Geboes, B.; Vanrenterghem, B.; Ustarroz, J.; Pauwels, D. Influence of the Morphology of Electrodeposited Nanoparticles on the Activity of Organic Halide Reduction. *Chem. Eng. Trans.* **2014**, *41*, 73–78.

(185) Lee, I.; Zhang, Q.; Ge, J.; Yin, Y.; Zaera, F. Encapsulation of Supported Pt Nanoparticles with Mesoporous Silica for Increased Catalyst Stability. *Nano Res.* **2011**, *4* (1), 115–123.

(186) Sasaki, K.; Zhang, L.; Adzic, R. R. Niobium Oxide-Supported Platinum Ultra-Low Amount Electrocatalysts for Oxygen Reduction. *Phys. Chem. Chem. Phys.* **2008**, *10* (1), 159–167.

(187) Wen, M.; Zhou, B.; Fang, H.; Wu, Q.; Chen, S. Novel-Phase Structural High-Efficiency Anode Catalyst for Methanol Fuel Cells: α-(NiCu)3Pd Nanoalloy. *J. Phys. Chem. C* **2014**, *118* (46), 26713–26720.

(188) Dokoutchaev, A.; James, J. T.; Koene, S. C.; Pathak, S.; Prakash, G. K. S.; Thompson, M. E. Colloidal Metal Deposition onto Functionalized Polystyrene Microspheres. *Chem. Mater.* **1999**, *11* (9), 2389–2399.

(189) Pilapil, B. K.; Wang, M. C. P.; Paul, M. T. Y.; Nazemi, A.; Gates, B. D. Self-Assembly of Nanoparticles onto the Surfaces of Polystyrene Spheres with a Tunable Composition and Loading. *Nanotechnology* **2015**, *26* (5), 55601.

(190) Zakhidov, A. A. Carbon Structures with Three-Dimensional Periodicity at Optical Wavelengths. *Science (80-. ).* **1998**, *282* (5390), 897–901.

(191) Zhong, Z.; Yin, Y.; Gates, B.; Xia, Y. Preparation of Mesoscale Hollow Spheres of TiO2 and SnO2 by Templating against Crystalline Arrays of Polystyrene Beads. *Adv. Mater.* **2000**, *12* (3), 206–209.

(192) Kim, K.; Thiyagarajan, P.; Ahn, H.-J.; Kim, S.-I.; Jang, J.-H. Optimization for Visible Light Photocatalytic Water Splitting: Gold-Coated and Surface-Textured TiO2 Inverse Opal Nano-Networks. *Nanoscale* **2013**, *5* (14), 6254–6260.

(193) Teranishi, T.; Kurita, R.; Miyake, M. Shape Control of Pt Nanoparticles. *J. Inorg. Organomet. Polym.* **2000**, *10* (3), 145–156.

(194) Teranishi, T.; Miyake, M. Size Control of Palladium Nanoparticles and Their Crystal Structures. *Chem. Mater.* **1998**, *10* (2), 594–600.

(195) Boyer, J. C.; Vetrone, F.; Cuccia, L. A.; Capobianco, J. A. Synthesis of Colloidal Upconverting $NaYF_4$ Nanocrystals Doped with $Er^{3+}$, $Yb^{3+}$ and $Tm^{3+}$, $Yb^{3+}$ via Thermal Decomposition of Lanthanide Trifluoroacetate Precursors. *J. Am. Chem. Soc.* **2006**, *128* (23), 7444–7445.

(196) Blanco, a; Chomski, E.; Grabtchak, S.; Ibisate, M.; John, S.; Leonard, S.; Lopez, C.; Meseguer, F.; Miguez, H.; Mondia, J.; Ozin, G.; Toader, O.; van Driel HM. Large-Scale Synthesis of a Silicon Photonic Crystal with a Complete Three-Dimensional Bandgap near 1.5 Micrometres. *Nature* **2000**, *405* (6785), 437–440.

(197) Van Drunen, J.; Pilapil, B. K.; Makonnen, Y.; Beauchemin, D.; Gates, B. D.; Jerkiewicz, G. Electrochemically Active Nickel Foams as Support Materials for Nanoscopic Platinum Electrocatalysts. *ACS Appl. Mater. Interfaces* **2014**, *6* (15), 12046–12061.

(198) Xia, Y.; Gates, B.; Yin, Y.; Lu, Y. Monodispersed Colloidal Spheres: Old Materials with New Applications. *Adv. Mater.* **2000**, *12* (10), 693–713.

(199) Van Blaaderen, A. Materials Science: Colloids Get Complex. *Nature*. **2006**, 439,545–546.

(200) Asher, S. A.; Holtz, J.; Liu, L.; Wu, Z. Self-Assembly Motif for Creating Submicron Periodic Materials. Polymerized Crystalline Colloidal Arrays. *J. Am. Chem. Soc.* **1994**, *116* (11), 4997–4998.

(201) Whitesides, G. M. Self-Assembly at All Scales. *Science (80).* **2002**, *295* (5564), 2418–2421.

(202) Colson, P.; Cloots, R.; Henrist, C. Experimental Design Applied to Spin Coating of 2D Colloidal Crystal Masks: A Relevant Method? *Langmuir* **2011**, *27* (21), 12800–12806.

(203) Ma, X.; Ni, X. Using Upconversion Nanoparticles to Improve Photovoltaic Properties of poly(3-Hexylthiophene)-$TiO_2$ Heterojunction Solar Cell. *J. Nanoparticle Res.* **2013**, *15* (4).

(204) Álvarez, G. F.; Mamlouk, M.; Scott, K. An Investigation of Palladium Oxygen Reduction Catalysts for the Direct Methanol Fuel Cell. *Int. J. Electrochem.* **2011**, *2011*, 1–12.

(205) Zhang, F.; Zhang, C. L.; Peng, H. Y.; Cong, H. P.; Qian, H. S. Near-Infrared Photocatalytic Upconversion Nanoparticles/$TiO_2$ Nanofibers Assembled in Large Scale by Electrospinning. *Part. Part. Syst. Charact.* **2016**, 248–253.

(206) Zhang, F.; Zhang, C. L.; Wang, W. N.; Cong, H. P.; Qian, H. S. Titanium Dioxide/Upconversion Nanoparticles/Cadmium Sulfide Nanofibers Enable Enhanced Full-Spectrum Absorption for Superior Solar Light Driven Photocatalysis. *ChemSusChem* **2016**, *9* (12), 1449–1454.

(207) Guo, X.; Di, W.; Chen, C.; Liu, C.; Wang, X.; Qin, W. Enhanced near-Infrared Photocatalysis of $NaYF_4$:Yb, Tm/CdS/$TiO_2$ Composites. *Dalton Trans.* **2014**, *43* (3), 1048–1054.

(208) Wang, W.; Li, Y.; Kang, Z.; Wang, F.; Yu, J. C. A NIR-Driven Photocatalyst Based on α-$NaYF_4$:Yb,Tm@$TiO_2$ Core–shell Structure Supported on Reduced Graphene Oxide. *Appl. Catal. B Environ.* **2016**, *182*, 184–192.

(209) Lü, Q.; Zhao, L.-C.; Guo, F.-Y.; Li, M.-C. Upconversion Emission Enhancement of $TiO_2$ Coated Lanthanide-Doped Y2O3 Nanoparticles. *Chinese Phys. B* **2009**, *18* (9), 4030–4036.

(210) Yu, J.; Yang, Y.; Fan, R.; Liu, D.; Wei, L.; Chen, S.; Li, L.; Yang, B.; Cao, W. Enhanced Near-Infrared to Visible Upconversion Nanoparticles of $Ho^{3+}$-$Yb^{3+}$-F–Tri-Doped $TiO_2$ and Its Application in Dye-Sensitized Solar Cells with 37% Improvement in Power Conversion Efficiency. *Inorg. Chem.* **2014**, *53* (15), 8045–8053.

(211) Priolo, F.; Gregorkiewicz, T.; Galli, M.; Krauss, T. F. Silicon Nanostructures for Photonics and Photovoltaics. *Nat. Nanotechnol.* **2014**, *9* (1), 19–32.

(212) Cho, I. S.; Lee, C. H.; Feng, Y.; Logar, M.; Rao, P. M.; Cai, L.; Kim, D. R.; Sinclair, R.; Zheng, X. Codoping Titanium Dioxide Nanowires with Tungsten and Carbon for Enhanced Photoelectrochemical Performance. *Nat. Commun.*

**2013**, *4*, 1723.

(213) Su, R.; Tiruvalam, R.; Logsdail, A. J.; He, Q.; Downing, C. A.; Jensen, M. T.; Dimitratos, N.; Kesavan, L.; Wells, P. P.; Bechstein, R.; Jensen, H. H.; Wendt, S.; Catlow, C. R. A.; Kiely, C. J.; Hutchings, G. J.; Besenbacher, F. Designer Titania-Supported Au-Pd Nanoparticles for Efficient Photocatalytic Hydrogen Production. *ACS Nano* **2014**, *8* (4), 3490–3497.

(214) Barakat, M. A.; Al-Hutailah, R. I.; Qayyum, E.; Rashid, J.; Kuhn, J. N. Pt nanoparticles/$TiO_2$ for Photocatalytic Degradation of Phenols in Wastewater. *Environ. Technol.* **2014**, *35* (1–4), 137–144.

(215) An, B. L.; Fu, Y. H.; Dai, F. Z.; Xu, J. Q. Platinum Nanoparticle Modified $TiO_2$ Nanorods with Enhanced Catalytic Performances. *J. Alloys Compd.* **2015**, *622*, 426–431.

(216) Li, X.; Zheng, W.; Pan, H.; Yu, Y.; Chen, L.; Wu, P. Pt Nanoparticles Supported on Highly Dispersed $TiO_2$ Coated on SBA-15 as an Efficient and Recyclable Catalyst for Liquid-Phase Hydrogenation. *J. Catal.* **2013**, *300*, 9–19.

(217) Song, Y. Y.; Gao, Z. Da; Schmuki, P. Highly Uniform Pt Nanoparticle Decoration on $TiO_2$ Nanotube Arrays: A Refreshable Platform for Methanol Electrooxidation. *Electrochem. commun.* **2011**, *13* (3), 290–293.

(218) Yu, J.; Qi, L.; Jaroniec, M. Hydrogen Production by Photocatalytic Water Splitting over Pt/$TiO_2$ Nanosheets with Exposed (001) Facets. *J. Phys. Chem. C* **2010**, *114* (30), 13118–13125.

(219) Zou, J. J.; He, H.; Cui, L.; Du, H. Y. Highly Efficient Pt / $TiO_2$ Photocatalyst for Hydrogen Generation Prepared by a Cold Plasma Method. *Int. J. Hydrogen Energy* **2007**, *32* (12), 1762–1770.

(220) Liewhiran, C.; Tamaekong, N.; Tuantranont, A.; Wisitsoraat, A.; Phanichphant, S. The Effect of Pt Nanoparticles Loading on $H_2$ Sensing Properties of Flame-Spray-Made $SnO_2$ Sensing Films. *Mater. Chem. Phys.* **2014**, *147* (3), 661–672.

(221) López-Cudero, A.; Solla-Gullón, J.; Herrero, E.; Aldaz, A.; Feliu, J. M. CO Electrooxidation on Carbon Supported Platinum Nanoparticles: Effect of Aggregation. *J. Electroanal. Chem.* **2010**, *644* (2), 117–126.

(222) Newton, J. E.; Preece, J. A.; Pollet, B. G. Control of Nanoparticle Aggregation in PEMFCs Using Surfactants. *Int. J. Low-Carbon Technol.* **2011**, 7 (1), 38-43

(223) Chen, M.; Xing, Y. Polymer-Mediated Synthesis of Highly Dispersed Pt Nanoparticles on Carbon Black. *Langmuir* **2005**, *21* (20), 9334–9338.

(224) Yoshii, K.; Tsuda, T.; Arimura, T.; Imanishi, A.; Torimoto, T.; Kuwabata, S. Platinum Nanoparticle Immobilization onto Carbon Nanotubes Using Pt-Sputtered Room-Temperature Ionic Liquid. *RSC Adv.* **2012**, *2* (22), 8262.

(225) Zhang, Z.; Wang, Z.; Cao, S. W.; Xue, C. Au/Pt Nanoparticle-Decorated $TiO_2$ Nanofibers with Plasmon-Enhanced Photocatalytic Activities for Solar-to-Fuel Conversion. *J. Phys. Chem. C* **2013**, *117* (49), 25939–25947.

(226) Carlson, E. J.; Kopf, P.; Sinha, J.; Sriramulu, S.; Yang, Y. Cost Analysis of PEM Fuel Cell Systems for Transportation. *Natl. Renew. Energy Lab.* published on https://www.nrel.gov/docs/fy06osti/39104.pdf (as of April 2018) **2005**, December

(227) Chen, L.; Lu, L.; Zhu, H.; Chen, Y.; Huang, Y.; Li, Y.; Wang, L. Improved Ethanol Electrooxidation Performance by Shortening Pd–Ni Active Site Distance in Pd–Ni–P Nanocatalysts. *Nat. Commun.* **2017**, *8*, 14136.

(228) Calderón, J.; Rios Ráfales, M.; Nieto-Monge, M.; Pardo, J.; Moliner, R.; Lázaro, M. Oxidation of CO and Methanol on Pd-Ni Catalysts Supported on Different Chemically-Treated Carbon Nanofibers. *Nanomaterials* **2016**, *6* (10), 187.

(229) Singh, R. N.; Singh, A.; Anindita. Electrocatalytic Activity of Binary and Ternary Composite Films of Pd, MWCNT and Ni, Part II: Methanol Electrooxidation in 1 M KOH. *Int. J. Hydrogen Energy* **2009**, *34* (4), 2052–2057.

(230) Wang, J. X.; Inada, H.; Wu, L.; Zhu, Y.; Choi, Y.; Liu, P.; Zhou, W. P.; Adzic, R. R. Oxygen Reduction on Well-Defined Core-Shell Nanocatalysts: Particle Size, Facet, and Pt Shell Thickness Effects. *J. Am. Chem. Soc.* **2009**, *131* (47), 17299–17302.

(231) Mu, Y.; Liang, H.; Hu, J.; Jiang, L.; Wan, L. Controllable Pt Nanoparticle Deposition on Carbon Nanotubes as an Anode Catalyst for Direct Methanol Fuel Cells. *J. Phys. Chem. B* **2005**, *109* (47), 22212–22216.

(232) Zhang, Z.; Xin, L.; Sun, K.; Li, W. Pd-Ni Electrocatalysts for Efficient Ethanol Oxidation Reaction in Alkaline Electrolyte. *Int. J. Hydrogen Energy* **2011**, *36* (20), 12686–12697.

(233) Hou, W.; Dehm, N. A.; Scott, R. W. J. Alcohol Oxidations in Aqueous Solutions Using Au, Pd, and Bimetallic AuPd Nanoparticle Catalysts. *J. Catal.* **2008**, *253* (1), 22–27.

(234) Xu, C.; Wang, H.; Shen, P. K.; Jiang, S. P. Highly Ordered Pd Nanowire Arrays as Effective Electrocatalysts for Ethanol Oxidation in Direct Alcohol Fuel Cells. *Adv. Mater.* **2007**, *19* (23), 4256–4259.

(235) Manzo-Robledo, A.; Costa, N. J. S.; Philippot, K.; Rossi, L. M.; Ramírez-Meneses, E.; Guerrero-Ortega, L. P. A.; Ezquerra-Quiroga, S. Electro-Oxidation of Methanol in Alkaline Conditions Using Pd–Ni Nanoparticles Prepared from Organometallic Precursors and Supported on Carbon Vulcan. *J. Nanoparticle Res.* **2015**, *17* (12), 1–8.

(236) Obradović, M. D.; Stančić, Z. M.; Lačnjevac, U.; Radmilović, V. V.; Gavrilović-Wohlmuther, A.; Radmilović, V. R.; Gojković, S. L. Electrochemical Oxidation of Ethanol on Palladium-Nickel Nanocatalyst in Alkaline Media. *Appl. Catal. B Environ.* **2016**, *189*, 110–118.

(237) Qiu, C.; Shang, R.; Xie, Y.; Bu, Y.; Li, C.; Ma, H. Electrocatalytic Activity of Bimetallic Pd-Ni Thin Films towards the Oxidation of Methanol and Ethanol. *Mater. Chem. Phys.* **2010**, *120* (2–3), 323–330.

(238) Zhang, M.; Yan, Z.; Xie, J. Core/shell Ni@Pd Nanoparticles Supported on MWCNTs at Improved Electrocatalytic Performance for Alcohol Oxidation in Alkaline Media. *Electrochim. Acta* **2012**, *77*, 237–243.

(239) Qi, Z.; Geng, H.; Wang, X.; Zhao, C.; Ji, H.; Zhang, C.; Xu, J.; Zhang, Z. Novel Nanocrystalline PdNi Alloy Catalyst for Methanol and Ethanol Electro-Oxidation in Alkaline Media. *J. Power Sources* **2011**, *196* (14), 5823–5828.

(240) Zhao, Y.; Yang, X.; Tian, J.; Wang, F.; Zhan, L. Methanol Electro-Oxidation on Ni@Pd Core-Shell Nanoparticles Supported on Multi-Walled Carbon Nanotubes in Alkaline Media. *Int. J. Hydrogen Energy* **2010**, *35* (8), 3249–3257.

(241) González-Cobos, J.; Baranton, S.; Coutanceau, C. A Systematic in Situ Infrared Study of the Electrooxidation of C3 Alcohols on Carbon-Supported Pt and Pt-Bi Catalysts. *J. Phys. Chem. C* **2016**, *120* (13), 7155–7164.

(242) Rymarczyk, J.; Piotr, D. The in Fl Uence of Technological PVD Process Parameters on the Topography , Crystal and Molecular Structure of Nanocomposite Fi Lms Containing Palladium Nanograins. **2014**, 18–24.

(243) Zangari, G. Electrodeposition of Alloys and Compounds in the Era of Microelectronics and Energy Conversion Technology. *Coatings* **2015**, *5* (2), 195–218.

(244) Zhang, X.; Yu, S.; Qiao, L.; Zheng, W.; Liu, P. Stabilization of Pt Monolayer Catalysts under Harsh Conditions of Fuel Cells. *J. Chem. Phys.* **2015**, *142* (19).

(245) Dubau, L.; Lopez-Haro, M.; Durst, J.; Guetaz, L.; Bayle-Guillemaud, P.; Chatenet, M.; Maillard, F. Beyond Conventional Electrocatalysts: Hollow Nanoparticles for Improved and Sustainable Oxygen Reduction Reaction Activity. *J. Mater. Chem. A* **2014**, *2* (43), 18497–18507.

(246) Geboes, B.; Ustarroz, J.; Sentosun, K.; Vanrompay, H.; Hubin, A.; Bals, S.; Breugelmans, T. Electrochemical Behavior of Electrodeposited Nanoporous Pt Catalysts for the Oxygen Reduction Reaction. *ACS Catal.* **2016**, *17* (i), 5856–5864.

(247) Wang, C.; Wang, S.; Peng, L.; Zhang, J.; Shao, Z.; Huang, J.; Sun, C.; Ouyang, M.; He, X. Recent Progress on the Key Materials and Components for Proton Exchange Membrane Fuel Cells in Vehicle Applications. *Energies* **2016**, *9* (8).

(248) Gröger, O.; Gasteiger, H. a.; Suchsland, J.-P. Review—Electromobility: Batteries or Fuel Cells? *J. Electrochem. Soc.* **2015**, *162* (14), A2605–A2622.

(249) McDonough, W. F.; Sun, S. s. The Composition of the Earth. *Chem. Geol.* **1995**, *120* (3–4), 223–253.

(250) Sneed, B. T.; Young, A. P.; Jalalpoor, D.; Golden, M. C.; Mao, S.; Jiang, Y.; Wang, Y.; Tsung, C. K. Shaped Pd-Ni-Pt Core-Sandwich-Shell Nanoparticles: Influence of Ni Sandwich Layers on Catalytic Electrooxidations. *ACS Nano* **2014**, *8* (7), 7239–7250.

(251) Zhou, Z. M.; Shao, Z. G.; Qin, X. P.; Chen, X. G.; Wei, Z. D.; Yi, B. L. Durability Study of Pt-Pd/C as PEMFC Cathode Catalyst. *Int. J. Hydrogen Energy* **2010**, *35* (4), 1719–1726.

(252) Gullá, A. F.; Saha, M. S.; Allen, R. J.; Mukerjee, S. Toward Improving the Performance of PEM Fuel Cell by Using Mix Metal Electrodes Prepared by Dual IBAD. *J. Electrochem. Soc.* **2006**, *153* (2), A366.

(253) Lim, B.; Jiang, M.; Camargo, P. H. C.; Cho, E. C.; Tao, J.; Lu, X.; Zhu, Y.; Xia, Y. Pd-Pt Bimetallic Nanodendrites with High Activity for Oxygen Reduction. *Science (80 ).* **2009**, *324* (5932), 1302–1305.

(254) Stamenkovic, V. R.; Mun, B. S.; Arenz, M.; Mayrhofer, K. J. J.; Lucas, C. A.; Wang, G.; Ross, P. N.; Markovic, N. M. Trends in Electrocatalysis on Extended and Nanoscale Pt-Bimetallic Alloy Surfaces. *Nat. Mater.* **2007**, *6* (3), 241–247.

(255) Geboes, B.; Mintsouli, I.; Wouters, B.; Georgieva, J.; Kakaroglou, A.; Sotiropoulos, S.; Valova, E.; Armyanov, S.; Hubin, A.; Breugelmans, T. Surface and Electrochemical Characterisation of a Pt-Cu/C Nano-Structured Electrocatalyst, Prepared by Galvanic Displacement. *Appl. Catal. B Environ.* **2014**, *150–151*, 249–256.

(256) Ferreira, P. J.; la O', G. J.; Shao-Horn, Y.; Morgan, D.; Makharia, R.; Kocha, S.; Gasteiger, H. A. Instability of Pt/C Electrocatalysts in Proton Exchange Membrane Fuel Cells. *J. Electrochem. Soc.* **2005**, *152* (11), A2256.

(257) Sun, W.; Peppley, B. A.; Karan, K. An Improved Two-Dimensional Agglomerate Cathode Model to Study the Influence of Catalyst Layer Structural Parameters. *Electrochim. Acta* **2005**, *50* (16–17), 3359–3374.

(258) Penner, R. M. Mesoscopic Metal Particles and Wires by Electrodeposition. *J. Phys. Chem. B* **2002**, *106* (13), 3339–3353.

(259) Saravanan, G.; Mohan, S. Pt Nanoparticles Embedded on Reduced Graphite Oxide with Excellent Electrocatalytic Properties. *Appl. Surf. Sci.* **2016**, *386*, 96–102.

(260) González, E.; Arbiol, J.; Puntes, V. F.; Sun, Y.; Xia, Y.; Yin, Y.; Sun, Y.; Xia, Y.; Yin, Y.; Erdonmez, C. K.; Cabot, A.; Hughes, J.; Alivisatos, A. P.; Kim, S. W.; Kim, M.; Lee, W. Y.; Hyeon, T.; Oldenburg, S. J.; Averitt, R. D.; Westcott, S. L.; Halas, N. J.; Marinakos, S. M.; Caruso, F.; Caruso, R. A.; Mohwald, H.; Im, S. H.; Jeong, U.; Xia, Y.; Erlebacher, J.; Aziz, M. J.; Karma, A.; Dimitrov, N.; Sieradzki, K. K.; Skrabalak, S. E.; Zeng, J.; Zhang, Q.; Chen, J.; Xia, Y.; Yavuz, M. S.; Chen, J.; Lou, X. W.; Archer, L. A.; Zhao, Q.; Gao, Y.; Bai, X.; Wu, C.; Xie, Y.; Pérez-Juste, J.; Liz-Marzán, L. M.; Carnie, S.; Chan, D. Y. C.; Mulvaney, P.; Sun, Y.; Mayers, B. T.; Xia, Y.; Yen, C. W.; Mahmoud, M. A.; El-Sayed, M. A.; Guisbiers, G.; Buchaillot, L.; Das, D.; Chatterjee, P. P.; Manna, I.; Pabi, S. K.; Shibata, T.; Bi, Y.; Lu, G.; Skrabalak, S. E.; Skrabalak, S. E.; Au, L.; Li, X.; Xia, Y.; Tu, K. N.; Gösele, U. Carving at the Nanoscale: Sequential Galvanic Exchange and Kirkendall Growth at Room Temperature. *Science* **2011**, *334* (6061), 1377–1380.

(261) Wang, C.; Chi, M.; Li, D.; Strmcnik, D.; Van Der Vliet, D.; Wang, G.; Komanicky, V.; Chang, K. C.; Paulikas, A. P.; Tripkovic, D.; Pearson, J.; More, K. L.; Markovic, N. M.; Stamenkovic, V. R. Design and Synthesis of Bimetallic Electrocatalyst with Multilayered Pt-Skin Surfaces. *J. Am. Chem. Soc.* **2011**, *133* (36), 14396–14403.

(262) Narayan, C.; Purushothaman, S.; Doany, F.; Deutsch, A. Thin-Film Transfer Process for Low-Cost Mcm-D

Fabrication. *IEEE Trans. Components Packag. Manuf. Technol. Part B-Advanced Packag.* **1995**, *18* (1), 42–46.

(263) Streletzky, K.; Phillies, G. D. J. Temperature Dependence of Triton X-100 Micelle Size and Hydration. *Langmuir* **1995**, *11* (7), 42–47.

(264) Zhang, H.; Jiang, F.; Zhou, R.; Du, Y.; Yang, P.; Wang, C.; Xu, J. Effect of Deposition Potential on the Structure and Electrocatalytic Behavior of Pt Micro/nanoparticles. *Int. J. Hydrogen Energy* **2011**, *36* (23), 15052–15059.

(265) Rajalakshmi, N.; Lakshmi, N.; Dhathathreyan, K. S. Nano Titanium Oxide Catalyst Support for Proton Exchange Membrane Fuel Cells. *Int. J. Hydrogen Energy* **2008**, *33* (24), 7521–7526.

(266) Marie, J.; Chenitz, R.; Chatenet, M.; Berthon-Fabry, S.; Cornet, N.; Achard, P. Highly Porous PEM Fuel Cell Cathodes Based on Low Density Carbon Aerogels as Pt-Support: Experimental Study of the Mass-Transport Losses. *J. Power Sources* **2009**, *190* (2), 423–434.

(267) Yu, Z.; Carter, R. N.; Zhang, J. Measurements of Pore Size Distribution, Porosity, Effective Oxygen Diffusivity, and Tortuosity of PEM Fuel Cell Electrodes. *Fuel Cells* **2012**, *12* (4), 557–565.

(268) Suzuki, A.; Hattori, T.; Miura, R.; Tsuboi, H.; Hatakeyama, N.; Takaba, H.; Williams, M. C.; Miyamoto, A. Porosity and Pt Content in the Catalyst Layer of PEMFC: Effects on Diffusion and Polarization Characteristics. *Int. J. Electrochem. Sci.* **2010**, *5* (12), 1948–1961.

(269) Ye, J. Y.; Attard, G. A.; Brew, A.; Zhou, Z. Y.; Sun, S. G.; Morgan, D. J.; Willock, D. J. Explicit Detection of the Mechanism of Platinum Nanoparticle Shape Control by Polyvinylpyrrolidone. *J. Phys. Chem. C* **2016**, *120* (14), 7532–7542.

(270) Habil, B. K.; Haschke, M. *Handbook of Practical X-Ray Fluorescence Analysis*, Springer-Verlag Berlin Heidelberg, **2006**.

(271) Chen, G.; Liao, M.; Yu, B.; Li, Y.; Wang, D.; You, G.; Zhong, C. J.; Chen, B. H. Pt Decorated PdAu/C Nanocatalysts with Ultralow Pt Loading for Formic Acid Electrooxidation. *Int. J. Hydrogen Energy* **2012**, *37* (13), 9959–9966.

# Appendix 1. Other Published Peer-Reviewed Journal Articles Completed During the PhD Studies

## 8.1.1 Ordered Porous Gold Electrodes to Enhance the Sensitivity of Enzyme-Based Glucose Sensors

Glucose sensors are essential tools for diabetes patients to use in monitoring their blood glucose levels. However, to be able to detect glucose in non-invasively collected physiological fluids, such as tears and urine, the sensitivity of these glucose sensors must be significantly higher than sensors that are currently used to detect glucose concentrations in blood. Increasing the specific surface area of enzyme-based glucose sensors through the use of ordered porous gold electrodes has been shown to enhance the sensitivity of these sensors. The enzyme-based ordered porous gold glucose sensor was demonstrated to be suitable in detecting glucose concentrations ranges that are similar to those occurring in tears. Although sensitivity of the glucose sensor is enhanced, the saturation threshold of the sensor is lowered. Further optimizations of the porous gold electrodes are required to eliminate signal saturation of these improved sensors.

**Graphical Abstract**

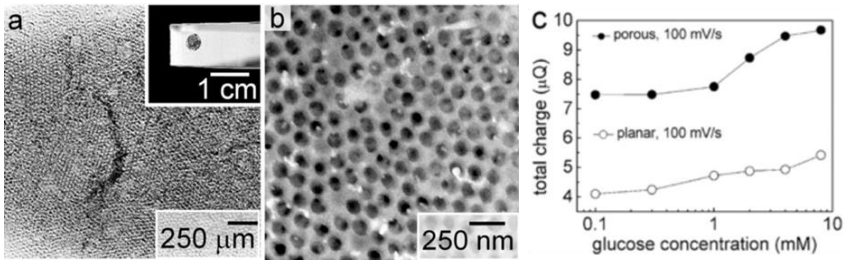


Paul, Michael T. Y.; Kinkead, Brandy; and Gates, Byron D., *J. Electrochem. Soc.*, **2014**, 161(2), B3130-3106

### 8.1.2 Verifying the Structure and Composition of Prepared Porous Catalytic Supports

The incorporation of catalytic nanoparticles (NPs) within nanostructured materials have been popular in recent years due to the excellent surface area to volume ratios that can be achieved for these materials and their ability to reduce the required loading of precious metal catalysts. The use of Pt and Pd NPs is especially attractive for power generating systems, such as proton exchange membrane and methanol oxidation fuel cells. Further studies on these nanoparticle incorporated materials have revealed the underlying support materials can enhance catalytic properties and stabilities of the NPs. However, due to processing constraints, loading of functional NPs is often limited to 2D supports. The incorporation of NPs into 3D porous supports can be performed by sophisticated systems, such as physical vapor and atomic layer depositions [7-9]. In this study, we demonstrate a relatively simple and cost effective method, which was developed previously in our research group, for preparing various combinations of NPs loaded into 3D structured materials. The NP loading and spatial distribution were characterized by SEM, STEM, and EDS. Our technique could be used to prepare novel electrochemical and photochemical porous materials for increased catalytic efficiency and stability.

**Graphical Abstract**

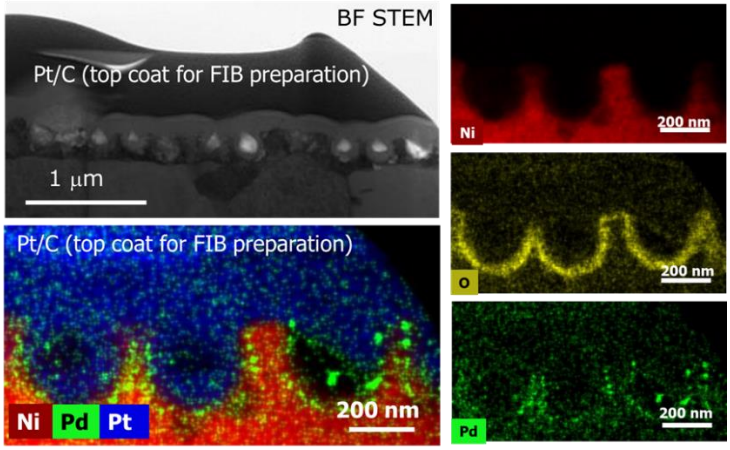


Paul, Michael T.Y.; Zhang, Xin; Yee, Brenden; Gates, Byron D., *Microsc. Microanal.*, **2015**, 21 (S3), 2131-2132

### 8.1.3 Hierarchical Surface Coatings of Polystyrene Nanofibers and Silica Microparticles with Rose Petal Wetting Properties

Surfaces with rose petal like properties, simultaneously exhibiting a high degree of hydrophobicity and a high adhesion to water, were prepared by spray coating of progressively smaller hydrophilic silica particles along with hydrophobic nanofibers onto surfaces of interest. Various polymer structures were achieved by tuning the spray coating flow rates during deposition of the polymer nanofibers and silica particles. At a reduced flow rate, polystyrene fibers were formed with diameters of less than 100 nm. Water contact angles (WCAs) of coatings prepared from the hierarchical assemblies of silica particles blended with polystyrene nanofibers were greater than 110°. Coatings prepared from the hierarchical assemblies either with or without incorporation of the polymer nanofibers pinned water droplets to their surfaces even after inverting the substrates, similar to the properties of a rose petal. Hierarchical coatings of silica particles without the polystyrene nanofibers also exhibited a high adhesion to water, pinning at least 30% more water on its surfaces. Conversely, hierarchical coatings containing the polystyrene nanofibers exhibited an increased water mobility across their surfaces. Further water retention experiments were performed to determine the ability of the different coatings to efficiently condense water vapor, as well as their efficiency to remove this condensed liquid from their surfaces. Both types of hierarchical coatings exhibited an excellent ability to retain water at a low humidity, while establishing a self-limiting condition for retaining water at a high humidity. These coatings could be prepared on a relatively large-scale and with a relatively low cost on the surfaces of a variety of materials to enhance their water resistance, water retention and/or ability to condense water vapor.

**Graphical Abstract**

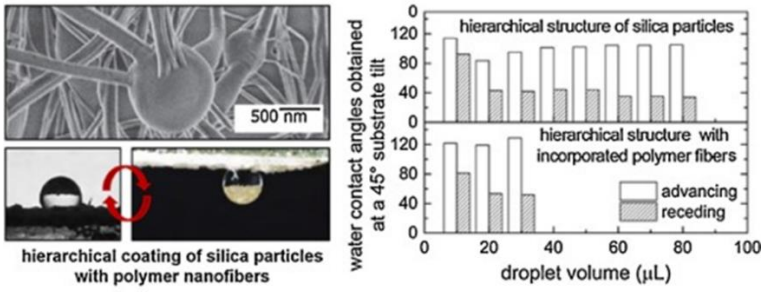


Paul, Michael T. Y.; and Gates, Byron D, *Colloids Surf., A*, **2016**, 498 (5), 42-49

### 8.1.4 Hexagonal Arrays of Cylindrical Nickel Microstructures for Improved Oxygen Evolution Reaction

Fuel-cell systems are of interest for a wide range of applications, in part for their utility in power generation from nonfossil-fuel sources. However, the generation of these alternative fuels, through electrochemical means, is a relatively inefficient process due to gas passivation of the electrode surfaces. Uniform microstructured nickel surfaces were prepared by photolithographic techniques as a systematic approach to correlating surface morphologies to their performance in the electrochemically driven oxygen evolution reaction (OER) in alkaline media. Hexagonal arrays of microstructured Ni cylinders were prepared with features of proportional dimensions to the oxygen bubbles generated during the OER process. Recessed and pillared features were investigated relative to planar Ni electrodes for their influence on OER performance and, potentially, bubble release. The arrays of cylindrical recesses were found to exhibit an enhanced OER efficiency relative to planar nickel electrodes. These microstructured electrodes had twice the current density of the planar electrodes at an overpotential of 100 mV. The results of these studies have important implications to guide the preparation of more active fuel generation by water electrolysis and related processes.

**Graphical Abstract**

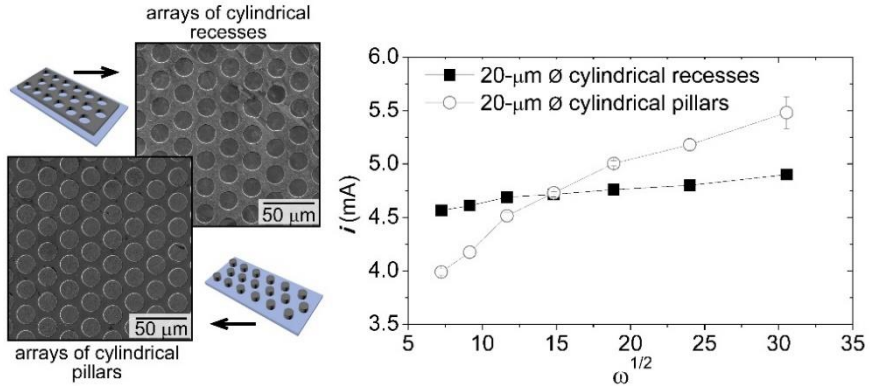


Paul, Michael T. Y.; Yee, Brenden B.; Bruce, David R.; and Gates, Byron D., *ACS Materials and Interfaces*, **2017**, 9 (8), pp 7036–7043

# Appendix 2 Fuel Cell Station Standard Operating Procedures

See additional thesis file for the Scribner proton exchange membrane fuel cell test station operating procedures. The initial release of the testing procedure was established by Michael Paul for 4D LABS for training purposes. The testing facility is available for access at 4D LABS in Simon Fraser University, 8888 University Drive, Burnaby BC, Canada, V5A 1S6.